Veröffentlichungen der DGK

Ausschuss Geodäsie der Bayerischen Akademie der Wissenschaften

Reihe C | Dissertationen | Heft Nr. 906

Matthias O. Willen

On the quantification of ice sheet mass changes and glacial isostatic adjustment effects by combining satellite data

München 2023

Bayerische Akademie der Wissenschaften

ISSN 0065-5325

ISBN 978-3-7696-5318-2

Diese Arbeit ist gleichzeitig veröffentlicht in:
Qucosa – Dokumenten- und Publikationsserver der Sächsischen Landesbibliothek – Staats- und Universitätsbibliothek (SLUB)
https://nbn-resolving.org/urn:nbn:de:bsz:14-qucosa2-839733, Dresden 2023

DGK Veröffentlichungen der DGK

Ausschuss Geodäsie der Bayerischen Akademie der Wissenschaften

Reihe C Dissertationen Heft Nr. 906

On the quantification of ice sheet mass changes and glacial isostatic adjustment effects by combining satellite data

Von der Fakultät Umweltwissenschaften

der Technischen Universität Dresden

zur Erlangung des akademischen Grades

Doktor-Ingenieur (Dr.-Ing.)

genehmigte Dissertation

von

Matthias Oskar Willen, M.Sc.

geboren am 16.10.1990 in Dresden

München 2023

Bayerische Akademie der Wissenschaften

ISSN 0065-5325 ISBN 978-3-7696-5318-2

Diese Arbeit ist gleichzeitig veröffentlicht in:

Qucosa – Dokumenten- und Publikationsserver der Sächsischen Landesbibliothek – Staats- und Universitätsbibliothek (SLUB)

https://nbn-resolving.org/urn:nbn:de:bsz:14-qucosa2-839733, Dresden 2023

Adresse der DGK:

Ausschuss Geodäsie der Bayerischen Akademie der Wissenschaften (DGK)

Alfons-Goppel-Straße 11 ● D – 80 539 München

Telefon +49 - 331 - 288 1685 ● E-Mail post@dgk.badw.de

http://www.dgk.badw.de

Prüfungskommission:

Vorsitzender:	Prof. Dr.-Ing. habil. Lambert Wanninger (Technische Universität Dresden)
Referent:	Prof. Dr.-Ing. Martin Horwath (Technische Universität Dresden)
Korreferenten:	Prof. Dr. techn. Roland Pail (Technische Universität München) Dr. rer. nat. Ingo Sasgen (Alfred-Wegener-Institut, Bremerhaven)

Tag der mündlichen Prüfung: 03.02.2023

ISSN 0065-5325 ISBN 978-3-7696-5318-2

"For a long time we believed that insight –
knowledge of the challenges at hand – would spur action.
But experience has shown that this is simply not the case.
The barriers to sustainable action are many and
we must fully understand them if we are to overcome them."

Mamphela Ramphele, Co-President of the Club of Rome, 2019

Abstract

The satellite gravimetry mission Gravity Record And Climate Experiment (GRACE), which was operational from 2002 to 2017, and its follow-on mission GRACE-Follow-On (GRACE-FO), which has been active since 2018, revolutionized the observation of temporal changes of the Earth's gravitational field. The measurement data from these missions enable the nuanced quantification of mass redistributions on Earth. Water redistributions between continents and oceans caused by climate change are of particular research interest because of their relevance for mankind. These are, for example, the ice mass changes (IMC) of the ice sheets in Antarctica and Greenland, which this work focuses on.

IMC estimates derived from satellite gravimetry data, like from other quantification methods, confirm that both the Greenland Ice Sheet (GIS) and the Antarctic Ice Sheet (AIS) have been losing mass over the last two decades. However, these estimates are subject to large uncertainties, which is particularly the case for the AIS. If the mass balance is obtained from gravimetric observations, a major source of uncertainty is the consideration of effects due to glacial isostatic adjustment (GIA). The uncertainty of the present-day gravitational field changes caused by the isostatic adjustment of the solid Earth to IMC during the last centuries and millennia propagates into estimates of the recent IMC. According to results of the Ice sheet Mass Balance Inter-comparison Exercise (IMBIE), the spread of different modelling results predicting the GIA-induced mass effect in Antarctica is almost as large as the estimated rate of the IMC itself. In Greenland, the spread of the mass effect from different GIA modelling results is approximately 20 % of the rate of IMC. Alternatively, the IMC can be determined using surface elevation changes derived from satellite altimetry observations. In this case, any GIA error hardly affects the results, but there is a significant source of uncertainty in the conversion of volume changes into mass changes.

It is possible to combine data from satellite gravimetry and satellite altimetry to jointly estimate IMC and GIA mass effects, e.g. by solving an inverse problem (joint data inversion). This is an alternative to the use of GIA modelling results in processing satellite gravimetry data. Results from data combination methods are not only a means to an end to improve the estimation of IMC. They also can contribute to answer geodynamic questions. However, previous estimation strategies for combining satellite gravimetry and satellite altimetry data are subject to some limitations. Many approaches only allow to estimate GIA in a regional framework and not in global framework. Other approaches strongly depend on a priori information from geophysical modelling which are subject to large uncertainties. Furthermore, limitations are due to processing choices, e.g. the use of deterministic parameters over defined time intervals or, e.g. due to the consideration of errors in the applied data sets. This work investigates advancements of data combination methods that allow to quantify IMC and present-day GIA effects. Specifically, the approaches investigated here combine measured gravitational field changes from satellite gravimetry, measured surface elevation changes from satellite altimetry, modelled surface mass balances from regional climate modelling, and modelled firn thickness changes from firn modelling.

This cumulative dissertation comprises three publications that investigated three aspects of data combination approaches. The first publication analysed a regional combination approach in Antarctica and results therein demonstrated a significant dependence of the estimated GIA effect on the input data sets and applied processing choices. A bias correction can significantly reduce an initial bias in the determined GIA effect associated to the spherical harmonic coefficients of degree-1 and c_{20}. However, this bias correction regionally constrains the GIA estimate and prevents to implement such an approach in a global framework. The second publication infers long-term mass trends with their temporal changes jointly observed from satellite gravimetry and satellite altimetry data. To do so, a state-space filtering framework was applied to the data sets allowing to estimate temporal changes of the parameters over time while accounting for temporal correlation of short-term fluctuations. Thereby, an accelerating ice-dynamically induced ice mass loss is found for drainage basins in West Antarctica. In contrast, the temporal variability of long-term trends in East Antarctica is low. Noteworthy, the trends in Dronning Maud Land and Enderby Land are positive. The third publication presents a global approach to jointly estimate IMC, GIA effects and firn thickness changes, while accounting for spatial error covariances of the input data sets. The intention of the utilized GIA parametrization in Antarctica is to spatially resolve GIA effects that were not predicted by GIA models. Simulation experiments demonstrated the feasibility of the approach under the presence of realistic limitations of satellite observations and model products.

This framework paper also reports a first application of the inversion method of Publication 3 to real data. The focus of this application is on Antarctcia over the time interval January 2011 to December 2020. Results for the AIS are: (i) an IMC of $(-150 \pm 5)\,\mathrm{Gt\,a^{-1}}$, (ii) a change of the firn air content of $(40 \pm 5)\,\mathrm{km^3\,a^{-1}}$, and (iii) an integrated GIA-induced mass effect of $(72 \pm 4)\,\mathrm{Gt\,a^{-1}}$. These results are promising with regard to the application of this methodology, as they are similar to previously published estimates. But they are estimated in a globally consistent framework and without applying conventional filtering strategies. Future work should further improve the methodology and eventually implement it in a global inversion framework that allows to jointly estimate all sea-level contributions.

Zusammenfassung

Die Satellitengravimetriemission Gravity Record And Climate Experiment (GRACE), die von 2002 bis 2017 aktiv war, sowie die seit 2018 aktive Nachfolgemission GRACE-Follow-On (GRACE-FO) revolutionierten die Beobachtung zeitlicher Änderungen des Gravitationsfeldes der Erde. Die Messdaten dieser Missionen ermöglichen die differenzierte Quantifizierung von Massenumverteilungen auf der Erde. Von besonderen Forschungsinteresse, aufgrund ihrer Relevanz für die Menschheit, sind dabei durch den Klimawandel verursachte Umverteilungen von Wasser zwischen den Kontinenten und dem Ozean. Das sind beispielsweise die Eismassenänderungen der Eisschilde in Antarktika sowie Grönland, die im Fokus dieser Arbeit stehen.

Aus Messdaten der Satellitengravimetrie ermittelte Eismassenänderungen bestätigen, wie auch andere Quantifizierungsmethoden, dass der Grönländische Eisschild sowie der Antarktische Eisschild während der letzten zwei Jahrzehnte an Masse verloren haben. Allerdings sind diese Schätzungen mit großen Unsicherheiten behaftet, was insbesondere auf den Antarktischen Eisschild zutrifft. Wird die Massenbilanz mit gravimetrischen Beobachtungen ermittelt, ist eine wesentliche Quelle für die Unsicherheit die Berücksichtigung der Effekte aufgrund des glazial-isostatischen Ausgleichs (GIA). Die Unsicherheit über die gegenwärtigen Änderungen des Gravitationsfeldes, aufgrund des isostatischen Ausgleichs der festen Erde an Eismassenänderungen während der letzten Jahrhunderte und Jahrtausende, pflanzt sich in die Schätzung rezenter Massenänderungen fort. Laut Ergebnissen von vergleichenden Untersuchungen zu Eisschildmassenbilanzen (Ice sheet Mass Balance Inter-comparison Exercise, IMBIE) ist in Antarktika die Bandbreite unterschiedlicher Modellierungen des GIA-induzierten Masseneffekts fast so groß wie die ermittelte Rate der Eismassenänderung selbst. In Grönland beträgt die Bandbreite des Masseneffekts unterschiedlicher GIA-Modellierungen ungefähr 20 % der Eismassenänderungsrate. Alternativ lassen sich die Eismassenänderungen mittels Oberflächenhöhenänderungen bestimmen, die aus Beobachtungen der Satellitenaltimetrie abgeleitet werden. Dabei beeinflussen GIA Fehler die Ergebnisse kaum, allerdings besteht dabei eine wesentliche Quelle der Unsicherheit bei der Konversion von Volumenänderungen in Massenänderungen.

Es besteht die Möglichkeit, Daten der Satellitengravimetrie sowie der Satellitenaltimetrie zu kombinieren und somit die Eismassenänderungen sowie GIA-Masseneffekte gemeinsam zu bestimmen, z. B. als Lösung eines inversen Problems (gemeinsame Dateninversion). Dies ist eine Alternative zur Verwendung von Ergebnissen der GIA-Modellierung in der Datenprozessierung der Satellitengravimetrie. Ergebnisse von Datenkombinationsmethoden sind dabei nicht nur ein Mittel zum Zweck, um die Schätzung von Eismassenänderungen zu verbessern. Sie können auch zur Beantwortung geodynamischer Fragestellungen beitragen. Allerdings unterliegen bisherige Schätzverfahren, die Daten der Satellitengravimetrie und Satellitenaltimetrie kombinieren, Limitierungen. Viele Ansätze ermöglichen die GIA Schätzungen nur in einem regionalen Rahmen und nicht in einem globalen Rahmen. Andere Ansätze hängen stark von Vorinformationen der geophysikalischen Modellierung ab, die aber große Unsicherheiten aufweisen. Außerdem ergeben sich Limitierungen durch gewählte Prozessierungsentscheidungen, wie z. B. durch die Verwendung deterministischer Parameter über definierte Zeitintervalle oder z. B. durch die Berücksichtigungen der Fehler der verwendeten Datensätze. Diese Arbeit untersucht Weiterentwicklungen von Datenkombinationsmethoden, welche die Quantifizierung von Eismassenänderungen und des gegenwärtigen GIA-induzierten Masseneffekts ermöglichen. Konkret kombinieren die hier untersuchten Ansätze: gemessene Gravitationsfeldänderungen der

Satellitengravimetrie, gemessene Oberflächenhöhenänderungen der Satellitenaltimetrie, modellierte Oberflächenmassenbilanzen sowie modellierte Firndickenänderungen der regionalen Klimamodellierung.

Diese kumulative Dissertation umfasst drei Publikationen, die drei Aspekte von Datenkombinationsansätzen untersuchten. Die erste Publikation analysierte einen regionalen Kombinationsansatzes in Antarktika und die Ergebnisse zeigten eine bedeutende Abhängigkeit des ermittelten GIA-Effekts von den verwendeten Eingangsdatensätzen und Prozessierungsentscheidungen. Ein ursprünglicher Bias im ermittelten GIA-Effekt, aufgrund der sphärisch-harmonischen Koeffizienten vom Grad-1 sowie c_{20}, kann durch eine Biaskorrektur erheblich reduziert werden. Dadurch sind die GIA-Schätzungen allerdings regional beschränkt und es wird verhindert, dass ein solcher Ansatz in einem globalen Rahmen implementiert werden kann. Die zweite Publikation ermittelt Langzeitmassentrends zusammen mit deren zeitlichen Änderungen, die von der Satellitengravimetrie und Satellitenaltimetrie gemeinsam beobachtet werden. Hierfür wurde ein Zustandsraumfilterverfahren auf die Datensätze angewandt, das es ermöglicht, die zeitlichen Veränderungen der Parameter über die Zeit zu bestimmen, unter der Berücksichtigung zeitlicher Korrelation kurzfristiger Fluktuationen. Dabei zeigt sich für Abflussbecken in der Westantarktis ein sich beschleunigender eisdynamisch induzierter Eismassenverlust. Dagegen ist die zeitliche Variabilität der Langzeittrends in der Ostantarktis gering. Bemerkenswert ist, dass die Trends im Dronning Maud Land und Enderby Land positiv sind. Die dritte Publikation präsentiert einen globalen Ansatz, der die gemeinsame Schätzung von Eismassenänderung, der GIA-Effekte sowie Änderungen der Firndicke ermöglicht, unter der Berücksichtigung räumlicher Fehlerkovarianzen. Bei der Wahl der GIA-Parametrisierung in Antarktika wurde die Intention verfolgt, GIA-Effekte räumlich aufzulösen, die bisher nicht von GIA-Modellen vorhergesagt wurden. Mit Simulationsexperimenten konnte die Machbarkeit des Ansatzes unter realistischer Limitierungen der Satelliten- und Modellprodukte demonstriert werden.

Diese Rahmenschrift präsentiert auch eine erste Anwendung der Inversionsmethode aus Publikation 3 unter Verwendung echter Daten. Der Fokus dieser Anwendung liegt auf Antarktika über das Zeitintervall Januar 2011 bis Dezember 2020. Ergebnisse für den Antarktischen Eisschild sind: (i) eine Eismassenänderung von $(-150 \pm 5)\,\mathrm{Gt\,a^{-1}}$, (ii) eine Änderung des Luftgehalts der Firnschicht von $(40 \pm 5)\,\mathrm{km^3\,a^{-1}}$ und (iii) ein integrierter GIA-induzierter Masseneffekt von $(72 \pm 4)\,\mathrm{Gt\,a^{-1}}$. Diese Ergebnisse sind vielversprechend mit Hinblick auf die Anwendbarkeit der Methode, da sie vergleichbar zu bereits publizierten Ergebnissen sind. Dabei wurden sie in einem global-konsistenten Rahmen ohne die Anwendung konventioneller Filterungen ermittelt. Im Zuge zukünftigen Arbeiten soll die Methodik weiter verbessert werden und schließlich in einem globalen Inversionsrahmen implementiert werden, der die Bestimmung aller Meeresspiegelbeiträge gemeinsam ermöglicht.

Contents

1 Introduction

Climate change affects the living conditions on Earth and thus is of crucial relevance for mankind. The quote by M. Ramphele on the first page of this thesis emphasizes that the knowledge gained by science about climate change and its consequences does not necessarily lead to action required to ensure sustainability. Nevertheless, scientific knowledge forms the objective basis in decision making. An essential and measurable indicator of global climate change is the redistribution of the water between the oceans and the continents. The two contemporary ice sheets on Earth (Figure 1.1)—the Greenland Ice Sheet (GIS) and the Antarctic Ice Sheet (AIS)—are the largest reservoirs of water on the continents. The ice sheets' ice mass change (IMC) caused $\sim$27 % of the global mean sea level rise from 2006 to 2018. During this time period estimates of the observed global mean sea level rise range from 3.21 to 4.17 mm a^{-1} and estimates of the ice sheets' contribution range from 0.75 to 1.24 mm a^{-1} (Fox-Kemper et al., 2021). This large spread in estimates of the ice sheets' contribution to sea level change motivates to investigate and resolve the underlying reasons.

The degree of continental glaciation indicates Earth's climate state. A cooling climate leads to glaciation of the continents and a decreasing sea level, vice versa a warming climate leads to deglaciation and a rising sea level. The last ice age ended $\sim$12 ka ago with the beginning of the Holocene. Already since the last glacial maximum ($\sim$20 ka ago) the climate has been warming and deglaciation has been occurring accompanied by a rising sea level (Lambeck et al., 2014), apart from shorter (regional) glaciation phases. Currently, the AIS and especially the GIS are losing ice mass and are already significant contributors to sea level rise. Simulations show a significant relevance of both ice sheets' contribution to sea level change in the course of a warming climate (Fox-Kemper et al., 2021; Palmer et al., 2020). Reliable estimates of the contemporary, i.e. recent, ice sheet mass changes and the attribution to the underlying processes form the basis for projections of future climate change impacts on the environment.

Mass redistributions between an ice sheet and the ocean occur via two interfaces: firstly, via the interface between the ice sheet and the ocean, and secondly, via the interface between the ice sheet and the atmosphere. Via the first interface, glaciers transport ice to the ocean termed *ice flow dynamics* (IFD), where it is discharged into the ocean by iceberg calving. In addition to the ice, meltwater of former ice, termed meltwater runoff, enters the ocean (including subglacial water runoff). The term *ice discharge* means the flux of ice from the continent across the grounding line of an ice sheet. Either glaciers calve icebergs close to the grounding line directly into the ocean (typical for the GIS), or the floating ice forms an ice shelf which calves icebergs off shore the grounding line into the ocean (typical for the AIS). The IFD depends on the basal conditions (e.g. friction), sediment transport, and, in the case of the AIS, is linked to processes affecting the ice shelves. For example, the ice shelves have a buttress effect on the continental glaciers and thus control their ice dynamic flow towards the ocean. Furthermore the grounding line is not fix and can retreat by basal ice shelf melting (Dupont and Alley, 2005). The involved processes causing mass changes via the second interface are summarized under the term *surface mass balance* (SMB). SMB includes precipitation (in particular surface accumulation by snowfall), sublimation, and wind drift processes. SMB also includes the triggering of snow, firn, and ice melt (surface melting) by radiation and atmospheric warming, which subsequently runs off the ice sheet as meltwater or refreezes. Conventionally, a distinction is made between accumulation (precipitation, snowdrift deposition) and ablation (melting, sublimation, wind erosion). In a

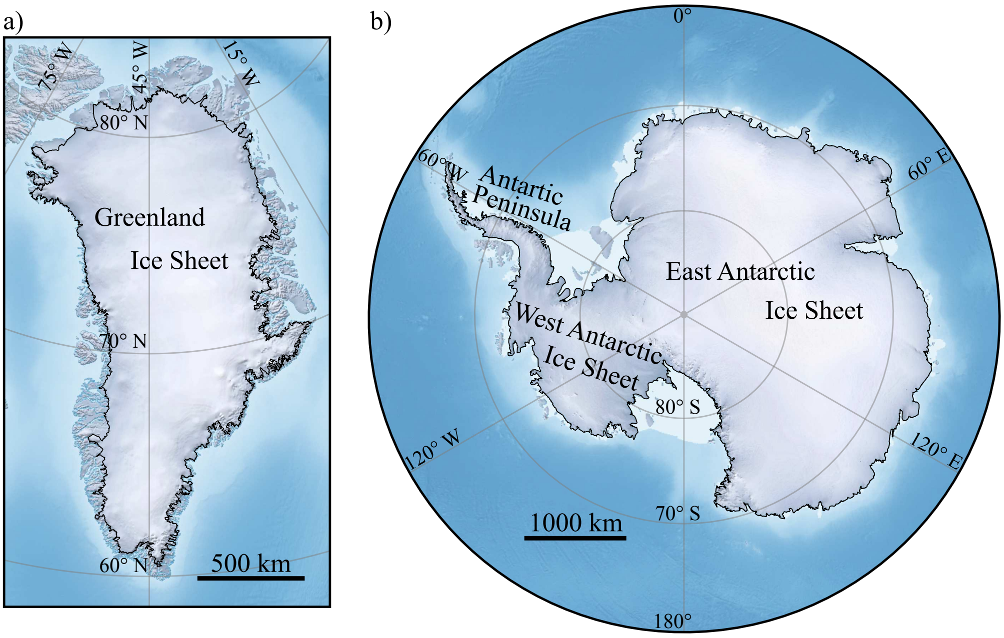

Figure 1.1: a) The Greenland Ice Sheet (GIS) and b) The Antarctic Ice Sheet (AIS) with their grounding lines (black solid line) from Zwally et al. (2012). The AIS is commonly divided into the East Antarctic Ice Sheet (EAIS), the West Antarctic Ice Sheet (WAIS), and the Antarctic Peninsula (APIS). The map dataset is obtained from Patterson and Kelso et al. (2022).

simplified view, accumulation refers to the input of an ice sheet, i.e. the mass that is added to the ice sheet (mass gain). Ablation and ice discharge refer to the output, i.e. the ice mass that leaves the ice sheet (mass loss). The (total) mass balance of an ice sheet is the difference between the input and output. If the mass balance is zero, it means that the ice sheet is stable or in equilibrium. If the input and output are not in balance, the ice sheet system will tend towards a new equilibrium state, e.g. the IFD adjusts to a changed accumulation (Hanna et al., 2020).

Changes in mass of the ice sheets and the ocean are accompanied by deformations of the solid Earth. This happens immediately, i.e. instantaneously. A change in load due to a displacement of mass leads to an elastic deformation of the solid Earth. In addition, the Earth also deforms visco-elastically. Every imposed load change causes the solid Earth to be out of isostatic equilibrium. The subsequent adjustment process of the solid Earth by its visco-elastic deformation is called glacial isostatic adjustment (GIA). This process is associated with displacement of material (mass redistribution) in the solid Earth by viscous flow and can last over time scales from decades to several millennia. The visco-elastic deformation of the solid Earth depends on its rheological properties and the history of induced changes in loading, referred to as ice history or glaciation history. A present-day GIA effect may have been triggered by load changes from a long time ago. In Antarctica, the IMC and the present-day GIA mass effect are on the same order of magnitude. Noticeably, there is a large uncertainty in predicting the present-day GIA effect with geophysical forward modelling. According to Shepherd et al. (2018), the mass balance of the AIS is $(-105 \pm 51)\,\mathrm{Gt\,a^{-1}}$ from 2003 until 2010 and the modelled GIA effect varies between $+3\,\mathrm{Gt\,a^{-1}}$ and $+81\,\mathrm{Gt\,a^{-1}}$. The mass balance of the GIS is $(-255 \pm 20)\,\mathrm{Gt\,a^{-1}}$ and the modelled GIA effect spreads from $-27\,\mathrm{Gt\,a^{-1}}$ to $+21\,\mathrm{Gt\,a^{-1}}$ (Shepherd et al., 2019). The uncertainty of modelled GIA also propagates to global mean sea level estimates from satellite gravimetry (Horwath et al., 2022; Kim et al., 2022). The Sixth Assessment Report of the Intergovernmental Panel on Climate Change (IPCC) (Fox-Kemper et al., 2021) concluded that there is only *medium confidence*

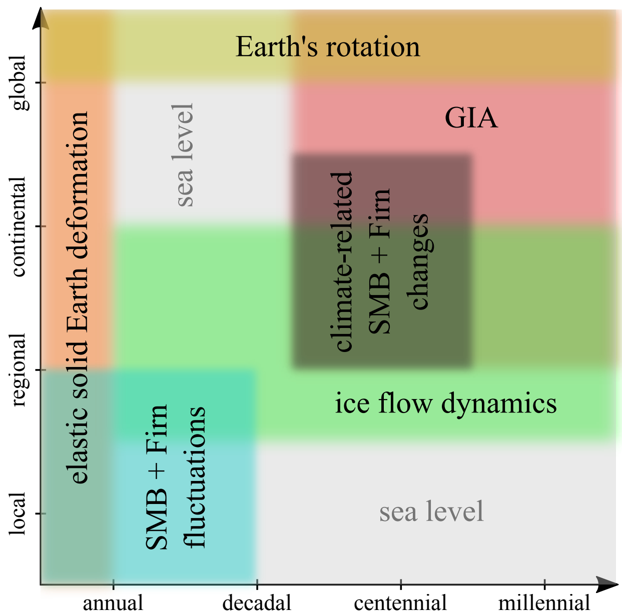

Figure 1.2: The qualitative relation of spatial and temporal response scales of the interconnected processes between ice sheets, the solid Earth, and sea level changes. Surface mass balance (SMB) and glacial isostatic adjustment (GIA) are abbreviated in the figure.

in understanding GIA.

Furthermore, mass redistribution between ice sheets and oceans as well as solid-Earth deformation change components of Earth's inertia tensor. This leads to Earth rotation changes, i.e. changes in rotation velocity and the orientation of the rotation axis referred to as polar motion or true polar wander depending on the considered time scales (Mitrovica and Wahr, 2011; Göttl et al., 2021). This also means that GIA is accompanied by a deformation of the entire figure of the Earth and by geocentre motion (Mitrovica and Wahr, 2011; Spada and Melini, 2019). Moreover, (de)glaciation and GIA may affect the stress regime in the lithosphere and are thus also related to brittle-tectonic deformation, e.g. through the reactivation of existing faults (Steffen et al., 2014). Further links between the solid Earth and the ice sheets are e.g. that deglaciation can favour volcanism due to unloading (Sigmundsson et al., 2010) or that geothermal heat flow affects the continental basal melting (Dziadek et al., 2021). GIA effects even play a role in understanding ancient human migration (Borreggine et al., 2022).

The ice sheets, the ocean, and the solid Earth can be distinguished as three components of the Earth system. They interact on mass redistribution between the continent and the ocean across a wide range of spatial and temporal scales (Figure 1.2). The comprehensive consideration of the coupled processes of these components and how they feed each other, e.g. due to self-gravitational effects, is a challenge in simulations and data evaluations (Whitehouse, 2018). Today and since several decades, global satellite methods are available that allow to measure the spatio-temporal changes of the Earth's gravity field and geometry. Data from these methods allow to investigate the coupled processes and feedbacks between ice sheets, ocean, and the solid Earth. In particular relevant for this are the mission Gravity Record And Climate Experiment (GRACE) (Tapley et al., 2004), and its follow-on mission (GRACE-FO) (Chen et al., 2022), as well as several satellite altimetry missions measuring surface elevation changes over ice sheets (Schröder et al., 2019; Nilsson et al., 2022).

This thesis results from research conducted in two consecutive research projects funded by Deutsche

Forschungsgemeinschaft (DFG, English: German Research Foundation): "Reconciling ocean mass change and GIA from satellite gravity and altimetry" (OMCG) and its successor OMCG-2, which are part of the Special Priority Programme (SPP-1889) Regional Sea Level Change & Society (SeaLevel)[1]. The SPP-1889 SeaLevel covers research projects from natural sciences to socio-economics. The topics range from quantifying sea level changes to their impacts on societies. The relevance of such a broad research programme, with its many interdisciplinary research projects, is also emphasized by the issue claimed in the quote at the beginning of this thesis. Both OMCG project proposals hypothesized that

- methodological issues in the satellite gravimetry data analysis and
- the large uncertainty in predicting the present-day GIA effect by geophysical modelling

lead to a large discrepancy of ocean mass change estimates. For example, WCRP Global Sea Level Budget Group (2018), Horwath et al. (2022), and Kim et al. (2022) demonstrated this. This work is a contribution to resolve these discrepancies by investigating the following research questions:

- What are appropriate estimation methods and parametrization strategies to attribute observed gravity field and surface elevation changes over ice sheets to their sources?
- What is a feasible approach to quantify GIA effects in a globally consistent framework using satellite observations rather than geophysical GIA modelling?

It is hypothesized that the quantification of GIA, along with IMC, can be improved with methodological developments that pursue the following objectives: Firstly, a combination method should take the spatio-temporal sampling and error characteristics of the input datasets rigorously into account. This refers to data from satellite gravimetry, satellite altimetry, climate modelling, and firn modelling. Secondly, a combination method should use a physically reliable parametrization. Thirdly, GIA and IMC should be resolved in a globally consistent framework. To achieve these objectives three research articles, the Publications 1–3 (P1–3), have been published within the framework of this cumulative dissertation (Chapter 5):

P1: Willen, M.O., M. Horwath, L. Schröder, A. Groh, S.R.M. Ligtenberg, P. Kuipers Munneke, and M.R. van den Broeke (2020). "Sensitivity of inverse glacial isostatic adjustment estimates over Antarctica". Published in: The Cryosphere 14.1, pp. 349–366.

P2: Willen, M.O., T. Broerse, A. Groh, B. Wouters, P. Kuipers Munneke, M. Horwath, M.R. van den Broeke, and L. Schröder (2021). "Separating Long-Term and Short-Term Mass Changes of Antarctic Ice Drainage Basins: A Coupled State Space Analysis of Satellite Observations and Model Products". Published in: Journal of Geophysical Research: Earth Surface 126.6, e2020JF005966.

P3: Willen, M.O., M. Horwath, A. Groh, V. Helm, B. Uebbing, and J. Kusche (2022). "Feasibility of a global inversion for spatially resolved glacial isostatic adjustment and ice sheet mass changes proven in simulation experiments". Published in: Journal of Geodesy, 96:75.

First, Chapter 2 presents the theoretical background of the processes that lead to mass and volume changes of ice sheets along with sea level change and solid Earth deformation. This is followed by Chapter 3, which provides an outline of the used satellite data sets and modelling outputs. Chapter 4 is an overview of the methodology for data combination strategies and Chapter 5 includes the peer-reviewed research articles published in the course of this work. Chapter 6 presents and discusses first results of an application of the inversion methodology described in P3 (Willen et al., 2022). The application focuses on Antarctica. Finally, Chapter 7 gives an outlook and Chapter 8 summarizes the most important conclusions.

[1] `https://spp-sealevel.de`

2 Processes over ice sheets inducing changes in Earth's gravity and geometry

2.1 Fundamentals of Earth's gravity and geometry

The potential of Earth's gravity, W, at a position, $\boldsymbol{x}$ ($\boldsymbol{x} \in \mathbb{R}^3$), is the sum of Earth's gravitational potential, V, and the centrifugal potential, Φ (Heiskanen and Moritz, 1967):

$$W(\boldsymbol{x}, t) = V(\boldsymbol{x}, t) + \Phi(\boldsymbol{x}, t). \tag{2.1}$$

The position vector has the spherical coordinates, $\boldsymbol{x} = (\theta, \lambda, r)^{\mathrm{T}}$, with the colatitude, θ, longitude, λ, and the Euclidean distance to the geocentre, $r \equiv |\boldsymbol{x}|$. The potentials depend on time, t. The gravitational potential is the potential of the force resulting from mass attraction of bodies and can be derived from Newton's law of universal gravitation. For the Earth body the gravitational potential results from its density distribution which can be described by dividing the Earth into infinitesimal mass elements. The (mass) density, ρ, links the mass element, $\mathrm{d}M$, and the volume element, $\mathrm{d}\mathcal{V}$, by $\mathrm{d}M = \rho\,\mathrm{d}\mathcal{V}$. The gravitational potential at the position, $\boldsymbol{x}$, is the volume integral over all elements of the Earth (at the time, t_0):

$$V(\boldsymbol{x}, t = t_0) = G \iiint\limits_{\text{Earth}} \frac{\mathrm{d}M}{l} = G \iiint\limits_{\text{Earth}} \frac{\rho}{l} \mathrm{d}\mathcal{V}, \tag{2.2}$$

with the gravitational constant, G, and the Euclidean distance, l, between the mass element, $\mathrm{d}M$, and $\boldsymbol{x}$ (Heiskanen and Moritz, 1967). Any displacement of mass element(s) over time, i.e. a change of the density distribution, affects the gravitational potential over time. The gravitational field in the exterior of the Earth can be described with a Laplace's differential equation of the second order. The solution of this differential equation with a boundary condition at the surface of a sphere (Dirichlet problem) leads to the expression of the gravitational potential developed into a series of spherical harmonic basis functions, Y_{nm}, of degree, n, and order, m (Heiskanen and Moritz, 1967). The gravitational potential in the exterior of a sphere with Earth's mass, M_E, and the radius, R, (the semi-major axis of the reference ellipsoid) then reads:

$$V(\boldsymbol{x}, t) = \frac{GM_E}{R} \sum_{n=0}^{\infty} \left(\frac{R}{r}\right)^{n+1} \sum_{m=-n}^{n} c_{nm}(t) Y_{nm}(\theta, \lambda). \tag{2.3}$$

$c_{nm}(t)$ is a spherical harmonic coefficient of the gravitational potential, the Stokes coefficient. Y_{nm} refers to fully normalized (or 4π-normalized) orthogonal spherical harmonics and $c_{nm}(t)$ are their amplitudes over time. The factor GM_E/R guarantees that the Stokes coefficient is dimensionless. Y_{nm} are defined at the surface of the sphere at the position $(\theta, \lambda)^{\mathrm{T}}$ as follows:

$$Y_{nm}(\theta, \lambda) = a_{n|m|} P_{n|m|}(\cos\theta) \begin{cases} \cos m\lambda, & \text{if } m \geq 0 \\ \sin |m|\lambda, & \text{if } m < 0 \end{cases}. \tag{2.4}$$

$P_{n|m|}(\cos\theta)$ is the Legendre function and the normalization factor, $a_{n|m|}$, ensures that the average square of each Y_{nm} over the sphere is unity (Heiskanen and Moritz, 1967).

The second term in Equation 2.1 is the centrifugal potential and results from the Earth's rotation with the rotation vector, $\boldsymbol{\omega}$, (Torge and Müller, 2012):

$$\Phi(\boldsymbol{x}, t) = \frac{(\boldsymbol{\omega}(t) \times \boldsymbol{x})^2}{2}. \tag{2.5}$$

The time dependence of $\boldsymbol{\omega}(t)$ denotes that the Earth's rotation vector changes over time, i.e. the orientation of the Earth's rotational axis (polar motion or true polar wander) and its angular velocity (length of day changes), $\omega = |\boldsymbol{\omega}|$, vary over time.

The gravity field, $\boldsymbol{g}$, is a conservative vector field defined as the gradient of Earth's gravity potential, $\boldsymbol{g} = \operatorname{grad} W$ (Heiskanen and Moritz, 1967) and results from the gravitational potential and the centrifugal potential (Equation 2.1). Note that the term gravitational field only refers to the conservative vector field of the gravitational potential, $\operatorname{grad} V$, without accounting for the centrifugal potential. A gravity vector is one vector of the gravity field at a certain position in the Earth's exterior, $\boldsymbol{x}_0$, i.e. the gravity vector is an acceleration vector. Its magnitude is called gravity, $g(\boldsymbol{x}_0) = |\boldsymbol{g}(\boldsymbol{x}_0)|$, i.e. the acceleration magnitude. With a spherical homogenous approximation of the Earth, the gravity is simply:

$$g(r) = \frac{GM_E}{r^2}, \qquad \text{if} \quad r \geq R. \tag{2.6}$$

Any redistribution of mass (elements) in the Earth system leads to temporal changes of the Earth's gravity potential (Equation 2.1). Temporal changes of physical quantities can be expressed as differences between two epochs, e.g. $\Delta V(\boldsymbol{x}) = V(\boldsymbol{x}, t = t_1) - V(\boldsymbol{x}, t = t_0)$ (Δ means a difference and is not to be confused with the Laplacian operator). Alternatively, temporal changes of physical quantities can be expressed with mean rates of change over a time interval, e.g. estimated using least-squares adjustment. For example, the temporal mean rate of the gravitational potential referring to a chosen time interval, $[t_0;\, t_0 + \Delta t]$, may be indicated using Newton's notation, $\dot{V}(\boldsymbol{x})\big|_{[t_0;\, t_0+\Delta t]}$, or simply, $\dot{V}$.

The time dependency of the Stokes coefficients (Equation 2.3) express the time dependency of the gravitational potential, i.e. any change of the gravitational potential is related to a change of the Stokes coefficients:

$$\dot{V}(\boldsymbol{x}) = \frac{GM_E}{R} \sum_{n=0}^{\infty} \left(\frac{R}{r}\right)^{n+1} \sum_{m=-n}^{n} \dot{c}_{nm} Y_{nm}(\theta, \lambda). \tag{2.7}$$

Note that the spherical harmonic coefficient c_{00} accounts for the total mass of the system under investigation, i.e. $c_{00} \propto M_E$, if the whole Earth is under investigation. Here, any mass exchange of the Earth with space is neglected and mass conservation in the Earth system is assumed, $\dot{c}_{00} \stackrel{!}{=} 0$. However, if only a region or subsystem, rather than the whole Earth, is under investigation using the global representation with spherical harmonic coefficients, the c_{00} coefficient in this particular case may change over time.

The spherical harmonic representation of the gravitational potential enables the direct evaluation of its spatial scales, as the degree can be interpreted as the spatial "frequency". The spatial resolution for each degree is roughly $20\,000\,\mathrm{km}/n$ and the degree variance, e.g. for Stokes coefficients, is (Heiskanen and

Moritz, 1967):

$$\mathrm{Var}(c_n) = \sum_{n=-m}^{m} c_{nm}^2. \tag{2.8}$$

Degree amplitudes are the square root of degree variances and the degree amplitude of a degree is analogous to an amplitude associated to a certain frequency in the 1-D case. The degree amplitudes of a certain range of degrees represent the amplitude spectrum over these spatial scales.

As an alternative to the formulation of a changing gravitational potential, geoid height changes may be used with a spherical approximation of the Earth surface:

$$\dot{N}(\theta, \lambda) = R \sum_{n=0}^{\infty} \sum_{m=-n}^{n} \dot{c}_{nm} Y_{nm}(\theta, \lambda). \tag{2.9}$$

However, the gravitational field changes expressed as changes of the gravitational potential (Equation 2.7) or geoid heights (Equation 2.9) do not allow a direct link to the underlying mass redistributions causing the gravitational field changes. Explaining gravitational field changes with mass redistributions within the Earth system is an ambiguity problem. A possibility to tackle this is to express gravitational field changes as surface density changes (also known as area density changes). This is appropriate in cases where the mass changes of interest occur near the Earth's surface, i.e. in the vicinity of R. Mass changes at the surface are also referred to as surface load changes. To do so, the ambiguity problem is simplified by assuming that all mass redistributions take place in a spherical layer with a radius that equals R (Wahr et al., 1998). This means any gravitational field change is expressed as a mass change per unit area in this spherical layer. Furthermore, any load change due to mass redistribution accompanies with elastic deformation of the solid Earth which induces an additional change of the gravitational potential (more details of solid-Earth deformation are provided in Section 2.3). The surface density change implicitly accounts for the elastic-induced potential change. The gravitational field change expressed as surface density change, $\dot{\kappa}$, at a position at the Earth's surface, can be developed into a series of spherical harmonic coefficients:

$$\dot{\kappa}(\theta, \lambda) = \sum_{n=0}^{\infty} \sum_{m=-n}^{n} \dot{\kappa}_{nm} Y_{nm}(\theta, \lambda). \tag{2.10}$$

The link between the coefficient of surface density change, $\dot{\kappa}_{nm}$ and the change of a Stokes coefficient is (Wahr et al., 1998):

$$\dot{\kappa}_{nm} = \frac{2n+1}{1+k'_n} \frac{M_E}{4\pi R^2} \dot{c}_{nm}. \tag{2.11}$$

$1+k'_n$ considers both, the gravitational change directly caused by the mass change ("1") and the gravitational effect due to elastic deformation of the solid Earth. The latter effect is described with the load Love number, k'_n, which can be estimated using a rheological model (Section 2.3). For $n \geq 2$ gravitational field changes available as Stokes coefficients can be uniquely expressed as surface density changes (Equation 2.10):

$$\dot{\kappa}(\theta, \lambda) = \frac{M_E}{4\pi R^2} \sum_{n=2}^{\infty} \frac{2n+1}{1+k'_n} \sum_{m=-n}^{n} \dot{c}_{nm} Y_{nm}(\theta, \lambda). \tag{2.12}$$

This equation is uniquely valid for degrees higher than one only, because, the degree-1-coefficients (c_{10}, c_{11}, c_{1-1}) depend on the chosen Earth's reference frame. Blewitt (2003) described isomorphic terrestrial reference frames that allow for linking the degree-1 component of a surface load to the load Love number theory. For instance, isomorphic reference frames are reference frames fixed to the centre of mass of the Earth system (CM), centre of mass of the solid Earth (CE), and centre of the Earth's surface figure (CF). Depending on the rheological model, specific load Love numbers of degree-1 can be derived for these reference frames which allow a conversion between the different reference frames. Note that CF and CE are close in proximity to each other and CF can be used to approximate CE. In the CM frame the degree-1 component of the surface load induced gravitational field effect is zero. In contrast, the CE or CF origin shifts in relation to the CM which reflects in non-zero degree-1 coefficients with respect to CE or CF fixed reference frames. The shift in relation to CM is called geocentre motion (Blewitt, 2003). The full recovery of surface mass changes from gravitational field changes requires the knowledge of their degree-1 mass contribution and is essential for the investigation of ice sheet and ocean mass redistributions (Swenson et al., 2008).

It is common to express the surface density as an *equivalent water height* (EWH). $1\,\mathrm{kg\,m^{-2}}$ corresponds to 1 mm EWH. 1 kg water with a density of $1000\,\mathrm{kg\,m^{-3}}$ (i.e. 1 L of water) distributed on an area of $1\,\mathrm{m^2}$ results in a water layer with a height of 1 mm. For instance, this is also how precipitation amounts are commonly reported.

The mass change, $\dot{M}$, of a region of interest, D, being part of Earth's surface, is the surface integral of the surface density changes of the surface elements, $\mathrm{d}D$, over this region (or domain). The surface integral is:

$$\dot{M}_D = \iint\limits_D \dot{\kappa}(\theta,\lambda)\,\mathrm{d}D = R^2 \iint\limits_D \dot{\kappa}(\theta,\lambda)\sin\theta\,\mathrm{d}\theta\,\mathrm{d}\lambda, \tag{2.13}$$

using a spherical approximation of an Earth's surface element, $\mathrm{d}D = R^2 \sin\theta\,\mathrm{d}\theta\,\mathrm{d}\lambda$.

Earth's geometry changes can be expressed with surface elevation changes, $\dot{h}$, and volume changes in a region, $\dot{\mathcal{V}}_D$. A surface elevation change is the change of the radial distance between a Earth surface element, $\mathrm{d}D$, and the coordinate origin of the reference frame over time. Analogous to Equation 2.13, $\dot{\mathcal{V}}_D$ can be defined as follows:

$$\dot{\mathcal{V}}_D = \iint\limits_D \dot{h}(\theta,\lambda)\,\mathrm{d}D = R^2 \iint\limits_D \dot{h}(\theta,\lambda)\sin\theta\,\mathrm{d}\theta\,\mathrm{d}\lambda. \tag{2.14}$$

An illustrative example for a region D may be an ice sheet. If the mass loss of the ice sheet is higher than the mass gain, $\dot{M}_D < 0$, the ice sheet shrinks, i.e. the volume of the ice sheet decreases, $\dot{\mathcal{V}}_D < 0$ assuming there is no significant decrease in snow and firn density which would compensate for the loss of volume.

2.2 The ice sheet mass balance and changes of the firn air content

The (total) mass balance of an ice sheet is the sum of the mass input and output. If the ice sheet is gaining (loosing) mass, the mass balance is positive (negative). The mass balance is governed, on the one hand, by mass fluxes due to SMB and, on the other hand, by ice discharge as well as (basal) meltwater runoff into the ocean. The base of the grounded ice sheet is the interface between the ice sheet and bedrock. At this interface basal sediments and basal meltwater are present (Singh et al., 2011).

The term *surface mass balance* (SMB) summarizes mass fluxes at the surface of an ice sheet, i.e. at

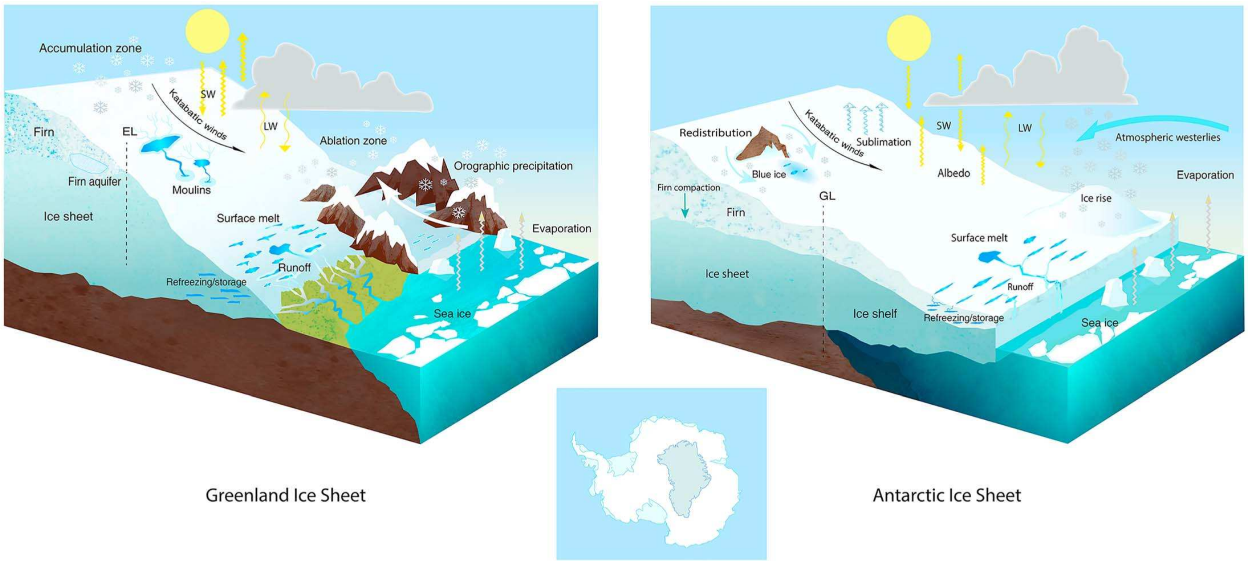

Figure 2.1: Artwork illustrating the ice sheets' surface processes with their atmospheric interactions governing the SMB in Greenland (left) and Antarctica (right) from Lenaerts et al. (2019). The equilibrium line (EL) divides the ice sheet into the accumulation zone and the ablation zone. The grounding line (GL) is the border between floating ice (ice shelf) and the grounded ice on the bedrock (ice sheet). SW and LW indicates shortwave and longwave radiation, respectively.

the interface between the ice sheet and the atmosphere (Figure 2.1). The surface of an ice sheet defines the interface between the subsystems ice sheet and atmosphere. As outlined in Chapter 1, one part of the SMB is the accumulation determined by precipitation and snowdrift deposit. The other part of the SMB is the ablation due to sublimation, melt, and wind erosion. Sublimation and melting (and freezing) depend on the available amount of energy at the ice sheet's surface. This amount of energy is controlled by the surface energy balance which results from the energy fluxes and includes incoming and outgoing fluxes of radiation, absorbed radiation, sensible and latent heat exchange as well as the heat flux. Further, the surface energy balance determines the surface temperature (Singh et al., 2011). The SMB is the change in mass over time per unit area, also referred to as the mass flux or the rate of mass flow. This mass flux fluctuates over different time scales. In particular seasonal SMB fluctuations are known (accumulation season and ablation season) but also interannual and long-term changes of the SMB are significant. Furthermore, the SMB-induced mass changes for the GIS and the AIS differ (Figure 2.1). Surface melting plays a significant role for the GIS, but only a minor role for the AIS as a whole, where a large part of the surface melt refreezes. The SMB in Antarctica is dominated by accumulation (Hanna et al., 2020).

A state of equilibrium of an ice sheet means the balance between SMB and IFD. This can be illustrated by the mass flow rate through a columnar element of an ice sheet. The positive (negative) surface mass flux into this column at the top is compensated with an increased (decreased) ice mass flux out of the column which equals the surface mass flux. The ice mass flow rate (or ice mass flux) of the whole ice sheet adjusts to the surface climate, i.e. to the long-term mean SMB. Short-term SMB fluctuations are anomalies to this long-term mean SMB. A simple example of such an anomaly is a snowfall event that leads to a positive SMB during this event which might be above the long-term mean SMB. In practice, the reference climate for the long-term mean SMB can be realized by a reference period over which the mean SMB is calculated assuming that this mean SMB represents the long-term mean SMB. The ice mass change can be—somewhat arbitrarily—attributed to an SMB-related contribution and an IFD-related contribution. The SMB-related contribution in a region over time consists in the (ac)cumulated SMB anomalies. The SMB-induced mass change, $\dot{M}^{\mathrm{SMB}}$, is the mean rate of the (ac)cumulated SMB anomalies and $\dot{\kappa}^{\mathrm{SMB}}$ is the SMB-induced surface density change. Note that the SMB contribution to the mass balance refers to the mean SMB over a chosen reference period which is a potential source of error if the chosen reference period is not fully representative for the actual surface climate. Further, any change of the surface climate (climate trends) will lead to changing IFD. Potentially there is a background imbalance between the long-term mean SMB and IFD. This background imbalance remains unknown, if there is no actual and independent knowledge on the long-term mean SMB and the IFD.

In order to examine volume changes of an ice sheet, it can be divided into a firn layer and an ice layer which reaches until the bedrock (Figure 2.1). In the following, these layers are indicated with the superscripts ICE and FIRN, respectively. SMB-related processes lead to volume changes, $\dot{\mathcal{V}}$, and surface elevation changes, $\dot{h}$, in both layers:

$$\dot{\mathcal{V}}^{\mathrm{SMB}} = \dot{\mathcal{V}}^{\mathrm{ICE}} + \dot{\mathcal{V}}^{\mathrm{FIRN}}, \tag{2.15}$$

$$\dot{h}^{\mathrm{SMB}} = \dot{h}^{\mathrm{ICE}} + \dot{h}^{\mathrm{FIRN}}. \tag{2.16}$$

Precisely, firn is compacted snow which persists more than one melt season or is somewhat metamorphosed and underlies a snow layer (Singh et al., 2011). Here, the term *firn* envelops everything in the transition from snow to ice. A separate snow layer is not considered here. The transition from snow to ice is also called firn densification and is the process from a granular material to a polycrystalline solid (Singh et al., 2011). The thickness of the firn layer is several tens of metres to more than 100 m (Singh et al., 2011). Any thickness change of the firn layer is referred to as the firn thickness change, $\dot{h}^{\mathrm{FIRN}}$, and integrated over an area the firn volume change, $\dot{\mathcal{V}}^{\mathrm{FIRN}}$. The firn thickness change and the surface density change of the firn layer, $\dot{\kappa}^{\mathrm{FIRN}}$, can be related with a firn density, ρ^{FIRN}:

$$\dot{\kappa}^{\mathrm{FIRN}} = \rho^{\mathrm{FIRN}} \dot{h}^{\mathrm{FIRN}}. \tag{2.17}$$

More precisely, this firn density is an effective density relating volume and mass changes of the firn column. This density is smaller than the ice density, $\rho^{\mathrm{FIRN}} < \rho^{\mathrm{ICE}} = 917\,\mathrm{kg\,m^{-3}}$, as the firn layer contains air in addition to particles of frozen water (ice particles). The amount of air being part of the firn layer is referred to as firn air content (FAC). For example, when fresh snow accumulates on top of an existing already compacted firn, the FAC of the firn layer increases. This is because the fresh snow contains a higher proportion of air compared to ice than the existing firn. Conversely, if there is no fresh snow accumulation and the firn layer continues to compact, the FAC decreases, as no new air is added to the firn layer. As the change of the FAC is assumed to have no mass effect, the firn thickness change can be expressed as the sum of the change of the FAC and the volume change that a mass change of the ice particles induces (Ligtenberg et al., 2014):

$$\dot{h}^{\mathrm{FIRN}} = \dot{h}^{\mathrm{FAC}} + \frac{\dot{\kappa}^{\mathrm{FIRN}}}{\rho^{\mathrm{ICE}}}. \tag{2.18}$$

Further, the SMB processes induce surface mass changes of the ice layer, if it is not covered by a firn layer. $\dot{h}^{\mathrm{ICE}}$ refers to SMB-induced surface elevation changes of the ice layer, e.g. the melting of pure ice. In this case, ice density links SMB-induced surface density changes and surface elevation changes:

$$\dot{\kappa}^{\mathrm{ICE}} = \rho^{\mathrm{ICE}} \dot{h}^{\mathrm{ICE}}. \tag{2.19}$$

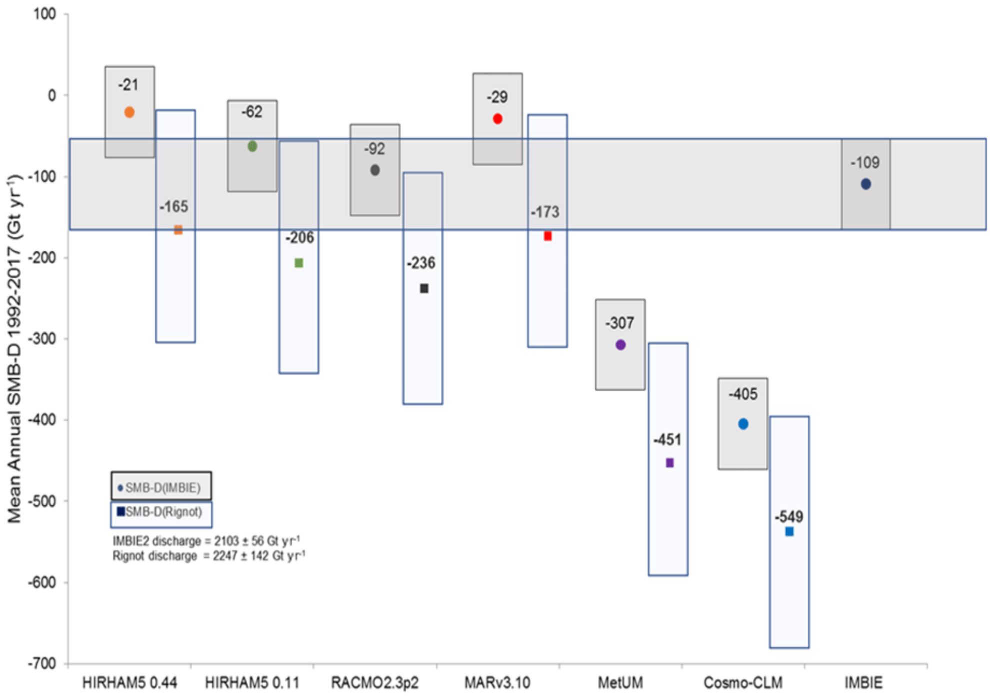

Figure 2.2: Comparison of the AIS mass balance estimates in terms of the mean rate over the 1992–2017 time period including the uncertainty range (Mottram et al., 2021). The mass balance estimates result from different variants of modelled SMB (absciss axis) minus two different ice discharge (D) estimates: circles, (Shepherd et al., 2018) and squares, (Rignot et al., 2019), illustrate the mean values.

If the ablation of the ice layer and the runoff plays only a very minor role in a region, as it is valid for large part of the AIS (Lenaerts et al., 2019), the SMB-induced mass changes approximate mass changes of the firn layer, $\dot{\kappa}^{\mathrm{SMB}} \approx \dot{\kappa}^{\mathrm{FIRN}}$.

Apart from the SMB-related contribution to the mass balance, there is an IFD-related contribution to the mass balance. IFD express themselves in the ice flow velocity. As discussed above in the equilibrium state of an ice sheet the IFD adjusted to the surface climate. Further, the ice flow depends on the environmental conditions such as the geometry of the bedrock surface (bedrock topography or geomorphology), basal friction, and buttress effects due to ice shelves. The geometry of the ice body and the mass flux evolves in response to any changes in the external and internal forces (Singh et al., 2011). An increased (decreased) ice flow will reduce (enhance) the ice sheet thickness referred to as dynamic thinning (dynamic thickening). More precisely, relevant for an IFD-related effects is the difference between the ice flow into a columnar unit volume element and the ice flow out of this element. This difference is referred to as the mass divergence, i.e. the rate of the net mass flux out of this columnar element (Singh et al., 2011). Ice density links the IFD-induced surface density change, $\dot{\kappa}^{\mathrm{IFD}}$, and surface elevation change, $\dot{h}^{\mathrm{IFD}}$:

$$\dot{\kappa}^{\mathrm{IFD}} = \rho^{\mathrm{ICE}} \dot{h}^{\mathrm{IFD}}. \tag{2.20}$$

In Greenland and Antarctica, mass changes due changing IFD are on long-term time scales (decadal scales and longer), if they are related to climate change or to the break off of ice shelves (Rignot et al., 2019; Mouginot et al., 2019). Almost exclusively in Greenland, when considering ice sheets, the IFD contribution to the mass balance additionally fluctuates on shorter time scales, e.g. seasonally or at surge-type glaciers (Müller et al., 2021).

Also basal mass and volume changes induce potentially measurable changes in surface density or surface elevation (Pattyn, 2010). But note that the basal mass balance of the grounded ice sheet is not considered in mass balance studies such as Shepherd et al. (2018) and Shepherd et al. (2019), as the mean basal melt rate of the AIS amounts to $\sim 3\,\%$ of the total surface accumulation only (Pattyn, 2010) and temporal changes of the basal mass balance remain unknown. Moreover, hydrostatic responses above subglacial lakes, e.g. above Lake Vostok (Richter et al., 2022), induce some more exceptional surface elevation changes over ice sheets.

According to Mottram et al. (2021), different SMB modelling results of the AIS over the time period from 1987 to 2015 spread from $(1961 \pm 70)\,\mathrm{Gt\,a^{-1}}$ to $(2519 \pm 118)\,\mathrm{Gt\,a^{-1}}$. Shepherd et al. (2019) stated the SMB of the GIS as $(361 \pm 40)\,\mathrm{Gt\,a^{-1}}$ by taking eight different modelling results into account. In Greenland the SMB trend is negative because of enhanced runoff.

2.3 The solid-Earth and sea-level response to present-day ice mass change

A load at the surface of the solid Earth exerts a surface force also referred to as stress; more precisely a surface load exerts the special case of a normal force (normal stress). In general, any load change at the surface of the solid Earth leads to a change in stress applied to the solid Earth and results in deformation. This deformation is termed *strain* if the resulting deformation is related to any original state, i.e. relative deformation. Apart from the change in stress, the mass redistribution along with the load change affects the acting body force due to gravity. Coevally, the deformation of the solid Earth itself results in a change of the gravity field in addition to a change of the solid-Earth geometry. Rheological models for Earth's materials link acting forces and the associated deformation behaviour (e.g. Karato, 2008). Derived from such models, Love numbers are parameters that provide the relationship between acting forces and Earth's deformation (Farrell, 1972; Farrell, 1973). They are calculated using an (rheological) Earth model with certain simplifications (e.g. assuming an incompressible, non-rotating, or radially symmetric Earth).

Above in Section 2.1, load Love numbers are already introduced to describe the link between surface load changes and the accompanying elastic deformation effect on gravity. Initially, Love numbers were used to describe the elastic deformation of the entire Earth (or other planets) due to external forces (e.g. tidal force), and to derive planets' stiffness (Love, 1909). This concept was extended to forces induced by surface load changes with the degree-dependent load Love numbers, h', k', l' (Farrell, 1972). Conventionally, these are indicated with a prime to avoid confusion with the (tidal) Love numbers. There is also a connection between tidal Love numbers and load Love numbers (Saito, 1978).

The evaluation of different temporal scales is necessary (Figure 1.2) in the scope of investigating the interconnected effects of sea-level change, solid-Earth deformation, and changes in Earth's rotation caused by the redistribution of mass between ice sheets and oceans. Satellite methods provide several decades of observations. On these time scales immediate effects are relevant, e.g. effects due to present-day IMC. Additionally relevant are present-day effects caused by past IMC, e.g. several thousand years ago. The origin of the latter effects are explained in more detail in Section 2.4. A reason for the distinction between *past* and *present* time scales is the time-scale-dependency of the deformation behaviour of Earth's materials. The choice of the rheological model to describe the deformation behaviour of Earth's materials depends on time scales under consideration.

For the consideration of surface load changes and deformation on short time scales of a few tens of years, the rheological model of a purely elastically deformable Earth is assumed to be sufficient (Blewitt and Clarke, 2003; Spada, 2017). This assumption can be justified by the rheological properties of Earth's materials, i.e. their deformation behaviour on different time scales (Ivins et al., 2020). According to Hooke's law, the elastic deformation means that in the case of an immediate reversal of a load, the solid Earth as a continuum will immediately and completely recover to the state it has before the load was applied. Such a purely elastic approach has already been used in Equation 2.11 for the calculation of surface densities when considering the gravitational potential effect caused by elastic deformation. The load Love number, k', links the gravitational potential effect caused by the solid-Earth deformation, $\dot{V}^{\mathrm{DEF}}$, to the change in the gravitational potential induced by the mass change itself (cf. Equation 2.7):

$$\dot{V}^{\mathrm{DEF}}(\boldsymbol{x}) = \sum_{n=0}^{\infty} k'_n \dot{V}_n(\boldsymbol{x}). \tag{2.21}$$

Both gravitational potential effects are considered when expressing gravitational field changes as surface density changes (Equation 2.11). In case of a load change, h'_n links the change in the gravitational potential with the radial surface elevation change due to the elastic deformation, $\dot{h}^{\mathrm{ELA}}$, at the spherical approximated Earth's surface:

$$\dot{h}^{\mathrm{ELA}}(\theta, \lambda) = \frac{R^2}{GM_E} \sum_{n=0}^{\infty} h'_n \dot{V}_n(\theta, \lambda). \tag{2.22}$$

Lastly the load Love number, l'_n, also referred to as load Shida number, connects the lateral elastic deformation to the change in gravitational potential:

$$\dot{l}^{\mathrm{ELA}}(\theta, \lambda) = \frac{R^2}{GM_E} \sum_{n=0}^{\infty} l'_n \boldsymbol{\epsilon}(\theta, \lambda) \cdot \nabla \dot{V}_n(\theta, \lambda). \tag{2.23}$$

$\dot{l}^{\mathrm{ELA}}$ is the horizontal displacement rate at the surface. It is calculated by projecting the directional derivative of the gravitational potential change into the horizontal direction given by the unit vector, $\boldsymbol{\epsilon}(\theta, \lambda)$. The relationships between load change, the gravity changes, and elastic deformation of the solid Earth can also be described in the spatial domain using Green's functions (e.g. Lambeck, 1988), which is not discussed further here.

The globally consistent consideration of the redistribution of mass between ice sheet and ocean requires the coupled consideration of IMC, sea-level changes, gravity field changes, solid-Earth deformation and changes in Earth rotation. This is described by the gravitationally self-consistent sea-level equation (Farrell and Clark, 1976; Dahlen, 1976). A detailed review on the current status of sea level theory is reviewed by Spada (2017). The relative sea level, S, is in principle the water depth (Whitehouse, 2018) and defined over the ocean described by $\mathcal{O}$, an ocean function which is "1" over the ocean and "0" over land. The sea level equation describes changes of S and implies two crucial assumptions: (1) mass conservation between continental ice sheets and the ocean; and (2) the surface of the ocean is an equipotential surface. Following Dahlen (1976) and Blewitt and Clarke (2003) the relative sea level in static equilibrium is:

$$S(\theta, \lambda) = \mathcal{O}(\theta, \lambda) \left(N(\theta, \lambda) - h^{\mathrm{BEDROCK}}(\theta, \lambda) + \frac{\Delta V}{g} \right). \tag{2.24}$$

The potential of the sea surface in relation to the potential at the geoid is ΔV (Blewitt and Clarke, 2003). $\Delta V/g$ accounts for the constant shift of the equipotential ocean surface in relation to an initial geoid to ensure mass conservation. For a purely elastic deformation, a bedrock motion, $\dot{h}^{\text{BEDROCK}}$, is $\dot{h}^{\text{ELA}}$.

The sea level equation is an integral equation which can be solved with iterative solving strategies (Spada, 2017). The quasi-spectral approach (Blewitt and Clarke, 2003; Clarke et al., 2005) is one reasonable approach to estimate the globally consistent relative sea level change in response to a surface load change. For calculations related to this work, an implementation from Groh (2014) is used: The calculation starts with the uniform approximation of the sea level, i.e. the total mass change of the surface load change, described by its degree-0 coefficient, is equally distributed over the ocean area. The relative sea level change is calculated by applying the ocean mask to the globally defined sea level change transferred to the spatial domain. The globally defined sea level, which is also defined over land, is referred to as the quasi-spectral sea level. Afterwards this approximated relative sea level change is transferred back into the spherical harmonic domain where it is used for updating the total load. The total load is the sum of the load change on land and the induced load caused by the approximated relative sea level change. The updated total load is then used to update the sea level. Additionally the change in sea level due to the rotational feedback is considered, which reflects in a change of the degree-2 coefficients (Rietbroek et al., 2012). The update in sea level, which includes the relative sea level, load update, and its rotational feedback effect, serves as an input for the next iteration to estimate an improved approximation of the relative sea level change. The iteration continues until the relative sea level change does not significantly differ from the estimation of the previous iteration. Finally the last update of the total load is used to calculate the globally consistent elastic deformation and the geoid change. The global spatial pattern in gravity field change, sea level change, or bedrock motion in response to a certain surface load is also termed *fingerprint* (e.g. Spada, 2017; Rietbroek, 2014).

2.4 Glacial isostatic adjustment to past ice mass change

The term glacial isostatic adjustment (GIA) envelopes the interconnected behaviour of the solid Earth, the ocean, and the ice sheets in response to glaciation and deglaciation (Whitehouse, 2018). In the previous section, the deformation of the solid Earth due to present-day surface load changes over a period of a few years was considered to be purely elastic, implemented with load Love numbers calculated from an elastic Earth model (Section 2.3). In addition to the elastic deformation, i.e. the immediate and completely reversible deformation, Earth materials deform irreversibly in response to applied stress. In general, Earth materials show elastic, plastic, and viscous deformation behaviour (Karato, 2008). The response of the solid-Earth to deglaciation and glaciation is a viscoelastic deformation. This means, in addition to elastic deformation the solid Earth adjusts to glaciation or deglaciation induced load changes by viscous flow of mantle material. With the simple assumption of the mantle material as a Newtonian fluid, surface load changes (stress change) and deformation changes due to viscous flow are linearly related. The (dynamic or Newtonian) viscosity is the proportional factor between stress and the strain rate. Qualitatively, a higher (lower) viscosity of a material means a lower (higher) strain rate in response to an applied stress. A common rheology model used in GIA modelling to implement linear viscoelasticity is the linear Maxwell body, which is used to develop linear viscoelastic Earth models (Whitehouse, 2018). The supplement of Spada and Melini (2019) provides a comprehensive overview of GIA modelling theory and includes, inter alia, the derivation of load Love numbers from viscoelastic Earth models. Analogously to elastic load Love numbers, viscoelastic load Love numbers are introduced with the same letters, h', k', and l', to describe the deformation response expressed as vertical displacement, gravity field change, and horizontal displacement, respectively (Spada and Melini, 2019). The viscoelastic load Love numbers consist of two parts: Firstly, the elastic part resulting from the elastic properties and the density profile of the Earth model (Section 2.3). Secondly, the viscous part derives from the viscosity profile of the utilized Earth model. For completeness it should be noted that apart from the viscoelastic load Love numbers, fluid load Love numbers are introduced to describe the deformation response on long time scales when a new state of equilibrium is reached after a surface load change (Spada and Melini, 2019).

In extension of the conventionally assumed Maxwell model, Ivins et al. (2020) provided an extensive review of linear viscoelasticity theory by an extended Burgers material model. This model enables a consistent time scale-spanning consideration of load changes and solid-Earth deformation for decadal to centennial time scales. This is also referred to as a frequency dependent viscoelasticity and currently an issue under investigation in geodynamic modelling (Lau et al., 2021). Additionally, the assumption of a Newtonian mantle viscosity may be inappropriate to explain observable solid-Earth deformation. This means there is a need to implement non-Newtonian viscosities in modelling (Kang et al., 2021). Further efforts currently pursued in GIA modelling are the consideration of the lateral inhomogeneities in the Earth's structure, e.g. in Antarctica (Coulon et al., 2021), and the implementation of 3-D rheological models (Wal et al., 2015; Bagge et al., 2021; Wan et al., 2022).

From the viewpoint of geodetic observations, the isostatic adjustment process to past IMC leads to measurable effects in present-day observations, e.g. in observations from gravimetry, GNSS, and to less extent, altimetry. One output of geophysical GIA models are present-day effects in Earth's gravity and geometry changes, which may be used for correcting these effects in geodetic observations. The principal goal of geophysical GIA modelling is the investigation of the coupled evolvement of the solid Earth, the ocean (sea level), and the ice sheets during (de)glaciation phases over space and time (Whitehouse, 2018). The basic prerequisites are the knowledge on Earth's rheology, Earth rotation parameters, and the glacial history (also termed ice history). The latter one is basically the induced surface load changes over space and time. Further, the ice history provides the information on the mass exchange between ice sheets and the ocean. A surface Green's function, Γ^{S}, can be obtained from the viscoelastic load Love numbers to describe the solid Earth's deformation as a gravity field change and a change of its geometry (e.g. Section S4 in Spada and Melini, 2019). This Green's function depends on the location and time. The sea level equation (Farrell and Clark, 1976) used for GIA modelling can be written in the following condensed form (Whitehouse, 2018; Spada, 2017):

$$S(\theta, \lambda, t) = +\frac{\rho^{\text{ICE}}}{g^{\text{S}}}\Gamma^{\text{S}} \otimes^{\text{ICE}} I + \frac{\rho^{\text{WATER}}}{g^{\text{S}}}\Gamma^{\text{S}} \otimes^{\text{OCEAN}} S + C^{\text{RSL}}(t). \tag{2.25}$$

g^{S} is the reference gravity at the Earth's surface (Equation 2.6) and I is the ice thickness variation over space and time (glacial history). In the first and second summand the surface Green's function is spatially and temporally convoluted with load changes over the ice sheets and the oceans, respectively, indicated by $\otimes$. The term $C^{\text{RSL}}(t)$ ensures the conservation of mass by a uniform shift of the relative sea level and includes the time-depend uniform part of the sea level change and the load change averages of the ice sheets and oceans. The case of the sea level equation discussed in the previous section (Equation 2.24) is actually only

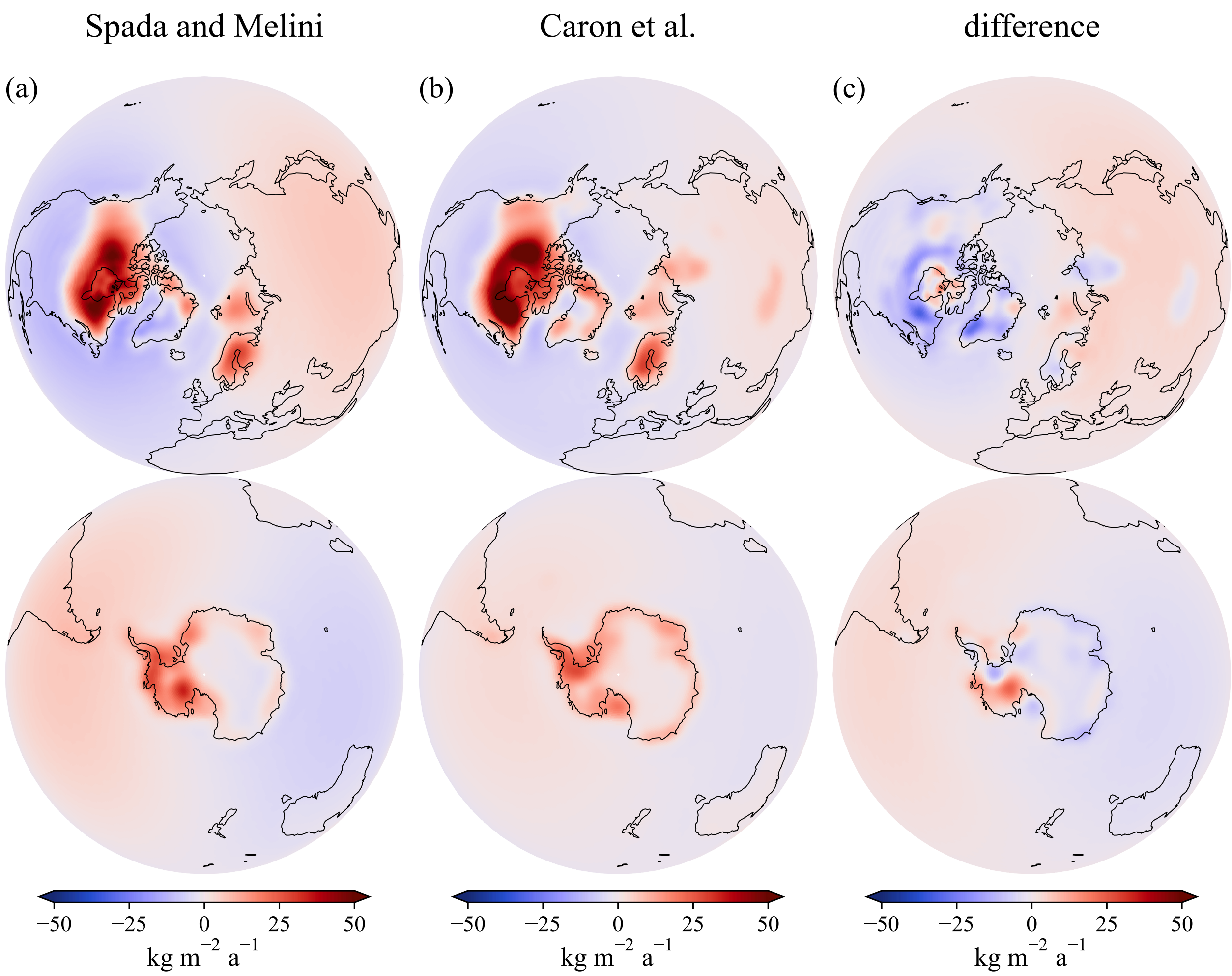

Figure 2.3: Comparison of two alternative GIA modelling outputs a) using the GIA modelling software SELEN (Spada and Melini, 2019) and b) from Caron et al. (2018) and c) their difference (a−b). The figure illustrates the present-day gravity field effect expressed as surface density rate. a) is simulated with the SELEN-software package applying VM5a rheology and ICE-6G ice history.

a special case of consideration. Namely, the exclusive study of present-day IMC. The viscoelastic response of the mantle to load changes within time scales of geodetic observations (a few decades) can be virtually neglected. On such short time scales of present-day IMC the solid-Earth deformation practically depends on the elastic properties of the Earth only (Spada, 2017). This assumption of a purely elastic responding solid Earth on IMC during geodetic observation periods is under debate in some particular regions, e.g. the Amundsen Sea Embayment (Barletta et al., 2018).

Extensions were made to the original form of the sea level equation according to Farrell and Clark (1976) to account for changes in Earth rotation (Mitrovica and Wahr, 2011) and shoreline migration (Whitehouse, 2018), referred to as the gravitationally and topographically self-consistent form. An example for a numerical implementation of the sea level equation including these extensions is the software package SELEN[4] (Spada and Melini, 2019) which is freely publicly available and used in this work. It assumes a spherically symmetric Earth, assumes a linear viscoelasticity, accounts for rotational feedback, and accounts for moving shorelines.

As outlined in Chapter 1, the rheology and the ice history used for geophysical GIA modelling (or forward modelling) are subject to large uncertainties, especially in Antarctica (Whitehouse et al., 2019). As an example, Figure 2.3 illustrates the present-day GIA gravity field effect from two alternative GIA model outputs and their difference. A pursued strategy to calibrate GIA modelling results is to constrain them with observational data, e.g. from GNSS measurements (e.g. King et al., 2010; Whitehouse et al., 2012; Ivins et al., 2013). Probabilistic modelling approaches are another strategy using inter alia GNSS data as test information for GIA predictions (Caron et al., 2018). There are also regional investigations that infer rheological parameters of GIA model results based on their agreement with GNSS (Barletta et al., 2018).

The present-day GIA effect needs a careful consideration when evaluating satellite gravimetry data such as from GRACE or GRACE-FO (Chen et al., 2022). Conventionally, there are three strategies to account for the GIA signal in satellite gravimetry observations. Firstly, one can use GIA forward modelling results and apply them as a correction for the GIA effect (e.g. Groh and Horwath, 2021). Secondly, a combination of satellite gravimetry data with satellite altimetry data and additional data allows to estimate the GIA effect (e.g. Wahr et al., 2000; Riva et al., 2009; Gunter et al., 2014; Engels et al., 2018). Thirdly, a priori information obtained from GIA forward modelling is utilized to parametrize GIA in data combination approaches using satellite gravimetry and additional data sets (e.g. Rietbroek et al., 2016; Martín-Español et al., 2016b; Sasgen et al., 2017). This work investigates and develops the latter two strategies in P1 and P3, also referred to as *inverse* approaches to distinguish them from geophysical forward modelling (Whitehouse, 2018).

3 Data sets

In publications P1–P3, methods for quantifying the effects induced by the processes described in Chapter 2 are investigated and developed. The data sets (Figure 3.1) used in all three publications were: (1) time-variable global gravitational field models from satellite gravimetry (from the GRACE mission), (2) surface elevation changes from satellite altimetry observations over ice sheets, as well as (3) SMB outputs over ice sheets from regional climate modelling and firn thickness changes from firn modelling. Similar data products illustrated in Figure 3.2 have been combined in this theses. The publications (Chapter 5) describe in detail the processing strategies of the data sets. This chapter provides some background information on the measurement methods and model setups.

3.1 Time-variable gravity from satellite gravimetry

The goal of satellite gravimetry is to determine the gravitational potential (Equation 2.3), or any of its functionals, in the Earth's exterior. The satellite gravimetry mission Gravity Recovery And Climate Experiment (GRACE, Tapley et al., 2004) was the first mission focusing on the changes of the Earth's gravitational potential over time. The mission was launched on 2002-03-17 and ended after more than 15 and half year on 2017-10-27. The follow-on mission GRACE-FO started on 2018-05-22 and is continuously collecting data. Both missions are based on the same concept: Each mission consists of two satellites in a polar Low Earth Orbit (89.5° inclination and ∼500 km altitude), which follow each other with a distance of ∼220 km. GNSS measurements provide information of the position over time of each satellite (orbit determination),

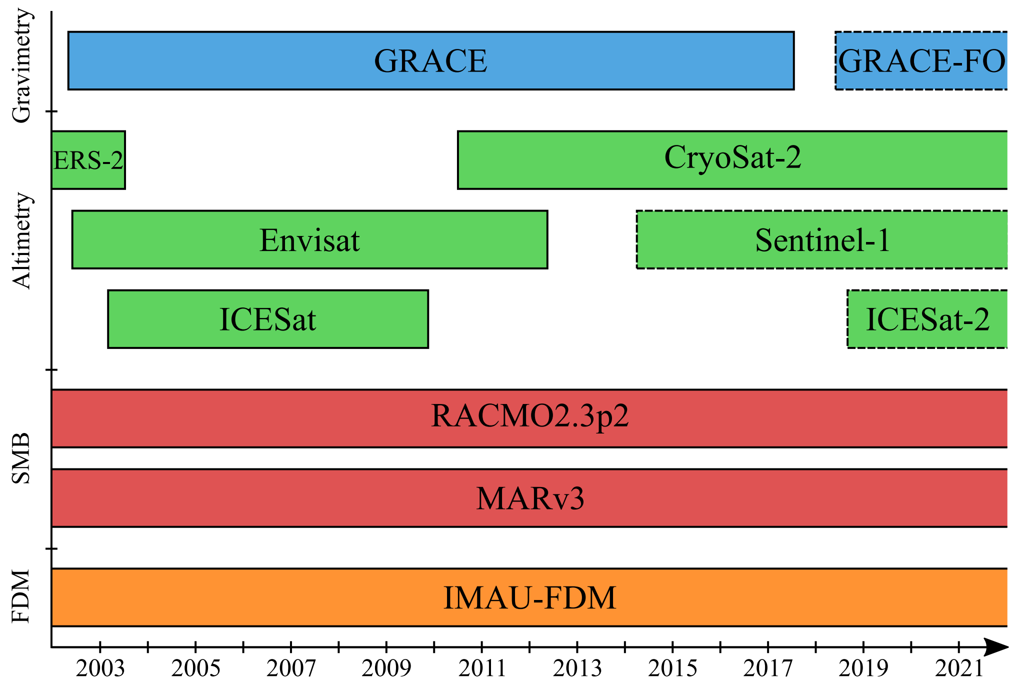

Figure 3.1: Availability over time of data sets from satellite missions as well as climate and firn modelling from 2002 until 2022 relevant in the perspective of this thesis. Data from missions indicated with a dashed contour line are not used in P1–P3, but are potentially useful in future data combinations. Surface mass balance (SMB) and firn densification model (FDM) products for Greenland and Antarctica are available since 1958 and 1979, respectively, and are continuously updated.

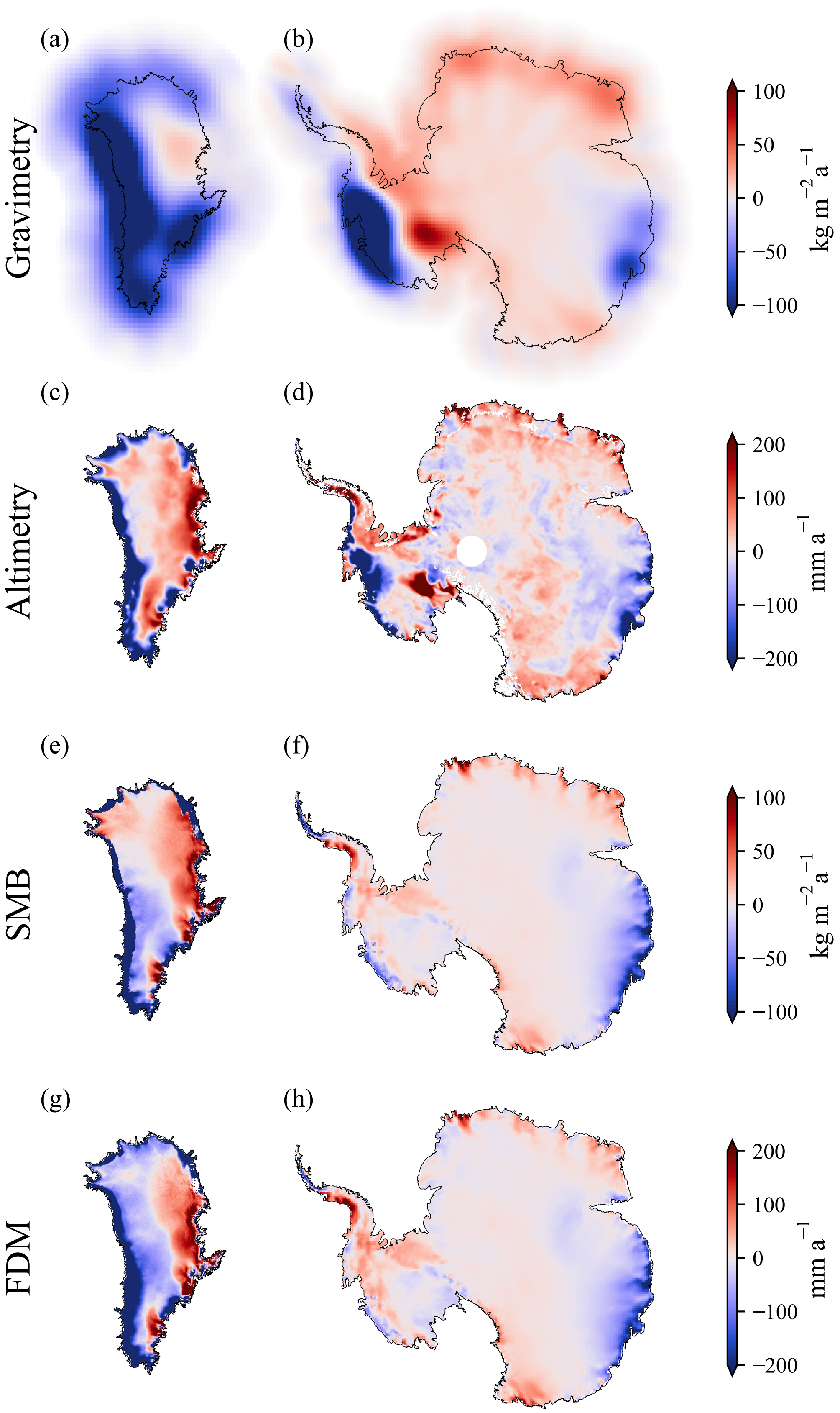

Figure 3.2: Mean rates of data sets for the time period Jan 2011–Dec 2020 for the GIS (a,c,e,g) and the AIS (b,d,f,h). a+b: GRACE and GRACE-FO derived surface density rates using ITSG monthly gravitational fields (Mayer-Gürr et al., 2018) smoothed with a 200 km Gaussian filter. c+d: CryoSat-2-derived surface elevation changes updated according to Helm et al. (2014). e+f: rates of cumulated SMB anomalies from RACMO2.3p2 (Noël et al., 2018; Wessem et al., 2018). g+h: firn thickness rates from IMAU-FDM (Ligtenberg et al., 2011; Brils et al., 2022; Veldhuijsen et al., 2022). Note that the GIS and the AIS are plotted with different scales (cf. Figure 1.1).

accelerometers in each satellite measures non-gravitational forces (e.g. atmospheric drag), and a microwave (K-band) ranging system allows for the precise determination of the distance change (range rate) between the satellites. Additionally, GRACE-FO carries a laser ranging interferometer to enhance the precision of the inter-satellite distance measurements (Ghobadi-Far et al., 2022). The concept of continuously measuring the inter-satellite distance of two low-orbiter satellites is referred to as low-low satellite-to-satellite tracking to distinguish it from other gravity mission concepts (e.g. Seeber, 2003). Furthermore, the satellites carry additional instruments, e.g. for attitude control (star cameras, magnetometer), data handling system, laser reflector.

Satellite gravimetry is a method to determine the gravitational field from the motion of satellites along their orbits. The special feature of the GRACE and GRACE-FO missions is the mentioned ranging system that allows to infer differences in acceleration of the satellites, in addition to the conventionally observed position of the satellites. The motion of the satellites (kinematic perspective) depends on all the forces acting on the satellites (dynamic perspective). As mentioned above, the accelerometers measure non-gravitational (or non-conservative) forces and thus allow the separate analysis of gravitational (or conservative) forces resulting from Earth's (changing) gravitational potential (e.g. Beutler and Jäggi, 2016). The term *gravitational* potential (Equation 2.3) is more precise than *gravity* potential as satellite gravimetry is not sensitive to any direct change of the centrifugal potential. Note that the literature sometimes uses the terms gravitational field and gravity field (or their functionals) synonymously when referring to satellite gravimetry products. A reliable variant applied for calculating the motion of the GRACE and GRACE-FO satellites is the dynamic orbit integration by using the variational equation approach (Ellmer and Mayer-Gürr, 2017). A dynamic orbit means the motion is attributed to the forces acting on the satellite. In one approach, short arcs of the satellites' trajectories are integrated with force models to calculate the dynamic orbit. These dynamic orbits are then fitted iteratively to the observations of the satellites' motion (kinematic orbits, range-rate measurements) (Kvas et al., 2019). The determined parameters of these orbits enable to calculate monthly solutions of the Earth's gravity field. These level-2 products are commonly provided as gravity fields in the form of monthly sets of spherical harmonic Stokes coefficients (e.g. Mayer-Gürr et al., 2018). For example, these can be used to derive surface density rates over the ice sheets (Figure 3.2a+b). There is a distinction of gravity field products into static models and time-variable models, because these models differ in magnitude, in resolution, and in the intended application scenarios. The reader is referred to Ellmer and Mayer-Gürr (2017) and Kvas et al. (2019) for more details on the GRACE/GRACE-FO data processing, e.g. the application of background models. An extensive list of available GRACE/GRACE-FO level-2 products and background information on global gravity field models is given by `http://icgem.gfz-potsdam.de/series` from the International Centre for Global Gravity Field Models (ICGEM, Ince et al., 2019).

By definition, the degree-1 time-variable gravity fields from GRACE and GRACE-FO are zero, because the gravity fields derived from these missions are in the CM reference frame. This means that the derivation of surface mass changes, e.g. due to ocean mass changes and IMC, from these gravity fields would remain incomplete. This is because the degree-1 mass effect cannot be resolved in the CM but in the CF reference frame (Swenson et al., 2008). The full recovery of surface mass redistributions in the Earth system requires to complement the GRACE/GRACE-FO gravity fields by degree-1 coefficients, i.e. by transferring into CF. This can be achieved by using a product based on Satellite Laser Ranging observations (e.g. Cheng et al., 2013) or by calculating the degree-1 coefficients from the gravity fields in the CM and an ocean model (Swenson et al., 2008). Furthermore, the monthly c_{20} coefficients (Earth's oblateness) can only be poorly determined from GRACE and GRACE-FO observations. In addition to that the c_{30} coefficients are of low quality in case of GRACE-FO and during GRACE accelerometer failures. Including information for these coefficients from Satellite Laser Ranging measurements improves the monthly gravity fields (Loomis et al., 2020). Note that the more consistent way is to combine GRACE/GRACE-FO and Satellite Laser Ranging normal equations in a joint framework (Beutler and Jäggi, 2016).

3.2 Surface elevation changes from satellite altimetry

The basic principle of satellite altimetry is the determination of the distance between a satellite and the surface elevation from the travel time of electromagnetic waves. For this purpose the satellite carries a radar or laser altimeter instrument which emits and receives electromagnetic waves (Seeber, 2003). Radar altimetry uses electromagnetic waves in the microwave frequency range. Laser altimetry uses electromagnetic waves in the visible light frequency range based on laser imaging, detection, and ranging (lidar). The altimeter instrument at the satellite emits electromagnetic waves in the direction of the Earth's surface. The waves propagate through the atmosphere and at the Earth's surface a part of the waves' energy is reflected back to the satellite where reflected waves are detected with a sensor. The distance between the satellite and the reflective surface can be determined from the propagation time and speed of the electromagnetic waves. The data processing of satellite altimetry to derive the surface elevation includes the determination of the position of the satellite in space and time (orbit determination), the determination of the propagation velocity of the electromagnetic waves (correction of atmospheric delay in relation to the speed of light in the vacuum), and in particular the assignment of the received reflected electromagnetic waves to the target reflective layer or feature (referred to as the (re)tracking of the received signal), i.e. commonly the reflective surface.

In case of radar altimetry over ice sheets, the assigning of the received signal to the surface may be challenging and requires the consideration for the time-dependent penetration of radar waves into the upper snow and firn layers. Laser altimetry measurements over ice sheets are hardly affected by time-varying signal penetration. However, the quality of laser altimetry measurements depends on the opacity of the atmosphere, e.g. laser light cannot penetrate through clouds. Additionally, corrections of tides and instrumental biases are necessary for both radar altimetry and laser altimetry. The continuous observation of the surface elevation of ice sheets allows the derivation of surface elevation changes (Schröder et al., 2019). These monitored changes enable to draw inferences on the processes described in Chapter 2. Furthermore, the detected reflected signal allows to extract properties of the reflective surface. For example, the ice sheet surface roughness and time-dependent firn structure affect the waveform of the returning radar waves. This means these waveforms are useful to explore the ice sheet's surface properties (Legrésy and Rémy, 1997).

Since the 1970s satellite altimetry missions have been monitoring surface elevation changes over ice sheets. Schröder et al. (2019) combined satellite missions, that have operated during the last four decades until Dec 2017, to calculate time series of the AIS surface elevation changes. This data product is used in this work. It includes surface elevation changes from missions that operated simultaneously to the GRACE mission (Figure 3.1). For the time period since the launch of GRACE, the data product covers data from ERS-2, Envisat, ICESat, and CryoSat-2 missions. ICESat is a laser altimetry mission and the other missions use pulse limited radar. Additionally, the CryoSat-2 mission incorporates Synthetic Aperture Radar Interferometric (SARIn) measurements to increase the spatial resolution in regions with high topography gradients.

Schröder et al. (2019) applied a repeat altimetry approach. After data reprocessing, including retracking, the observations are collected in boxes on a regular grid. Within a radius of 1 km around the centre of each grid cell, all observations are assigned to that grid cell. For each box, a spatio-temporal and mission-specific model is adjusted (repeat-track parameter fit) which includes parameters of the temporal linear trend and the topography. Additionally, in case of pulse limited radar altimetry, parameters are fitted to account for the backscatter signatures in the received signal caused by the surface properties. The estimated parameters and the residuals of the model fit are then used to compute a mission-specific time series for each box. These time series of the individual missions are merged, i.e. calibrated to each other, depending on certain conditions arising from the mission lifetimes and the observation technique applied (pulse limited radar, SARIn, laser). Finally, both a temporal and a spatial smoothing is applied. The final product is made available as grids with a monthly temporal resolution and 10 km spatial resolution. For the GIS, Zhang et al. (2022) applied a similar approach as Schröder et al. (2019) and provide a multi-mission altimetry time series which is based on radar alimetry only from 1991 until 2020. In this work, an updated CryoSat-2 product according to Helm et al. (2014) is used in Greenland (Figure 3.2c).

The spatio-temporal coverage of satellite altimetry data poses a particular challenge for the application to ice sheet-wide research questions. The ERS-2 and Envisat missions allow the derivation of monthly surface elevation changes from May 1995 until July 2003 and May 2002 until April 2012, respectively (Figure 3.1). However, the inclination of the orbits of both missions is 98.5°, so that the polar gap starts at a latitude of $\pm 81.5°$. In Greenland, only the northernmost part remains unobserved, unlike in Antarctica, where substantial parts of the ice sheet are unobserved by these missions (Figure 1a in P2). Note that in a similar orbit the successor mission Sentinel-1 from the European Space Agency (ESA) was launched in Apr 2014 but its data is not included in altimetry products used in this work. The ICESat mission operated from Feb 2003 until Oct 2009 and covered up to a maximum latitude of $\pm 86°$, but not continuously, as it applied a campaign-style observation strategy with two to three campaigns per year, each lasting about one month. Unfortunately, this temporal sampling does not allow for monthly resolved surface elevation changes. CryoSat-2 started in July 2010 and observes up to a maximum latitude of $\pm 88°$, i.e. an almost full spatial coverage of the AIS, and it measures with a spatio-temporal sampling that allows to derive monthly surface elevation changes. Lastly, it should be noted that in September 2018 ICESat-2, the laser altimetry follow-on mission of ICESat, launched into an orbit with 92° inclination similar to CryoSat-2. The data from this mission are not included in the analysis of Schröder et al. (2019) and are not used in P1–P3. But this data will provide new prospects, e.g. in terms of spatial resolution for future combined evaluations with GRACE-FO data. Potentially useful for this is the recently published multi-mission altimetry product from Nilsson et al. (2022). This product provides the AIS surface elevation changes covering data from 1985 until 2020 and includes ICESat-2-data.

3.3 Regional climate and firn modelling outputs

A climate model enables to simulate atmospheric processes on climate-relevant time scales by the numerical implementation of laws of fluid dynamics and thermodynamics. Such models can be in a global domain or tailored to regions. Two examples of regional climate models, which are also specifically tailored to the polar regions Antarctica and Greenland, are the Regional Atmospheric Climate Model (RACMO) and the Modèle Atmosphérique Régional (MAR, English: Regional Atmosphere Model). In these models processes are implemented which are specific for glaciated regions and govern the SMB (Section 2.2, Lipzig et al., 2002). These models allow the simulation of SMB components, which are made available as SMB model outputs and can be used with satellite data for combined investigations. Profound details about the recent model developments and modelling results for Greenland and Antarctica are provided by Noël et al. (2018) and Wessem et al. (2018), respectively, in case of RACMO2 (second version of RACMO) and by Fettweis et al. (2017) and Agosta et al. (2019), respectively, in case of MARv3 (third version of MAR). The most recent updates of the climate models are RACMO2.3p2 (the second polar update of RACMO2.3) and MARv3.12. Over Antarctica, Mottram et al. (2021) investigated outputs of five regional climate models including RACMO2 and MARv3 (Figure 2.2). A less recent intercomparison study for the GIS is provided by Vernon et al. (2013). The comparison of SMB measured by stake observations and modelled with regional climate models over whole Antarctica revealed common biases of SMB models (Mottram et al., 2021). Very locally in the Lake Vostok area on the East Antarctic Plateau, Richter et al. (2021) showed good agreement between stake observations and RACMO2 outputs but found a bias to MARv3 outputs.

Both RACMO2 and MAR are regional climate models which require lateral boundary information about the state of the atmosphere: the model forcing. RACMO2 and MARv3 are forced at their boundaries with a six-hourly information on temperature, specific humidity, pressure, wind speed, and wind direction (Noël et al., 2018; Agosta et al., 2019). This is practically realized using reanalysis products, e.g. from the European Centre for Medium Range Weather Forecasts (ECMWF) which provides the ECMWF re-analysis (ERA) products. The reanalysis products are generated by running global numerical weather prediction models (forecast models) while assimilating historical observational data. The current SMB outputs from RACMO2 and MAR are obtained from model runs forced with ERA-Interim and/or ERA-5 reanalysis products. Agosta et al. (2019) ran simulations with MARv3 over Antarctica by using three alternative reanalysis products and found that all three simulations similarly reproduced the SMB on spatial and temporal scales. Both RACMO2 and MAR are nudged with information from the reanalysis products within their model domain.

To properly account for the interactions between the atmosphere and the snow/firn surface, MARv3 includes a layered snowpack and RACMO2 has implemented snow/firn layers from the semi-empirical firn densification model (FDM) IMAU-FDM (Ligtenberg et al., 2011). A FDM simulates numerically the processes in the snow and firn layer, i.e. firn compaction, vertical melt water transport and refreezing, and thermodynamics of the firn layer. Semi-empirical models are tuned to density observations and are to be distinguished from physics-based models which do not require an observational tuning (Keenan et al., 2021). For comprehensive background information on firn modelling, implementation strategies, and further references, the reader is referred to Lundin et al. (2017) who ran a firn model intercomparison with synthetic signals. The IMAU-FDM is not only operated as part of RACMO2 (online), but also offline with higher vertical resolution to study firn processes (inluding firn thickness changes) in Greenland (Kuipers Munneke et al., 2015; Brils et al., 2022) and Antarctica (Ligtenberg et al., 2011; Veldhuijsen et al., 2022). For this purpose, the FDM is forced at the surface with model outputs from RACMO2, i.e. precipitation, snow drift, sublimation, erosion–deposition, surface melt, and surface temperature. For the initialization of the FDM, a firn layer needs to be simulated, but a stable firn layer is typically formed over longer time periods than forcing data is available. In order to create an equilibrium firn layer, which can be used for numerical simulation, the firn layer is created in a spin-up run. For this purpose, a reference period is chosen in which no significant climate trends are expected, and which is thus assumed to be representative for a long-term stable climate. The simulation is iterated over the reference period until a stable firn layer is formed. For Antarctica, the entire period modelled with RACMO2 have been used (e.g. 1979–2016 in P2). However, the assumption of a stable climate within the reference period may not reflect reality. For example, on the Antarctic Peninsula climate trends have been identified and need consideration (Pritchard et al., 2012; Thomas et al., 2017). For Greenland, the time period from Jan 1960 to Dec 1979 may be assumed as the reference period being representative for a long-term stable climate (Kuipers Munneke et al., 2015). Note that a major part of the uncertainty of the firn trends can be attributed to assumptions on the reference climate (Kuipers Munneke et al., 2015; Pritchard et al., 2012). Recently, Verjans et al. (2021) investigated the uncertainty of firn thickness changes of the East Antarctic Ice Sheet using a statistically generated model ensemble and identified the climate forcing as the largest uncertainty contributor.

The SMB outputs from RACMO2 and MARv3 provide monthly SMB from which $\dot{\kappa}^{\mathrm{SMB}}$ (Section 2.2) can be obtained (Figure 3.2e+f). The IMAU-FDM output is a surface elevation time series representing all surface elevation changes induced by processes in the firn layer (accumulation, compaction etc.) from which $\dot{h}^{\mathrm{FIRN}}$ can be estimated (Figure 3.2g+h).

4 Data combinations over ice sheets

The processes described in Chapter 2 lead to changing physical quantities—gravity and geometry—over time which can be observed by a wide variety of methods. During the last three decades numerous studies were published making use of satellite data over ice sheets to estimate their mass balance along with their contribution to the global sea level budget, and to investigate the driving processes (e.g. Shepherd et al., 2018; Shepherd et al., 2019; Horwath et al., 2022, and references therein). These investigations utilize, in addition to data from satellite gravimetry, satellite altimetry mentioned in Chapter 3, observational data from other satellite methods, e.g. GNSS, passive remote sensing, imaging radar (with SAR), as well as combinations of these.

To begin with, the data from single satellite methods may be used to quantify the changing physical quantities, e.g. to quantify mass redistributions from gravitational field changes observed by satellite gravimetry. Additional information may be necessary to analyse the observations, e.g. from geophysical modelling. This is because the changing physical quantities caused by various processes superimpose and thus the detectable effects of the individual processes are superimposed in the measurements. A conventional example is the IMC and GIA effect inherent in satellite gravimetry data. The GIA effect can be predicted by geophysical modelling and utilized in satellite gravimetry analyses to isolate IMC. This is referred to as the gravimetric mass balances in Shepherd et al. (2018). However, evaluating individual data types may be limited due to the utilized a priori information. This is because the uncertainty of this information is potentially hardly characterized. For example, this is the case of modelled GIA effects in Antarctica. Approaches that combine different data types (also referred to as joint data inversion) can loose the dependency on such a priori information from modelling by assembling information from more than one observation method. From this perspective, combination approaches aim to disentangle and quantify the superimposed sources by drawing on the characteristics of how the processes affect the assembled quantities over space and time. Moreover, single data type evaluations are limited because the individual sensors are limited to a technically defined spatial and temporal coverage. Data combinations intend to enhance the spatial and temporal coverage of the estimated parameters by assembling the spatial-temporal sampling characteristics of several observation methods.

There are two directions of evaluation between the changing physical quantities and the observational data. One direction is the forward problem which describes how the changing physical quantities map into the observational data. An observation method (sensor or detector) can be described by a forward operator, a spatio-temporal sampling function (cf. P3) obtained by forward modelling. The other direction, which is inverse to the forward problem, is the inverse problem (e.g. Koch, 1999; Tarantola, 2005; Menke, 2012) and encapsulates obtaining information about the processes from observational data. The aim of solving the inverse problem—that is the inversion—is to determine parameters of a model from the data. This implies the careful parametrization, i.e. the formulation of the model with the parameters to be determined, along with the careful consideration of data limitations. These are the limited spatio-temporal resolution of the observation types, systematic errors, and random errors. In a joint data inversion the parametrization builds upon the characteristic link between an observation type and the processes of interest. Relevant for this work is how the causing processes (Chapter 2) characteristically change the quantities gravity and geometry observed by satellite gravimetry and altimetry. Note that the sensitivity of a certain observation type towards the causing process may differ. An example is GIA which strongly affects the Earth's gravity field measured by satellite gravimetry. But the geometric GIA effect (almost) disappears in the noise level of satellite altimetry data. Alternatively to the inversion including a thorough parametrization, the inverse problem can be somewhat simplified with the perspective of a deterministic signal-separation problem (e.g. Wahr et al., 2000; Gunter et al., 2014). In this sense, 'signal' means the change of a physical quantity (effect) caused by a certain process. The observation is the sum of the signals (apart from errors) which can be deterministically separated.

In the following, previous combination approaches applying satellite gravimetry and satellite altimetry data over ice sheets, and eventually incorporating further data sets, are briefly reviewed and broadly classified in three categories. The publications P1-P3 are categorized accordingly and placed within the current state of the research.

Firstly, the combination of satellite gravimetry and satellite altimetry has been applied in regional studies in Antarctica to determine the GIA effect and IMC from the observational data, rather than determining GIA a priori from geophysical forward modelling: Wahr et al. (2000) were the first to investigate a combination of the two satellite methods by simulations. They found that it will be possible to improve AIS mass balance estimates by no longer relying on error-prone GIA modelling outputs. Velicogna and Wahr (2002) further developed this combination method with the additional use of GNSS data. Riva et al. (2009) were then the first to combine satellite gravimetry (GRACE data) and satellite altimetry (ICESat data) in Antarctica to jointly determine IMC and GIA effects. Compared to forward models, the GIA-related bedrock motion determined in this way fits better with GNSS-based GIA rates (Thomas et al., 2011). Groh et al. (2012) applied this methodology to the Amundsen Sea Embayment in West Antarctica for a regional investigation of GIA-induced bedrock motion. Gunter et al. (2014) extended the approach from Riva et al. (2009) by adding outputs from regional climate and firn modelling. Thus firn and SMB induced volume and mass changes were explicitly considered. Gunter et al. (2014) investigated the sensitivity of their results towards different GRACE products but they left open how individual processing choices, alternative surface elevation change products from satellite altimetry, or alternative time periods affect the GIA estimate. Nor did they rigorously consider the uncertainties of the SMB and firn thickness change model products that were used. These points were investigated in P1 (Willen et al., 2020). Martín-Español et al. (2016b) published results of a stochastic modelling approach (Zammit-Mangion et al., 2015) using satellite gravimetry, satellite altimetry, and GNSS data as observations. The spatio-temporal stochastic characterization (i.e. the parametrization) of the processes over the AIS is based on outputs from forward models. Sasgen et al. (2018) and Sasgen et al. (2017) were then the first to present a methodology combining satellite gravimetry, satellite altimetry, and GNSS, that, in addition to determining IMC and GIA effects, allowed to touch the investigation of rheological properties in Antarctica. Zhang et al. (2017) and Gao et al. (2019) demonstrated benefits from utilizing GNSS data as a constraint in the approach according to Gunter et al. (2014). Engels et al. (2018) further developed the approach from Gunter et al. (2014) with a patch parametrization, in particular to increase the spatial resolution of the estimated GIA effect. They made use of GNSS observations to constrain the spatial scales of the GIA estimate. Also Hardy (2019) presented combination methods of GRACE, ICESat as well as GNSS over the AIS, to enhance spatial resolution of IMC and to assign the source of the mass change. Similar to Riva et al. (2009), Zwally et al. (2021) combined GRACE and satellite altimetry observations over the AIS to constrain the GIA effect.

Secondly, there are approaches that combine satellite gravimetry and satellite altimetry data with a regional focus, but without co-estimating the GIA effect. They focus on investigating the processes causing IMC. In Antarctica these are e.g. estimating rates of IMC with enhanced spatial resolution (Sasgen et al., 2019) or separating processes in the firn and ice layer by Mémin et al. (2014) and also by Kallenberg et al. (2017), who applied a similar approach as Gunter et al. (2014) but made use of GIA forward modelling outputs. Horwath et al. (2012), Mémin et al. (2015), and Kaitheri et al. (2021) investigated the interannual variations due to climate variability. In this context, P2 (Willen et al., 2021) can also be categorized. In P2 long-term and short-term mass changes on the drainage basin level were separated by using state space methods to allocate IMC to their source. This state-space model framework allows to overcome limitations of analyses that artificially choose time periods. Further investigations using state space methods to investigate geodetic time series in Antarctica have been published by Davis et al. (2012), Didova et al. (2016), and Wang et al. (2021) but they do not incorporate ice altimetry observations. In Greenland Slobbe et al. (2009), Ewert et al. (2012), and Yang et al. (2019) combined information from GRACE and satellite altimetry to investigate volume and mass changes of the GIS. Kappelsberger et al. (2021) used IMC estimates with enhanced spatial resolution from a combination of GRACE and CryoSat-2 data to evaluate GNSS-observed bedrock motion in North-East Greenland. Finally, Forsberg et al. (2017) demonstrated the spatial-resolution enhancement of GRACE-derived IMC by incorporating Envisat and CryoSat-2 data over both ice sheets.

Thirdly, there are combination approaches that allow to co-estimate for present-day GIA effects in global frameworks. However, so far only Jiang et al. (2021) utilized data inter alia from GRACE, ICESat, firn and climate modelling in a global framework. Their work builds upon Wu et al. (2010). The parametrization of GIA and the GIA uncertainty is based on GIA forward modelling results. Also Rietbroek et al. (2016) presented a global approach allowing for co-estimating GIA and applied a GIA parametrization based on forward modelling results. However, GIA remains a major source of uncertainty in the global inversion for all sea level budget components (Uebbing et al., 2019). Further global frameworks, that estimate GIA solely from GNSS data and solely from GRACE data, have been published by Sha et al. (2018) and Sun and Riva (2020), respectively, however without implementing the information over ice sheets from satellite altimetry data. P3 (Willen et al., 2022) presents the methodology and investigates the feasibility of a global approach for a spatially resolved GIA estimate enabled by incorporating satellite altimetry in addition to satellite gravimetry observations over ice sheets as well as firn and climate modelling data.

5 Publications

In summary, the three publications of this thesis can be interpreted as three contributions towards resolving the inverse problem of spatio-temporal signal separation over ice sheets by combining satellite gravimetry and satellite altimetry data with climate and firn modelling outputs. In a simplified view, in P1 the signal-separation task is led back to solving an arithmetic problem, in P2 it is led back to solving a stochastic filtering problem, and in P3 it is led back to solving a linear parameter estimation problem. These three research articles within this cumulative dissertation can be found in this chapter. Supplementary material (SM) is published along each article and is included in the appendix. In particular for P2, a more detailed description of the applied methodology can be found in the appendix.

In addition to the research extensively documented in the articles below, a brief classification of some motivational and methodological aspects is provided first from the overall perspective of this thesis.

P1 (Willen et al., 2020) focuses on the investigation of the sensitivity of regional GIA estimates over Antarctica towards input data sets and processing choices. Therefore a combination approach according to Gunter et al. (2014) is investigated. In this approach GIA is resolved arithmetically as follows:

$$\dot{h}^{\mathrm{GIA}} = \frac{\dot{\kappa}^{\mathrm{GRAV}} - \rho^{\alpha}(\dot{h}^{\mathrm{ALT}} - \dot{h}^{\mathrm{FIRN}}) - \dot{\kappa}^{\mathrm{FIRN}}}{\rho^{\mathrm{GIA}} - \rho^{\alpha}}. \tag{5.1}$$

$\dot{\kappa}^{\mathrm{GRAV}}$ is the surface density rate derived from satellite gravimetry observations in the spatial domain, $\dot{h}^{\mathrm{ALT}}$ the surface elevation rate from satellite altimetry, and $\dot{h}^{\mathrm{FIRN}}$, $\dot{\kappa}^{\mathrm{FIRN}}$ surface density and surface elevation rate in the firn layer. ρ^{GIA} relates the mass and volume effect induced by GIA and ρ^{α} is a spatial and input-data dependent density mask which allows to distinguish between IFD and SMB induced mass and volume changes. In order to apply this equation to the datasets, the data sets are harmonized in terms of spatial resolution by filtering (smoothing) and corrected for bias. Furthermore, P1 investigates an Antarctic GIA estimate from a combination on time series level rather than combining mean rates.

P2 (Willen et al., 2021) focuses on the temporal separation of long-term and short-term Antarctic ice mass and volume changes on drainage basin level without the attempt to co-estimate GIA. The aim of this investigation was to disentangle and quantify the sources of the AIS mass and volume changes commonly observed by satellite gravimetry and satellite altimetry. The different temporal characteristics of IMC are exploited and form the basis for separating long-term and short-term changes in the time series. The central perspective is that short-term changes are fluctuations in the firn layer and (temporally correlated) errors. The long-term changes are mainly interpreted as the IFD contribution to the mass balance and are parametrized with a smooth time-variable rate. It should be noted that this perspective requires to correct for all alternative sources of long-term and short-term mass and volume changes. The temporal stochastic parametrization of the involved processes is mapped into a state space model linking the observation time series and the state vector (model). The state estimation problem is solved using a Kalman filter and smoother. The applied state space framework builds upon work from Frederikse et al. (2016) and applies the state space methods from Durbin and Koopman (2012). The states are estimated in four consecutive steps: (1) The irregular and disturbance variances and covariances (hyperparameters or process noise) are estimated by statistical optimization. (2) The Kalman filter is applied to estimate the states in a forward loop. (3) The states are smoothed in a backward loop. This enables to improve the estimation of each state by incorporating all observations. (4) Finally, the disturbance variances are smoothed in a backward loop to base the smoothed disturbance variance estimates on all observations.

P3 (Willen et al., 2022) focuses on the spatial separation of IMC, GIA, and changing FAC in a global framework while accounting for spatially correlated errors of the input data sets. Observations and parameters are linked in a Gauss Markov model which is solved by generalized least squares adjustment (e.g. Koch, 1999). An essential element of P3 is the advancement of the GIA fingerprint parametrization according to Rietbroek et al. (2016) based on findings from Sasgen et al. (2017) and Gunter et al. (2014). The utilized parametrization for GIA in Antarctica aims to spatially resolve the GIA effect. This is done to potentially unravel GIA effects unpredicted by GIA modelling. In Antarctica, the predicted patterns of GIA forward modelling are incompatible with geodetic observations due to deficiencies in the knowledge about the rheological Earth structure (Ivins et al., 2021) and the ice loading history governing the present-day GIA effects (Whitehouse et al., 2019). In the other regions of the world, the spatial patterns of modelled present-day GIA effects is trusted to capture the present-day GIA effects for the largest part. Apart from the parametrization, an essential element of P3 is the characterization of the spatially correlated errors of the observations along with the investigation of the feasibility of the global inversion approach under the presence of these spatially correlated errors.

The Cryosphere, 14, 349–366, 2020
https://doi.org/10.5194/tc-14-349-2020

The Cryosphere
Open Access
EGU

Sensitivity of inverse glacial isostatic adjustment estimates over Antarctica

Matthias O. Willen[1], **Martin Horwath**[1], **Ludwig Schröder**[1,a], **Andreas Groh**[1], **Stefan R. M. Ligtenberg**[2], **Peter Kuipers Munneke**[2], and **Michiel R. van den Broeke**[2]

[1]Institut für Planetare Geodäsie, Technische Universität Dresden, Dresden, Germany
[2]Institute for Marine and Atmospheric research Utrecht (IMAU), Utrecht University, Utrecht, the Netherlands
[a]now at: Alfred Wegener Institute, Helmholtz Centre for Polar and Marine Research, Bremerhaven, Germany

Correspondence: Matthias O. Willen (matthias.willen@tu-dresden.de)

Received: 30 April 2019 – Discussion started: 17 May 2019
Revised: 3 December 2019 – Accepted: 21 December 2019 – Published: 30 January 2020

Abstract. Glacial isostatic adjustment (GIA) is a major source of uncertainty for ice and ocean mass balance estimates derived from satellite gravimetry. In Antarctica the gravimetric effect of cryospheric mass change and GIA are of the same order of magnitude. Inverse estimates from geodetic observations hold some promise for mass signal separation. Here, we investigate the combination of satellite gravimetry and altimetry and demonstrate that the choice of input data sets and processing methods will influence the resultant GIA inverse estimate. This includes the combination that spans the full GRACE record (April 2002–August 2016). Additionally, we show the variations that arise from combining the actual time series of the differing data sets. Using the inferred trends, we assess the spread of GIA solutions owing to (1) the choice of different degree-1 and C_{20} products, (2) viable candidate surface-elevation-change products derived from different altimetry missions corresponding to different time intervals, and (3) the uncertainties associated with firn process models. Decomposing the total-mass signal into the ice mass and the GIA components is strongly dependent on properly correcting for an apparent bias in regions of small signal. Here our ab initio solutions force the mean GIA and GRACE trend over the low precipitation zone of East Antarctica to be zero. Without applying this bias correction, the overall spread of total-mass change and GIA-related mass change using differing degree-1 and C_{20} products is 68 and 72 $\mathrm{Gt\,a^{-1}}$, respectively, for the same time period (March 2003–October 2009). The bias correction method collapses this spread to 6 and 5 $\mathrm{Gt\,a^{-1}}$, respectively. We characterize the firn process model uncertainty empirically by analysing differences between two alternative surface mass balance products. The differences propagate to a 10 $\mathrm{Gt\,a^{-1}}$ spread in debiased GIA-related mass change estimates. The choice of the altimetry product poses the largest uncertainty on debiased mass change estimates. The spread of debiased GIA-related mass change amounts to 15 $\mathrm{Gt\,a^{-1}}$ for the period from March 2003 to October 2009. We found a spread of 49 $\mathrm{Gt\,a^{-1}}$ comparing results for the periods April 2002–August 2016 and July 2010–August 2016. Our findings point out limitations associated with data quality, data processing, and correction for apparent biases.

1 Introduction

The quantification of recent and current sea level changes plays a crucial role for local, regional, and global projections. Mass changes of the Greenland and Antarctic ice sheets are responsible for approximately 20 % of the global mean sea level rise between 1991 and 2010 (Church et al., 2013). Space gravimetry observes temporal gravity changes which result from mass redistribution on and in Earth. An ice mass trend estimation can be determined using time-variable gravity fields from the Gravity Recovery And Climate Experiment (GRACE) mission (e.g. Groh et al., 2014; Forsberg et al., 2017), which is continued by its follow-on mission GRACE-FO.

Large uncertainty in the ice mass change estimates derived from space gravimetry is related to viscoelastic deformation of the solid Earth by glacial isostatic adjustment (GIA). This

Published by Copernicus Publications on behalf of the European Geosciences Union.

is the deformation of the solid Earth due to loading variations through sequences of past glacial advance and retreat over many millennia. The manifestation of ice sheet and GIA mass change signals is superimposed and is of the same order of magnitude over Antarctica (Sasgen et al., 2017). This requires GIA to be carefully considered when determining ice mass change. Moreover, quantified GIA provides insights into the glacial history of ice sheets or changing tectonic stress (Johnston et al., 1998).

One approach to determine the GIA signal is forward modelling (e.g. Ivins and James, 2005). GIA forward models are obtained using assumptions about the ice load history and the solid-Earth rheology, which are both subject to large uncertainties (Whitehouse, 2018; Whitehouse et al., 2019). GIA-induced vertical bedrock elevation change (BEC) derived from the Global Navigation Satellite System (GNSS) observations have been used to constrain forward models (e.g. King et al., 2010; Ivins et al., 2013; Whitehouse et al., 2012) or, more recently, to test probabilistic information of a suite of globally consistent forward models (Caron et al., 2018). Caron and Ivins (2020) used this method to investigate the regional GIA signal over Antarctica and to separate the contributions from oceanic and far-field regions.

In an alternative approach, satellite gravimetry and altimetry are combined to separate the GIA and ice-related mass signals (Wahr et al., 2000). Both spaceborne techniques observe a superposition of GIA and ice sheet change signals. For example, satellite altimetry observes surface elevation changes (SECs), some of which are caused by GIA-induced BEC. The combination requires assumptions about the relation between surface geometry changes and gravity field changes induced by GIA and likewise between the respective changes induced by ice sheet processes. These relations may be expressed in terms of effective densities. This combination approach was first implemented by Riva et al. (2009) and later refined by Groh et al. (2012) and Gunter et al. (2014). Hereinafter they are called the *inverse* (Whitehouse, 2018) because they use present-day observations to determine the GIA signal (in contrast to forward models). Results from Riva et al. (2009) fit better with GNSS-derived GIA rates than forward models (Thomas et al., 2011).

Recent studies separate the individual processes of the ice sheet and the underlying bedrock with statistical modelling (Zammit-Mangion et al., 2015; Martín-Español et al., 2016a). They use spatial and temporal a priori information (from numerical simulations), additional GNSS observations, and altimetry data of several satellite missions. Furthermore, a joint inversion has been presented that takes into account the rheological parameters of the solid Earth (Sasgen et al., 2017). Engels et al. (2018) use a regularized parameter estimation approach (dynamic patch) to resolve the superimposed mass trends in Antarctica. Martín-Español et al. (2016b) compared available GIA solutions from forward modelling and inverse estimation and have shown that differences are larger than indicated uncertainties.

We analyse the sensitivity of inverse GIA estimation on the choice of data input and methodology, thereby identifying both the possible causes of discrepancies and the uncertainty. Our inverse GIA estimation is based on the approach of Gunter et al. (2014) but uses both contrasting and updated data sets. Special attention is paid to surface processes, namely changes of mass and volume of the firn layer. By the term *firn*, we assume both snow and firn. In inverse GIA estimation, changes in the firn layer need to be separated from those in the ice layer below. For that purpose, the surface mass balance (SMB) as well as the volume change from the firn layer are needed. These are usually provided by regional climate models like RACMO2 (van Wessem et al., 2018) and firn densification models (FDMs) forced with climate models, like IMAU FDM (Ligtenberg et al., 2011). Uncertainties of these model products are poorly known. Here, we characterize the uncertainty by comparing the RACMO2.3p2 SMB products with those of the MAR model (Agosta et al., 2019).

Another focus of this research is on the use of ice altimetry data. Different altimeter missions such as Envisat, ICESat, or CryoSat-2 use different observation techniques and differ in their spatial and temporal coverage. The multi-mission (MM) altimetry data set delivered by Schröder et al. (2019a) is well suited for a GIA inversion over nearly the full GRACE observation period (April 2002–August 2016). The effect of using different gravity field solutions from the GRACE processing centres and different filtering options is shown by Gunter et al. (2014). We use different degree-1 and C_{20} products to quantify their effect on inverse GIA estimation. We contrast estimates derived by combining linear trends of input data to estimates derived by combining monthly-sampled time series of input data.

Section 2 derives and describes in detail the combination approach, bias corrections using the low-precipitation zone (LPZ) of East Antarctica, estimation of the mass balance, and filtering. Afterwards, we explain how the errors for the firn process models are characterized and how the sensitivity analysis is performed. Furthermore, the approach is adapted to extract a more nuanced and self-consistent combination of input-data time series. Section 3 describes the products employed, processing steps, and additional assumptions. Section 4 presents results of derived uncertainties of the firn process models, the sensitivity analysis, and the time-series-based combination. Finally, the results are discussed and the most important findings are summarized in the conclusions.

2 Methods

2.1 Combination approach

Wahr et al. (2000) were the first to suggest the combination of satellite geodetic methods – gravimetry and altimetry – to estimate GIA. We use the analytical approach from Wahr et al. (1998) to explain gravity changes by mass changes projected into a spherical layer (with radius a) – termed area density changes (ADCs) or surface density changes. Note that a change of mass is with respect to a reference mass distribution. Based on GRACE solutions given in the spherical harmonic domain, the conversion of changes in Stokes coefficients with degree n and order m (Δc_{nm}) into spherical harmonic coefficients of ADC ($\Delta\kappa_{nm}$) is

$$\Delta\kappa_{nm} = \frac{2n+1}{1+k'_n}\frac{M_\mathrm{E}}{4\pi a^2}\Delta c_{nm}, \tag{1}$$

where M_E is the total mass of the Earth, a the equatorial radius of the reference ellipsoid, and k'_n the second-load Love number to account for the deformation potential of the solid Earth induced by the mass redistribution. The linear ADC $\dot{\kappa}_{nm}$ is synthesized into spatial domain $\dot{m}_\mathrm{grav}$, which is the superposition of the ADC through GIA, and processes in the ice (ID) and firn layer:

$$\dot{m}_\mathrm{grav} = \dot{m}_\mathrm{GIA} + \dot{m}_\mathrm{ID} + \dot{m}_\mathrm{firn}. \tag{2}$$

While GIA is not a process of ADC, $\dot{m}_\mathrm{GIA}$ is defined as the apparent ADC that would induce a gravity field effect equal to the GIA-induced gravity field effect. We refer to $\dot{m}_\mathrm{GIA}$ (as well as spatial integrals of $\dot{m}_\mathrm{GIA}$) as *GIA-related mass change*. ID summarizes all processes which are weighted with ice density, e.g. ice-dynamic flow or basal melt. We summarize the ice-induced, or cryospheric, area density trend as $\dot{m}_\mathrm{ice} = \dot{m}_\mathrm{ID} + \dot{m}_\mathrm{firn}$.

Analogously, the overall linear SEC derived from altimetry $\dot{\tilde{h}}_\mathrm{alt}$ is the sum of the linear SEC through ID, firn, GIA, and elastic BEC:

$$\dot{\tilde{h}}_\mathrm{alt} = \dot{h}_\mathrm{GIA} + \dot{h}_\mathrm{elastic} + \dot{h}_\mathrm{ID} + \dot{h}_\mathrm{firn}. \tag{3}$$

Note that GIA refers to the viscoelastic deformation of the solid Earth. The elastic BEC ($\dot{h}_\mathrm{elastic}$) triggered by present-day ice mass changes needs to be subtracted from the overall SEC observed by altimetry $\dot{\tilde{h}}_\mathrm{alt}$ prior to the combination. We define $\dot{h}_\mathrm{alt} = \dot{\tilde{h}}_\mathrm{alt} - \dot{h}_\mathrm{elastic}$. Doing this, the SEC signals in $\dot{h}_\mathrm{alt}$ are consistent with ADC signals in $\dot{m}_\mathrm{grav}$.

The process-related elevation and area density changes are linked with effective density assumptions (ρ_GIA, ρ_ID):

$$\dot{m}_\mathrm{GIA} = \rho_\mathrm{GIA}\cdot\dot{h}_\mathrm{GIA}, \tag{4}$$
$$\dot{m}_\mathrm{ID} = \rho_\mathrm{ID}\cdot\dot{h}_\mathrm{ID}. \tag{5}$$

Rearranging Eq. (3) to

$$\dot{h}_\mathrm{ID} = \dot{h}_\mathrm{alt} - \dot{h}_\mathrm{firn} - \dot{h}_\mathrm{GIA} \tag{6}$$

and substituting it together with Eqs. (4) and (5) into Eq. (2) leads to

$$\dot{m}_\mathrm{grav} = \rho_\mathrm{GIA}\dot{h}_\mathrm{GIA} + \rho_\mathrm{ID}(\dot{h}_\mathrm{alt} - \dot{h}_\mathrm{firn} - \dot{h}_\mathrm{GIA}) + \dot{m}_\mathrm{firn}, \tag{7}$$

which can be solved for

$$\dot{h}_\mathrm{GIA} = \frac{\dot{m}_\mathrm{grav} - \rho_\mathrm{ID}(\dot{h}_\mathrm{alt} - \dot{h}_\mathrm{firn}) - \dot{m}_\mathrm{firn}}{\rho_\mathrm{GIA} - \rho_\mathrm{ID}}. \tag{8}$$

In Gunter et al. (2014), Eq. (8) is modified with a criterion to include assumptions about the difference $\dot{h}_\mathrm{alt} - \dot{h}_\mathrm{firn}$ using a priori uncertainties. ρ_ID is replaced by ρ_α to permit the following case distinction:

$$\dot{h}_\mathrm{GIA} = \frac{\dot{m}_\mathrm{grav} - \rho_\alpha(\dot{h}_\mathrm{alt} - \dot{h}_\mathrm{firn}) - \dot{m}_\mathrm{firn}}{\rho_\mathrm{GIA} - \rho_\alpha}, \tag{9}$$

where

$$\rho_\alpha = \begin{cases} \rho_\mathrm{ID}, \mathrm{(I)} & \text{if } \dot{h}_\mathrm{alt} - \dot{h}_\mathrm{firn} < 0 \\ & \text{and } |\dot{h}_\mathrm{alt} - \dot{h}_\mathrm{firn}| > 2\sigma_h \\ \rho_\mathrm{firn}, \mathrm{(II)} & \text{if } \dot{h}_\mathrm{alt} - \dot{h}_\mathrm{firn} > 0 \\ & \text{and } |\dot{h}_\mathrm{alt} - \dot{h}_\mathrm{firn}| > 2\sigma_h \\ 0, \mathrm{(III)} & \text{otherwise} \end{cases} \tag{10}$$

with

$$\sigma_h = \sqrt{\sigma^2_{\dot{h}_\mathrm{alt}} + \sigma^2_{\dot{h}_\mathrm{firn}}}. \tag{11}$$

The case distinction accounts for uncertainties in altimetry and in the firn densification model (FDM) as well as a priori knowledge on ice sheet processes. The GIA-induced BEC is in the millimetre per year range, whereas $\dot{h}_\mathrm{firn}$ and $\dot{h}_\mathrm{ID}$ can be in the centimetre to metre per year range. If altimetry and FDM are perfect, $\dot{h}_\mathrm{alt} - \dot{h}_\mathrm{firn}$ would leave essentially $\dot{h}_\mathrm{ID}$ (apart from a very small $\dot{h}_\mathrm{GIA}$). The following case distinctions are made.

- *Case I.* If differences between $\dot{h}_\mathrm{alt}$ and $\dot{h}_\mathrm{firn}$ are significantly negative, an ice-dynamic-induced SEC is assumed (glacial thinning). Gunter et al. (2014) argue that only one region in Antarctica is known to show glacial thickening: the area of the Kamb Ice Stream (Retzlaff and Bentley, 1993; Wingham et al., 2006). This region is therefore treated separately by a mask which sets ρ_α to ρ_ID. The mask is generated from positive SEC from altimetry in this area.
- *Case II.* If differences between $\dot{h}_\mathrm{alt}$ and $\dot{h}_\mathrm{firn}$ are significantly positive, it is assumed that the FDM underestimates SEC due to firn processes and the remaining part therefore must not be weighted with ice density but with firn density.
- *Case III.* If differences between $\dot{h}_\mathrm{alt}$ and $\dot{h}_\mathrm{firn}$ are not significant (with an absolute value smaller than $2\sigma_h$), those differences are ignored by setting $\rho_\alpha = 0$, which means $\dot{m}_\mathrm{GIA} = \dot{m}_\mathrm{grav} - \dot{m}_\mathrm{firn}$. That is, no mass change in the ice layer is considered and a mass trend of the ice sheet only arises by the trend of cumulated surface mass balance anomalies.

Making this case distinction for ρ_α has the advantage of solving for GIA without a predefined spatial mask to distinguish between firn and ice processes (e.g. density mask in Riva et al., 2009) except for the Kamb Ice Stream. An underestimated σ_h leads to differences between $\dot{h}_{\mathrm{alt}}$ and $\dot{h}_{\mathrm{firn}}$ being included in the mass balance, although they are within their true uncertainty bounds and vice versa if σ_h is overestimated.

2.2 Bias corrections and estimation of the mass balance

The following steps are performed in sequence.

- *Step 1*. Estimation of biased $\dot{h}_{\mathrm{GIA}}$ using the data combination approach (Eq. 9).
- *Step 2*. Removing the bias from $\dot{h}_{\mathrm{GIA}}$, leading to the debiased $\tilde{\dot{h}}_{\mathrm{GIA}}$.
- *Step 3*. Removing the bias from $\dot{m}_{\mathrm{grav}}$, leading to the debiased $\tilde{\dot{m}}_{\mathrm{grav}}$.
- *Step 4*. Estimation of the debiased ice mass trend from debiased GIA-related mass trend (Step 2) and debiased total-mass trend (Step 3).

The bias corrections are necessary to consider offsets introduced by systematic errors in degree-1 and C_{20}. The estimation of the bias is done using the same strategy as Gunter et al. (2014). They argue that the effect of such offsets is significantly larger than potential mass signals in a low-precipitation zone (LPZ) of the East Antarctic Ice Sheet.

In Step 2, the *LPZ-based GIA bias correction* is applied. It is assumed that the GIA-induced BEC should be negligibly small in this area. The GIA estimate from Step 1, averaged over the LPZ, $\overline{\dot{h}}_{\mathrm{GIA,LPZ}}$, is interpreted as a bias due to the input data sets. It is subtracted from $\dot{h}_{\mathrm{GIA}}$. The debiased GIA-induced BEC is

$$\tilde{\dot{h}}_{\mathrm{GIA}} = \dot{h}_{\mathrm{GIA}} - \overline{\dot{h}}_{\mathrm{GIA,LPZ}}. \tag{12}$$

From this we derive the debiased GIA-related mass trend

$$\tilde{\dot{m}}_{\mathrm{GIA}} = \tilde{\dot{h}}_{\mathrm{GIA}} \cdot \rho_{\mathrm{GIA}}. \tag{13}$$

This means that input-data-set biases are jointly removed. Removing a small GIA-induced BEC introduces an error in the final result. GIA models predict approximately -3 to $+1\,\mathrm{mm\,a^{-1}}$ in the area of the LPZ (Whitehouse et al., 2019). Gunter et al. (2014) argue that the error introduced by the LPZ bias correction is smaller than other bias contributors.

In Step 3, the *LPZ-based GRACE bias correction* is applied. ADCs from gravimetry are calibrated to the LPZ by removing the mean ADC in this area, $\overline{\dot{m}}_{\mathrm{grav,LPZ}}$. The debiased gravimetric ADC is

$$\tilde{\dot{m}}_{\mathrm{grav}} = \dot{m}_{\mathrm{grav}} - \overline{\dot{m}}_{\mathrm{grav,LPZ}}. \tag{14}$$

In Step 4, the debiased ice mass trend is calculated as

$$\tilde{\dot{m}}_{\mathrm{ice}} = \tilde{\dot{m}}_{\mathrm{grav}} - \tilde{\dot{m}}_{\mathrm{GIA}}. \tag{15}$$

Note that the gravimetric bias correction is not applied to $\dot{m}_{\mathrm{grav}}$ used in Step 1, the initial combination (Eq. 9).

2.3 Filtering

For the necessary noise suppression we use GRACE data with a de-striping filter applied ($\mathcal{F}_{\mathrm{DS}}(\dot{m}_{\mathrm{grav}})$) in addition to the filtering implied by the spherical harmonic truncation. Ideally, the data and models involved in the combination should have consistent spatial resolution; that is, they should be filtered consistently. This is not strictly possible for the quotient $(\dot{m}_{\mathrm{grav}})/(\rho_{\mathrm{GIA}} - \rho_\alpha)$ in Eq. (9) because no unfiltered $\dot{m}_{\mathrm{grav}}$ is available that could be divided by $(\rho_{\mathrm{GIA}} - \rho_\alpha)$ before filtering. Pragmatically, components with a similar spatial resolution are combined before they are filtered with a Gaussian filter $\mathcal{F}$. Hence, we obtain a filtered GIA-induced BEC:

$$\tilde{\mathcal{F}}(\dot{h}_{\mathrm{GIA}}) = \frac{\mathcal{F}(\mathcal{F}_{\mathrm{DS}}(\dot{m}_{\mathrm{grav}}))}{\mathcal{F}(\rho_{\mathrm{GIA}} - \rho_\alpha)} - \mathcal{F}\left(\frac{\rho_\alpha(\dot{h}_{\mathrm{alt}} - \dot{h}_{\mathrm{firn}}) - \dot{m}_{\mathrm{firn}}}{\rho_{\mathrm{GIA}} - \rho_\alpha}\right). \tag{16}$$

For integrating mass trends in space, the signal redistribution (leakage) is taken into account by a buffer zone equal to the half-response width of the Gaussian filter appended to the grounding line of the ice sheet (Sect. 4.2). We do not correct for leakage through ocean mass signal separately as it amounts to only $4.5\,\mathrm{Gt\,a^{-1}}$ (Gunter et al., 2014). This ocean mass leakage is the same in every experiment, because we do not test the sensitivity to filters.

2.4 Uncertainty characterization of firn process models

In Eqs. (9) and (10), assumptions on uncertainties of the FDM and altimetry are crucial. Gunter et al. (2014) take $\sigma_{\dot{h}_{\mathrm{alt}}}$ from the formal uncertainty of the least-squares estimation. $\sigma_{\dot{h}_{\mathrm{firn}}}$ can be derived in the same way from the estimated trend of FDM SEC for the observation period. Note that both uncertainties are derived from stochastic information of the least-squares estimation rather than from an uncertainty characterization of the measurements and the model. Gunter et al. (2014) have also performed an uncertainty analysis of the combination result. For this purpose, they define the SMB-related uncertainty as 10 % of the estimated trend value, referring to Rignot et al. (2008). Note that the uncertainty assessment by Rignot et al. (2008), which amounts to 10 %–30 % of the signal, is applied to a different physical quantity than $\dot{h}_{\mathrm{firn}}$: namely to the snow accumulation in a drainage basin.

Because there is no comprehensive regional climate model ensemble, we quantify the error of firn process models by statistics on differences between two models. We use differences of trends of cumulated surface mass balance anomalies (cSMBAs) and of firn thickness trends. We assume those differences are due to modelling errors. This characterization comprises only a part of the full uncertainty, because it is based on two alternative climate model products.

2.5 Time-series-based combination

Previous studies combining gravimetry and altimetry are based on linear seasonal deterministic models over certain periods (Riva et al., 2009; Gunter et al., 2014; Martín-Español et al., 2016a; Sasgen et al., 2017; Engels et al., 2018). However, signals in the firn and ice layer over the Antarctic Ice Sheet (AIS) show inter-annual changes (Horwath et al., 2012; Ligtenberg et al., 2012; Mémin et al., 2015). In theory, combining observations on a time series level will lead to a linear GIA signal. For T months the vector

$$\boldsymbol{m}_{\mathrm{grav}} = \{m_{\mathrm{grav}}(t=1), \ldots, m_{\mathrm{grav}}(t=T)\} \tag{17}$$

contains the differences in mass at month $t = 1, \ldots, T$ with respect to a reference mass distribution. The combination of all time series is

$$\boldsymbol{h}_{\mathrm{GIA}} = \frac{\boldsymbol{m}_{\mathrm{grav}} - \rho_{\mathrm{ID}}(\boldsymbol{h}_{\mathrm{alt}} - \boldsymbol{h}_{\mathrm{firn}}) - \boldsymbol{m}_{\mathrm{firn}}}{\rho_{\mathrm{GIA}} - \rho_{\mathrm{ID}}}. \tag{18}$$

This requires that all data are available as monthly gridded products. To simplify, we assume that effective densities do not change over time. To be consistent with the combination of trends, ρ_{ID} is replaced with ρ_α from the trend-based approach.

The data and models of every month are filtered in the same way as for the trend-based approach to make the resolution consistent (Sect. 2.3). Afterwards they are combined according to Eq. (18), which results in a GIA time series for each grid cell.

By assumption the GIA signal in the resulting time series $\boldsymbol{h}_{\mathrm{GIA}}$ is linear over decades of satellite observations (e.g. Huybrechts and Le Meur, 1999). A fitted trend to $\boldsymbol{h}_{\mathrm{GIA}}$ is $\dot{h}_{\mathrm{GIA}}$. We are aware that for regions with a low-viscosity asthenosphere, e.g. Pine Island Bay, the viscoelastic deformation associated with GIA may be non-linear even for decadal periods (Barletta et al., 2018). In this case, the assumption of a linear GIA-induced BEC introduces an error.

2.6 Sensitivity analysis

The sensitivity of inverse GIA estimates to different data, models, and assumptions is quantified. Starting from a reference experiment, certain parameters are changed. Every experiment is performed with and without the two LPZ-based bias corrections to demonstrate their effect. It is examined how different altimetry data (Sect. 3.1), degree-1 and C_{20} products (Sect. 3.2), and the empirically determined errors of the firn process models (Sect. 4.1) affect the GIA solution. Analogous to Riva et al. (2009) and Gunter et al. (2014), a Gaussian filter (half-response width = 400 km) is applied to all data sets. For the integration of mass trends over the AIS, the West Antarctic Ice Sheet (WAIS), and the East Antarctic Ice Sheet (EAIS), we use a buffer zone of 400 km grounding-line distance to mitigate leakage. The Antarctic Peninsula (AP) is not considered separately here.

For each inverse GIA solution, the integrated mass change is calculated. In addition, a root-mean-square (rms) difference with respect to the reference experiment is determined, hereinafter referred to as the *rms difference from reference experiment* ($\mathrm{RMS_{RE}}$),

$$\mathrm{RMS_{RE}} = \sqrt{\frac{1}{N}\sum_{i=1}^{N}\left(\dot{h}_{\mathrm{GIA,comp},i} - \dot{h}_{\mathrm{GIA,ref},i}\right)^2}. \tag{19}$$

Here, N is the number of grid cells of a Cartesian grid in the polar stereographic projection of the AIS area (EPSG: 3031) including the buffer zone. $\dot{h}_{\mathrm{GIA,comp}}$ refers to the GIA solution which is compared to the reference experiment ($\dot{h}_{\mathrm{GIA,ref}}$). The $\mathrm{RMS_{RE}}$ values are sensitive to regional differences, which may be hidden in the comparison of integrated mass trends.

The sensitivity to the choice of firn process models is investigated as follows: based on the comparison of two firn process models, empirical samples of error patterns are generated. They are added to $\dot{h}_{\mathrm{firn}}$ and $\dot{m}_{\mathrm{firn}}$ and propagated to the empirical GIA estimates. Additionally, all identified trend differences of cSMBAs are added to $\dot{h}_{\mathrm{firn}}$ and $\dot{m}_{\mathrm{firn}}$.

Furthermore, the dependency on differing time periods is investigated. Under the assumption that GIA is linear in time, the used time interval should have negligible influence. While the time interval for the reference experiment is March 2003–October 2009 (according to Gunter et al., 2014), alternative periods are the main GRACE observation period (April 2002–August 2016) and the overlap period between GRACE and CryoSat-2 (July 2010–August 2016).

3 Data and models

This section specifies the data sets and processing steps used in the sensitivity experiments which are summarized in Table 1. Furthermore, models and assumptions are explained. Reference system parameters are chosen according to the IERS Conventions (Petit and Luzum, 2010).

3.1 Altimetry

The SECs from Schröder et al. (2019a) are based on a repeat-altimetry analysis in a multi-mission altimetry (MM altimetry) framework. Data from the Seasat, Geosat, ERS-1, ERS-2, Envisat, ICESat, and CryoSat-2 missions are combined, resulting in a monthly sampled time series on a 10 km grid. The reader is referred to Schröder et al. (2019a) for details on processing and background information. In order to combine the altimetry time series with GRACE, we use the monthly results from April 2002 at the earliest to August 2016 at the latest. This period involves observations of ERS-2, Envisat, ICESat, and CryoSat-2 missions (Fig. 1a). The altimetry missions have a different spatial and temporal sampling, e.g. ICESat's campaign-style temporal sampling.

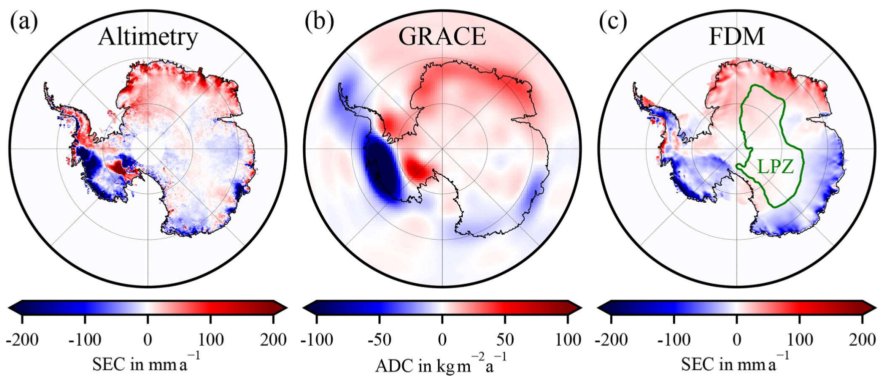

Figure 1. (a) Surface elevation change (SEC) from the multi-mission altimetry product (Schröder et al., 2019a), **(b)** GRACE-derived area density changes (ADC), and **(c)** FDM-derived SEC (time period: April 2002–August 2016). A Gaussian filter was applied to the GRACE result (half-response 250 km). Low-precipitation zone (LPZ) (green, **c**).

Further, the data quality varies over mission lifetime. For this reason every month of the combined time series differs in spatial coverage. We obtain a linear rate over the respective intervals by adjusting an offset and a linear trend to the MM time series for each cell of the 10 km grid. For the reference experiment no annual periodic signal is co-estimated in order to be consistent with Gunter et al. (2014). We apply weights according to the uncertainty estimates of each epoch of the MM time series. We took the criterion that the trend would only be estimated for a grid cell if more than 5 months with observations are available and at least 80 % of the selected total time span is covered. This criterion should avoid outlier trends through insufficient sampling. The uncertainty $\sigma_{\dot{h}_{\mathrm{alt}}}$ used in Eq. (11) is the a posteriori standard deviation derived from the least-squares adjustment of the MM time series.

To investigate how the choice of altimetry products affects the GIA estimation, single-mission time series are calculated for Envisat and ICESat. They consistently use the same processing steps as the MM altimetry from Schröder et al. (2019a), with the exception that the final step of weighted spatio-temporal smoothing is applied to single-mission data rather than multi-mission data. In total three different altimetry time series are used for testing the gravimetry–altimetry combination approach. To assess the sensitivity of results to the co-estimation of seasonal signals, an additional version of the MM altimetry trends is calculated by co-estimating the annual sinusoidal signal (*MM seasonal* in Table 1). This is consistent with the treatment of GRACE and the firn process models.

Part of the altimetry-derived SEC is caused by the elastic BEC of the solid Earth due to present-day ice mass change ($\dot{h}_{\mathrm{elastic}}$), which needs to be subtracted from the altimetry observations ($\dot{\tilde{h}}_{\mathrm{alt}}$) prior to the combination (Eq. 9). We estimate $\dot{h}_{\mathrm{elastic}}$ to be $-1.5\,\%$ of $\dot{\tilde{h}}_{\mathrm{alt}}$ (Riva et al., 2009). Hence, the elastic-corrected altimetry-derived SEC is

$$\dot{h}_{\mathrm{alt}} = \dot{\tilde{h}}_{\mathrm{alt}} - \dot{h}_{\mathrm{elastic}} \approx 1.015 \cdot \dot{\tilde{h}}_{\mathrm{alt}}. \tag{20}$$

The approximative nature of this elastic correction leaves an error, but its influence on the GIA estimate is negligible (Gunter et al., 2014).

3.2 Gravimetry

GRACE-derived monthly mass variations are calculated from the ITSG-Grace2016 monthly gravity field solutions up to a degree and order of 90 (Mayer-Gürr et al., 2016) using Eq. (1). Monthly solutions from other processing centres are not considered because ITSG-Grace2016 is identified through internal comparison as the gravity field solution series with a high signal-to-noise ratio. This is supported by Jean et al. (2018), who found that the precursor ITSG-Grace2014 show a lower noise level compared to solutions from other processing centres. The influence of the different GRACE monthly solutions on the inverse GIA result was shown and discussed in Gunter et al. (2014). We do not use solutions after August 2016. Those solutions show a much higher noise level due to accelerometer issues.

GRACE monthly solutions need to be complemented by the degree-1 term of the spherical harmonic coefficients, as this is not observed by GRACE. Three different products to replace the degree-1 coefficients are evaluated. (1) A product is determined following Swenson et al. (2008) using ITSG-Grace2016 monthly solutions (d1_ITSG). (2) A satellite laser ranging (SLR) product by Cheng et al. (2013b) (d1_SLR) and (3) degree-1 coefficients by Rietbroek et al. (2016) are used (d1_ITG).

Furthermore, the influence of the flattening term C_{20} is investigated. Because C_{20} is poorly determined by GRACE (Cheng and Ries, 2017), external products are compared. (1) SLR-based time series are used from the Center for Space Research at the University of Texas, USA (c20_SLR_CSR;

Cheng et al., 2013a). (2) SLR-based time series from the German Research Centre for Geosciences, Potsdam, Germany are used (c20_SLR_GFZ; König et al., 2019). (3) A time series from the Delft University of Technology, Delft, Netherlands (c20_TU_Delft), which is derived from GRACE observations themselves and an ocean model is used (Sun et al., 2015).

A critical point is filtering because the monthly solutions are noisy and have a correlated error pattern (Horwath and Dietrich, 2009). A de-striping filter is applied in the spherical harmonic domain (Swenson and Wahr, 2006).

A linear seasonal model is adjusted to fit the filtered Stokes coefficients (offset, linear, annual periodic, and 161 d periodic). The trend is synthesized from the spherical harmonic into the spatial domain on the altimetry grid with 50 km resolution. In this way for each grid cell a linear area density trend in kilogrammes per square metre per year is determined (Fig. 1b).

3.3 Firn process models

Information on variations in the firn layer is required in the combination approach (Eq. 10). SMB is the sum of precipitation, snow drift, sublimation, and meltwater runoff. The SMB components are numerically simulated with the RACMO2.3p2 model, which contains a multilayer snow model developed by the Royal Netherlands Meteorological Institute (KNMI) and the Institute for Marine and Atmospheric Research, Utrecht, Netherlands (IMAU) (van Wessem et al., 2018). These results are compared to the MAR model of the Laboratory of Climatology, Liège, Belgium (Agosta et al., 2019). The regional climate models are forced at their lateral boundaries with the ERA-40 and ERA-Interim reanalyses. Mass fluxes (snowfall, snow drift, sublimation, erosion–deposition, and surface melt) as well as surface temperature are then used to force an offline firn densification model that includes firn compaction, vertical meltwater transport and refreezing, and thermodynamics of the firn layer.

The RACMO2 and MAR SMB products are appropriate for comparison as both are similar in terms of temporal (monthly) and spatial resolution (RACMO2: 27 km; MAR: 35 km). Moreover, both variants considered here use the same forcing. There is no independent knowledge (in a spatial resolution similar to that of SMB models) about the ice flow contribution to ice mass balance and hence about the degree of balance or imbalance between SMB and ice flow. Therefore, the modelled SMB is only used to derive SMB-induced mass variations with respect to any background signal of mass change. The unknown background signal of mass change is the possible imbalance between the mean SMB over a multi-year reference period and the mean effect of ice flow over the same reference period. The considered SMB-induced mass variations hence arise from the temporal cumulation of SMB anomalies with respect to the mean SMB over the reference period. Here, we define the reference period to be the entire model period for RACMO2.3p2 and MAR (January 1979–December 2016). For the satellite observation periods (e.g. April 2002–August 2016) the surface mass trend ($\dot{m}_{\mathrm{firn}}$), or literally the trend of cumulated surface mass balance anomalies (cSMBAs), is estimated (co-estimated with bias and annual periodic signal).

The used firn model IMAU FDM (Ligtenberg et al., 2011) is forced at the upper boundary by SMB components from RACMO2. The firn layer is initialized by forcing the FDM repeatedly with the 1979–2016 surface mass fluxes and temperature, until an equilibrium firn layer is established. This implies that present-day conditions represent a state of equilibrium and that there is no net firn thickness change over the model period January 1979–December 2016. One result of the actual model run is the firn-elevation-change time series. A linear seasonal model (bias, trend, annual periodic signal) of firn-process-induced SEC is adjusted to fit the FDM time series for the observation periods under investigation (Fig. 1c).

The LPZ (Fig. 1c) is defined based on the ECMWF ERA-Interim reanalysis precipitation product. We use $20\,\mathrm{mm\,a^{-1}}$ annual precipitation as a threshold for low precipitation (Riva et al., 2009), rather than $21.9\,\mathrm{mm\,a^{-1}}$ used by Gunter et al. (2014).

The trend differences between RACMO2.3p2 and MAR SMB products are used for uncertainty characterization of firn process models. In order to gain statistical information on possible trend differences over a 7-year interval, we calculate trend differences over 32 intervals of 7 years (January 1979–December 1965; January 1980–December 1966;...; January 2010–December 2016) covered by RACMO2.3p2 and MAR. The 7-year length is the approximate length of the observation period of our reference experiment (March 2003–October 2009) defined by the ICESat observation period. A FDM forced with MAR SMB does not exist. However, the RACMO2.3p2 SMB and the derived FDM are directly linked to each other. For this reason we assume that derived conclusions on errors of SMB are transferable to the FDM as a lower bound. Pseudo FDM trend differences are estimated out of the cSMBA trends by

$$\Delta\dot{h}_{\mathrm{firn},j} = \frac{\Delta\dot{m}_{\mathrm{firn},j}}{\rho_{\mathrm{MAR}}}. \tag{21}$$

$\Delta\dot{m}_{\mathrm{firn},j}$ is the jth trend difference between cSMBA from RACMO2 and cSMBA from MAR. ρ_{MAR} is calculated from MAR density fields by taking their average over the near-surface layers (0–1 m) and over the whole model period. This does not consider the evolution of the firn layer, as an independent FDM driven by MAR outputs would consider it. Furthermore, uncertainties associated with equilibrium assumptions are not considered.

Prior to the combination, cSMBA and FDM trends are linearly interpolated to the polar stereographic grid. The high-resolution products (altimetry and firn process models) are modified as follows. NaN-Grid cells on the grounded part of the ice sheet (missing data) are treated as case III in Eq. (10).

3.4 Density assumptions

The ratio between volume changes and area density changes is defined by the effective densities ρ_{GIA}, ρ_{firn}, and ρ_{ID} for GIA-related, firn-related, and ice-related processes, respectively. We use a ρ_{ID} of $917\,\mathrm{kg\,m^{-3}}$. The firn density is variable in space and time. The location-dependent estimation for ρ_{firn} is calculated using the empirical Eq. (2) in Ligtenberg et al. (2011).

The density mask for ρ_{GIA} is generated as follows: The ratio between the GIA-induced BEC and the GIA-induced ADC is about $3700\,\mathrm{kg\,m^{-3}}$ (Wahr et al., 2000). We use $4000\,\mathrm{kg\,m^{-3}}$ over the Antarctic continent and $3400\,\mathrm{kg\,m^{-3}}$ under the ice shelves and the ocean with a smooth transition (according to Riva et al., 2009; Gunter et al., 2014). These numbers account for the redistribution of ocean mass through GIA and are derived from forward-model results. This density is not a density in a material-science sense. It is an effective value which sets GIA-induced BEC and the ADC in relation. The term *rock* used in the literature might be misleading.

4 Results

4.1 SMB uncertainty

There are considerable differences between the time series of cSMBA from the RACMO2 and MAR SMB products for each cell. Figure 2 shows the integrated values for the AIS. Note that a ~ 400 Gt cSMBA difference in 1987 (8 years after model start) represents a $50\,\mathrm{Gt\,a^{-1}}$ difference in SMB, which is $\sim 2\,\%$ of the total grounded ice sheet SMB. The integrated SMB from RACMO2.3p2 is $2229\,\mathrm{Gt\,a^{-1}}$ with an interannual variability of $109\,\mathrm{Gt\,a^{-1}}$ (van Wessem et al., 2018). We use the 32 trend differences from the moving 7-year intervals to quantify discrepancies of derived cSMBA trends between both models. Figure 3 shows (1) the rms of all trend differences and compares it with (2) the formal uncertainty we derive from the least-squares estimation and with (3) the 10 % uncertainty assumption (Sect. 2.4). The last two are derived from the estimated cSMBA trends of the RACMO2.3p2 SMB product over the ICESat observation period (March 2003–October 2009). The formal uncertainty and the 10 % assumption are similar in spatial pattern and magnitude. The rms of trend differences is similar in spatial pattern, too, but approximately 3 times larger in magnitude.

To extract the dominant error patterns, a spectral decomposition of the 32 7-year trend differences (see Sect. 3.3) is carried out using principal-component analysis (using singular value decomposition). Hence, the dominant empirical orthogonal functions (EOFs) and accompanying principal components are computed. From this analysis we obtain the dominant error patterns that are uncorrelated to each other and capture characteristic features of uncertainty. The first three EOFs of the trend differences explain $\sim 68\,\%$ of the total variance (Fig. 4a–c). The normalized EOF is scaled with the square root of the particular eigenvalue. Figure 4d shows the principle components indicating the scaling of the corresponding EOF. For instance, EOF-1 is dominated by variations in the WAIS. EOF-2 shows more variations on smaller scales. Without an attempt to further interpret the patterns of trend differences between the two models, the explored trend differences are used here to investigate the sensitivity of the inverse GIA estimates to these differences characterizing firn process uncertainty. For this purpose, (1) we add the EOFs to the firn process trends ($\dot{m}_{\mathrm{firn}}$, $\dot{h}_{\mathrm{firn}}$), which we use as input for the data combination. Because a FDM forced with MAR products does not exist, we transfer the cSMBA-derived EOFs to FDM EOFs by calculating pseudo EOFs using MAR density fields (see Sect. 3.3, Eq. 21). The pseudo EOFs account for a lower bound of uncertainties of the firn thickness trends. True firn thickness trend differences are presumably higher as they would contain the potential mismodelling of firn densification. From the added EOFs we get three GIA estimates to be compared with our reference solution. (2) Moreover, we add each trend difference separately to the cSMBA trend and each pseudo trend difference separately to the firn thickness trend. The pseudo firn thickness trend differences are likewise calculated using MAR density. This results in another 32 GIA estimates.

4.2 Sensitivity analysis

Inverse GIA estimates are calculated using different choices of (1) degree-1 solutions, (2) C_{20} substitutions, (3) altimetry products, (4) empirical orthogonal functions (EOFs) of firn process errors, and (5) time intervals (Table 1). The reference experiment refers to the time period March 2003–October 2009 and uses the MM-altimetry-derived SEC, ITSG-Grace2016 monthly solution (degree-1: d1_ITSG, C20: SLR_CSR) and the firn process trends from RACMO2.3p2 over this period. The rms of the reference GIA-induced BEC estimate is $2.2\,\mathrm{mm\,a^{-1}}$. The estimated ρ_α (Eq. 10) is shown in Fig. 5a. Apart from the gridded GIA-induced BEC (Figs. 5b, S5 in the Supplement), we compare the integrated trends $\dot{\bar{m}}_{\mathrm{grav}}$, $\dot{\bar{m}}_{\mathrm{GIA}}$, and $\dot{\bar{m}}_{\mathrm{ice}}$ corresponding to total-mass change (from GRACE), GIA-related mass change, and ice mass change, respectively. The results are summarized in Table 2. Furthermore, the $\mathrm{RMS_{RE}}$ (Eq. 19) quantifies the discrepancy to the reference experiment GIA estimate. Figure 6 shows the mass balance estimates for March 2003–October 2009.

Biased total-mass changes for different C_{20} and degree-1 products vary between $-43\,\mathrm{Gt\,a^{-1}}$ (c20_TU_Delft) and $+25\,\mathrm{Gt\,a^{-1}}$ (d1_SLR), a range of $68\,\mathrm{Gt\,a^{-1}}$. Debiased total-mass change (Eq. 14) only differ by $6\,\mathrm{Gt\,a^{-1}}$ for the same time period (Table 2). Figure 6 illustrates biased and debi-

Table 1. Overview of all performed experiments of the sensitivity analysis (Sects. 2.6 and 4.2, Table 2). All experiments use ITSG-Grace2016 monthly solutions (Mayer-Gürr et al., 2016) over the March 2003–October 2009 time period, except for the last two experiments which use the quoted time period.

Experiment	Degree-1 repl. Sect. 3.2	C_{20} repl. Sect. 3.2	Used altimetry Sect. 3.1	Used firn process model Sect. 3.3
Reference	d1_ITSG	c20_SLR_CSR	Multi-mission (incl. ERS-2, Envisat, ICESat)	RACMO2.3p2
d1_SLR	d1_SLR	c20_SLR_CSR	Multi-mission	RACMO2.3p2
d1_ITG	d1_ITG	c20_SLR_CSR	Multi-mission	RACMO2.3p2
c20_SLR_GFZ	d1_ITSG	c20_SLR_GFZ	Multi-mission	RACMO2.3p2
c20_TU_Delft	d1_ITSG	c20_TU_Delft	Multi-mission	RACMO2.3p2
ICESat only	d1_ITSG	c20_SLR_CSR	ICESat	RACMO2.3p2
Envisat only	d1_ITSG	c20_SLR_CSR	Envisat	RACMO2.3p2
MM seasonal	d1_ITSG	c20_SLR_CSR	Multi-mission, co-estimation of seasonal components	RACMO2.3p2
RACMO2+EOFx	d1_ITSG	c20_SLR_CSR	Multi-mission	RACMO2.3p2 with empirical orthogonal functions (EOFs) of firn process uncertainty (Sect. 4.1)
Jul 2010–Aug 2016	d1_ITSG	c20_SLR_CSR	Multi-mission (incl. Envisat, CryoSat-2)	RACMO2.3p2
Apr 2002–Aug 2016	d1_ITSG	c20_SLR_CSR	Multi-mission (incl. ERS-2, Envisat, ICESat, CryoSat-2)	RACMO2.3p2

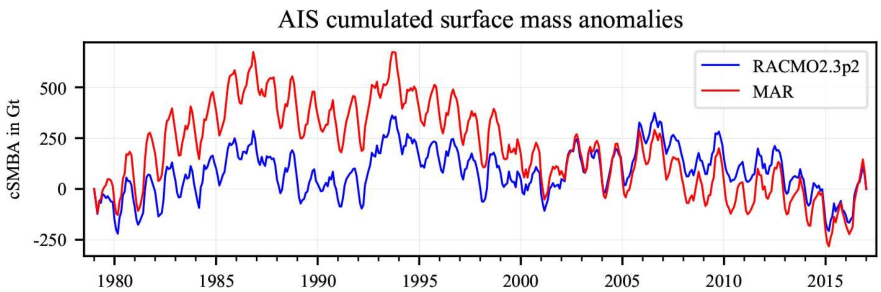

Figure 2. Cumulated surface mass balance anomalies (cSMBAs) of the regional climate models RACMO2.3p2 (blue; van Wessem et al., 2018) and MAR (red; Agosta et al., 2019), integrated over the grounded AIS.

ased total-mass changes of the entire AIS. Note that the biased total-mass change of $0\,\mathrm{Gt\,a^{-1}}$ in Table 2 arises coincidentally.

The biased GIA-related mass change of the AIS with MM altimetry (reference experiment) is very close to the Envisat-only estimate (174 vs. $172\,\mathrm{Gt\,a^{-1}}$). The biased ICESat-only result differs from the reference experiment by about $30\,\mathrm{Gt\,a^{-1}}$ (142 vs. $172\,\mathrm{Gt\,a^{-1}}$). Debiased estimates that use Envisat-only or ICESat-only results differ from the estimate of the reference experiment by 10 and $15\,\mathrm{Gt\,a^{-1}}$, respectively. The differences due to the co-estimation of seasonal components are marginal ($\sim 2\,\mathrm{Gt\,a^{-1}}$).

Applying the approach to different time intervals April 2002–August 2016 and July 2010–August 2016 leads to debiased total-mass changes of -121 and $-181\,\mathrm{Gt\,a^{-1}}$, respectively (biased estimates: -48 and $-70\,\mathrm{Gt\,a^{-1}}$).

The addition of the EOFs (Sect. 4.1) propagates to differences in the GIA solution of up to $7\,\mathrm{Gt\,a^{-1}}$ for the debiased GIA-related mass change and up to $18\,\mathrm{Gt\,a^{-1}}$ for the biased GIA-related mass change. Additionally, Fig. S6 shows the standard deviation of the 32 GIA estimates resulting from propagating the 32 trend differences between RACMO2 and MAR.

Table 2. Results from the sensitivity experiments. This table is structured like Table 2 in Gunter et al. (2014). Each line reports results from one experiment, where line one reports the reference experiment. The time period is March 2003–October 2009 except where it is quoted by experiment name. Column 1: experiment name, according to Table 1. Column 2: rms difference of the GIA-induced bedrock elevation change (BEC) estimate (RMS_{RE}) to the reference experiment. Columns 3 and 4: applied LPZ-based bias correction (see Sect. 2.2) for GIA-induced BEC and GRACE area density change, respectively. Columns 5, 6, and 7: spatial integral of total-mass change (Eq. 14) over the Antarctic Ice Sheet (AIS), the West Antarctic Ice Sheet (AIS), and the East Antarctic Ice Sheet (EAIS), including a 400 km buffer zone. Columns 8–10 and 11–13: same as columns 5–7, but for the GIA-related mass change (Eq. 13) and for the ice mass change (Eq. 15), respectively. Numbers in brackets give results of experiments with no bias corrections.

Experiment	RMS_{RE}	LPZ bias		Total-mass change			GIA-related mass change			Ice mass change		
	$mm\,a^{-1}$	GIA $mm\,a^{-1}$	GRACE $kg\,m^{-2}\,a^{-1}$	AIS	WAIS $Gt\,a^{-1}$	EAIS	AIS	WAIS $Gt\,a^{-1}$	EAIS	AIS	WAIS $Gt\,a^{-1}$	EAIS
Reference	0.0	1.6	1.9	−40	−78	39	44	21	24	−84	−99	15
	(1.6)	(0.0)	(0.0)	(0)	(−68)	(68)	(172)	(53)	(119)	(−173)	(−121)	(−51)
Degree-1												
d1_SLR	0.1	2.0	3.2	−42	−79	38	43	20	23	−85	−99	15
	(2.0)	(0.0)	(0.0)	(25)	(−62)	(86)	(199)	(60)	(139)	(−174)	(−122)	(−53)
d1_ITG	0.1	1.8	2.5	−41	−80	39	43	19	24	−84	−99	15
	(1.8)	(0.0)	(0.0)	(12)	(−66)	(78)	(185)	(55)	(130)	(−173)	(−121)	(−52)
C_{20}												
c20_SLR_GFZ	0.0	1.4	1.2	−39	−78	39	46	21	25	−85	−99	15
	(1.4)	(0.0)	(0.0)	(−14)	(−72)	(57)	(157)	(49)	(108)	(−171)	(−121)	(−50)
c20_TU_Delft	0.1	1.0	−0.4	-36	−77	42	48	21	26	−83	−99	15
	(1.1)	(0.0)	(0.0)	(−43)	(−79)	(36)	(127)	(41)	(85)	(−170)	(−121)	(−49)
Altimetry												
ICESat only	1.1	1.1	1.9	−40	−78	39	59	20	39	−99	−98	−1
	(1.7)	(0.0)	(0.0)	(0)	(−68)	(68)	(142)	(41)	(101)	(−142)	(−109)	(−34)
Envisat only	0.8	1.5	1.9	−40	−78	39	54	33	22	−94	−111	17
	(1.8)	(0.0)	(0.0)	(0)	(−68)	(68)	(174)	(63)	(111)	(−174)	(−131)	(−43)
MM seasonal	0.1	1.7	1.9	−40	−78	39	46	21	25	−86	−99	14
co-estimated	(1.7)	(0.0)	(0.0)	(0)	(−68)	(68)	(177)	(54)	(122)	(−177)	(−122)	(−55)
Firn process error												
RACMO2+EOF1	0.5	1.8	1.9	−40	−78	39	48	29	18	−87	−108	20
	(1.9)	(0.0)	(0.0)	(0)	(−68)	(68)	(190)	(65)	(124)	(−190)	(−133)	(−57)
RACMO2+EOF2	0.3	1.7	1.9	−40	−78	39	51	31	20	−90	−109	19
	(1.8)	(0.0)	(0.0)	(0)	(-68)	(68)	(181)	(64)	(117)	(−181)	(−132)	(−50)
RACMO2+EOF3	0.3	1.6	1.9	−40	−78	39	41	20	21	−80	−98	18
	(1.6)	(0.0)	(0.0)	(0)	(−68)	(68)	(169)	(52)	(117)	(−169)	(−120)	(−49)
Time interval												
Apr 2004–Aug 2016	1.1	1.8	3.5	−121	−160	39	18	−4	22	−140	−156	17
	(1.7)	(0.0)	(0.0)	(−48)	(−141)	(93)	(158)	(32)	(126)	(−205)	(−172)	(−33)
Jul 2010–Aug 2016	1.4	2.2	5.3	−181	−189	8	67	37	30	−248	−227	−21
	(2.9)	(0.0)	(0.0)	(−70)	(−160)	(90)	(239)	(81)	(158)	(−309)	(−241)	(−68)
Time-series-based combination												
Jul 2010–Aug 2016		2.1	5.3	−181	−189	8	39	17	23	−220	−206	−14
		(0.0)	(0.0)	(−70)	(−160)	(90)	(207)	(59)	(148)	(−277)	(−219)	(58)

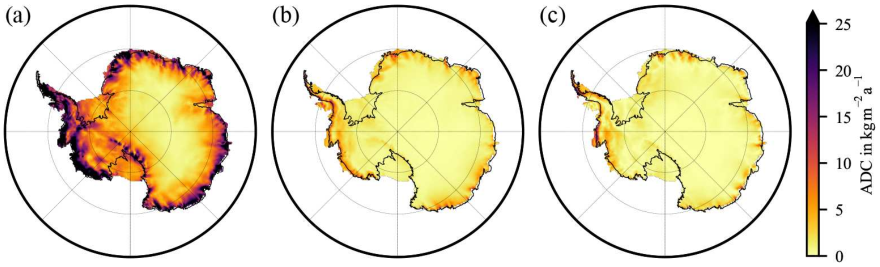

Figure 3. Three uncertainty assessments for the area density change (ADC) trend induced by cumulated surface mass balance anomalies (cSMBA). **(a)** The rms of cSMBA trend differences between RACMO2.3p2 and MAR for all 7-year intervals (Sect. 3.3), **(b)** the formal uncertainty from least-squares estimation for March 2003–October 2009, and **(c)** the 10 % uncertainty assumption.

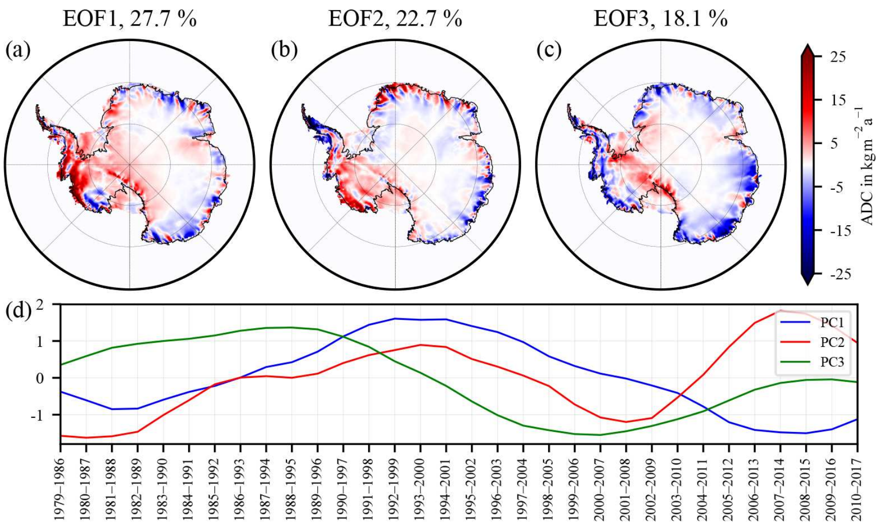

Figure 4. **(a)–(c)** Area density change (ADC) of the first three EOFs of the trend differences between RACMO2.3p2 and MAR cumulated surface mass balance anomalies (cSMBA). **(d)** The respective principal components (PCs).

4.3 Time-series-based combination

Our time-series-based combination takes advantage of the fact that gravimetry, altimetry, SMB, and FDM are available as monthly gridded products with sufficient spatial coverage from July 2010 to August 2016, owing to the availability of GRACE, CryoSat-2, and RACMO2.3p2. Riva et al. (2009) and Gunter et al. (2014) only use ICESat altimetry data, which does not allow a monthly sampling, as it has only 2–3 months of observation per year.

We used the values of ρ_α estimated from the trend-based combination during the same time interval (Fig. S4I) to be consistent for comparison. Figure 7 shows the GIA-related mass change time series for the AIS (with 400 km bufferzone). For applying the LPZ-based GIA bias correction, the linear GIA trend in the LPZ is estimated (offset and trend only). Figure 8A shows the debiased GIA-induced BEC based on the time series combination. Figure 8c shows its formal uncertainty from least-squares estimation, which should be considered as a lower bound. For comparison, Fig. 8B shows the GIA-induced BEC following the trend-based combination approach. The GIA-related mass changes from the time-series-based and trend-based combinations are 39 and 67 Gt a^{-1} for the AIS, 17 and 37 Gt a^{-1} for the WAIS, and 23 and 30 Gt a^{-1} for the EAIS, respectively (Table 2). The ice mass changes are −220 and −248 Gt a^{-1} for the AIS, −206 and −227 Gt a^{-1} for the WAIS, and −14 and −21 Gt a^{-1} for the EAIS, respectively. The integrated formal uncertainty of the GIA-related mass change for the AIS with a 400 km buffer zone is 25 Gt a^{-1} (Fig. 8c).

5 Discussion

Since the aim of this study is to examine the sensitivity of the inverse approach to several data input and methodological choices, differences from the reference experiment are discussed on the basis of the selected processing parameters.

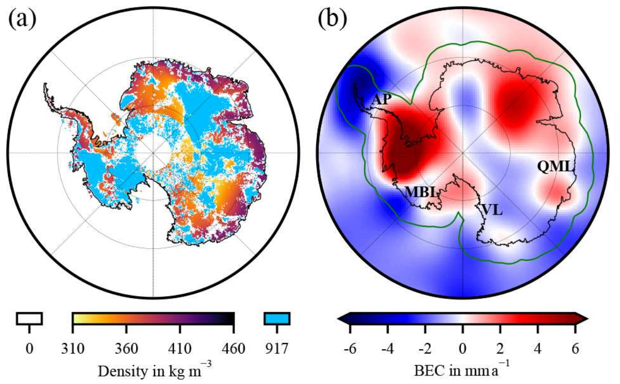

Figure 5. **(a)** Estimated ρ_α density (Eq. 10) of the reference experiment. **(b)** GIA-induced bedrock elevation change (BEC) of the reference experiment (rms: $2.2\,\mathrm{mm\,a^{-1}}$); 400 km buffer zone (green line); geographical regions indicated: Antarctic Peninsula (AP), Marie Byrd Land (MBL), Victoria Land (VL), and Queen Mary Land (QML). For results from the other simulation experiments see Figs. S4 and S5.

5.1 Assessment of the results

To test our data processing we performed a run with similar input data as used in Gunter et al. (2014). We used GFZ RL05 GRACE solutions, ICESat Altimetry, the RACMO2.1 SMB product, and the corresponding IMAU FDM. Table 3 shows the comparison of both results. AIS total-mass, GIA-related mass, and ice mass change estimates reproduce results by Gunter et al. (2014) to within 6, 5, and $1\,\mathrm{Gt\,a^{-1}}$, respectively. Those differences might be attributed to a slightly different LPZ, altimetry processing, and the missing ocean mass leakage correction. Gunter et al. (2014) indicate that the uncertainty for the GIA-related mass change and ice mass change from various GRACE solutions and filtering variants is 40 and $44\,\mathrm{Gt\,a^{-1}}$, respectively.

In general our GIA estimate (Fig. 5b) shows a similar spatial pattern compared to estimates by Gunter et al. (2014). Nonetheless, notable differences appear in the AP, Marie Byrd Land (MBL), Victoria Land (VL), and Queen Mary Land (QML).

In the AP, altimetry-derived SECs are available for a part of the area only (Fig. S1). As a result of missing altimetry data, GRACE-derived area density changes are attributed mainly to GIA-related mass change. The result is a negative GIA-induced BEC. Although negative GIA-induced BECs are predicted by forward models for other regions (e.g. Whitehouse et al., 2019), we consider it unphysical for this particular region because we cannot find any further indications to substantiate it. Furthermore, the missing altimetry leads to unconsidered elastic deformation. The negative signal in MBL is of a similar order of magnitude as in Riva et al. (2009) and Sasgen et al. (2017). A negative GIA signal in QML can be found in Martín-Español et al. (2016a). The uncertainty of the GIA signal is sometimes so large that even its sign cannot be determined.

For example, propagating trend differences between RACMO2.3p2 and MAR cSMBA products to GIA estimates (Fig. S6) leads to a high standard deviation of the GIA signal in MBL and Victoria Land (VL). This issue cannot be resolved by considering the results of forward models because they also show large variations and sign differences in the predicted spatial pattern of the GIA-induced BEC (Martín-Español et al., 2016b; Whitehouse et al., 2019).

5.2 Sensitivity to degree-1 and C_{20} products and the effect of bias estimation

The use of several degree-1 and C_{20} products for the GRACE processing leads to a differing total-mass trend for the AIS (Barletta et al., 2013). The Gunter et al. (2014) Supplement showed the influence of two different degree-1 products. Here we show how the bias corrections eliminate those differences in total-mass and GIA-related mass change (Sect. 4.2, Table 2). The $\mathrm{RMS_{RE}}$ of all debiased GIA estimates amounts to only $0.1\,\mathrm{mm\,a^{-1}}$ (Table 2). As discussed in Sect. 2.2, any GIA signal over the LPZ would be removed erroneously in the method of Gunter et al. (2014), but the uncertainty in low-degree harmonics is assumed to be much higher than a potential GIA signal within the LPZ. The bias correction regionalizes the GIA estimate; i.e. derived mass changes are always given relative to the mean LPZ mass change. The bias correction defines how the total-mass change is decomposed into mass signals and is made to ensure that the combination approach produces robust mass estimates. The large uncertainty introduced by degree-1 and C_{20} is suppressed at the cost of global consistency.

Several objections can be made to the assumption that over the LPZ the mean GIA-induced BEC, the mean total-mass change, and hence the mean ice mass change are zero. (1) The precipitation of the last 40 years is not directly linked to GIA. (2) Areas are included which show quite relevant GIA-induced BEC in forward models, e.g. close to the Ross Ice Shelf (Martín-Español et al., 2016b). (3) The threshold for low precipitation is arbitrary and cannot be based on physical reasons in relation to GIA. For a given threshold, the definition of the LPZ still depends on the precipitation product used. (4) The LPZ is a large area in which even a low GIA effect can cause several gigatonnes per year of mass changes. (5) The LPZ bias correction does not allow for a simple transfer of the approach to Greenland or to a global framework. Nevertheless, the calibration over the LPZ is at least one possibility to consider the presumably existing biases.

Shepherd et al. (2012, Fig. 3) show large differences in the EAIS mass change estimates derived from satellite gravimetry and altimetry. In principle, the question of quantifying GIA in the EAIS arises. For this discussion, the reader is re-

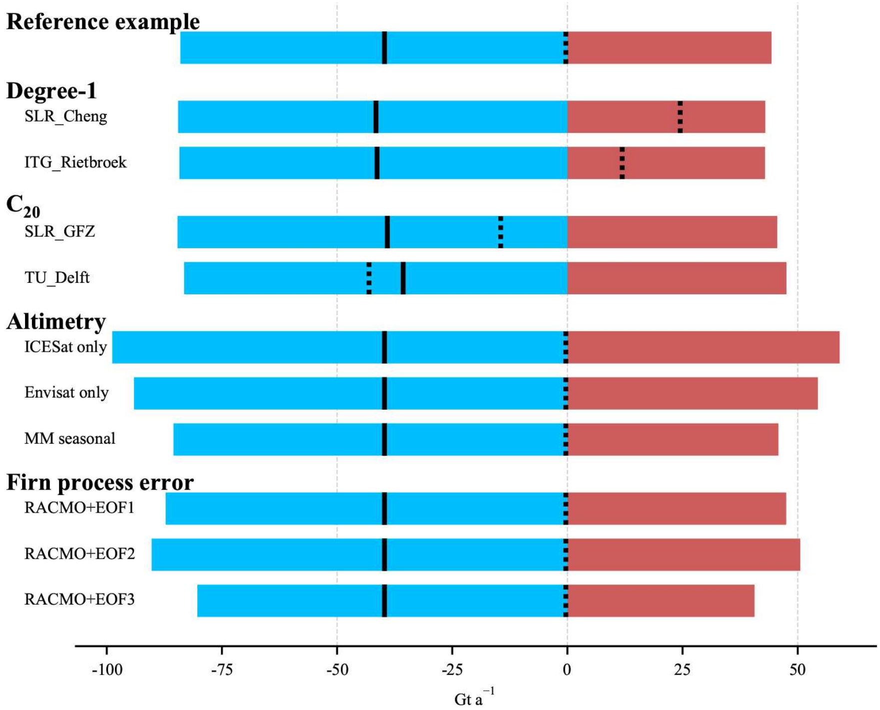

Figure 6. Mass change results for the entire AIS over the interval March 2003–October 2009 from experiments with different data products and methodological choices. The LPZ-based bias correction was applied. Debiased total-mass change (solid black lines) is separated into debiased GIA-related mass (red) and ice mass change (blue). Dotted lines show the total-mass changes that arise when no bias corrections are applied. The case of no bias correction is further illustrated in Fig. S7.

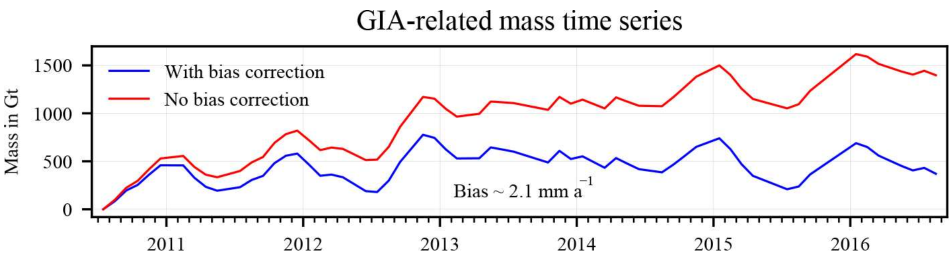

Figure 7. The GIA-related mass time series of the AIS (with 400 km buffer zone) resulting from the combination of the monthly gridded time series (July 2010–August 2016) with (blue) and without (red) LPZ-based bias correction of the determined GIA signal.

ferred to Whitehouse (2018) and Whitehouse et al. (2019), for example.

5.3 Sensitivity to altimetry product

The choice of the altimetry product has a major effect on the GIA estimate. Using ICESat-only and Envisat-only products leads to a $\mathrm{RMS_{RE}}$ of 1.1 and 0.8 mm a^{-1}, respectively (Table 2). Both missions use different observation methods and have different spatial coverage. The radar altimetry time series of Envisat is sampled monthly but only to a latitude of 81.5° south. ICESat uses laser altimetry and its polar gap is smaller (south of 86°). These differences affect the results across Kamb Ice Stream where a dominant ice-dynamic signal is expected (Retzlaff and Bentley, 1993). ICESat's campaign-style temporal sampling may affect the trend estimation significantly. For the time period March 2003–October 2009 the MM altimetry product uses mainly observations from ICESat and Envisat. The trend derived from the MM altimetry product shows a spatial discontinuity at the 81.5° latitude limit of Envisat coverage (Figs. S1A, 5a). We attribute this to the sparse time sampling of the ICESat mission. The spread of debiased GIA-related mass change estimates of the AIS using various altimetry products is 15 Gt a^{-1} (Table 2). Furthermore, differences in the spatial GIA pattern are remarkable in MBL and VL (Fig. S5f, g). The co-estimation of an annual seasonal

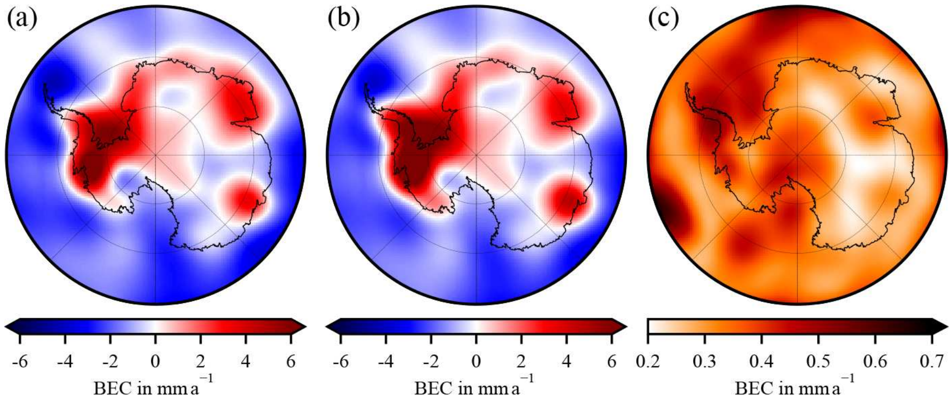

Figure 8. For the July 2010–August 2016 time period. **(a)** Debiased GIA bedrock elevation change (BEC) by combining time series of all data sets and models, **(b)** combination of trends, and **(c)** the formal uncertainty from least-squares estimation.

Table 3. The comparison of integrated mass changes calculated in this study and those published in Gunter et al. (2014). For this we used GFZ RL05 GRACE solutions, ICESat-only altimetry, and RACMO2.1 products during March 2003–October 2009.

Solution	Total-mass change in Gt a^{-1}			GIA-related mass change in Gt a^{-1}			Ice mass change in Gt a^{-1}		
	AIS	WAIS	EAIS	AIS	WAIS	EAIS	AIS	WAIS	EAIS
This study	−51	−90	39	49	12	37	−100	−102	2
Gunter et al. (2014)	−45	−86	41	54	18	36	−99	−104	5

signal in altimetry only leads to small changes in the overall result (Sect. 4.2, $\mathrm{RMS_{RE}}$: 0.1 mm a^{-1}) but is more consistent with processing of other data and models.

5.4 Firn process assumptions and uncertainties

A crucial point in the combination approach is the case distinction for ρ_α (Eq. 9). As mentioned in Sect. 2.1, it accounts for the uncertainty of altimetry and the FDM but does not account for the uncertainty of GRACE and the cSMBA trends. The resulting map of ρ_α (Figs. 5a, S4) does not agree with predefined, physically reasonable density maps. For example, ρ_α is set to ice density in large areas of the EAIS where dynamically induced ice mass losses are not plausible. The values of ρ_α largely depend on used data sets (Fig. S4b, c). An alternative to the ρ_α approach could be the formal approach shown in Eq. (8). Technically this would be correct. However, it results in an ice density weight for the whole AIS. We are aware that this is not correct either because presumable processes in the firn layer are not completely considered by input data and models. Another strategy may use a predefined density mask similar to Riva et al. (2009), but with a predefined significance criterion for all input data sets. This would need further investigation.

The ρ_α approach (Eq. 10) to assign height changes to either ice dynamics or firn processes may be a source of bias. For example, if a negative SEC is firn-related, but erroneously attributed to the density of ice by Eq. (10), this will lead to a higher ice mass decrease assigned to altimetry. GRACE would sense the true smaller ice mass decrease. Through combination of both, this discrepancy in ice mass change would be assigned to a positive GIA signal. We suppose this is qualitatively visible for ice-density-weighted regions in the EAIS (Fig. 5a, b), e.g. the sector between a longitude of 30 and 100° (Dome F). We presume this erroneously introduced positive GIA signal explains a part of the GIA bias.

The propagation of the empirically determined error patterns (EOFs 1–3) of the firn process models (Sect. 4.1) shows small effects on the spatial pattern of inverse GIA estimates (Fig. S5i–k). The $\mathrm{RMS_{RE}}$ for the EOF 1, EOF 2, and EOF 3 experiments is 0.5, 0.3, and 0.3 mm a^{-1}, respectively (Table 2). Note that this deviation arises solely from differences in similar climate models that use the same forcing data.

Uncertainties assumed in Gunter et al. (2014) for $\sigma_{\dot{h}_{\mathrm{firn}}}$ are very small compared to our results (Sect. 4.1, Fig. 3). In addition, any long-term trend in firn mass and firn thickness is ignored by the equilibrium assumption made by the firn modelling. SEC from Altimetry and the IMAU FDM show major differences even with a different sign for some areas, such as the AP and QML (Fig. 1a, c). These differences may indicate that the equilibrium assumption of the FDM (Sect. 3.3) is not fulfilled for those areas of the AIS, i.e. that net firn thickness changes occur over the modelling period.

5.5 Sensitivity to time interval

We also investigate a GIA solution derived from data sets over almost the entire GRACE period (April 2002–August 2016) and the approximately 6-year period of CryoSat-2 overlapping with GRACE (July 2010–August 2016). The variability of these estimates cannot be attributed to a single processing choice. On the one hand, different data sets are used (depending on assembled altimetry missions). On the other hand, cSMBA trends and FDM-derived SEC differ largely depending on the selected time interval (Sect. 3.3, Fig. S3). Ice mass change estimates are very high for the time interval July 2010–August 2016 (Table 2). The quality of input data varies over time, e.g. due to the changing availability of data. Therefore the GIA estimates show large discrepancies among different time intervals, which is incompatible with the assumption of a constant linear rate of GIA-induced BEC. However, regions (e.g. Pine Island Bay) are known where a non-linear deformation through GIA is plausible during decadal periods (Barletta et al., 2018).

5.6 The role of time-series-based combination

The combination of time series leads to similar results compared to the trend-based approach for the same July 2010–August 2016 interval (Sect. 4.3). We combined time series only for this time period, where CryoSat-2 and GRACE data are available with monthly sampling and sufficient spatial coverage. A closer examination of the time series approach is the aim of ongoing research. It needs to account for monthly uncertainties in all input data sets. Similar to the trend-based combination, challenges include (1) the consideration of uncertainties of all data sets, (2) differences in spatio-temporal sampling of both sensors, and (3) dealing with the resolution discrepancies including the consideration of signal leakage in GRACE observations. For further discussion of the challenges associated with combining geodetic time series, the reader is referred to King et al. (2006), for example. It should be noted that state-space approaches in geodetic Earth system research show promising results dealing with time-variable geophysical signals in observational time series (Didova et al., 2016; Frederikse et al., 2016).

6 Conclusions

We investigated a combination method to isolate the GIA signal from satellite gravimetry and altimetry data. Our analysis is an extension of ideas presented by Gunter et al. (2014) for the inverse estimation of GIA-induced BEC. We investigated the sensitivity of this approach (Eq. 9) to the variation in input parameters (Table 1): (1) degree-1 and C_{20} products in satellite gravimetry, (2) different satellite altimetry products, (3) empirically determined errors of firn process models (SMB and FDM), and (4) the use of different time epochs including diverse data.

The comparison between the data sets used in this study shows impressive similarities in terms of the spatial pattern of determined trends (Fig. 1), given that the results of altimetry, gravimetry, and the FDM are independent. The separation of GIA and ice mass signals following Gunter et al. (2014) depends strongly on the input parameters and processing steps (Table 2).

Following Gunter et al. (2014), gravimetry data are treated differently for (1) estimating the GIA signal and (2) determining the mass balance (Sect. 2.2). (1) A Gaussian filter and a de-striping filter are applied to gravimetry observations. This predetermines the smoothness of the GIA solution. The GIA-induced BEC is calibrated over the LPZ. It is converted to mass change by an effective density mask. (2) GRACE-derived area density change is calibrated over the LPZ, too. The mass balance is the difference between the debiased total-mass change and the debiased GIA-related mass change. The estimated biases and the Gaussian filtering are an implementation of a priori information which regionally constrains the GIA solution and the ice mass balance. We conclude that the LPZ-based bias correction facilitates regional but robust mass change estimates (Figs. 6, S7, Tables 2, S1).

The definition of ρ_α according to Eq. (10) does not lead to a readily decipherable density pattern that can account for processes in the firn and ice layer (Figs. 5a, S4). Furthermore, it is highly sensitive to input data sets.

A critical feature of the combination approach is the observational constraints that are imposed on the inversions by the limitations of the actual geodetic satellite sensors. On the one hand, altimetry enables the derivation of SEC with a high resolution. However, observations are missing in some areas, especially in areas of high topographic relief, such as valleys and mountainous coastal regions. In many of these regions lateral ice mobility may have a more complex relationship to ice heights that are extracted from altimetry as SEC. On the other hand, GRACE records all mass changes, albeit with lower resolution and signal-to-noise ratio. Because of the availability of the MM altimetry from Schröder et al. (2019a), the used GRACE observations limit the time period to 14 years from April 2002 to August 2016. This may be extended with GRACE-FO (and bridging solutions). We note that Sasgen et al. (2019) have presented a new combination approach in the spherical harmonic domain with the potential to take advantage of both sensors.

For the integrated mass changes over the AIS area, results of our sensitivity analysis are as follows. (1) The use of different degree-1 and C_{20} products in GRACE processing leads to biased total-mass changes from -43 to $25\,\mathrm{Gt\,a^{-1}}$. The LPZ-based bias correction almost completely eliminates the effect on the GIA estimate ($\mathrm{RMS_{RE}} \leq 0.1\,\mathrm{mm\,a^{-1}}$) and on derived mass change estimates. (2) Using different altimetry products generates a spread of GIA-related mass change of

15 $Gt\,a^{-1}$ if the GIA bias correction is applied. The spread is 35 $Gt\,a^{-1}$ without correcting for a bias. (3) The uncertainty patterns empirically estimated from the firn process models generate a spread of debiased and biased GIA-related mass estimates of 7 and 21 $Gt\,a^{-1}$, respectively. (4) The spread of GIA-related mass change estimated between the time periods April 2002–August 2016 and July 2010–August 2016 is 49 (debiased) and 81 $Gt\,a^{-1}$ (biased). (5) The debiased GIA-related mass change derived by the time-series-based combination is 28 $Gt\,a^{-1}$ smaller than the corresponding trend-based estimate.

Our results do not fully address the uncertainty introduced by input parameters. Especially important may be the assumption of an equilibrium state assumed in the firn model. In future work, improvement is needed for the correction of apparent biases and for the separation of processes in the firn and the ice layer. This might improve the self-consistency of GIA inverse estimates from satellite observations and generate a more appropriate time-series-based estimate.

Data availability. GRACE monthly solutions: https://doi.org/10.5880/icgem.2016.007 (Mayer-Gürr et al., 2016). Altimetry time series: https://doi.org/10.1594/PANGAEA.897390 (Schröder et al., 2019b). Sensitivity results: this study. Contact: matthias.willen@tu-dresden.de.

Supplement. The supplement related to this article is available online at: https://doi.org/10.5194/tc-14-349-2020-supplement.

Author contributions. MOW and MH conceptualized the study. MOW performed the investigation, computation, and visualization tasks and wrote the manuscript. LS provided the ice altimetry time series. AG supported the GRACE data processing and the development of the data combination approach. SRML, PKM, and MRvdB provided the SMB output from RACMO2.3p2, the FDM, and assistance in their uncertainty characterization. All co-authors discussed and improved the manuscript.

Competing interests. Michiel R. van den Broeke is a member of the editorial board of the journal. The authors declare that they have no conflict of interest.

Acknowledgements. We thank Cécile Agosta (Université de Liège, Belgium) for providing the SMB output and density fields of the MAR model, Erik Ivins (JPL, Caltech, Pasadena, USA) for improving the manuscript, and Olga Engels (Universität Bonn, Germany) for discussion on details of data combination strategies. We thank the editor Pippa Whitehouse and the two anonymous referees for their constructive reviews which helped to improve the manuscript. We acknowledge the German Space Operations Center (GSOC) of the German Aerospace Center (DLR) for providing continuously and nearly 100 % of the raw telemetry data of the twin GRACE satellites. Further, we thank the developers of Matplotlib (Hunter, 2007) and the Matplotlib Basemap Toolkit which we used to create the figures.

Financial support. This work was supported in part through grant no. HO 4232/4-1 "Reconciling ocean mass change and GIA from satellite gravity and altimetry (OMCG)" from the Deutsche Forschungsgemeinschaft (DFG) as part of the Special Priority Program (SPP)-1889 "Regional Sea Level Change and Society" (SeaLevel).

Review statement. This paper was edited by Pippa Whitehouse and reviewed by two anonymous referees.

References

Agosta, C., Amory, C., Kittel, C., Orsi, A., Favier, V., Gallée, H., van den Broeke, M. R., Lenaerts, J. T. M., van Wessem, J. M., van de Berg, W. J., and Fettweis, X.: Estimation of the Antarctic surface mass balance using the regional climate model MAR (1979–2015) and identification of dominant processes, The Cryosphere, 13, 281–296, https://doi.org/10.5194/tc-13-281-2019, 2019.

Barletta, V. R., Sørensen, L. S., and Forsberg, R.: Scatter of mass changes estimates at basin scale for Greenland and Antarctica, The Cryosphere, 7, 1411–1432, https://doi.org/10.5194/tc-7-1411-2013, 2013.

Barletta, V. R., Bevis, M., Smith, B. E., Wilson, T., Brown, A., Bordoni, A., Willis, M., Khan, S. A., Rovira-Navarro, M., Dalziel, I., Smalley Jr., R., Kendrick, E., Konfal, S., Caccamise II, D. J., Aster, R. C., Nyblade, A., and Wiens, D. A.: Observed rapid bedrock uplift in Amundsen Sea Embayment promotes ice-sheet stability, Science, 360, 1335–1339, https://doi.org/10.1126/science.aao1447, 2018.

Caron, L. and Ivins, E. R.: A baseline Antarctic GIA correction for space gravimetry, Earth Planet. Sc. Lett., 531, 115957, https://doi.org/10.1016/j.epsl.2019.115957, 2020.

Caron, L., Ivins, E. R., Larour, E., Adhikari, S., Nilsson, J., and Blewitt, G.: GIA Model Statistics for GRACE Hydrology, Cryosphere, and Ocean Science, Geophys. Res. Lett., 45, 2203–2212, https://doi.org/10.1002/2017GL076644, 2018.

Cheng, M. and Ries, J.: Decadal variation in Earth's oblateness (J2) from satellite laser ranging data, Geophys. J. Int., 212, 1218–1224, https://doi.org/10.1093/gji/ggx483, 2017.

Cheng, M., Tapley, B. D., and Ries, J. C.: Deceleration in the Earth's oblateness, J. Geophys. Res.-Solid Earth, 118, 740–747, https://doi.org/10.1002/jgrb.50058, 2013a.

Cheng, M. K., Ries, J. C., and Tapley, B. D.: Reference Frames for Applications in Geosciences, Vol. 138 of International Association of Geodesy Symposia, chap. Geocenter Variations from Analysis of SLR Data, 19–25, Springer Berlin Heidelberg, https://doi.org/10.1007/978-3-642-32998-2_4, 2013b.

Church, J. A., Clark, P. U., Cazenave, A., Gregory, J. M., Jevrejeva, S., Levermann, A., Merrifield, M. A., Milne, G. A., Nerem, R. S., Nunn, P. D., Payne, A. J., Pfeffer, W. T., Stammer, D., and Unnikrishnan, A. S.: Climate Change 2013: The Physical Science Basis. Contribution of Working Group I to the Fifth

Assessment Report of the Intergovernmental Panel on Climate Change, chap. Sea Level, Cambridge University Press, Cambridge, United Kingdom and New York, NY, USA, 2013.

Didova, O., Gunter, B., Riva, R. E. M., Klees, R., and Roese-Koerner, L.: An approach for estimating time-variable rates from geodetic time series, J. Geod., 90, 1207–1221, https://doi.org/10.1007/s00190-016-0918-5, 2016.

Engels, O., Gunter, B., Riva, R. E. M., and Klees, R.: Separating Geophysical Signals Using GRACE and High-Resolution Data: A Case Study in Antarctica, Geophys. Res. Lett., 45, 12340–12349, https://doi.org/10.1029/2018GL079670, 2018.

Forsberg, R., Sørensen, L., and Simonsen, S.: Greenland and Antarctica Ice Sheet Mass Changes and Effects on Global Sea Level, Surv. Geophys., 38, 89–104, https://doi.org/10.1007/s10712-016-9398-7, 2017.

Frederikse, T., Riva, R. E. M., Slobbe, C., Broerse, T., and Verlaan, M.: Estimating decadal variability in sea level from tide gauge records: An application to the North Sea, J. Geophys. Res.-Oceans, 121, 1529–1545, https://doi.org/10.1002/2015JC011174, 2016.

Groh, A., Ewert, H., Scheinert, M., Fritsche, M., Rülke, A., Richter, A., Rosenau, R., and Dietrich, R.: An Investigation of Glacial Isostatic Adjustment over the Amundsen Sea sector, West Antarctica, Global Planet. Change, 98–99, 45–53, https://doi.org/10.1016/j.gloplacha.2012.08.001, 2012.

Groh, A., Ewert, H., Rosenau, R., Fagiolini, E., Gruber, C., Floricioiu, D., Abdel Jaber, W., Linow, S., Flechtner, F., Eineder, M., Dierking, W., and Dietrich, R.: Mass, volume and velocity of the Antarctic Ice Sheet: present-day changes and error effects, Surv. Geophys., 35, 1481–1505, https://doi.org/10.1007/s10712-014-9286-y, 2014.

Gunter, B. C., Didova, O., Riva, R. E. M., Ligtenberg, S. R. M., Lenaerts, J. T. M., King, M. A., van den Broeke, M. R., and Urban, T.: Empirical estimation of present-day Antarctic glacial isostatic adjustment and ice mass change, The Cryosphere, 8, 743–760, https://doi.org/10.5194/tc-8-743-2014, 2014.

Horwath, M. and Dietrich, R.: Signal and error in mass change inferences from GRACE: the case of Antarctica, Geophys. J. Int., 177, 849–864, https://doi.org/10.1111/j.1365-246X.2009.04139.x, 2009.

Horwath, M., Legrésy, B., Rémy, F., Blarel, F., and Lemoine, J.-M.: Consistent patterns of Antarctic ice sheet interannual variations from ENVISAT radar altimetry and GRACE satellite gravimetry, Geophys. J. Int., 189, 863–876, https://doi.org/10.1111/j.1365-246X.2012.05401.x, 2012.

Hunter, J.: Matplotlib: A 2D Graphics Environment, Comput. Sci. Eng., 9, 90–95, https://doi.org/10.1109/MCSE.2007.55, 2007.

Huybrechts, P. and Le Meur, E.: Predicted present-day evolution patterns of ice thickness and bedrock elevation over Greenland and Antarctica, Polar Res., 18, 299–306, https://doi.org/10.3402/polar.v18i2.6588, 1999.

Ivins, E. R. and James, T. S.: Antarctic glacial isostatic adjustment: a new assessment, Ant. Sci., 14, 541–553, https://doi.org/10.1017/S0954102005002968, 2005.

Ivins, E. R., James, T. S., Wahr, J., O. Schrama, E. J., Landerer, F. W., and Simon, K. M.: Antarctic contribution to sea level rise observed by GRACE with improved GIA correction, J. Geophys. Res.-Solid Earth, 118, 3126–3141, https://doi.org/10.1002/jgrb.50208, 2013.

Jean, Y., Meyer, U., and Jäggi, A.: Combination of GRACE monthly gravity field solutions from different processing strategies, J. Geod., 92, 1313–1328, https://doi.org/10.1007/s00190-018-1123-5, 2018.

Johnston, P., Wu, P., and Lambeck, K.: Dependence of horizontal stress magnitude on load dimension in glacial rebound models: Glacial rebound models, Geophys. J. Int., 132, 41–60, https://doi.org/10.1046/j.1365-246x.1998.00387.x, 1998.

King, M., Moore, P., Clarke, P., and Lavallée, D.: Choice of optimal averaging radii for temporal GRACE gravity solutions, a comparison with GPS and satellite altimetry, Geophys. J. Int., 166, 1–11, https://doi.org/10.1111/j.1365-246X.2006.03017.x, 2006.

King, M. A., Altamimi, Z., Boehm, J., Bos, M., Dach, R., Elosegui, P., Fund, F., Hernández-Pajares, M., Lavallee, D., Mendes Cerveira, P. J., Penna, N., Riva, R. E. M., Steigenberger, P., Dam, T., Vittuari, L., Williams, S., and Willis, P.: Improved Constraints on Models of Glacial Isostatic Adjustment: A Review of the Contribution of Ground-Based Geodetic Observations, Surv. Geophys., 31, 465–507, https://doi.org/10.1007/s10712-010-9100-4, 2010.

König, R., Schreiner, P., and Dahle, C.: Monthly estimates of C(2,0) generated by GFZ from SLR satellites based on GFZ GRACE/GRACE-FO RL06 background models. V. 1.0., GFZ Data Services, https://doi.org/10.5880/GFZ.GRAVIS_06_C20_SLR, 2019.

Ligtenberg, S. R. M., Helsen, M. M., and van den Broeke, M. R.: An improved semi-empirical model for the densification of Antarctic firn, The Cryosphere, 5, 809–819, https://doi.org/10.5194/tc-5-809-2011, 2011.

Ligtenberg, S. R. M., Horwath, M., van den Broeke, M. R., and Legrésy, B.: Quantifying the seasonal “breathing” of the Antarctic ice sheet, Geophys. Res. Lett., 39, L23501, https://doi.org/10.1029/2012GL053628, 2012.

Martín-Español, A., King, M. A., Zammit-Mangion, A., Andrews, S. B., Moore, P., and Bamber, J. L.: An assessment of forward and inverse GIA solutions for Antarctica, J. Geophys. Res.-Solid Earth, 121, 6947–6965, 2016a.

Martín-Español, A., Zammit-Mangion, A., Clarke, P. J., Flament, T., Helm, V., King, M. A., Luthcke, S. B., Petrie, E., Rémy, F., Schön, N., Wouters, B., and Bamber, J. L.: Spatial and temporal Antarctic Ice Sheet mass trends, glacio-isostatic adjustment and surface processes from a joint inversion of satellite altimeter, gravity and GPS data, J. Geophys. Res.-Earth Surf., 121, 182–200, https://doi.org/10.1002/2015JF003550, 2016b.

Mayer-Gürr, T., Behzadpour, S., Ellmer, M., Klinger, B., Kvas, A., and Zehentner, N.: ITSG-Grace2016 – Monthly and Daily Gravity Field Solutions from GRACE, GFZ Data Services, https://doi.org/10.5880/icgem.2016.007, 2016.

Mémin, A., Flament, T., Alizier, B., Watson, C., and Rémy, F.: Interannual variation of the Antarctic Ice Sheet from a combined analysis of satellite gravimetry and altimetry data, Earth Planet. Sci. Lett., 422, 150–156, https://doi.org/10.1016/j.epsl.2015.03.045, 2015.

Petit, G. and Luzum, B.: IERS Conventions. IERS Technical Note No. 36, p. 179, Verlag des Bundesamts für Kartographie und Geodäsie, Frankfurt am Main, Germany, ISBN 3-89888-989-6, 2010.

Retzlaff, R. and Bentley, C.: Timing of stagnation of Ice Stream C, West Antarctica, from short-pulse radar studies of buried surface crevasses, J. Glac., 39, 553–561, 1993.

Rietbroek, R., Brunnabend, S.-E., Kusche, J., Schröter, J., and Dahle, C.: Revisiting the contemporary sea-level budget on global and regional scales, P Natl. Acad. Sci. USA, 113, 1504–1509, https://doi.org/10.1073/pnas.1519132113, 2016.

Rignot, E., Bamber, J., van den Broeke, M. R., Davis, C., Li, Y., van de Berg, W. J., and van Meijgaard, E.: Recent Antarctic ice mass loss from radar interferometry and regional climate modelling, Nat. Geosci., 1, 106–110, https://doi.org/10.1038/ngeo102, 2008.

Riva, R. E. M., Gunter, B. C., Urban, T. J., Vermeersen, B. L. A., Lindenbergh, R. C., Helsen, M. M., Bamber, J. L., van de Wal, R. S. W., van den Broeke, M. R., and Schutz, B. E.: Glacial Isostatic Adjustment over Antarctica from combined ICESat and GRACE satellite data, Earth Planet. Sci. Lett., 288, 516–523, https://doi.org/10.1016/j.epsl.2009.10.013, 2009.

Sasgen, I., Martín-Español, A., Horvath, A., Klemann, V., Petrie, E. J., Wouters, B., Horwath, M., Pail, R., Bamber, J. L., Clarke, P. J., Konrad, H., and Drinkwater, M. R.: Joint inversion estimate of regional glacial isostatic adjustment in Antarctica considering a lateral varying Earth structure (ESA STSE Project REGINA), Geophys. J. Int., 211, 1534–1553, https://doi.org/10.1093/gji/ggx368, 2017.

Sasgen, I., Konrad, H., Helm, V., and Grosfeld, K.: High-Resolution Mass Trends of the Antarctic Ice Sheet through a Spectral Combination of Satellite Gravimetry and Radar Altimetry Observations, Remote Sens., 11, 144, https://doi.org/10.3390/rs11020144, 2019.

Schröder, L., Horwath, M., Dietrich, R., Helm, V., van den Broeke, M. R., and Ligtenberg, S. R. M.: Four decades of Antarctic surface elevation changes from multi-mission satellite altimetry, The Cryosphere, 13, 427–449, https://doi.org/10.5194/tc-13-427-2019, 2019a.

Schröder, L., Horwath, M., Dietrich, R., Helm, V., van den Broeke, M. R., and Ligtenberg, S. R. M.: Gridded surface elevation changes from multi-mission satellite altimetry 1978–2017, PANGAEA, https://doi.org/10.1594/PANGAEA.897390, 2019b.

Shepherd, A., Ivins, E. R., A, G., Barletta, V. R., Bentley, M. J., Bettadpur, S., Briggs, K. H., Bromwich, D. H., Forsberg, R., Galin, N., Horwath, M., Jacobs, S., Joughin, I., King, M. A., Lenaerts, J. T. M., Li, J., Ligtenberg, S. R. M., Luckman, A., Luthcke, S. B., McMillan, M., Meister, R., Milne, G., Mouginot, J., Muir, A., Nicolas, J. P., Paden, J., Payne, A. J., Pritchard, H., Rignot, E., Rott, H., Sorensen, L. S., Scambos, T. A., Scheuchl, B., Schrama, E. J. O., Smith, B., Sundal, A. V., van Angelen, J. H., van de Berg, W. J., van den Broeke, M. R., Vaughan, D. G., Velicogna, I., Wahr, J., Whitehouse, P. L., Wingham, D. J., Yi, D., Young, D., and Zwally, H. J.: A Reconciled Estimate of Ice-Sheet Mass Balance, Science, 338, 1183–1189, https://doi.org/10.1126/science.1228102, 2012.

Sun, Y., Ditmar, P., and Riva, R. E. M.: Observed changes in the Earth's dynamic oblateness from GRACE data and geophysical models, J. Geod., 90, 81–89, https://doi.org/10.1007/s00190-015-0852-y, 2015.

Swenson, S. and Wahr, J.: Post-processing removal of correlated errors in GRACE data, Geophys. Res. Lett., 33, L08402, https://doi.org/10.1029/2005GL025285, 2006.

Swenson, S., Chambers, D., and Wahr, J.: Estimating geocenter variations from a combination of GRACE and ocean model output, J. Geophys. Res., B113, B08410, https://doi.org/10.1029/2007JB005338, 2008.

Thomas, I., King, M., Bentley, M., Whitehouse, P., Penna, N., Williams, S., Riva, R., Lavallee, D., Clarke, P., King, E., Hindmarsh, R., and Koivula, H.: Widespread low rates of Antarctic glacial isostatic adjustment revealed by GPS observations, Geophys. Res. Lett., 38, L22302, https://doi.org/10.1029/2011GL049277, 2011.

van Wessem, J. M., van de Berg, W. J., Noël, B. P. Y., van Meijgaard, E., Amory, C., Birnbaum, G., Jakobs, C. L., Krüger, K., Lenaerts, J. T. M., Lhermitte, S., Ligtenberg, S. R. M., Medley, B., Reijmer, C. H., van Tricht, K., Trusel, L. D., van Ulft, L. H., Wouters, B., Wuite, J., and van den Broeke, M. R.: Modelling the climate and surface mass balance of polar ice sheets using RACMO2 – Part 2: Antarctica (1979–2016), The Cryosphere, 12, 1479–1498, https://doi.org/10.5194/tc-12-1479-2018, 2018.

Wahr, J., Molenaar, M., and Bryan, F.: Time variability of the Earth's gravity field: Hydrological and oceanic effects and their possible detection using GRACE, J. Geophys. Res., 103, 30205–30229, https://doi.org/10.1029/98JB02844, 1998.

Wahr, J., Wingham, D., and Bentley, C.: A method of combining ICESat and GRACE satellite data to constrain Antarctic mass balance, J. Geophys. Res., 105, 16279–16294, https://doi.org/10.1029/2000JB900113, 2000.

Whitehouse, P., Gomez, N., King, M., and Wiens, D.: Solid Earth change and the evolution of the Antarctic Ice Sheet, Nat. Commun., 10, 503, https://doi.org/10.1038/s41467-018-08068-y, 2019.

Whitehouse, P. L.: Glacial isostatic adjustment modelling: historical perspectives, recent advances, and future directions, Earth Surf. Dynam., 6, 401–429, https://doi.org/10.5194/esurf-6-401-2018, 2018.

Whitehouse, P. L., Bentley, M. J., Milne, G. A., King, M. A., and Thomas, I. D.: A new glacial isostatic adjustment model for Antarctica: calibrated and tested using observations of relative sea-level change and present-day uplift rates, Geophys. J. Int., 190, 1464–1482, https://doi.org/10.1111/j.1365-246X.2012.05557.x, 2012.

Wingham, D., Shepherd, A., Muir, A., and Marshall, G.: Mass balance of the Antarctic ice sheet, Phil. Trans. R. Soc. Lond. A, 364, 1627–1635, 2006.

Zammit-Mangion, A., Rougier, J., Schön, N., Lindgren, F., and Bamber, J.: Multivariate spatio-temporal modelling for assessing Antarctica's present-day contribution to sea-level rise, Environmetrics, 26, 159–177, https://doi.org/10.1002/env.2323, 2015.

JGR Earth Surface

RESEARCH ARTICLE
10.1029/2020JF005966

Key Points:
- We have developed a state space filter framework to simultaneously evaluate GRACE and altimetry data, with climate and firn model products
- This approach allows the estimation of time-variable mass and volume changes of Antarctic ice drainage basins
- We identify the long-term trend of Antarctic ice drainage basins, which is presumably linked to variations in ice dynamics

Supporting Information:
Supporting Information may be found in the online version of this article.

Correspondence to:
M. O. Willen,
matthias.willen@tu-dresden.de

Citation:
Willen, M. O., Broerse, T., Groh, A., Wouters, B., Kuipers Munneke, P., Horwath, M., et al. (2021). Separating long-term and short-term mass changes of Antarctic ice drainage basins: A coupled state space analysis of satellite observations and model products. *Journal of Geophysical Research: Earth Surface*, *126*, e2020JF005966. https://doi.org/10.1029/2020JF005966

Received 16 DEC 2020
Accepted 18 MAY 2021

Author Contributions:
Conceptualization: M. O. Willen, T. Broerse, B. Wouters
Data curation: A. Groh, P. Kuipers Munneke, L. Schröder
Formal analysis: M. O. Willen, T. Broerse
Funding acquisition: M. Horwath
Investigation: M. O. Willen, T. Broerse
Methodology: T. Broerse
Software: T. Broerse

Separating Long-Term and Short-Term Mass Changes of Antarctic Ice Drainage Basins: A Coupled State Space Analysis of Satellite Observations and Model Products

M. O. Willen[1], T. Broerse[2], A. Groh[1], B. Wouters[3,4], P. Kuipers Munneke[3], M. Horwath[1], M. R. van den Broeke[3], and L. Schröder[5]

[1]Institut für Planetare Geodäsie, Technische Universität Dresden, Dresden, Germany, [2]Department of Geosciences, Utrecht University, Utrecht, The Netherlands, [3]Institute for Marine and Atmospheric Research Utrecht (IMAU), Utrecht University, Utrecht, The Netherlands, [4]Faculty of Civil Engineering and Geosciences, Delft University of Technology, Delft, The Netherlands, [5]Federal Agency for Cartography and Geodesy, Leipzig, Germany

Abstract Satellite gravimetry and altimetry measurements record gravity and elevation changes, respectively, which are useful for determining mass and volume change of the Antarctic Ice Sheet. Common methods employ products from regional climate modeling and firn modeling to aid interpretation and to link volume changes to mass changes. Estimating deterministic parameters over defined time periods is a conventional way to evaluate those changes. To overcome limitations of deterministic analyses with respect to time-variable signals, we have developed a state-space model framework. Therein, we jointly evaluate four mass and volume data sets by coupling of temporal signal variations. We identify long-term signals of ice drainage basins that are observed by the satellite gravimetry mission GRACE and several satellite altimetry missions from April 2002 until August 2016. The degree to which we can separate long-term and short-term variations strongly depends on the similarity of the mass and volume change time series. For the drainage system of the Pine Island Glacier (West Antarctica), our results show noticeable variations of the long-term trend with an acceleration of the contribution of ice dynamics to the mass balance from -11 ± 8 to -58 ± 8 Gt a^{-1}. Our results in Dronning Maud Land (East Antarctica) show a positive long-term contribution to the mass balance at almost a constant rate. The presented approach can fit time-variable changes without artificial selection of periods of interest. Furthermore, because we only enforce common long-term time variations between mass and volume data, differences in mean trend rates help to uncover model discrepancies.

Plain Language Summary The ice sheet in Antarctica is constantly changing in volume and mass. Overall, the ice sheet is shrinking, but there are regions with large losses and regions with small mass gains. Mass loss can be caused either by faster flow of ice into the ocean (ice-dynamical change) or by less snowfall (surface climate). We aim to separate these two processes. GRACE satellites measure the changes in the gravity field of the Earth caused by mass changes. Other satellites that carry an altimeter can measure the volume changes of the ice sheet by recording changes in ice surface elevation. The surface climate can be simulated by a regional climate model for Antarctica. We combine these sources of information to extract long-term signals of mass change and find they are mainly due to ice dynamics. As an advantage over earlier methods, the change of our long-term signal does not have to be constant in time. We show that there is an accelerated ice-dynamical mass loss in the glacier drainage basins of West Antarctica. In contrast, we identify almost constant rates of the trend in drainage basins in East Antarctica.

1. Introduction

The response of the Antarctic Ice Sheet (AIS) to climate change is a major public concern due to its potential impact on sea level rise. Meredith et al. (2019) concluded that the ice mass loss of the West Antarctic Ice Sheet (WAIS) has increased during the last two decades. In contrast, some drainage basins of the East Antarctic Ice Sheet (EAIS) show both mass losses and mass gains (Rignot et al., 2019). The Gravity Recovery And Climate Experiment (GRACE) mission and its follow-on (GRACE-FO) mission have monitored gravity changes due to mass redistribution. Simultaneously, several altimetry missions have monitored

Journal of Geophysical Research: Earth Surface 10.1029/2020JF005966

Supervision: B. Wouters, M. Horwath, M. R. van den Broeke
Validation: M. O. Willen, T. Broerse
Visualization: M. O. Willen, T. Broerse
Writing – original draft: M. O. Willen, T. Broerse
Writing – review & editing: M. O. Willen, T. Broerse, A. Groh, B. Wouters, P. Kuipers Munneke, M. Horwath, M. R. van den Broeke, L. Schröder

changes of the ice surface geometry. Reconciled estimates of the mass balance of the AIS are -73 ± 52 and -219 ± 43 Gt a^{-1} over the period 2002–2007 and 2012–2017, respectively (Shepherd et al., 2018).

The mass balance of an ice sheet has two (major) components. One component is the surface mass balance (SMB) involving precipitation, surface and drifting snow sublimation, drifting snow erosion, and meltwater runoff (van Wessem et al., 2018). Those processes take place mainly in the snow and firn layer of the ice sheet, hereinafter referred to as *SMB-driven signals*. The other component is ice dynamics (ID) taking place in the ice layer, hereinafter referred to as *ID-driven signals*. We do not account for changes of basal (or bottom) melting of the grounded ice sheet separately. There are very few direct observations of basal melting of the grounded ice sheet (Seroussi et al., 2017). Pattyn (2010) found that the mean of the basal melt rate of the grounded AIS is ~3% of the total surface accumulation, but it remains an open question how this contribution changes temporally. If the ice sheet is in a state of equilibrium, SMB-driven and ID-driven mass changes are in balance. Due to changing boundary conditions, for example, as a result of a changing climate, we expect mass and volume changes on *long-term* and *short-term* time scales. Long-term changes are characterized by a rate that varies only slowly at decadal scales. Short-term changes oscillate around zero at sub-decadal scales and tend to average out over decadal scales (Zwally et al., 2015). In Antarctica, the dominant ID-driven changes are on long time scales (Rignot et al., 2019). Here we consider long-term ice dynamic changes as dynamic thinning or dynamic thickening if the ice discharge is larger or smaller than the long-term SMB, respectively.

Satellite gravimetry and altimetry cannot distinguish between the two components of the mass balance, but only observe the sum of all mass and volume changes. SMB-driven mass and volume changes can be obtained from the SMB product from a regional climate model and from the firn thickness change product from a firn densification model (FDM). On drainage basin scale GRACE and SMB as well as altimetry and FDM show strong correlations of the nonlinear signal components (Figure 1), which motivates us to further investigate the temporal variations of mass and volume changes.

Horwath et al. (2012) and Mémin et al. (2015) found common interannual variability in GRACE and altimetry observations and could make links to their geophysical origin. They point out the limitations of treating long-term signals as a simple linear trend with a constant rate. Davis et al. (2012) and Didova et al. (2016) applied state space modeling to geodetic observations of ice mass changes. These studies showed the advantages of state space modeling for estimating trends with time-variable rates and more realistic trend uncertainties from GRACE and global navigation satellite system (GNSS) time series, compared to deterministic results from conventional least-squares adjustment. Zammit-Mangion et al. (2015) and Martín-Español et al. (2016) used a Bayesian hierarchical model to estimate annual ID-driven, annual SMB-driven, and linear glacial isostatic adjustment (GIA) mass changes from satellite altimetry, satellite gravimetry, and GNSS. In this approach, spatio-temporal parameters are taken from auxiliary observations and models, and were adjusted to GRACE, altimetry, and GNSS observations using a statistical inversion scheme.

In this study, we separate the long-term changes and the short-term changes on the drainage basin scale in Antarctica. For this purpose, we examine the GIA-corrected residual GRACE and altimetry time series after subtracting modeled SMB-driven mass change and firn-related volume change, respectively, to account for the bulk of SMB and firn signals. In our approach, we assume that (a) short-term variations of those residual time series consist of regional climate model and firn model errors next to observational errors; (b) gravimetry and altimetry are sensitive to the same long-term ID-driven variations; and (c) decadal and centennial SMB-driven signals and firn-thickness trends (e.g., Medley & Thomas, 2019) unaccounted by the model products are not predominant in the regions under investigation. We use a coupled state space model to jointly evaluate these four data sets. We estimate the time-variable signals and simultaneously relate common temporal variations from gravimetry and altimetry data.

The basins in this study refer to drainage systems defined by Zwally et al. (2012). In the main text we focus on three drainage basins (Figure 1), namely a part of Dronning Maud Land (basin 6), Wilkes Land (basin 13), and the drainage basin of the Pine Island Glacier (basin 22). We have chosen these basins because they differ in the dominance of long-term and short-term changes (Rignot et al., 2019) and should illustrate the feasibility of our approach. In the supporting information (SI), we provide material of all investigated drainage systems.

AGU ADVANCING EARTH AND SPACE SCIENCE
Journal of Geophysical Research: Earth Surface
10.1029/2020JF005966

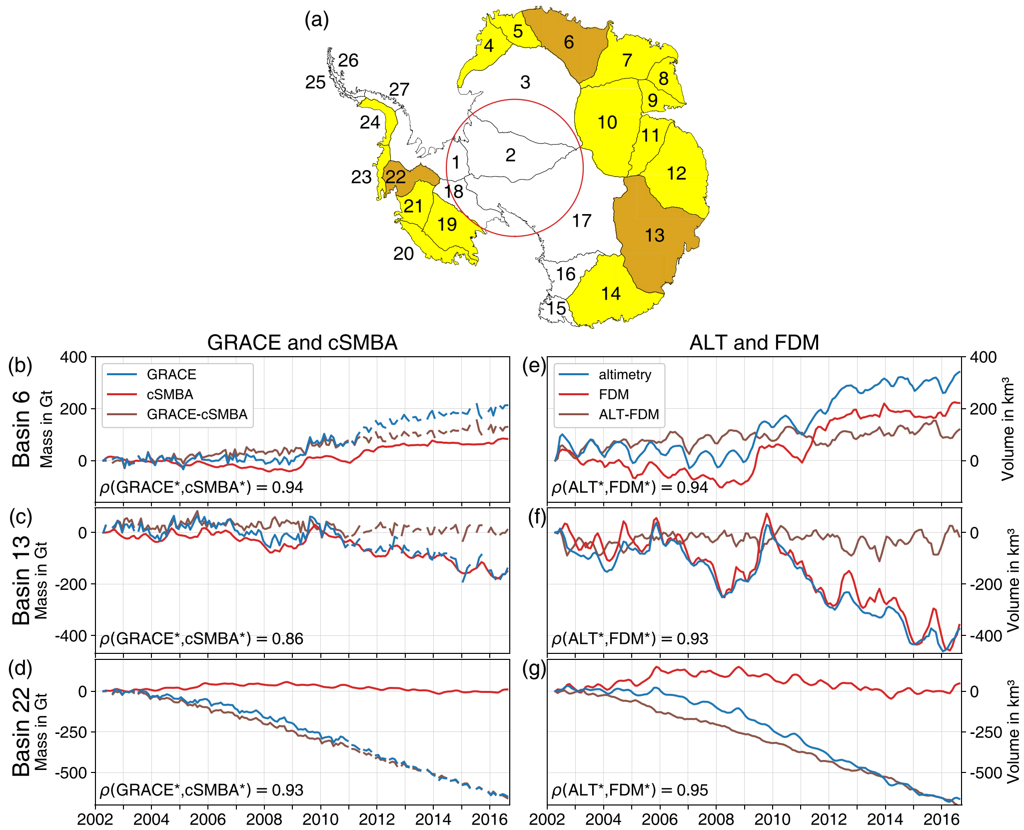

Figure 1. (a) Basins that we investigate in this study are colored, the focus basins (6, 13, 22) are indicated with dark yellow. The polar gap of ERS-2 and Envisat is indicated with a red circle. Basin borders and numbers from Zwally et al. (2012). (b–d) GRACE-derived mass time series, cumulated surface mass balance anomalies (cSMBA), and the difference between both (GRACE-cSMBA) for basins 6, 13, and 22. (e–g) Altimetry-derived volume time series and the volume change from the firn densification model (FDM), and the difference between both (Altimetry-FDM).The correlation coefficient shows the correlation between detrendend GRACE and cSMBA (ρ(GRACE*,cSMBA*)) as well as detrended ALT and FDM (ρ(ALT*,FDM*)). Table S1 summarizes the deterministic linear trends for GRACE, cSMBA, altimetry, and FDM-derived time series, the GIA correction applied to GRACE, correlation coefficients, and the basin area of all investigated basins.

2. Data and Methods

2.1. Model Products

To model the SMB-driven mass change we use the RACMO2.3p2 SMB product (van Wessem et al., 2018). The continent-wide version of this product has a spatial resolution of 27 km and is sampled monthly from January 1979 to December 2016 for the whole AIS. SMB anomalies are derived by assuming a representative climatology over a long-term period, that is, more than 30 years (van den Broeke et al., 2009). SMB anomalies are the residuals to this long-term mean SMB. In our case we define the whole modeling period from January 1979 to December 2016 as the reference period. This is consistent with the period considered during the spin-up of the FDM that we use. All our mass change estimates refer to this reference period. Table S1 summarizes the mean SMB over the reference period with an uncertainty estimate analogous to Wouters et al. (2015). For this, we have calculated the standard deviation of mean SMB values over all 25-, 30-, and 35-year time periods within the reference period (Table S1). Because satellite gravimetry and satellite altimetry observe cumulated mass balance anomalies over time, we temporally integrate SMB anomalies, which we hereinafter refer to as cumulated surface mass balance anomalies (cSMBA).

The IMAU-FDM (Ligtenberg et al., 2011) firn thickness change time series is consistent with the RACMO2.3p2 SMB product used because it applies the SMB components as forcing parameters at the up-

Journal of Geophysical Research: Earth Surface 10.1029/2020JF005966

per ice sheet boundary. It is available with the same spatial resolution. During model creation the spin-up of the firn layer is achieved by looping over the time series from January 1979 to December 2016 until an equilibrium firn layer is established. This assumes that the 38-years reference period is representative for the centuries before 1979 during which the firn layer was formed. Ligtenberg et al. (2014) found that the present-day RACMO2 forcing is a realistic reference climate. We also assume that the firn does not exhibit a trend during the reference period itself, because we consider it an equilibrated firn layer due to the spin-up run (Ligtenberg et al., 2011).

2.2. GRACE Time Series

We use CSR RL06 monthly gravity field solutions (Bettadpur, 2018) from April 2002 to August 2016. Because of accelerometer issues after August 2016 (Loomis et al., 2020), we only include solutions up to this time. We compute degree-1 coefficients following Swenson et al. (2008) and Sun et al. (2016) to complement the monthly gravity field solutions. Further, we replace the C_{20} coefficients with a product derived by satellite laser ranging (Loomis et al., 2019). We apply error and leakage optimized sensitivity kernels on the complemented gravity field time series to derive basin-wide mass changes (Groh & Horwath, 2021). We correct for GIA by using the model product from Ivins et al. (2013). A residual GIA signal can still be present in the time series, because GIA models are subject to large uncertainties. The net GIA signal predicted by current models differ over a range of ∼40–80 Gt a^{-1} (Whitehouse et al., 2019). We do not attempt to take GIA errors into account in the state-space filtering approach. They will be reflected in the temporal mean of our results (Sections 2.4 and 2.5). In Table S1, we provide the GIA uncertainty and the spread for every drainage basin that is estimated from a GIA model ensemble. We propagate the GIA uncertainty to uncertainty estimates involving GRACE. The SI provides technical details.

2.3. Altimetry Time Series

Schröder et al. (2019a) provide a monthly sampled altimetry-derived elevation change product from a multi-mission analysis using a repeat altimetry approach. Temporal and spatial smoothing is applied during processing using a moving average of 3 months and a 10-km-sigma Gaussian smoother, respectively. Within the radius of 10 km there are at least four satellite ground tracks (depending on orbit geometry), each is measured at least twice in 3 months. This means that the monthly surface elevation change in a grid cell is based on an average of at least eight satellite passes.

For our investigation, we use data over the period from April 2002 to August 2016 corresponding to the availability of GRACE observations. The altimetry-derived elevation changes during this time period include observations from ERS-2, Envisat, ICESat, and CryoSat-2. We selected all drainage basins that are covered at monthly resolution over that period. This criterion requires coverage by ERS-2 and Envisat and excludes basins 1, 2, 3, 17, and 18 that extend beyond the 81.5°S limit of coverage of these two missions. Furthermore, we do not include basins where the altimetry data are of lower quality due to strong topographic gradients. This is the case for the basins in the region of the Antarctic Peninsula (25, 26, 27) and Victoria Land (15, 16). For further details on uncertainties and altimetry quality limitations, see Schröder et al. (2019a) and Strößenreuther et al. (2020).

We correct for the elastic deformation of the solid earth and use the model product from Ivins et al. (2013) to correct for GIA. GIA and elastic-induced elevation changes are very small compared to elevation changes induced by SMB-driven and ID-driven changes. To illustrate the order of magnitude in case of basin 13, the integrated elastic-induced volume change and the GIA-related volume change are ∼0.4 and ∼0.4 $km^3\ a^{-1}$, respectively, whereas the corrected altimetry observed volume change (Table S1) is $-27.1 \pm 1.3\ km^3\ a^{-1}$ from April 2002 to August 2016.

2.4. Long-Term Uncertainties in Model Products

If we examine long-term signals, we have to accept three limitations imposed by the data that we use: (a) Any long-term SMB-driven signal would violate the assumption that the mean SMB over the chosen

AGU ADVANCING EARTH AND SPACE SCIENCE

Journal of Geophysical Research: Earth Surface 10.1029/2020JF005966

reference period is a long-term mean SMB and would thereby introduce a SMB contribution to the mean rate in our analysis. (b) Any long-term firn-thickness change over the reference period will affect the mean trend of firn-induced elevation change. Thomas et al. (2017) showed that, especially, in the Antarctic Peninsula, there seems to have been a long-term increase in snowfall, by about 10%–15% over the past century. Ligtenberg et al. (2014) predicted an increase in firn air content of 150 km^3 a^{-1} over the 21st century for the AIS. Thus, the assumption that the firn is in steady-state at the start of the integration may not be valid everywhere. Furthermore, the firn densification model output is affected by errors in the input data, which include SMB variations apart from temperature variations. We expect that errors of firn-thickness change will be correlated with errors of SMB because the IMAU-FDM is forced by RACMO2 outputs. However, uncertainty estimates are not available. Data from firn cores could quantify this long-term uncertainty, but this is beyond the scope of this study. (c) Any uncertainty in the GIA trend directly propagates to the temporal mean of the estimated trend. These three long-term uncertainties are superimposed on the mean rate of mass and volume time series, but gravimetry and altimetry are affected by them differently. First, long-term trends in SMB induce volume trends that involve some effective firn density, which is generally smaller than ice density. Therefore, the volume effects of long-term trends in SMB are more pronounced than the mass effects. Second, any long-term trend of the firn air content is solely part of altimetry observations. Finally, an unaccounted GIA-signal predominantly affects the gravimetry observations due to the large effective density of GIA-induced deformation of the solid earth (Wahr et al., 2000).

2.5. Signal Separation Strategy of Basin Time Series

GRACE and altimetry detect long-term and short-term mass and volume changes, which we define as a rate varying on decadal scales and variability at sub-decadal scales, respectively. The model products account for a large part of the short-term variability. The differences between (a) GRACE and cSMBA (GRACE–cSMBA) and (b) altimetry and FDM (ALT–FDM) include the ID-driven variability (Zwally et al., 2015) in addition to long-term errors (Section 2.4). Furthermore, the differences include a remaining short-term signal, due to modeling or observational errors.

We assume that the same ID-driven signal is present in GRACE–cSMBA and ALT–FDM and that this ID-driven signal is most likely only long-term in Antarctica (Rignot et al., 2019). Thereby, we do not presuppose that the rate of the long-term signal is constant over time. Rather, we suppose that changes of this rate are slow. We parameterize the long-term signal through a trend with a time-variable rate. This is in contrast to deterministic approaches where, for example, a trend is used with a constant rate. To enable a coupled evaluation of the four data sets (1) we link the temporal variations of the rate of GRACE–cSMBA and ALT–FDM with the density of ice (917 kg m^{-3}) in the state space model framework. This density is a conceptual assumption and we assume it is free of errors. (2) We model the long-term signal for both time series using the *seemingly unrelated time series* model (Commandeur & Koopman, 2007). This implies that the changes in the rate of the long-term parts of both time series are fully correlated. However, the mean rate may differ over the entire time series. In this way, we allow potential long-term errors (Section 2.4) to be reflected differently in both results.

We approach the remaining short-term signal of the GRACE–cSMBA and ALT–FDM time series in three ways: (1) We use annual and semi-annual cycle components with time-variable phase offset and amplitude. (2) We use a residual component to model uncorrelated noise. (3) We assume that noncyclic short-term signals can be described as an integrated random walk starting at zero at the first observation epoch. We assume that unmodeled SMB can be represented with white noise. Therefore, the errors of cumulated SMB anomalies are cumulated white noise, that is, an integrated random walk. It can be modeled as an autoregressive process of the order one (AR(1) process) in which each time step is the previous one (AR-coefficient equals 1) plus a disturbance term (Section 2.6). King and Watson (2020) showed that Generalized Gauss Markov models are better suited than an AR(1) process to explain the full SMB-driven variability. However, here we presume an AR(1) process is suited for modeling the remaining short-term variability of differential time series, which contains observational errors beside the SMB-driven variability. We test which AR-coefficient between 0 and 1 best describes the auto-correlation length of the noncyclic short-term signals. This implies that any error that is not an unmodeled SMB signal but behaves like an autoregressive process is interpreted with the same AR(1) process. That is, the AR(1) process also absorbs correlated short-term GRACE and altimetry errors. Consequently, we do not necessarily expect that the same remaining short-term signal is present in GRACE–cSMBA and ALT–FDM time series and we do not enforce a coupling of the remaining short-term variations.

2.6. State Space Modeling of Time-Series

2.6.1. State Space Setup

A state space model describes a time series, for every time t_i, $i = 1, ..., n$ with $[p \times 1]$ observation vector $\boldsymbol{y}_i$, using the $[m \times 1]$ time-variable state vector $\boldsymbol{\alpha}_i$ of m model coefficients. We extend the state space model approach from Frederikse et al. (2016) to the simultaneous filtering of multiple time series, where in our case the dimension is $p = 2$ (bivariate): the first dimension is ALT–FDM and the second is GRACE–cSMBA. We set up a state space model as (Durbin & Koopman, 2012):

$$\boldsymbol{y}_i = \boldsymbol{\mu}_i + \sum_j \boldsymbol{c}_{i,j} + \boldsymbol{\zeta}_i + \boldsymbol{\epsilon}_i \tag{1}$$

with trend $\boldsymbol{\mu}_i$, cycle (seasonal harmonic) terms $\boldsymbol{c}_{i,j}$, AR(1) process $\boldsymbol{\zeta}_i$ and irregular term (residual) $\boldsymbol{\epsilon}_i$, each a vector of size $[p \times 1]$, in total $m = p \cdot 7 = 14$ model coefficients. Each of these terms is modeled as a time variable process, where at each epoch a stochastic disturbance term allows for time variability.

First, the trend is defined as:

$$\boldsymbol{\mu}_{i+1} = \boldsymbol{\mu}_i + \boldsymbol{\nu}_i dt_i \tag{2}$$

$$\boldsymbol{\nu}_{i+1} = \boldsymbol{\nu}_i + \boldsymbol{\xi}_i \quad \boldsymbol{\xi}_i \sim N(0, \textstyle\sum_{\xi} dt_i) \tag{3}$$

with $[p \times 1]$ rates of the trend $\boldsymbol{\nu}_i$, $[p \times 1]$ Gaussian rate disturbance vector $\boldsymbol{\xi}_i$ with the $[p \times p]$ variance-covariance matrix $\sum_{\xi}$, and normalized time step

$$dt_i = \frac{t_i - t_{i-1}}{\frac{1}{n}\sum_{i=1}^{n-1}(t_{i+1} - t_i)} \tag{4}$$

that is, dt_i is generally close to 1 for an approximately regularly spaced time. As the trend $\boldsymbol{\mu}$ is updated at each epoch with a time-variable rate $\boldsymbol{\nu}$—due to the disturbance term $\boldsymbol{\xi}_i$—a smoothly changing trend is possible. Second, cycle terms can be iteratively defined as (Harvey, 1990):

$$\boldsymbol{c}_{i+1,j} = \boldsymbol{c}_{i,j} \cdot cos(\lambda_j dt_i) + \boldsymbol{c}^*_{i,j} \cdot sin(\lambda_j dt_i) + \boldsymbol{\omega}_{i,j} \quad \boldsymbol{\omega}_{i,j} \sim N(0, \textstyle\sum_{\omega} dt_i) \tag{5}$$

$$\boldsymbol{c}^*_{i+1,j} = -\boldsymbol{c}_{i,j} \cdot sin(\lambda_j dt_i) + \boldsymbol{c}^*_{i,j} \cdot cos(\lambda_j dt_i) + \boldsymbol{\omega}^*_{i,j} \quad \boldsymbol{\omega}^*_{i,j} \sim N(0, \textstyle\sum_{\omega^*} dt_i) \tag{6}$$

where $\boldsymbol{c}_{i,j}$ is the cycle component, and $\boldsymbol{c}^*_{i,j}$ an auxiliary cycle term that allows for the recursive description of the cycle term, $\lambda_j = \frac{2\pi}{T_j}$ with T_j the jth cycle period, $\boldsymbol{\omega}_{i,j}$ the Gaussian cycle disturbance with $[p \times p]$ variance-covariance matrix $\sum_{\omega}$.

Third, the autoregressive AR(1) process is modeled as (Harvey, 1990; Laine et al., 2013):

$$\boldsymbol{\zeta}_{i+1} = \boldsymbol{\zeta}_i \boldsymbol{\phi}^{dt_i} + \boldsymbol{\psi}_i \quad \boldsymbol{\psi}_i \sim N(0, \textstyle\sum_{\psi} dt_i) \tag{7}$$

with $[p \times 1]$ AR-coefficients $\boldsymbol{\phi}$ in the range [0,1], and $[p \times 1]$ Gaussian disturbance vector $\boldsymbol{\psi}_i$ with $[p \times p]$ variance-covariance matrix $\sum_{\psi}$.

Finally, the model includes a $[p \times 1]$ Gaussian irregular component vector $\boldsymbol{\epsilon}_i$ with $[p \times p]$ variance-covariance matrix $\sum_{\epsilon}$:

Journal of Geophysical Research: Earth Surface 10.1029/2020JF005966

$$\epsilon_i \sim N(0, \textstyle\sum_{\epsilon} dt_i) \tag{8}$$

In our case, the $[m \times 1]$ state vector $\boldsymbol{\alpha}_i$ contains the trend $\boldsymbol{\mu}_i$, rate $\boldsymbol{\nu}_i$, seasonal cycles $\boldsymbol{c}_{i,j}$ and $\boldsymbol{c}^*_{i,j}$ ($j = 1, 2$), AR(1) $\boldsymbol{\zeta}_i$ terms. Then, the state space model can be cast in state space form by:

$$\boldsymbol{y}_i = \boldsymbol{Z}_i \boldsymbol{\alpha}_i + \epsilon_i \tag{9}$$

where the $[p \times m]$ design matrix $\boldsymbol{Z}_i$ relates the current state $\boldsymbol{\alpha}_i$ to the observations $\boldsymbol{y}_i$. Subsequent states are related by $[m \times m]$ transition matrix $\boldsymbol{T}_i$:

$$\boldsymbol{\alpha}_{i+1} = \boldsymbol{T}_i \boldsymbol{\alpha}_i + \boldsymbol{Q}_i \tag{10}$$

and $[m \times m]$ variance matrix $\boldsymbol{Q}_i$ that contains all disturbance variance-covariances. The SI contains an explicit description of all relevant vectors and matrices.

2.6.2. Estimation of the State and Disturbance Variance-Covariance

We use a Kalman filter and smoother to estimate the state $\boldsymbol{\alpha}$, irregular term ϵ and their error variances for both time series simultaneously (Koopman, 1993). We co-estimate the uncertainties of the time-variable model coefficients such as of the trend and its rate. We describe technical details in section B of the SI. As we do not have reliable knowledge about the disturbance and irregular variances and covariances, as well as the AR-coefficients $\boldsymbol{\phi}$, we estimate these parameters a priori. A common approach in state space modeling is to statistically optimize these parameters by maximizing the likelihood: the goodness of fit of the observations given a choice of (co)variance and AR parameters. Using the expectation maximization (EM)-algorithm, we iteratively estimate variance-covariance matrices (Koopman, 1993) while we do a two-dimensional grid search for an optimal ϕ^{v}-ϕ^{m}-combination. We enforce a ratio of the rate disturbance variances between GRACE–cSMBA $\sigma^2_{\xi^{\mathrm{m}}}$ and ALT–FDM $\sigma^2_{\xi^{\mathrm{v}}}$ of

$$\frac{\sigma^2_{\xi^{\mathrm{m}}}}{\sigma^2_{\xi^{\mathrm{v}}}} = \frac{(0.917\,\mathrm{Gt})^2}{(1\,\mathrm{km}^3)^2}. \tag{11}$$

In this way, we couple the common long-term variability of GRACE–cSMBA and ALT–FDM with ice density, because we assume that this is predominately ID-driven (Section 2.5).

2.6.3. Mean Trend Rates

We compute the mean rate from the trend and propagate estimated time variable uncertainties for a mean rate uncertainty. The SI provides the formal mathematical description. For comparison to the results from state-space filtering, we compute deterministic results by estimating trends with constant rates of GRACE–cSMBA and ALT–FDM. The deterministic rates are co-estimated with bias, annual and semi-annual cycle components using least-squares adjustment.

3. Results

Primarily, we focus on the long-term contributions to the mass balances of the drainage systems. We illustrate the basin-integrated time series of the three focus basins in Figures 1b–1g. Figure 2 shows the estimated components together with the original observation, and model time series. As it shows, the AR(1) and cycle terms absorb the largest part of the differential time series that is not explained by the trend. The residual, irregular term absorbs the uncorrelated noise of GRACE–cSMBA, but is negligible in case of ALT–FDM. Figure 3 shows the GRACE–cSMBA and ALT–FDM time series (observation minus model), the trend with time-variable rates and its uncertainty, and the deterministic trend of the focus basins. We observe that the uncertainties of the trend with time-variable rates vary among basins. High uncertainties are accompanied with a high auto-correlation of the estimated AR(1) component (Figures S2 and S6) and reveal that the trend is less independent of the AR(1) process (Section 4.1). Figure 4 visualizes that the estimated time-variable rate from GRACE–cSMBA and ALT–FDM is fully correlated as the time variability for both is identical, even though the mean rate may differ (Section 2.6).

Journal of Geophysical Research: Earth Surface 10.1029/2020JF005966

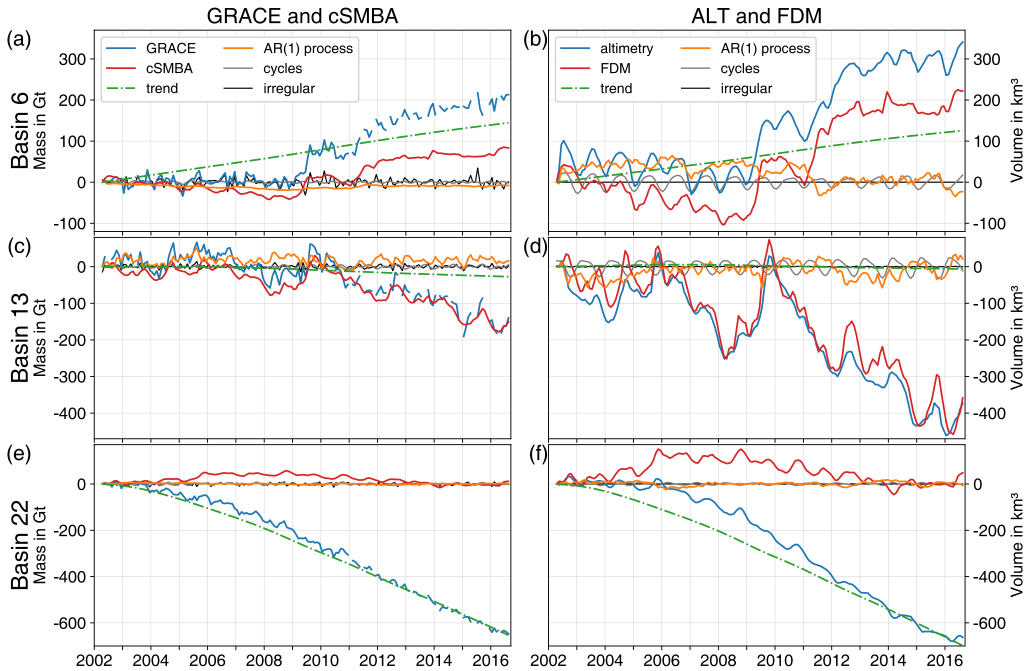

Figure 2. Estimated components of the focus basins: For GRACE–cSMBA (a, c, and e) and ALT–FDM (b, d, and f) the satellite observations (blue) are the sum of model products (red), the trend (green), the AR(1) process (orange), the cycle component (gray), and the irregular component (black). We provide results of all investigated basins in the SI. For interpretation of short-term signals [AR(1), cycles, irregular], the reader is referred to Figure S4.

When we compare between the mean rates of GRACE–cSMBA and ALT–FDM for the focus basins 6, 13, and 22, we find differences of ~2.1, ~1.5, and ~0.9 Gt a^{-1}, respectively, (we use a density of 917 kg m^{-3} to convert ALT–FDM volume changes to mass changes). For basin 22 these differences are small compared to the estimated trend. Basin 22 shows a clear acceleration of the GRACE–cSMBA trend: the rate changes from -11 ± 8 in April 2002 to -58 ± 8 Gt a^{-1} in August 2016 (Figure 4c). Figures of all investigated time series can be found in the SI.

Figures 5a and 5d illustrate mean rates of GRACE–cSMBA and ALT–FDM. Further we compare the mean rates to the deterministic results in Figure 5, and include the mean rate uncertainties (values are provided in Table S2). The absolute values of the mean rate are highest for the Amundsen Sea Embayment (basins 20, 21, and 22). In basins 19 and 24 the mean rate and the deterministic rate from GRACE–cSMBA have opposite signs to the mean rate and the deterministic rate from ALT–FDM.

The root mean square (RMS) of the AR(1) component, $RMS_{AR(1)}$, and the irregular component, RMS_{irr}, reflect the magnitude of the signal that is not explained by the trend or cycle terms. Similarly—in the deterministic case—the RMS of post-fit residuals, RMS_{resid}, represents the unexplained signal. Table S2 compares these values. In the case of ALT–FDM a large part of the remaining short-term signal can be explained by an AR(1) process. In the case of GRACE–cSMBA there is a significant irregular component, whereas this is negligible in ALT–FDM. The RMS of the post-fit residuals from the deterministic fit is highest in basins 22 and 14 in case of GRACE–cSMBA and ALT–FDM, respectively.

4. Discussion

4.1. Interpretation of the Results

The state space model is able to separate long-term variability shared by both GRACE–cSMBA and ALT–FDM, and remaining short-term signals in these differential time series. We argue that the estimated long-term

AGU ADVANCING EARTH AND SPACE SCIENCE
Journal of Geophysical Research: Earth Surface
10.1029/2020JF005966

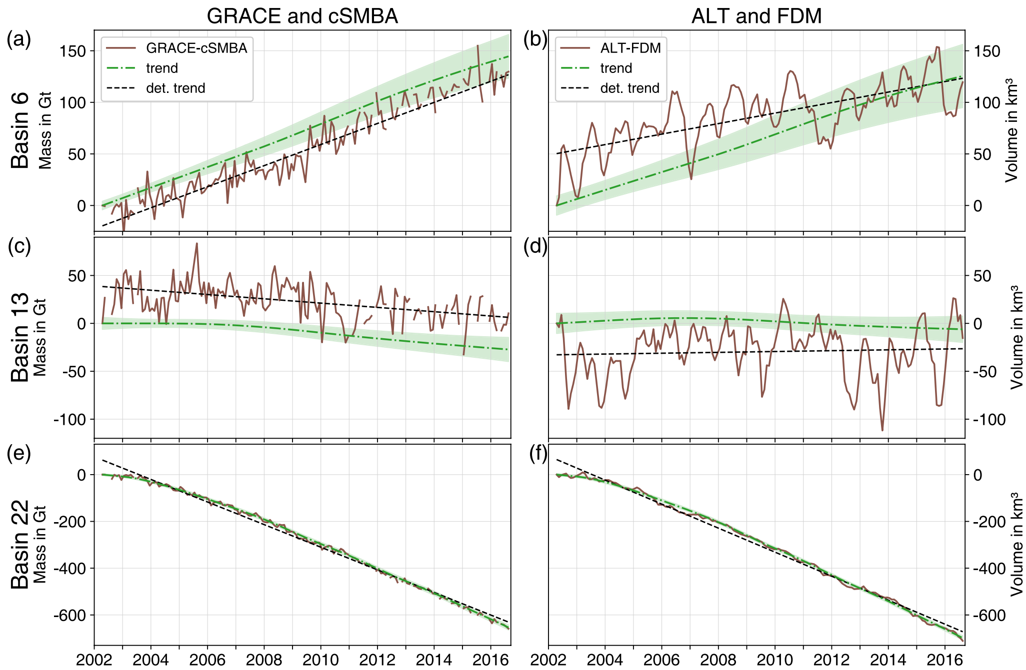

Figure 3. Estimated trends of the focus basins: For GRACE–cSMBA (a, c, and e) and ALT–FDM (b, d, and f). The difference between satellite observations and model products (brown) is illustrated with the trend with a time-variable rate, its 1-σ-uncertainty (green), and the deterministic trend with a constant rate (black). GRACE–cSMBA uncertainties include GIA uncertainties. We provide results of all investigated basins in the SI.

signal is approximately equivalent to the ID-driven time variable mass and volume changes. This has the limitation that the long-term signal may be affected by errors of the model products and the assumptions involved therein (Section 2.4). Particularly, the SMB anomalies and firn thickness anomalies considered in GRACE–cSMBA and ALT–FDM imply assumptions on a steady-state mean SMB and firn structure as a reference. Consequently, a negative rate (positive rate, respectively) of the ID-driven contribution means that ice discharge is larger (smaller) than the mean SMB thus defined. Based on the trend uncertainties, we conclude that the separation performs best when the trend rates are either large (basins 21 and 22) or the unexplained, auto-correlated, signals have short correlation lengths (e.g., basins 7 and 11–14 in Figure S6). When the unexplained AR signals contain substantial long-term signals (large correlation length) either in GRACE–cSMBA or ALT–FDM, it will be increasingly difficult to discriminate between the AR process and the trend. This is reflected by larger estimated uncertainties of the trend. The cross-correlation of the AR(1) between time series for GRACE–cSMBA and ALT–FDM is small or negative (Figure S6, except for basins 6 and 8), affirming that the common signals have been absorbed in the trend. Because the ALT–FDM time series are more sensitive than GRACE–cSMBA to variability in SMB, due to the relatively low firn density, the GRACE–cSMBA is dominant in the definition of the trend.

Our estimated trends vary substantially with the region. We find a clear difference between the WAIS and the EAIS (Figure 5). In particular, long-term signals are dominant over basins 21 and 22. An accelerated decrease of volume and mass is already visible in the basin integrals of the satellite observations (Figures 1d and 1g). The accelerating long-term change can be fitted with the trend with time-variable rates and interpreted as an accelerating ID-driven signal.

Basin 6 shows strong inter-annual variations, with a significant step in the year 2009. This step can be attributed to an accumulation anomaly (as already present in the SMB model) (Boening et al., 2012; Lenaerts et al., 2013). The rate of the trend is almost constant over time. From this, we conclude that there is a positive long-term contribution to the mass balance, which only slightly changes over time. Similarly to basin 6, a positive trend with a low variability is visible in all investigated basins of the EAIS except for basins 10, 11,

AGU ADVANCING EARTH AND SPACE SCIENCE
Journal of Geophysical Research: Earth Surface
10.1029/2020JF005966

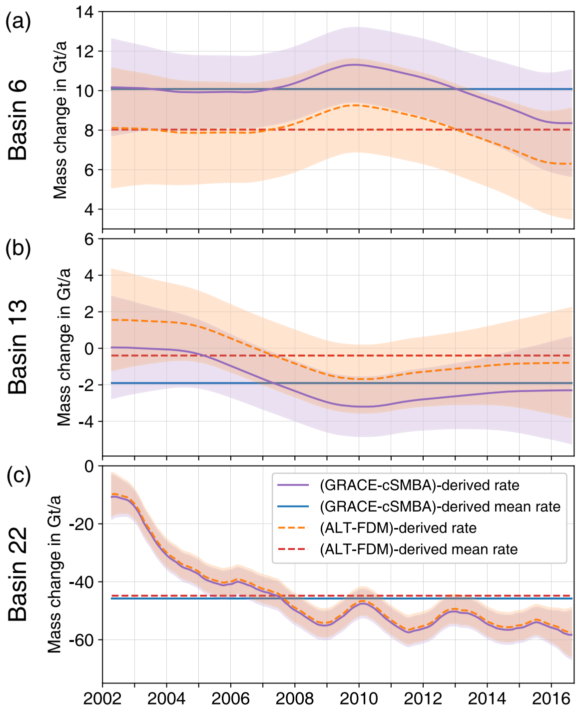

Figure 4. Estimated time-variable rates of the focus basins: The rates of the trends over time, their uncertainties (purple and orange), and the mean rates (blue and red) from GRACE–cSMBA and ALT–FDM, respectively. The rate from ALT–FDM is converted to mass change with ice density. GRACE–cSMBA uncertainties include GIA uncertainties. We provide results of all investigated basins in the SI.

13, and 14 (Figures S2 and S3). In these basins, we interpret the positive trend as ice dynamic thickening. However, this positive trend may also have causes in the violation of the assumptions we made in Section 2.4, for example, that there is a long-term SMB-driven signal that is not part of the model products.

In basin 13, the trend is small. Here, the altimetry-derived and the FDM-derived volume time series are very similar, whereas the mass time series show a small long-term difference compared to the cSMBA values (Figure 4b). Explanations for this discrepancy include: altimetry missions have insufficiently sampled the mass change of Totten Glacier; there are unaccounted long-term climate signals that affect mass and volume changes differently (Section 2.4); the GIA correction of GRACE is underestimated. The spread of the GIA signal predicted by models is 3 Gt a^{-1} in basin 13, which is higher than the difference of the mean rates (1.5 Gt a^{-1}).

4.2. Differences in Mean Rates

For both GRACE–cSMBA or ALT–FDM the mean rates using the state space model agree well with the deterministic trends using least-squares adjustment. Mean rates of GRACE–cSMBA and ALT–FDM agree within the indicated 2-σ-uncertainties for basins: 4–13 and 22 (Figure 6) using the state space model. For the deterministic approach the GRACE–cSMBA and ALT–FDM rates match within the 2-σ-uncertainties for basins: 9–12 and 22. The state space model allows for a more realistic uncertainty estimation compared to unrealistic small standard uncertainties derived by least-squares adjustment. Further biases remain unconsidered. For example, GRACE detects mass changes only at a low spatial resolution and signal leakage may distort the results (Horwath & Dietrich, 2009). On the other hand, the altimetry product provides a high resolution but biases are present due to topographic characteristics or interpolation (Strößenreuther et al., 2020). Other factors that may contribute to the differences between the mean rate of GRACE–cSMBA and ALT–FDM are due to GIA uncertainties and assumptions about long-term equilibrium in the SMB and firn models (Section 2.4). Our approach allows for different mean values to reflect those potential long-term uncertainties. For example, if we use a different reference period to calculate cSMBA, this would lead to a different mean rate—or in other words it would lead to a shift of the time-variable rates of the trend—and therefore create a different discrepancy between the mean rates from GRACE–cSMBA and ALT–FDM. Due to limitations of the input datasets, we cannot conclude whether GRACE–cSMBA or ALT–FDM results have a smaller (systematic) bias. Because we assume that the AR(1) component represents an accumulating error, we force it to start from zero (from which it may deviate by incorporating disturbance variance). The deterministic fit does not include this assumption and therefore it may lead to an underestimation of the residual and its correlation length. It cannot capture the auto-correlated signal around the trend (e.g., basins 4, 5, 6, and 9 in Figure S2).

4.3. Unexplained Short-Term Signals

Except for basins 9–11, the estimated short-term signals are small compared to the cSMBA and FDM time series (Figure S1 and Table S2), which indicates that the cSMBA and FDM time series already explain a large part of the short-term variability of the GRACE and altimetry data. In basins 9–11, we find residual short-term components in the same order of magnitude as the time series of total mass and volume variations, especially in the volume time series (Figure S1). Furthermore, the discrepancy between satellite observations and model products is evident by the low correlation between the time series here (Table S1). We find the lowest correlation of 0.12 in basin 10 between the altimetry and the FDM time series.

AGU ADVANCING EARTH AND SPACE SCIENCE

Journal of Geophysical Research: Earth Surface

10.1029/2020JF005966

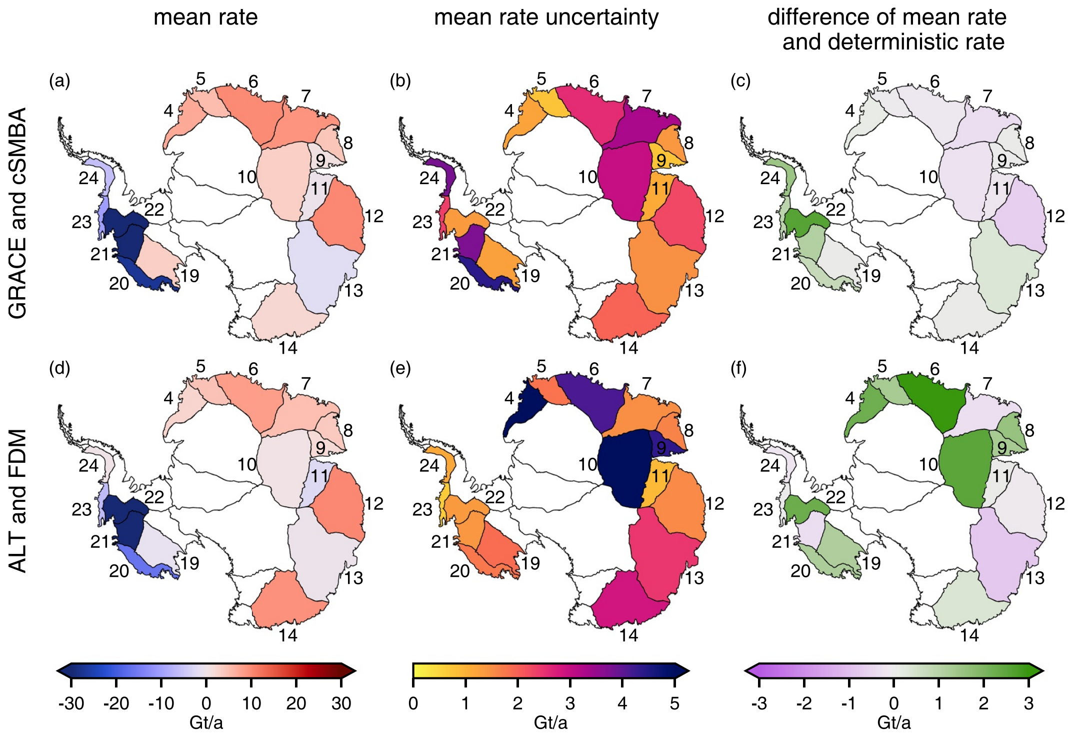

Figure 5. The mean rates, the 1-σ-uncertainties, and differences to deterministic rate are color coded. Results from ALT–FDM are converted to mass with ice density (917 kg m^{-3}). GRACE–cSMBA uncertainties include GIA uncertainties. Table S2 provides the underlying numbers.

The estimated AR(1) process absorbs two main parts. (1) It absorbs short-term SMB-driven signals that are not included in the model products. In this sense, a part of the AR(1) process can be understood as modeled short-term error of cSMBA and FDM. (2) Errors of the satellite data, or errors due to different temporal sampling of observations and model products, are absorbed in the AR(1) process, too. We find a larger AR(1) process in ALT–FDM than in GRACE–cSMBA. A major reason for this is the temporal smoothing applied during the processing of altimetry (Schröder et al., 2019a). This artificially correlates temporally uncorrelated errors. The AR(1) process captures these correlated errors and this also explains the small irregular component in case of ALT–FDM. We observe that the AR(1) process from ALT–FDM generally contains relatively large signals on timescales of more than a year in basins 4–11. We also find larger residual seasonal signals in ALT–FDM than GRACE–cSMBA (Figures S1 and S4). If the seasonal signal and the AR(1) process are an unmodeled SMB signal, a low firn density could explain the comparatively large volume change and relatively small mass change. In order to enable the attribution of the error to either the satellite data or the model products, these errors would have to be parameterized separately. So far we have not identified a suitable parameterization for either errors in the model products, or errors in the satellite data. We have tried to constrain the errors of the model products by means of an error assessment analogous to Willen et al. (2020). Doing so, we made use of the SMB product of another regional climate model, namely MAR (Agosta et al., 2019). But the error estimation based on only two SMB products does not provide sufficient error information, resulting in an unrealistic error budget. Moreover, no FDM based on MAR is available.

The filtering results of basin 6 show that most of the short-term variations in GRACE–cSMBA can be explained by the irregular component and can thus be described as temporally uncorrelated Gaussian noise. The AR(1) process is very small and accounts for a minor trend (Figures 2a and S4). This can be prevented by choosing a slightly reduced irregular disturbance variance. This would result in an

Journal of Geophysical Research: Earth Surface 10.1029/2020JF005966

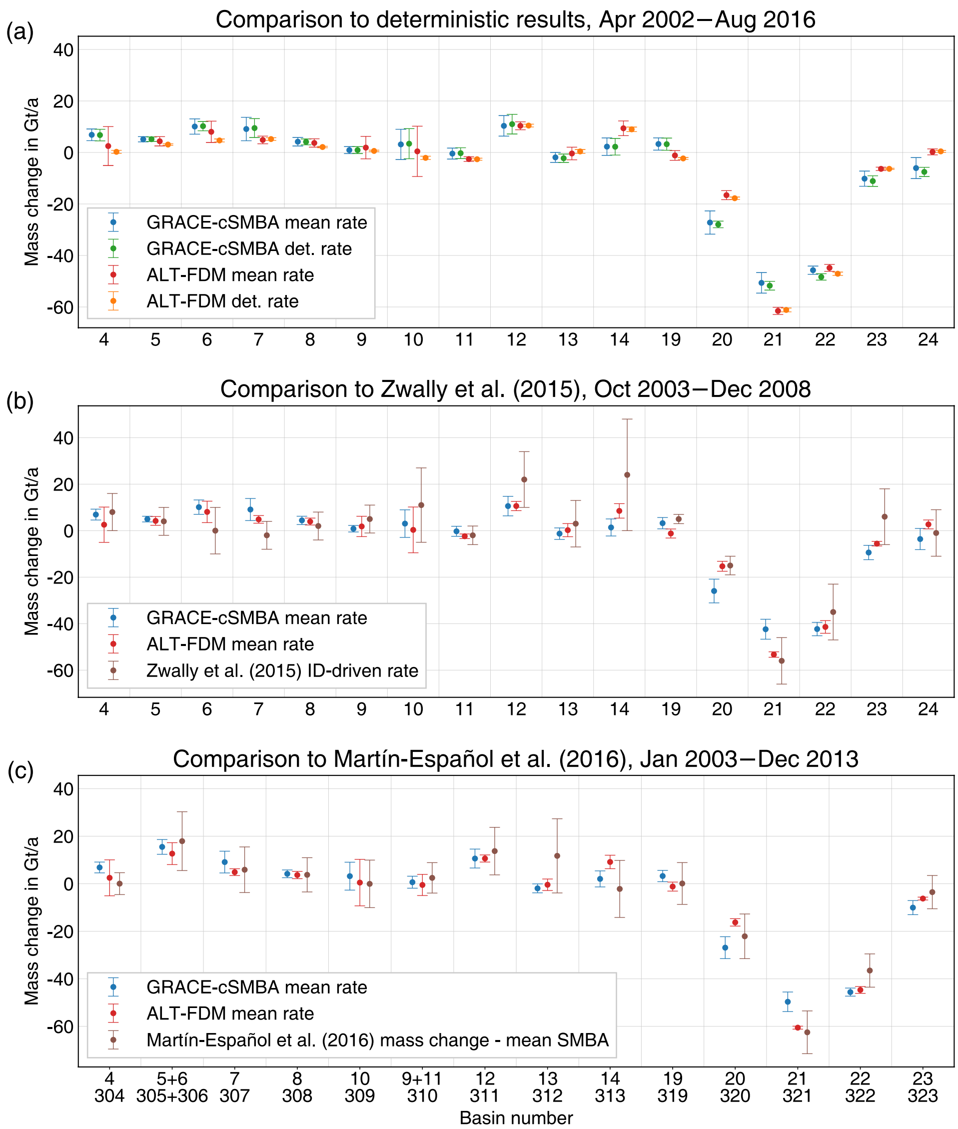

Figure 6. (a) Mean rates and deterministic results for investigated basins (cf. Table S2). (b) Comparison of mean trend rates to ID-driven estimates published by Zwally et al. (2015). (c) Comparison of mean trend rates to the mass balance estimates published by Martín-Español et al. (2016). To enable the comparison, we removed the mean SMB anomalies during the indicated time period from the published mass balance estimates. We used basin numbers from Zwally et al. (2012) (first row of labels), basin numbers from Martín-Español et al. (2016) indicated in the second row of labels. The sum of basins 5 and 6 approximately equals the sum of basins 305 and 306 and the sum of basins 9 and 11 approximately equals basin 310. The time periods are indicated in the subfigure titles. The mean rates from ALT–FDM are converted to mass change with ice density (917 kg m^{-3}). 2-σ-uncertainties are indicated with error bars. GRACE–cSMBA uncertainties include GIA uncertainties.

Journal of Geophysical Research: Earth Surface 10.1029/2020JF005966

increased part of the short-term variations being explained by the AR(1) process, at the expense of a lower likelihood.

Furthermore, we have investigated the sensitivity of the approach to an alternative GRACE product based on monthly GRACE solutions from Mayer-Gürr et al. (2016). A clear difference in the estimated AR(1) process is visible for most basins (Figure S7). From this we conclude that a large amount of the AR(1) process in the GRACE–cSMBA time series can be explained by errors due to GRACE data processing, which needs further investigation (Section 4.5). Our results suggest that considerable signals are present in the GRACE–cSMBA and ALT–FDM time series that are not correlated for the two time series and cannot be attributed to long-term changes.

4.4. Comparison With Other Published Results

Martín-Español et al. (2016) estimate annual ID-driven and SMB-driven mass changes along with linear GIA from altimetry, GRACE, and GNSS. A priori information is included from models (among others RACMO2.3p2 outputs) and further observations to constrain the spatio-temporal characteristics of ID, SMB, and GIA. Table 2 in Martín-Español et al. (2016) summarizes integrated mass changes over different basins than we used. Figure 6c compares mass changes from approximately the same basins (or approximately the same basin aggregations) over the time period January 2003–December 2013. To be able to make a comparison, we remove the mean SMB anomalies during this time period from the mass balance estimates of Martín-Español et al. (2016), because our trends are based on time series with the effect of the mean SMB removed (Section 2.5). Our ALT–FDM results agree with mass balance estimates from Martín-Español et al. (2016) within 2-σ-uncertainties. This is also the case comparing GRACE–cSMBA results, except for basins 4 and 22 where our mass rate from GRACE–cSMBA is slightly more positive and more negative, respectively. The temporal evolution of the estimated long-term signal (Figures 4b and 4c) and the ID-driven signal from Martín-Español et al. (2016) (Figures 4c and 4a therein, respectively) are very similar.

Zwally et al. (2015) use ICESat data and global reanalysis products to separate SMB-driven and ID-driven signals from October 2003 to December 2008 in altimetry data. Our mean rates of the trends during this time period agree well with the ID-driven mass changes published by Zwally et al. (2015) (Figure 6b). If we compare mean rates over this time period from ALT–FDM and Zwally et al. (2015) they agree within the uncertainties except for basin 19. We find the largest differences (>10 but <15 Gt a^{-1}) for basins 10, 12, 14, and 23. The smallest discrepancies (<1 Gt a^{-1}) arise for basins 5, 11, and 20. It is remarkable that even the results with the largest differences agree within the uncertainties. Zwally et al. (2015) use a different methodological framework and use laser altimetry observations (ICESat) only, whereas we use an altimetry product (Section 2.3) that includes radar altimetry (Envisat) in addition to ICESat laser altimetry and involves a calibration of ICESat laser operation period biases (Schröder et al., 2017) that differs from that by Zwally et al. (2015). Note that , we do not investigate all drainage basins of the EAIS (Figure 1), where Zwally et al. (2015) identified large positive ID-driven mass changes, which are however under debate (Martín-Español et al., 2017; Richter et al., 2016).

High loss rates and an ID-driven acceleration are known in the Amundsen Sea Embayment of the WAIS (Shepherd et al., 2018). Therefore, we discuss this region in more detail. Basin 21 (includes Thwaites Glacier) and basin 22 (includes Pine Island Glacier) belong to this region. Martín-Español et al. (2016) published mass changes of -64.8 ± 4.5 and -37.4 ± 3.5 Gt a^{-1} for basins 21 and 22 (equal to 321 and 322 from Martín-Español et al. (2016)), respectively during January 2003 until December 2013. SMB anomalies during this time period contribute -2 and -1 Gt a^{-1} to the mass balance, respectively (removed in Figure 6c). The results from Martín-Español et al. (2016) and Zwally et al. (2015) are similar to the estimated mean rates from GRACE–cSMBA and ALT–FDM (Figure 6). Furthermore, our results in the Amundsen Sea Embayment agree well with ice discharge estimates from Rignot et al. (2019), which they estimated from ice velocity and ice thickness data. The drainage systems defined by Rignot et al. (2019) differ to those that we use. (1) Basin 21 corresponds approximately to the aggregation of Thwaites Glacier, Haynes Glacier, Crosson Glacier, and Dotson Glacier; (2) basin 22 corresponds to Pine Island Glacier (Table 1 in Rignot et al., 2019). For the time period 2009–2017, they quantified the ice discharge of (1) and (2) at 190.7 ± 4.7 and 133.2 ± 5.8 Gt a^{-1}, respectively. The absolute ice discharge values from our results (sum of

Journal of Geophysical Research: Earth Surface 10.1029/2020JF005966

the mean SMB and the estimated mean rate) between January 2009 and August 2016 from GRACE–cSMBA for basin 21 and basin 22 are 176 ± 2 and 136 ± 2 Gt a^{-1}, respectively. ALT–FDM results are 186 ± 2 and 135 ± 2 Gt a^{-1}, respectively.

4.5. Outlook

During the selected time period of 14 years and 4 months covering the available GRACE observations, we have not investigated all Antarctic drainage basins due to the limited quality of the altimetry data (Section 2.3). High-quality altimetry data of the almost entire AIS is available from the CryoSat-2 mission and ICESat-2 mission since July 2010 and October 2018, respectively. Gravity fields from the GRACE-FO mission are available since June 2018. Through the continuous observation of the AIS it will become possible to investigate further areas of Antarctica within the near future. Moreover, an error model for the satellite data and the model products is needed to improve the estimation of the time-variable signals. An error model should account for the temporal heteroscedasticity (nonconstant variability of errors), especially of the observation products. To properly understand the mechanisms that are responsible for ice volume and mass changes we argue that more attention should be focused on the temporal behavior of the observed mass and volume changes. The state space method is a likely candidate for future temporal analyses of ice mass changes. In particular, the approach can unravel interannual signals and aid to overcome limitations due to deterministic methods pointed out, for example, in Horwath et al. (2012) and Mémin et al. (2015). Our estimated AR process and time-variable (seasonal) cycle time series can be instrumental in assessing unmodeled SMB-driven signals.

5. Conclusions

Our data-driven approach is able to estimate common time-variable signals in both geodetic data sets with the aid of products from regional climate modeling and firn modeling. We interpret these common signals as most likely ID driven. We find residual auto-correlated and seasonal signals in these time series, with often significant variance if compared to the climate and firn model products. However, we cannot yet attribute the short-term signals to a specific source.

Furthermore, our results confirm the accelerating ice loss of the WAIS in the Amundsen Sea Embayment. Our approach allows us to fit the acceleration without the artificial selection of time periods. The results for the investigated basins of the EAIS show small long-term signals with a low temporal variability. The temporal variability of mass and volume changes of the EAIS can mainly be attributed to the SMB component. Residual short-term signals are most likely not ID driven because these signals are not positively correlated between the GRACE and altimetry time series.

Limitations of the presented approach are due to the treatment of short-term and long-term errors. So far we have not been able to assign uncertainties to the input data sets. The estimated mean rate is sensitive to long-term uncertainties of the SMB and the FDM product, for example, by the chosen reference period. However, we do not expect large errors in the mean rates of the model products for the Antarctic drainage basins.

Data Availability Statement

Basin time series of inputs and results (Willen et al., 2021) are publicly available via https://doi.org/10.1594/PANGAEA.930250. Gravimetric mass balance products (Groh & Horwath, 2021) are available via https://data1.geo.tu-dresden.de/ais_gmb/. Altimetry elevation changes (Schröder et al., 2019b) are available via https://data1.geo.tu-dresden.de/ais_alt/ (interactive access) or https://doi.org/10.1594/PANGAEA.897390. RACMO2.3p2 SMB and IMAU-FDM are available on request via https://www.projects.science.uu.nl/iceclimate/.

AGU ADVANCING EARTH AND SPACE SCIENCE

Journal of Geophysical Research: Earth Surface 10.1029/2020JF005966

Acknowledgments
M. O. Willen was funded through grants HO 4232/4-1 and HO 4232/4-2 "Reconciling ocean mass change and GIA from satellite gravity and altimetry (OMCG)" from the Deutsche Forschungsgemeinschaft (DFG) as part of the Special Priority Program (SPP) 1889 "Regional Sea Level Change and Society" (SeaLevel). B. Wouters was funded by NWO VIDI Grant 016.Vidi.171.063. We thank Brooke Medley, three anonymous reviewers, the editor Olga Sergienko, and the associate editor Christine Dow for their helpful reviews and suggestions to improve the manuscript. Furthermore, we thank Erik Ivins, Eric Larour (both JPL, Caltech, USA), and Mirko Scheinert (TU Dresden, Germany) for the discussion of measuring and modeling basal melting of ice sheets. Open access funding enabled and organized by Projekt DEAL.

References

Agosta, C., Amory, C., Kittel, C., Orsi, A., Favier, V., Gallée, H., et al. (2019). Estimation of the Antarctic surface mass balance using the regional climate model MAR (1979–2015) and identification of dominant processes. *The Cryosphere*, *13*(1), 281–296. https://doi.org/10.5194/tc-13-281-2019

Bettadpur, S. (2018). *GRACE field geopotential coefficients CSR release 6.0*. University of Texas Center for Space Research and NASA Physical Oceanography DAAC. https://doi.org/10.5067/GRGSM-20C06

Boening, C., Lebsock, M., Landerer, F., & Stephens, G. (2012). Snowfall-driven mass change on the East Antarctic ice sheet. *Geophysical Research Letters*, *39*(21), L21501. https://doi.org/10.1029/2012GL053316

Commandeur, J. J. F., & Koopman, S. J. (2007). *An introduction to state space time series analysis*. Oxford University Press.

Davis, J. L., Wernicke, B. P., & Tamisiea, M. E. (2012). On seasonal signals in geodetic time series. *Journal of Geophysical Research*, *117*(B1). https://doi.org/10.1029/2011jb008690

Didova, O., Gunter, B., Riva, R., Klees, R., & Roese-Koerner, L. (2016). An approach for estimating time-variable rates from geodetic time series. *Journal of Geodesy*, *90*(11), 1207–1221. https://doi.org/10.1007/s00190-016-0918-5

Durbin, J., & Koopman, S. J. (2012). *Time series analysis by state space methods*. Oxford University Press. https://doi.org/10.1093/acprof:oso/9780199641178.001.0001

Frederikse, T., Riva, R., Slobbe, C., Broerse, T., & Verlaan, M. (2016). Estimating decadal variability in sea level from tide gauge records: An application to the North Sea. *Journal of Geophysical Research: Oceans*, *121*(3), 1529–1545. https://doi.org/10.1002/2015JC011174

Groh, A., & Horwath, M. (2021). Antarctic Ice mass change products from GRACE/GRACE-FO using tailored sensitivity kernels. *Remote Sensing*, *13*(9), 1736. https://doi.org/10.3390/rs13091736

Harvey, A. C. (1990). *Forecasting, structural time series models and the kalman filter*. Cambridge University Press. https://doi.org/10.1017/cbo9781107049994

Horwath, M., & Dietrich, R. (2009). Signal and error in mass change inferences from GRACE: The case of Antarctica. *Geophysical Journal International*, *177*(3), 849–864. https://doi.org/10.1111/j.1365-246X.2009.04139.x

Horwath, M., Legrésy, B., Rémy, F., Blarel, F., & Lemoine, J.-M. (2012). Consistent patterns of Antarctic ice sheet interannual variations from ENVISAT radar altimetry and GRACE satellite gravimetry. *Geophysical Journal International*, *189*(2), 863–876. https://doi.org/10.1111/j.1365-246X.2012.05401.x

Ivins, E. R., James, T. S., Wahr, J., Schrama, E. J., Landerer, F. W., & Simon, K. M. (2013). Antarctic contribution to sea level rise observed by GRACE with improved GIA correction. *Journal of Geophysical Research*, *118*(6), 3126–3141. https://doi.org/10.1002/jgrb.50208

King, M. A., & Watson, C. S. (2020). Antarctic surface mass balance: Natural variability, noise, and detecting new trends. *Geophysical Research Letters*, *47*(12). https://doi.org/10.1029/2020GL087493

Koopman, S. J. (1993). Disturbance smoother for state space models. *Biometrika*, *80*(1), 117–126. https://doi.org/10.1093/biomet/80.1.117

Laine, M., Latva-Pukkila, N., & Kyrölä, E. (2013). Analyzing time varying trends in stratospheric ozone time series using state space approach. *Atmospheric Chemistry and Physics Discussions*, *13*(8).

Lenaerts, J. T. M., van Meijgaard, E., van den Broeke, M. R., Ligtenberg, S. R. M., Horwath, M., & Isaksson, E. (2013). Recent snowfall anomalies in Dronning Maud Land, East Antarctica, in a historical and future climate perspective. *Geophysical Research Letters*, *40*(11), 2684–2688. https://doi.org/10.1002/grl.50559

Ligtenberg, S. R. M., Helsen, M. M., & van den Broeke, M. R. (2011). An improved semi-empirical model for the densification of Antarctic firn. *The Cryosphere*, *5*(4), 809–819. https://doi.org/10.5194/tc-5-809-2011

Ligtenberg, S. R. M., Kuipers Munneke, P., & van den Broeke, M. R. (2014). Present and future variations in Antarctic firn air content. *The Cryosphere*, *8*(5), 1711–1723. https://doi.org/10.5194/tc-8-1711-2014

Loomis, B. D., Rachlin, K. E., & Luthcke, S. B. (2019). Improved earth oblateness rate reveals increased ice sheet losses and mass-driven sea level rise. *Geophysical Research Letters*, *46*(12), 6910–6917. https://doi.org/10.1029/2019GL082929

Loomis, B. D., Rachlin, K. E., Wiese, D. N., Landerer, F. W., & Luthcke, S. B. (2020). Replacing GRACE/GRACE-FO with satellite laser ranging: Impacts on Antarctic Ice Sheet mass change. *Geophysical Research Letters*, *47*(3). https://doi.org/10.1029/2019GL085488

Martin-Español, A., Bamber, J. L., & Zammit-Mangion, A. (2017). Constraining the mass balance of East Antarctica. *Geophysical Research Letters*, *44*, 4168–4175. https://doi.org/10.1002/2017GL072937

Martín-Español, A., Zammit-Mangion, A., Clarke, P., Flament, T., Helm, V., King, M., & Bamber, J. (2016). Spatial and temporal Antarctic Ice Sheet mass trends, glacio-isostatic adjustment and surface processes from a joint inversion of satellite altimeter, gravity and GPS data. *Journal of Geophysical Research: Earth Surface*, *121*(2), 182–200. https://doi.org/10.1002/2015JF003550

Mayer-Gürr, T., Behzadpour, S., Ellmer, M., Kvas, A., Klinger, B., & Zehentner, N. (2016). *ITSG-Grace2016—Monthly and daily gravity field solutions from GRACE*. GFZ Data Services. https://doi.org/10.5880/icgem.2016.007

Medley, B., & Thomas, E. R. (2019). Increased snowfall over the Antarctic Ice Sheet mitigated twentieth-century sea-level rise. *Nature Climate Change*, *9*(1), 34–39. https://doi.org/10.1038/s41558-018-0356-x

Mémin, A., Flament, T., Alizier, B., Watson, C., & Rémy, F. (2015). Interannual variation of the Antarctic Ice Sheet from a combined analysis of satellite gravimetry and altimetry data. *Earth and Planetary Science Letters*, *422*, 150–156. https://doi.org/10.1016/j.epsl.2015.03.045

Meredith, M., Sommerkorn, M., Cassotta, S., Derksen, C., Ekaykin, A., Hollowed, A., et al. (2019). Polar Regions. *IPCC special report on the ocean and cryosphere in a changing climate* (pp. 203–320). The Intergovernmental Panel on Climate Change (IPCC).

Pattyn, F. (2010). Antarctic subglacial conditions inferred from a hybrid ice sheet/ice stream model. *Earth and Planetary Science Letters*, *295*(3–4), 451–461. https://doi.org/10.1016/j.epsl.2010.04.025

Richter, A., Horwath, M., & Dietrich, R. (2016). Comment on Zwally and others (2015)—Mass gains of the Antarctic ice sheet exceed losses. *Journal of Glaciology*, *62*(223), 604–606. https://doi.org/10.1017/jog.2016.60

Rignot, E., Mouginot, J., Scheuchl, B., van den Broeke, M., van Wessem, M. J., & Morlighem, M. (2019). Four decades of Antarctic Ice Sheet mass balance from 1979–2017. *Proceedings of the National Academy of Sciences of the United States of America*, *116*(4), 1095–1103. https://doi.org/10.1073/pnas.1812883116

Schröder, L., Horwath, M., Dietrich, R., Helm, V., van den Broeke, M. R., & Ligtenberg, S. R. M. (2019a). Four decades of Antarctic surface elevation changes from multi-mission satellite altimetry. *The Cryosphere*, *13*(2), 427–449. https://doi.org/10.5194/tc-13-427-2019

Schröder, L., Horwath, M., Dietrich, R., Helm, V., van den Broeke, M. R., & Ligtenberg, S. R. M. (2019b). Gridded surface elevation changes from multi-mission satellite altimetry 1978-2017. *PANGAEA*. https://doi.org/10.1594/PANGAEA.897390

Schröder, L., Richter, A., Fedorov, D. V., Eberlein, L., Brovkov, E. V., Popov, S. V., et al. (2017). Validation of satellite altimetry by kinematic GNSS in central East Antarctica. *The Cryosphere*, *11*(3), 1111–1130. https://doi.org/10.5194/tc-11-1111-2017

AGU ADVANCING EARTH AND SPACE SCIENCE

Journal of Geophysical Research: Earth Surface 10.1029/2020JF005966

Seroussi, H., Ivins, E. R., Wiens, D. A., & Bondzio, J. (2017). Influence of a West Antarctic mantle plume on ice sheet basal conditions. *Journal of Geophysical Research: Solid Earth*, *122*, 7127–7155. https://doi.org/10.1002/2017JB014423

Shepherd, A., Ivins, E., Rignot, E., Smith, B., van den Broeke, M., Velicogna, I., & Wouters, B. (2018). Mass balance of the Antarctic Ice Sheet from 1992 to 2017. *Nature*, *558*(7709), 219–222. https://doi.org/10.1038/s41586-018-0179-y

Strößenreuther, U., Horwath, M., & Schröder, L. (2020). How different analysis and interpolation methods affect the accuracy of ice surface elevation changes inferred from satellite altimetry. *Mathematical Geosciences*, *52*, 499–525. https://doi.org/10.1007/s11004-019-09851-3

Sun, Y., Riva, R., & Ditmar, P. (2016). Optimizing estimates of annual variations and trends in geocenter motion and J^2 from a combination of GRACE data and geophysical models. *Journal of Geophysical Research: Solid Earth*, *121*(11), 8352–8370. https://doi.org/10.1002/2016JB013073

Swenson, S., Chambers, D., & Wahr, J. (2008). Estimating geocenter variations from a combination of GRACE and ocean model output. *Journal of Geophysical Research*, *113*, B08410. https://doi.org/10.1029/2007JB005338

Thomas, E. R., van Wessem, J. M., Roberts, J., Isaksson, E., Schlosser, E., Fudge, T. J., et al. (2017). Regional Antarctic snow accumulation over the past 1000 years. *Climate of the Past*, *13*(11), 1491–1513. https://doi.org/10.5194/cp-13-1491-2017

van den Broeke, M., Bamber, J., Ettema, J., Rignot, E., Schrama, E., van de Berg, W. J., et al. (2009). Partitioning recent Greenland mass loss. *Science*, *326*(5955), 984–986. https://doi.org/10.1126/science.1178176

van Wessem, J. M., van de Berg, W. J., Noël, B. P. Y., van Meijgaard, E., Amory, C., Birnbaum, G., et al. (2018). Modeling the climate and surface mass balance of polar ice sheets using RACMO2—Part 2: Antarctica (1979–2016). *The Cryosphere*, *12*(4), 1479–1498. https://doi.org/10.5194/tc-12-1479-2018

Wahr, J., Wingham, D., & Bentley, C. (2000). A method of combining ICESat and GRACE satellite data to constrain Antarctic mass balance. *Journal of Geophysical Research*, *105*(B7), 16279–16294. https://doi.org/10.1029/2000JB900113

Whitehouse, P. L., Gomez, N., King, M. A., & Wiens, D. A. (2019). Solid Earth change and the evolution of the Antarctic Ice Sheet. *Nature Communications*, *10*(1). https://doi.org/10.1038/s41467-018-08068-y

Willen, M. O., Broerse, T., Groh, A., Wouters, B., Kuipers Munneke, P., Horwath, M., et al. (2021). Mass and volume time series of Antarctic drainage systems derived by a coupled state space analysis of satellite observations and model products. *PANGAEA*. https://doi.org/10.1594/PANGAEA.930250

Willen, M. O., Horwath, M., Schröder, L., Groh, A., Ligtenberg, S. R. M., Kuipers Munneke, P., & van den Broeke, M. R. (2020). Sensitivity of inverse glacial isostatic adjustment estimates over Antarctica. *The Cryosphere*, *14*(1), 349–366. https://doi.org/10.5194/tc-14-349-2020

Wouters, B., Martín-Español, A., Helm, V., Flament, T., van Wessem, J. M., Ligtenberg, S. R. M., et al. (2015). Dynamic thinning of glaciers on the Southern Antarctic Peninsula. *Science*, *348*(6237), 899–903. https://doi.org/10.1126/science.aaa5727

Zammit-Mangion, A., Rougier, J., Schön, N., Lindgren, F., & Bamber, J. (2015). Multivariate spatio-temporal modeling for assessing Antarctica's present-day contribution to sea-level rise. *Environmetrics*, *26*(3), 159–177. https://doi.org/10.1002/env.2323

Zwally, H., Giovinetto, M., Beckley, M., & Saba, J. (2012). *Antarctic and Greenland drainage systems*. GSFC Cryospheric Sciences Laboratory. Retrieved from https://earth.gsfc.nasa.gov/cryo/data/polar-altimetry/antarctic-and-greenland-drainage-systems

Zwally, H. J., Li, J., Robbins, J. W., Saba, J. L., Yi, D., & Brenner, A. C. (2015). Mass gains of the Antarctic ice sheet exceed losses. *Journal of Glaciology*, *61*(230), 1019–1036. https://doi.org/10.3189/2015JoG15J071

Journal of Geodesy (2022) 96:75
https://doi.org/10.1007/s00190-022-01651-8

ORIGINAL ARTICLE

Feasibility of a global inversion for spatially resolved glacial isostatic adjustment and ice sheet mass changes proven in simulation experiments

Matthias O. Willen[1] · **Martin Horwath**[1] · **Andreas Groh**[1] · **Veit Helm**[2] · **Bernd Uebbing**[3] · **Jürgen Kusche**[3]

Received: 28 August 2021 / Accepted: 3 August 2022 / Published online: 10 October 2022

Abstract

Estimating mass changes of ice sheets or of the global ocean from satellite gravimetry strongly depends on the correction for the glacial isostatic adjustment (GIA) signal. However, geophysical GIA models are different and incompatible with observations, particularly in Antarctica. Regional inversions have resolved GIA over Antarctica without ensuring global consistency, while global inversions have been mostly constrained by a priori GIA patterns. For the first time, we set up a global inversion to simultaneously estimate ice sheet mass changes and GIA, where Antarctic GIA is spatially resolved using a set of global GIA patterns. The patterns are related to deglaciation impulses localized along a grid over Antarctica. GIA associated with four regions outside Antarctica is parametrized by global GIA patterns induced by deglaciation histories. The observations we consider here are satellite gravimetry, satellite altimetry over Antarctica and Greenland, as well as modelled firn thickness changes. Firn thickness changes are also parametrized to account for systematic errors in their modelling. Results from simulation experiments using realistic signals and error covariances support the feasibility of the approach. For example, the spatial RMS error of the estimated Antarctic GIA effect, assuming a 10-year observation period, is 31% and 51%, of the RMS of two alternative global GIA models. The integrated Antarctic GIA error is 8% and 5%, respectively, of the integrated GIA signal of the two models. For these results realistic error covariances incorporated in the parameter estimation process are essential. If error correlations are neglected, the Antarctic GIA RMS error is more than twice as large.

Highlights

- We present a globally consistent inversion approach to co-estimate glacial isostatic adjustment effects together with changes of the ice mass and firn air content in Greenland and Antarctica.
- The inversion method utilizes data sets from satellite gravimetry, satellite altimetry, regional climate modelling, and firn modelling together with the full error-covariance information of all input data.
- The simulation experiments show that the proposed GIA parametrization in Antarctica can resolve GIA effects unpredicted by geophysical modelling, despite realistic input-data limitations.

Keywords Satellite geodesy · Ice sheets · Mass balance · Glacial isostatic adjustment

1 Introduction

Ice mass changes (IMCs) of the Greenland ice sheet (GIS) and the Antarctic ice sheet (AIS) are important signs of global climate change. The main causes of IMC are changing surface mass balance (SMB) components (e.g. precipitation, surface melting, sublimation, wind drift) and changing ice flow dynamics (ID). In turn, IMCs induce global mass redistributions in the ocean and induce solid-Earth deformation: the elastic deformation due to present-day IMC and

Matthias O. Willen
matthias.willen@tu-dresden.de

1 Institut für Planetare Geodäsie, Technische Universität Dresden, Dresden, Germany

2 Helmholtz Centre for Polar and Marine Research, Alfred Wegener Institute, Bremerhaven, Germany

3 Institute of Geodesy and Geoinformation, University of Bonn, Bonn, Germany

the viscoelastic deformation due to the isostatic adjustment to past IMC, i.e. the glacial isostatic adjustment (GIA). Satellite gravimetry and satellite altimetry measure these superimposed signals in terms of gravity change and elevation change, respectively, which allow to quantify GIA, IMC, and thereby the contribution of ice sheets to sea level change.

The GIA signals from geophysical forward models disagree significantly due to different assumptions on ice load histories, viscosity profiles (rheology), and the data and methods used to constrain such underlying assumptions (Whitehouse et al. 2019). In Greenland, GIA model outputs, expressed in terms of equivalent surface mass change, vary between $-27\,\mathrm{Gt\,a^{-1}}$ and $+21\,\mathrm{Gt\,a^{-1}}$ according to Shepherd et al. (2019). The ice mass balance estimate of the GIS is $-255 \pm 20\,\mathrm{Gt\,a^{-1}}$ from 2005 to 2015 (Shepherd et al. 2019). GIA forward models in Antarctica vary between $+3\,\mathrm{Gt\,a^{-1}}$ and $+81\,\mathrm{Gt\,a^{-1}}$ according to Shepherd et al. (2018) and from $+40$ to $+80\,\mathrm{Gt\,a^{-1}}$ according to Whitehouse et al. (2019). The ice mass balance of the AIS is $-105 \pm 51\,\mathrm{Gt\,a^{-1}}$ from 2003 until 2010 (Shepherd et al. 2018). In addition, a disagreement in the spatial patterns of GIA forward modelling results is evident to some extent for the GIS (Kappelsberger et al. 2021) and to a large extent for the AIS (Whitehouse et al. 2019). Furthermore, GIA from geophysical modelling would suggest a remarkable difference to GIA-induced bedrock motion observed with GNSS in Antarctica (MartínspsEspañol et al. 2016a) and in Greenland (Bevis et al. 2012; Kappelsberger et al. 2021). This difference raises questions on the rheological properties of the solid Earth. For example, Barletta et al. (2018) showed that the high rates of bedrock motion observed with GNSS in the Amundsen Embayment region can be explained by a GIA effect due to a low mantle viscosity. Such low viscosity implies that the present-day GIA is dominated by the recent decadal to centennial part of the ice loading history which is so far not included in global GIA modelling.

Wu et al. (2010), Rietbroek et al. (2016), and Jiang et al. (2021) demonstrated the inverse determination of GIA using geodetic data in a global framework as an alternative to relying on forward modelling results. Rietbroek et al. (2016) co-estimated GIA in a global inversion framework using GRACE and ocean altimetry data. They used five globally consistent GIA fingerprints from geophysical GIA modelling by Klemann and Martinec (2011) which are based on regional ice histories. Rietbroek et al. (2016) found that the Antarctic a priori fingerprint needed to be downscaled to 18% of the initial fingerprint magnitude to obtain the best fit to the data. The GIA fingerprint of Greenland is scaled to 77% of its original magnitude. As a reason for the downscaling of the prescribed Antarctic GIA pattern, we suspect that the true GIA pattern and the prescribed GIA pattern are incompatible. Thus, the true GIA cannot be effectively resolved by any scaling of the prescribed GIA pattern (cf. Fig. S3). In consequence, the unresolved GIA signals are misattributed as IMC signals and vice versa. Jiang et al. (2021) incorporated the GIA signal-covariance information in a global inversion framework to loosen the dependence on geophysical modelling results and to enable the revealing of GIA effects that are not predicted by geophysical GIA modelling.

In order to derive IMC and GIA over ice sheets without relying on GIA forward models, regional inversions have combined geodetic satellite observations in Antarctica (Riva et al. 2009; Gunter et al. 2014; Martín-Español et al. 2016b; Sasgen et al. 2017; Engels et al. 2018). Gunter et al. (2014) combined satellite gravimetry, altimetry, and climate modelling products and provided regionally robust estimates of IMC and GIA. Engels et al. (2018) built on this approach and, with the additional inclusion of GNSS, determined present-day GIA and IMC with an increased spatial resolution. In contrast, Martín-Español et al. (2016b) applied a statistical modelling approach. In this approach, the authors derived the spatio-temporal characteristics of the signals over the AIS from forward models and quantified the signals in a Bayesian framework using observations from satellite gravimetry, altimetry, and GNSS. These three types of observation are also used in the data combination approach by Sasgen et al. (2017), while this framework allows for determining lateral rheological heterogeneities. These regional inversions presented strategies for obtaining spatially resolved estimates of the present-day GIA effect in Antarctica. However, these approaches cannot simply be utilized in a global inversion framework. One reason is that these approaches implement regional constraints to remove bias in the GIA estimate (Willen et al. 2020).

Here, we present a global inversion framework with the aim to improve the co-estimation of GIA and IMC from satellite observations over ice sheets. This approach incorporates three empirical estimation strategies: First, the approach uses the combination of satellite gravimetry and altimetry with climate and firn modelling products (Gunter et al. 2014). Second, it builds on the estimation, in a global framework, of scaling factors for GIA fingerprints related to the deglaciation of particular regions ('regional GIA fingerprints') (Rietbroek et al. 2016). Finally, the inversion framework makes use of GIA patterns related to localized deglaciation impulses ('local GIA fingerprints') for parametrizing GIA without relying an a priori regional pattern (Sasgen et al. 2017). The GIA parametrization by local GIA fingerprints is applied for GIA associated to Antarctica where GIA patterns from forward models are particularly unreliable, as discussed above. The presented approach combines observations of satellite gravimetry, satellite altimetry over the AIS and the GIS, as well as climate and firn model products over both ice sheets. Furthermore, the approach incorporates a parametrization of volume changes of the ice sheets' firn layer inherent in satellite altimetry observations, in order to accommodate errors of climate and firn modelling results in quantifying these firn volume changes.

We analyse the feasibility of this approach using simulated signals and observations. We investigate the quality of the estimates for ice mass change, firn volume change, and GIA that can be expected depending on the input data quality. For this purpose, we simulate realistic errors of the observations based on error covariances assessed from real data. We perform three simulation experiments: (1) The observations solely contain the geophysical signals without any error. (2) The observations contain the geophysical signals and correlated errors, but we only assume uncorrelated errors in the parameter estimation. (3) The observations contain the geophysical signals and correlated errors. We account for the error covariances in the parameter estimation. We perform these three experiments with two variants of simulated observations. These two variants differ in terms of the GIA model output that is used to generate the observations. To simplify the simulation experiments, we focus on mass effects due to IMC of ice sheets and GIA only and do not investigate the ocean mass change contributors hydrology and glaciers in this study. But eventually in a full inversion evaluating real data, we will make use of a parametrization accounting all contributors (e.g. Rietbroek et al. 2016).

Section 2 introduces the physical quantities and their relation to the observations over the ice sheets. In Sect. 3, we present the methodology of the inversion approach and describe how we set up the simulation environment. We show the results of the simulation experiments in Sect. 4 and discuss them in Sect. 5. The Supplementary Material (SM) provides supporting information.

2 Theoretical background

We express temporal gravity field changes as equivalent surface density changes in a spherical layer (also referred to as area density changes) with the unit of mass per surface area. The surface density change $\Delta\kappa$ at a position $\boldsymbol{x}$ can be developed into a series of spherical harmonic basis functions Y_{nm} of degree n and order m:

$$\Delta\kappa(\boldsymbol{x}) = \sum_{n=0}^{\infty} \sum_{m=-n}^{n} \Delta\kappa_{nm} Y_{nm}(\boldsymbol{x}). \tag{1}$$

Following Wahr et al. (1998), a change of a Stokes coefficient (Δc_{nm}) is converted to the spherical harmonic coefficient of a surface density change

$$\Delta\kappa_{nm} = \frac{2n+1}{1+k'_n} \frac{M_E}{4\pi R^2} \Delta c_{nm}, \tag{2}$$

where M_E is the total mass of the Earth, R the semi-major axis of the reference ellipsoid, and k'_n the load Love number to account for the elastic solid-Earth deformation induced by surface load variations.

We express the temporal change of physical quantities (gravity, mass, volume, etc.) over a certain time period by a mean rate of change over this period. This mean rate is obtained in practice from fitting a linear function to the underlying time series. Although arising from a linear regression, the mean rates do not intend to isolate any intrinsically linear process. Therefore, nonlinear signals contained in the time series are not a source of error for the determination of the mean rates.

Mass redistributions due to GIA in the solid Earth (and to a lesser extent in the ocean) lead to a change of Earth's gravity field, which can be expressed as the equivalent surface density rate $\dot\kappa^{\mathrm{GIA}}$. Likewise, mass changes of ice sheets and the induced ocean mass change and the elastic load deformation of the solid Earth lead to gravity field changes which can be expressed by their equivalent surface mass change $\dot\kappa^{\mathrm{IMC}}$. The surface density rate $\dot\kappa^{\mathrm{TOTAL}}$

$$\dot\kappa^{\mathrm{TOTAL}} = \dot\kappa^{\mathrm{IMC}} + \dot\kappa^{\mathrm{GIA}} + \dot\kappa^{\mathrm{OTHER}}, \tag{3}$$

contains the IMC and GIA effects together with other effects ($\dot\kappa^{\mathrm{OTHER}}$) such as terrestrial water mass changes that we do not consider here, explicitly. Contributions from changing SMB, $\dot\kappa^{\mathrm{SMB}}$, and changing ice dynamics, $\dot\kappa^{\mathrm{ID}}$, induce IMC which can be expressed as the sum of surface density rates in the firn layer ($\dot\kappa^{\mathrm{FIRN}}$) and surface density rates in the ice layer ($\dot\kappa^{\mathrm{ICE}}$) of an ice sheet

$$\dot\kappa^{\mathrm{IMC}} = \dot\kappa^{\mathrm{FIRN}} + \dot\kappa^{\mathrm{ICE}}. \tag{4}$$

For a large part $\dot\kappa^{\mathrm{FIRN}}$ is induced by changing SMB, and $\dot\kappa^{\mathrm{ICE}}$ by changing ice dynamics.

The surface elevation rate over ice sheets, $\dot h^{\mathrm{TOTAL}}$, is the sum of elevation changes in the ice layer ($\dot h^{\mathrm{ICE}}$), firn thickness change ($\dot h^{\mathrm{FIRN}}$), the deformation of the solid Earth surface (bedrock motion) due to GIA ($\dot h^{\mathrm{GIA}}$) as well as the elastic-induced bedrock motion due to present-day load variations ($\dot h^{\mathrm{ELA}}$):

$$\dot h^{\mathrm{TOTAL}} = \dot h^{\mathrm{ICE}} + \dot h^{\mathrm{FIRN}} + \dot h^{\mathrm{GIA}} + \dot h^{\mathrm{ELA}}. \tag{5}$$

Analogous to $\dot\kappa^{\mathrm{ICE}}$, $\dot h^{\mathrm{ICE}}$ is for a large part due to changing ice dynamics. The density of pure ice ($\rho^{\mathrm{ICE}} = 917\,\mathrm{kg\,m^{-3}}$) links changes of the surface elevation in the ice layer $\dot h^{\mathrm{ICE}}$ and of the surface density $\dot\kappa^{\mathrm{ICE}}$:

$$\dot h^{\mathrm{ICE}} = \frac{\dot\kappa^{\mathrm{ICE}}}{\rho^{\mathrm{ICE}}}. \tag{6}$$

The firn thickness change $\dot{h}^{\mathrm{FIRN}}$ and the surface density rate in the firn layer $\dot{\kappa}^{\mathrm{FIRN}}$ can be related by a firn density ρ^{FIRN}:

$$\dot{h}^{\mathrm{FIRN}} = \frac{\dot{\kappa}^{\mathrm{FIRN}}}{\rho^{\mathrm{FIRN}}}. \tag{7}$$

Alternatively, volume changes of the ice sheet's firn layer can be described using changes of the firn air content (FAC) $\dot{h}^{\mathrm{FAC}}$ (Ligtenberg et al. 2014). This enables the avoidance of the firn density. Instead of Eq. 7 we can write

$$\dot{h}^{\mathrm{FIRN}} = \frac{\dot{\kappa}^{\mathrm{FIRN}}}{\rho^{\mathrm{ICE}}} + \dot{h}^{\mathrm{FAC}}. \tag{8}$$

We can rewrite Eq. 5 as

$$\dot{h}^{\mathrm{TOTAL}} = \dot{h}^{\mathrm{IMC}} + \dot{h}^{\mathrm{FAC}} + \dot{h}^{\mathrm{GIA}} + \dot{h}^{\mathrm{ELA}}, \tag{9}$$

where

$$\dot{h}^{\mathrm{IMC}} = \frac{\dot{\kappa}^{\mathrm{IMC}}}{\rho^{\mathrm{ICE}}} = \frac{\dot{\kappa}^{\mathrm{FIRN}} + \dot{\kappa}^{\mathrm{ICE}}}{\rho^{\mathrm{ICE}}} = \frac{\dot{\kappa}^{\mathrm{FIRN}}}{\rho^{\mathrm{ICE}}} + \dot{h}^{\mathrm{ICE}}. \tag{10}$$

3 Materials and methods

3.1 Inversion approach

Our aim is to jointly estimate GIA and IMC for both ice sheets (GIS and AIS) from satellite gravimetry and satellite altimetry. Unlike other combination strategies (e.g. Gunter et al. 2014), we do not suggest to address the effect of firn processes in the altimetry observations by correcting for modelled firn thickness changes in a deterministic manner. Instead, we use modelled FAC as an additional observation subject to uncertainties, and we co-estimate FAC jointly with GIA and IMC.

We set up a *Gauss–Markov-model* (or *general linear model* or *general regression model*) (e.g. Koch 1999),

$$\boldsymbol{d} + \boldsymbol{e} = \boldsymbol{X}\boldsymbol{\beta} \quad \text{with} \quad C(\boldsymbol{d}) = \sigma^2 \boldsymbol{P}^{-1}, \tag{11}$$

where the observations assembled in the vector $\boldsymbol{d}$ are linked to the sought-for parameters assembled in the vector $\boldsymbol{\beta}$ by the design matrix $\boldsymbol{X}$. The vector $\boldsymbol{e}$ contains the residuals, $C(\boldsymbol{d})$ is the covariance matrix of the observation errors, $\boldsymbol{P}$ is the weight matrix and σ^2 is the factor of unit weight. The estimate $\hat{\boldsymbol{\beta}}$ of the parameters $\boldsymbol{\beta}$ and the error covariance of the estimate $C(\hat{\boldsymbol{\beta}})$ are calculated by *generalized least squares adjustment* (e.g. Koch 1999) as

$$\hat{\boldsymbol{\beta}} = (\boldsymbol{X}^{\mathrm{T}}\boldsymbol{P}\boldsymbol{X})^{-1}\boldsymbol{X}^{\mathrm{T}}\boldsymbol{P}\boldsymbol{d} \quad \text{and} \quad C(\hat{\boldsymbol{\beta}}) = \sigma^2(\boldsymbol{X}^{\mathrm{T}}\boldsymbol{P}\boldsymbol{X})^{-1}. \tag{12}$$

More specifically, the observation vector $\boldsymbol{d}$ assembles the following observations subject to errors $\boldsymbol{\varepsilon}$: satellite gravimetry data,

$$\boldsymbol{d}^{\mathrm{GRAV}} = F^{\mathrm{GRAV}}(\dot{\kappa}^{\mathrm{TOTAL}}) + \boldsymbol{\varepsilon}^{\mathrm{GRAV}}, \tag{13}$$

represented as a set of spherical harmonic coefficients of surface mass density change and containing the superimposed signals according to (3). F^{GRAV} is the forward operator, that maps the signal $\dot{\kappa}^{\mathrm{TOTAL}}$ into the discrete gravimetry observations. The ice-sheet surface elevation changes observed by altimetry with the altimetry forward operator F^{ALT},

$$\boldsymbol{d}^{\mathrm{ALT}} = F^{\mathrm{ALT}}(\dot{h}^{\mathrm{TOTAL}}) + \boldsymbol{\varepsilon}^{\mathrm{ALT}}, \tag{14}$$

are expressed in spatial grids covering the ice sheets and contain the superimposed signals according to (5) and (9). The modelled FAC changes with the forward operator F^{FAC},

$$\boldsymbol{d}^{\mathrm{FAC}} = F^{\mathrm{FAC}}(\dot{h}^{\mathrm{FAC}}) + \boldsymbol{\varepsilon}^{\mathrm{FAC}}, \tag{15}$$

are likewise expressed in grids over the ice sheets and contain the signal expressed by (8).

The parameter vector $\boldsymbol{\beta}$ contains parameters related to GIA ($\boldsymbol{\beta}^{\mathrm{GIA}}$), to IMC ($\boldsymbol{\beta}^{\mathrm{IMC}}$) and to FAC ($\boldsymbol{\beta}^{\mathrm{FAC}}$). An additional distinction of parts related exclusively to the AIS or the GIS is indicated by according superscripts and subscripts. Hence, the observation equation (11) reads

$$\begin{pmatrix} \boldsymbol{d}^{\mathrm{GRAV}} \\ \boldsymbol{d}^{\mathrm{GIS\text{-}ALT}} \\ \boldsymbol{d}^{\mathrm{GIS\text{-}FAC}} \\ \boldsymbol{d}^{\mathrm{AIS\text{-}ALT}} \\ \boldsymbol{d}^{\mathrm{AIS\text{-}FAC}} \end{pmatrix} + \boldsymbol{e}
= \begin{pmatrix}
\boldsymbol{X}^{\mathrm{GRAV}}_{\mathrm{GIA}} & \boldsymbol{X}^{\mathrm{GRAV}}_{\mathrm{GIS\text{-}IMC}} & \boldsymbol{0} & \boldsymbol{X}^{\mathrm{GRAV}}_{\mathrm{AIS\text{-}IMC}} & \boldsymbol{0} \\
\boldsymbol{X}^{\mathrm{GIS\text{-}ALT}}_{\mathrm{GIA}} & \boldsymbol{X}^{\mathrm{GIS\text{-}ALT}}_{\mathrm{GIS\text{-}IMC}} & \boldsymbol{X}^{\mathrm{GIS\text{-}ALT}}_{\mathrm{GIS\text{-}FAC}} & \boldsymbol{X}^{\mathrm{GIS\text{-}ALT}}_{\mathrm{AIS\text{-}IMC}} & \boldsymbol{0} \\
\boldsymbol{0} & \boldsymbol{0} & \boldsymbol{X}^{\mathrm{GIS\text{-}FAC}}_{\mathrm{GIS\text{-}FAC}} & \boldsymbol{0} & \boldsymbol{0} \\
\boldsymbol{X}^{\mathrm{AIS\text{-}ALT}}_{\mathrm{GIA}} & \boldsymbol{X}^{\mathrm{AIS\text{-}ALT}}_{\mathrm{GIS\text{-}IMC}} & \boldsymbol{0} & \boldsymbol{X}^{\mathrm{AIS\text{-}ALT}}_{\mathrm{AIS\text{-}IMC}} & \boldsymbol{X}^{\mathrm{AIS\text{-}ALT}}_{\mathrm{AIS\text{-}FAC}} \\
\boldsymbol{0} & \boldsymbol{0} & \boldsymbol{0} & \boldsymbol{0} & \boldsymbol{X}^{\mathrm{AIS\text{-}FAC}}_{\mathrm{AIS\text{-}FAC}}
\end{pmatrix}
\cdot \begin{pmatrix} \boldsymbol{\beta}_{\mathrm{GIA}} \\ \boldsymbol{\beta}_{\mathrm{GIS\text{-}IMC}} \\ \boldsymbol{\beta}_{\mathrm{GIS\text{-}FAC}} \\ \boldsymbol{\beta}_{\mathrm{AIS\text{-}IMC}} \\ \boldsymbol{\beta}_{\mathrm{AIS\text{-}FAC}} \end{pmatrix}. \tag{16}$$

We describe the parametrization and the setup of the design matrix in Sect. 3.2. The description of the simulated observations and their error covariance information follows in Sects. 3.3 and 3.4, respectively.

3.2 Parametrization of signals

Glacial isostatic adjustment (GIA) Rietbroek et al. (2016) and Sun and Riva (2020) demonstrated that fitting globally consistent fingerprints from GIA forward modelling to GRACE observations in a global inversion framework represents a promising strategy to estimate the GIA signal. However, as mentioned in Sect. 1, the GIA signal predicted by geophysical models over Antarctica is uncertain (Shepherd et al. 2018; Whitehouse et al. 2019). Whitehouse et al. (2019) showed that not just the magnitude but also the spatial pattern of several GIA modelling results varies significantly (Fig. 2 therein). The GIA patterns predicted by different models are so different that scaling of one pattern cannot reproduce another pattern. Moreover, we showed in a test experiment that scaling a pattern inferred from a single GIA model is inappropriate to resolve the pattern predicted by an another GIA model (cf. Fig. S3). Albeit Rietbroek et al. (2016) implemented a single Antarctic GIA pattern that disagrees with GNSS observations for large parts (Thomas et al. 2011). We suspect that using a single Antarctic GIA fingerprint with inherent modelling errors—as done by Rietbroek et al. (2016)—might be insufficient to resolve discrepancies between observations and model predictions. This presumably leads to the significant damping of the Antarctic GIA fingerprint in the inversion results. Here, we propose an extension of the fingerprint parametrization for Antarctica. In case of Greenland, we argue that the parametrization using a single fingerprint is appropriate, because the GIA pattern does not need to be scaled as extensively to fit the data in Rietbroek et al. (2016). Thus, we apply two methodological approaches of either a more model-independent (AIS) or a more model-dependent (GIS) GIA parametrization.

We parametrize GIA due to Antarctic glacial history based on B globally consistent GIA patterns. Each pattern is based on a generic glacial history at a single position represented by a disk-shaped element on the Tegmark-grid (Tegmark 1996) used by the SELEN software (Spada and Melini 2019). The glacial history is a step function in time where at 10 ka before present an ice column is removed. This timing is motivated by the approximate beginning of the Holocene. For the generic glacial 'impulses' defined this way we model the globally consistent viscoelastic response with the SELEN software. These resulting GIA responses may be interpreted as 'GIA mascons' or 'globally consistent GIA radial-like basis functions'. The shape of the GIA response to a deglaciation impulse is similar to a Gaussian function ("bell curve") with a half response radius and one-sigma radius of ∼300 and ∼250 km, respectively (Fig. 1). The choice of the generic deglaciation history and the rheology could be chosen within wide limits, they induce patterns of present-day GIA gravity field rates and bedrock motion rates that are similar to patterns induced by different rheology and different deglaciation histories, limited to the same local deglaciation source. Therefore, the parametrized patterns may capture a large range of realistic GIA signals.

We considered those AIS nodes of the Tegmark grid that have an ice layer in the ICE-6G glacial history leading to a full coverage of the Antarctic continent. We assume that the ICE-6G glaciation history does not miss any larger regions of deglaciation since the last glacial maximum. To reduce the parameter space, we decimate the grid to an approximate

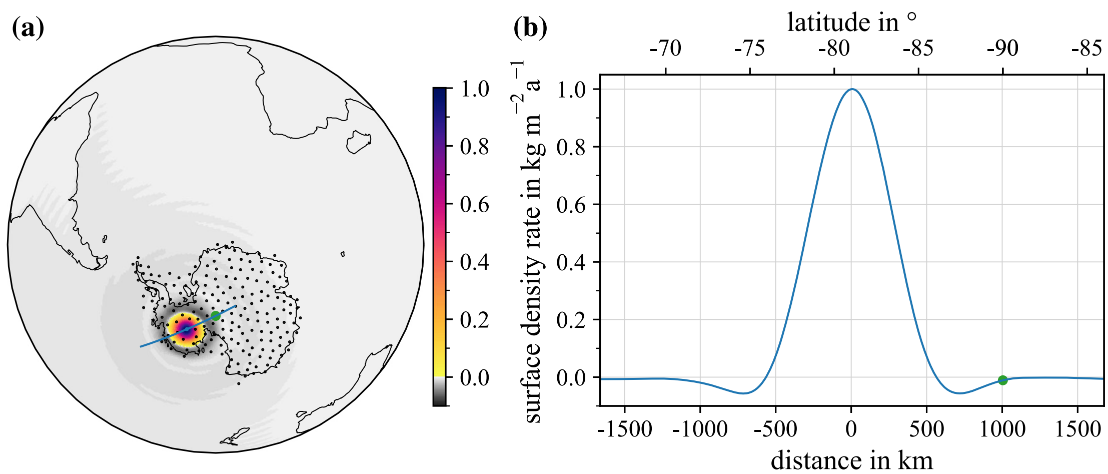

Fig. 1 **a** The global pattern of the present-day GIA effect of a generic ice history at one position in Antarctica, i.e. the normalized deglaciation impulse response. The blue line indicates the section shown in (**b**). Globally consistent GIA patterns were calculated for all highlighted positions (black dots). **b** The section of the GIA pattern along a part of the meridian of the deglaciation impulse centre shown in (**a**). The lower x-axis is the ellipsoidal distance along the meridian from the centre of the deglaciation impulse. The upper x-axis is the latitude along the meridian. The green point in (**a, b**) highlights the South Pole

spacing of 250 km, justified by the shape of the response functions. Thus we obtain $B = 189$ Antarctic GIA parameters related to 189 positions shown in Fig. 1a. Section 5 provides further discussion of the chosen properties of these GIA patterns.

Outside Antarctica, we parametrize GIA due to the glacial history in Greenland, Laurentia, Fennoskandia, and other regions (Patagonia, Barents and Kara Sea, etc., referred to as Other) by 4 fingerprints from forward modelling similar to fingerprints from Klemann and Martinec (2011) used in Rietbroek et al. (2016). We generate these fingerprints by GIA forward modelling using the SELEN software package (Spada and Melini 2019). We isolated the ICE-6G glacial history (Stuhne and Peltier 2015) for each region and model the GIA signal which would result solely from the loading variation in the selected regions. All model runs use the Green's function based on VM5a rheology included in the SELEN software package. Caron et al. (2018) found that the C_{21}-S_{21}-pattern of their optimized GIA result differed systematically from the modelling result by Purcell et al. (2016) which is based on the ICE-6G ice history with VM5a rheology (Figure S2 in Caron et al. 2018). Caron et al. (2018) attribute this difference in the rotational feedback to an underestimated mantle viscosity in their GIA result. We additionally include 2 fingerprints (one for C_{21} and one for S_{21}) to capture a potential residual GIA-induced rotational feedback component that the other fingerprints do not account for.

The GIA parameters $\boldsymbol{\beta}_{\text{GIA}}$ are scaling factors for each of the $B + 6$ prescribed global GIA patterns: B local Antarctic patterns, 4 regional patterns, and 2 polar motion patterns. With $\boldsymbol{\xi}_1 \dots \boldsymbol{\xi}_{B+6}$ denoting the representation of these patterns in terms of the SH coefficients of the equivalent surface density trends, the block of the design matrix $\boldsymbol{X}_{\text{GIA}}^{\text{GRAV}}$ that links satellite gravimetry observations to GIA is

$$\boldsymbol{X}_{\text{GIA}}^{\text{GRAV}} = \left(\boldsymbol{\xi}_1 \; \boldsymbol{\xi}_2 \dots \boldsymbol{\xi}_{B+6}\right). \tag{17}$$

The blocks of the design matrix $\boldsymbol{X}_{\text{GIA}}^{\text{AIS-ALT}}$ and $\boldsymbol{X}_{\text{GIA}}^{\text{GIS-ALT}}$ that link observed surface elevation changes to the parametrized GIA patterns realize the evaluation of GIA-induced bedrock motion in the spatial domain at the positions of the AIS and GIS grid nodes. For this purpose, the modelling results from SELEN, representing the present-day geometric changes, are used.

Hence, each row of $\boldsymbol{X}_{\text{GIA}}^{\text{AIS-ALT}}$ (and $\boldsymbol{X}_{\text{GIA}}^{\text{GIS-ALT}}$, respectively) contains the $B + 6$ parametrized bedrock-motion GIA patterns evaluated at the grid position to which the row refers.

Once the GIA parameters are estimated as $\hat{\beta}_1^{\text{GIA}} \dots \hat{\beta}_{B+6}^{\text{GIA}}$, the estimated GIA signal at a position $\boldsymbol{x}$ is the weighted superposition of the GIA patterns:

$$\hat{\kappa}^{\text{GIA}}(\boldsymbol{x}) = \sum_{b=1}^{B+6} \hat{\beta}_b^{\text{GIA}} \, \xi_b(\boldsymbol{x}). \tag{18}$$

We use the software SELEN[4] (Spada and Melini 2019) for the computation, because it is a publicly available open-source program and allows the gravitationally and topographically self-consistent solving of the sea level equation. Furthermore, the rotational feedback and the migration of shorelines are taken into account. So far, a 1-D Maxwell rheological profile is used.

We perform test experiments to demonstrate to what extent the GIA parametrization is suitable to reproduce GIA signals induced by different glacial histories and different Earth rheologies (Figs. S2–S5). The first test experiment uses a global GIA signal that we model in the similar environment as we use it for generating the GIA parameters, i.e. the SELEN software run by ICE-6G ice history and VM5a rheology. In the second and third experiment, we fit the parameters to the present-day GIA signal from Caron et al. (2018). We can resolve the GIA signal when we include the C_{21} and S_{21} fingerprints demonstrated by the second test experiment (Fig. S3). However, in the third test experiment we exclude the C_{21} and S_{21} fingerprints to demonstrate their necessity. Doing so, we could only partly resolve the original GIA signal due to discrepancies of the C_{21} and S_{21} coefficients between the GIA model from Caron et al. (2018) and the parametrization (Fig. S4c, Figure S2 in Caron et al. 2018). The fourth test experiment is a regional fit in the spatial domain of the present-day GIA signal found by Barletta et al. (2018).

Ice mass change (IMC) We parametrize IMC based on two grids in Greenland and Antarctica. The grids are located over the grounded ice sheets with a resolution of 50 km × 50 km using the polar stereographic projections EPSG:3413 and EPSG:3031 for GIS and AIS, respectively. This resolution allows a spatially resolved estimation of IMC, similar to other GRACE-derived products (Groh and Horwath 2021) and is not computationally expensive. We assign a mass change to each grid cell i with an area A. This mass change is transferred to the spherical-harmonic domain by assuming this mass change is concentrated in a point (Pollack 1973). This is done up to the maximum degree of 96 according to how GRACE monthly gravity fields are provided (e.g. Mayer-Gürr et al. 2018). We solve the sea level equation (Farrell and Clark 1976) for each mass change to ensure mass conservation in the Earth system. Thereby, we assume the ice sheets only exchange mass with the ocean. The globally consistent set of spherical harmonic coefficients related to the i-th point mass is $\boldsymbol{\psi}_i$. Furthermore, each $\boldsymbol{\psi}_i$ can be transferred in the spatial domain.

The matrix blocks of the design matrix which link the gravimetry observations to the IMC-induced surface density rate are $\boldsymbol{X}_{\text{GIS-IMC}}^{\text{GRAV}}$ and $\boldsymbol{X}_{\text{AIS-IMC}}^{\text{GRAV}}$, each with a number of columns equal to the number of grid cells either in Greenland u or

Antarctica v:

$$\begin{aligned} \boldsymbol{X}_{\text{GIS-IMC}}^{\text{GRAV}} &= \left(\boldsymbol{\psi}_1\ \boldsymbol{\psi}_2 \ldots \boldsymbol{\psi}_u\right) \\ \boldsymbol{X}_{\text{AIS-IMC}}^{\text{GRAV}} &= \left(\boldsymbol{\psi}_1\ \boldsymbol{\psi}_2 \ldots \boldsymbol{\psi}_v\right). \end{aligned} \tag{19}$$

$\boldsymbol{X}_{\text{GIS-IMC}}^{\text{GIS-ALT}}$ and $\boldsymbol{X}_{\text{AIS-IMC}}^{\text{AIS-ALT}}$ link the satellite altimetry observations of the indicated ice sheet to the surface elevation change caused by IMC and to the IMC-induced elastic deformation. Note that we retrieve the elastic pattern of the mass change in each pixel by solving the sea level equation up to degree 400 to obtain the intended altimetry resolution of 50 km (Sect. 3.3). $\boldsymbol{X}_{\text{AIS-IMC}}^{\text{GIS-ALT}}$ and $\boldsymbol{X}_{\text{GIS-IMC}}^{\text{AIS-ALT}}$ formally account for the global elastic effect of AIS IMC on the altimetry observations over GIS and vice versa. Note that these effects are negligibly small.

The parameter being estimated is the scaling factor of the mass rate in each grid cell i ($\hat{\beta}_i^{\text{IMC}}$). Assuming a mass rate of $1\,\text{kg}\,\text{a}^{-1}$, we can write

$$\hat{\beta}_i^{\text{IMC}} \cdot 1\,\text{kg}\,\text{a}^{-1} = \hat{\dot{\kappa}}_i^{\text{IMC}} A_i. \tag{20}$$

Firn Air Content (FAC) Similar to IMC, we use two grids over the grounded ice sheets in Greenland and Antarctica to parametrize FAC. The blocks of the design matrix which link the altimetry observations to changes of FAC ($\boldsymbol{X}_{\text{GIS-FAC}}^{\text{GIS-ALT}}$ and $\boldsymbol{X}_{\text{GIS-FAC}}^{\text{GIS-ALT}}$) are identity matrices here, because we use the same grids for the observations and parametrization (cf. Sect. 3.3). Likewise $\boldsymbol{X}_{\text{GIS-FAC}}^{\text{GIS-FAC}}$ and $\boldsymbol{X}_{\text{AIS-FAC}}^{\text{AIS-FAC}}$ are identity matrices.

The parameter being estimated is the scaling factor of the FAC-related elevation rate in the grid cell i ($\hat{\beta}_i^{\text{FAC}}$). Assuming an elevation rate of $1\,\text{m}\,\text{a}^{-1}$, we can write

$$\hat{\beta}_i^{\text{FAC}} \cdot 1\,\text{m}\,\text{a}^{-1} = \hat{\dot{h}}_i^{\text{FAC}}. \tag{21}$$

3.3 Synthetic signals and observables

In this section, we describe the synthetic environment we use for the simulation experiments. To this end, we generate synthetic signals, i.e. mean rates over a 10-year period for GIA, IMC (ID and SMB), and FAC, which represent the synthetic true signals in our investigations (Fig. 2). We choose a 10-year period according to the availability of real data sets (cf. Sect. 5.1). From those signals we compute observations (Fig. 3). We simulate satellite gravimetry observations and satellite altimetry observations. Additionally we use products from regional climate and firn modelling to simulate pseudo-observations for FAC. We use the same grids for altimetry and FAC observations and for the IMC and FAC parametrization (Sect. 3.2).

We generate the synthetic GIA signal (Fig. 2a+g) for the first variant of observations (variant A) by forward modelling using SELEN with the ICE-6G glacial history (Spada and Melini 2019). The Stokes coefficients are converted to coefficients of surface densities using Eq. 2. The model output of the bedrock motion expressed by its spherical harmonic coefficients is transferred into the spatial domain. For the second variant of observations (variant B), we use the GIA modelling output from Caron et al. (2018) which represents an alternative GIA model derived from a different modelling environment.

The RACMO2 SMB modelling product (Noël et al. 2018; van Wessem et al. 2018) is the basis to compute $\dot{\kappa}^{\text{SMB}}$. We estimate changes of the SMB with respect to a reference period. We choose the whole modelling period from Jan 1979 to Dec 2016 as the reference period. This is consistent with the reference period of the IMAU-FDM firn thickness change product (Ligtenberg et al. 2011). We remove the mean SMB over this reference period from the SMB values to calculate the surface mass balance anomalies and we cumulate the anomalies, which is referred to as cumulated SMB anomalies. We define $\dot{\kappa}^{\text{SMB}}$ (Fig. 2c+i) as the least-squares estimated rate of cumulated SMB anomalies from Jan 2003 until Dec 2012. The rate of the SMB-driven contribution to the mass balances obtained in this way is $-163\,\text{Gt}\,\text{a}^{-1}$ (GIS) and $-6\,\text{Gt}\,\text{a}^{-1}$ (AIS).

Similarly, we obtain $\dot{h}^{\text{FIRN}}$ from the IMAU-FDM firn thickness change product (Ligtenberg et al. 2011). $\dot{h}^{\text{FIRN}}$ (Fig. 2d+j) is the least-squares estimated rate of the firn-thickness change time series from Jan 2003 until Dec 2012. We obtain FAC (Fig. 2e+k) from $\dot{\kappa}^{\text{SMB}}$ and $\dot{h}^{\text{FIRN}}$ following Eq. 8. In result, the simulated volume rate of the FAC is $-289\,\text{km}^3\text{a}^{-1}$ and $-10\,\text{km}^3\text{a}^{-1}$ for the GIS and the AIS, respectively.

The synthetic ID signal (Fig. 2b+h) is obtained from altimetry observations over ice sheets. We use the linear surface elevation rates from altimetry observations (Schröder et al. 2019; Strößenreuther et al. 2020) to define these signals with a minimum threshold of $0.05\,\text{m}\,\text{a}^{-1}$ of the absolute value of the observed surface elevation rate. Additionally in Antarctica, we apply a mask based on McMillan et al. (2014) to define regions where we assume ID-driven mass changes. In Greenland, we apply a mask based on ice flow velocities from Joughin et al. (2018) and use a minimum threshold of $1\,\text{m}\,\text{a}^{-1}$ to define regions where we assume ID-driven mass changes. We use ρ^{ICE} of $917\,\text{kg}\,\text{m}^{-3}$ to convert surface elevation rates into surface density rates. The simulated rates of the ID-driven contribution to the mass balances are $-79\,\text{Gt}\,\text{a}^{-1}$ (GIS) and $-109\,\text{Gt}\,\text{a}^{-1}$ (AIS). The obtained total rate of IMC is $-243\,\text{Gt}\,\text{a}^{-1}$ (GIS) and $-115\,\text{Gt}\,\text{a}^{-1}$ (AIS).

To simulate gravimetry observations (Fig. 3a+g), we generate spherical harmonic coefficients of the surface density rate in $\text{kg}\,\text{m}^{-2}\,\text{a}^{-1}$ up to degree and order 96 according to a typical GRACE level 2 product (e.g. Mayer-Gürr et al. 2018) which allows a theoretical resolution up to approximately 208 km. To do so, we generate globally consistent coefficients

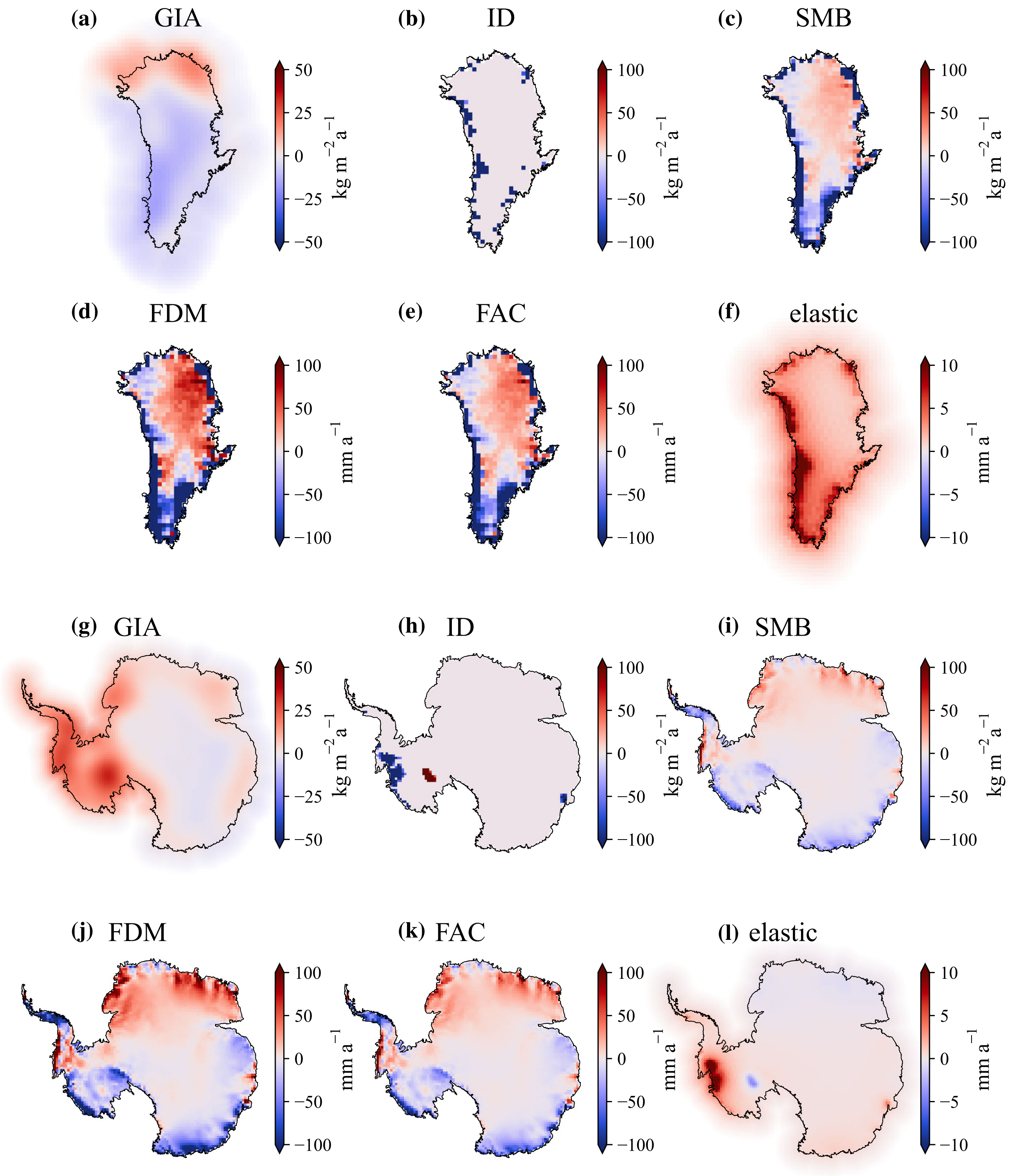

Fig. 2 The synthetic signals for GIS (**a–f**) and AIS (**g–l**) used for variant A of synthetic observations: bedrock motion due to glacial isostatic adjustment (GIA), surface density change due to ice dynamics (ID), surface density change due to surface mass balance (SMB), elevation change due to firn thickness change from firn densification modelling (FDM), the rate of the firn air content (FAC), and the elastic signal due to surface load changes. Figure S1 illustrates the GIA signal from Caron et al. (2018) which we use for generating variant B of synthetic observations

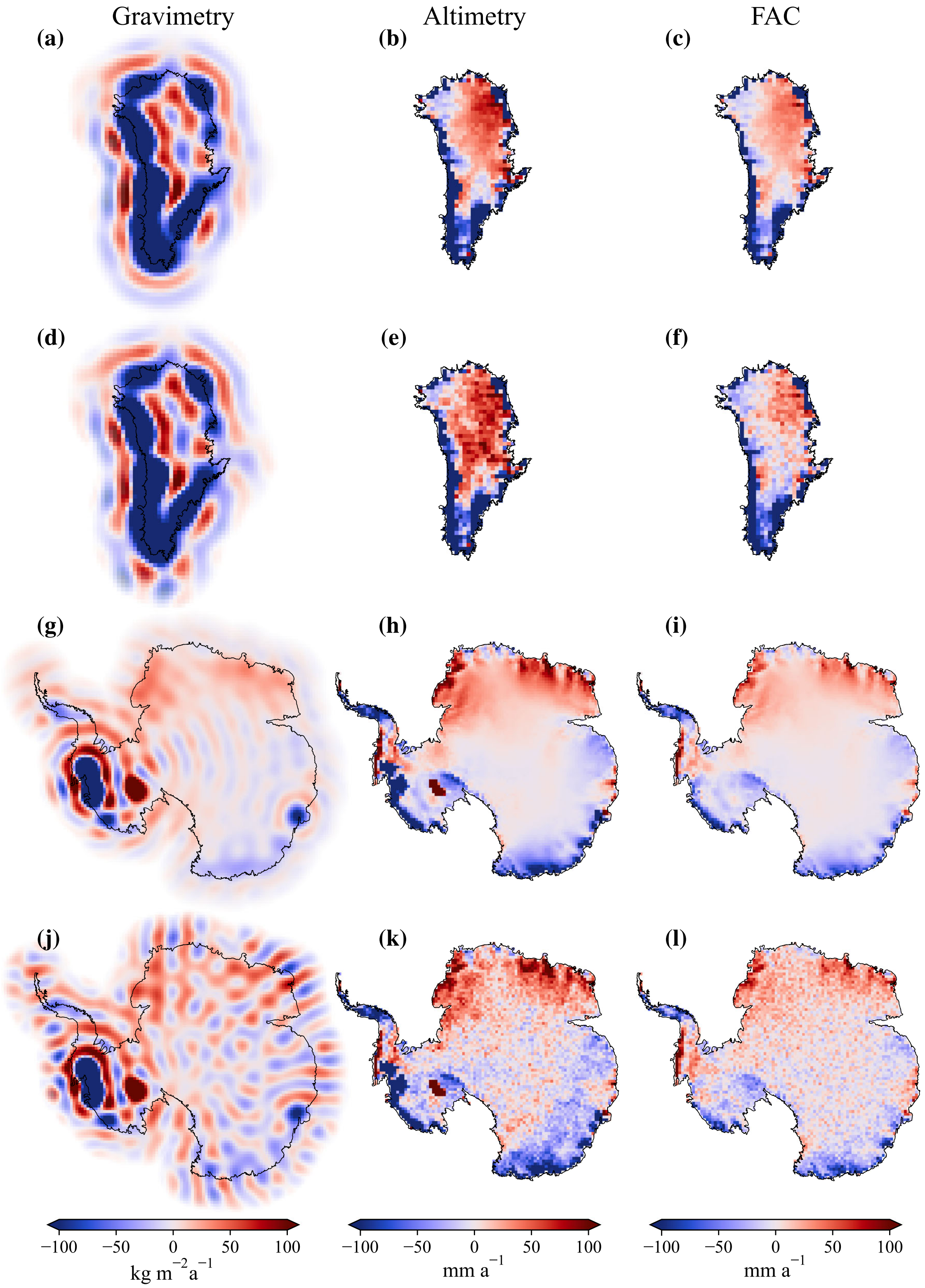

Fig. 3 The synthetic gravimetry (first column), altimetry observations (second column), and FAC data (third column) for GIS (**a–f**) and AIS (**g–l**) without errors (**a–c** and **g–i**) and including errors (**d–f** and **j–l**). We transferred the gravimetry observations to the spatial domain for illustration. We provide a figure of the errors in the SM (Fig. S3)

of IMC from the synthetic IMC defined on the grids which include the ocean response and solid-Earth elastic response. First, we convert the mass change of each grid cell into its spherical harmonic point mass representation (Pollack 1973) and calculate the sum over all grid cells. Second, we solve the sea level equation (Farrell and Clark 1976) to achieve mass conservation in the Earth system. Along with this step we compute the elastic deformation of the solid Earth due to IMC (Fig. 2f+l). The synthetic gravimetry observable is the sum of the globally consistent IMC coefficients and the GIA surface density rates (Eq. 3).

The synthetic altimetry observable (Fig. 3b+h) is the sum of the synthetic gridded surface elevation rates due to ID, firn thickness change, GIA, and elastic bedrock motion (Eq. 5), evaluated over the grid for GIS and AIS.

3.4 Stochastic error characterization

We represent the covariance matrix $C(\boldsymbol{d})$ as a composite block matrix of the $[l \times l]$ covariance matrices $C(\boldsymbol{d}^{\text{GRAV}})$, $C(\boldsymbol{d}^{\text{GIS-ALT}})$, $C(\boldsymbol{d}^{\text{GIS-FAC}})$, $C(\boldsymbol{d}^{\text{AIS-ALT}})$, and $C(\boldsymbol{d}^{\text{AIS-FAC}})$. In case of gravimetry observations, $l = (n+1)^2 - 1$, the number of spherical harmonic coefficients. In case of altimetry observations and FAC data, l is the number of grid cells for either the GIS or the AIS.

Here, we assume that the error covariance matrix for gravimetry observations $C(\boldsymbol{d}^{\text{GRAV}})$ can be identified with the inverse of the normal equations provided along with ITSG-Grace2018 (Mayer-Gürr et al. 2018) using the approach by Kvas et al. (2019) which includes background model uncertainties (Kvas and Mayer-Gürr 2019). We base the uncertainty information of the surface density rates on the mean covariance matrix of the monthly solutions over the period from Jan 2003 to Aug 2016. This averaging period avoids the months of exceptionally low quality solutions (Loomis et al. 2020). We assume no temporal correlations of GRACE monthly solution errors. In case of degree 1, we empirically estimate the covariance using an ensemble of degree-1 solutions and we ignore covariances between degree 1 and the other degrees. The SM (Sect. B) provides more details how we estimate $C(\boldsymbol{d}^{\text{GRAV}})$.

For altimetry observations, we retrieve the spatial covariance information ($C(\boldsymbol{d}^{\text{GIS-ALT}})$ and $C(\boldsymbol{d}^{\text{AIS-ALT}})$) from an ensemble of surface elevation rates from CryoSat-2 data (from Jan 2011 to Dec 2019) for GIS and AIS. The ensemble has 140 members for both GIS and AIS, including solutions obtained by 7 retrackers (AWIICE2, EWIDTH, ICE1, ICE2, OCEAN, OCOG, TFMRA), 4 topographic fits, and 5 interpolation methods. To implement uncorrelated noise, we add a variance of $(0.01\,\text{m}\,\text{a}^{-1})^2$ to the diagonal of the covariance matrix, which is the median variance from the ensemble of surface elevation changes. The empirical error covariance thus obtained includes effects of temporal error correlations in the time series that underlie the 140 ensemble members of mean rates.

We characterize the uncertainty of FAC ($C(\boldsymbol{d}^{\text{GIS-FAC}})$ and $C(\boldsymbol{d}^{\text{AIS-FAC}})$) similar to Willen et al. (2020): We approach the uncertainty of FAC by differences between two variants of FAC rates assuming that these differences express modelling errors. One variant is computed based on the RACMO2 SMB and the IMAU-FDM. The other variant is calculated using MAR SMB output from Fettweis et al. (2017) and Agosta et al. (2019) for GIS and AIS, respectively, and empirical relations between SMB variations and FAC variations established based on IMAU-FDM results (Willen et al. 2020). We calculate differences of the FAC rates between both variants over all 10 year time periods over the whole modelling period, i.e. we use a 10-year moving window with monthly increments. The time periods where SMB and FDM outputs are available are Jan 1960 to Dec 2015 and Jan 1979 to Dec 2016 for GIS and AIS, respectively, resulting in two ensembles of FAC rates with 553 (GIS) and 337 (AIS) members. Finally, the spatial covariance of each FAC rate is computed empirically using the ensembles. Similarly to the altimetry observations, we add a variance of $(0.01\,\text{m}\,\text{a}^{-1})^2$ to the diagonal of the covariance matrix. The empirical error covariance thus obtained includes the effect of temporal error correlations in the time series that underlie the ensemble members of mean rates.

Note that no FDM forced by MAR outputs is available. Therefore, our uncertainty characterization of FAC trends does not fully account for the uncertainty from firn modelling. Results by Verjans et al. (2021) for East Antarctica suggest that the uncertainty of firn model outputs is predominantly related to the uncertainty of their climate model inputs, rather than to uncertainties in the modelling of firn densification mechanisms.

We calculate the multivariate normal random vector $\boldsymbol{\epsilon}$, containing the random variables from the covariance information $C(\boldsymbol{d})$ assuming a multivariate normal distribution with an expectation vector of $\mathbf{0}$. To ensure reproducibility, we use the pseudorandom number generator *Mersenne Twister* (Matsumoto and Nishimura 1998) initialized with the same seed to compute a realization of $\boldsymbol{\epsilon}$, i.e. the errors $\boldsymbol{\varepsilon}$.

3.5 Experimental setup

Here, our aim is to perform three kinds of experiments with two variants of synthetic observations (variants A and B). We base the observations of the variant A on the GIA output from SELEN run with ICE-6G ice loading history. This variant is consistent to the GIA parametrization (Sect. 3.2). Alternatively, we use the GIA modelling output from Caron et al. (2018) to compute the observations of the variant B (Sect. 3.3). In Experiment 1A (E1A) and Experiment 1B (E1B), observations contain no errors and we apply a weighting based on the full spatial covariance (Sect. 3.4). Thus, we demonstrate potential misattribution of signal as an error by using the covariance information. In Experiment 2A (E2A) and Experiment 2B (E2B), the observations contain correlated errors (Sect. 3.4) but during the estimation we pretend uncorrelated errors only. To do so, we apply a weighting matrix $\tilde{\boldsymbol{P}}$ which only contains the diagonal elements from $\boldsymbol{P}$ (Eq. 11). With this experiment we investigate whether real, possibly unknown correlations can be safely neglected in the inversion. In Experiment 3A (E3A) and Experiment 3B (E3B), the observations contain correlated errors and we involve the full covariance information during the parameter estimation.

To enable comparison of the results from the experiments, we calculate the root mean squares (RMS) of the signals. For example, for the synthetic true GIA-induced surface density rate in Antarctica, the RMS signal is

$$\mathrm{RMS}_{\mathrm{AIS}}^{\mathrm{GIA}} = \sqrt{\frac{1}{v}\sum_{i=1}^{v}(\dot{\kappa}_i^{\mathrm{GIA}})^2}. \tag{22}$$

Further, we assess the results from the experiments by the misfit between the original signal and the estimated signal. For example, the RMS of the Antarctic GIA misfit is:

$$\Delta\mathrm{RMS}_{\mathrm{AIS}}^{\mathrm{GIA}} = \sqrt{\frac{1}{v}\sum_{i=1}^{v}(\dot{\kappa}_i^{\mathrm{GIA}} - \hat{\dot{\kappa}}_i^{\mathrm{GIA}})^2}. \tag{23}$$

In case of GIA, we perform this integration over the GIS and AIS and include a buffer zone of 400 km around the area of the grounded ice sheet (Gunter et al. 2014) because the GIA signal is not limited to this area.

Moreover, we calculate the integrated mass and volume rates of the signals, e.g. for the synthetic true GIA and FAC signal in Antarctica,

$$\dot{M}_{\mathrm{AIS}}^{\mathrm{GIA}} = \sum_{i=1}^{v}\dot{\kappa}_i^{\mathrm{GIA}} A_i \tag{24}$$

$$\dot{V}_{\mathrm{AIS}}^{\mathrm{FAC}} = \sum_{i=1}^{v}\dot{h}_i^{\mathrm{FAC}} A_i \tag{25}$$

Table 1 Results from Experiments 1A, 2A, and 3A (E1A, E2A, E3A) that use the SELEN ICE-6G output as the synthetic GIA signal and results from Experiments 1B, 2B, and 3B (E1B, E2B, E3B) that use the GIA modelling output from Caron et al. (2018)

	GIA				IMC				FAC			
	RMS in kg/m² a	RMS ratio	$\dot{M}$ in Gt/a	$\lvert\dot{M}\rvert$ ratio	RMS in kg/m² a	RMS ratio	$\dot{M}$ in Gt/a	$\lvert\dot{M}\rvert$ ratio	RMS in mm/a	RMS ratio	$\dot{V}$ in km³/a	$\lvert\dot{V}\rvert$ ratio
Greenland ice sheet												
signalA	8.1		− 17.5		154.7		− 242.7		454.8		− 288.7	
E1A	0.3	4%	1.0	6%	1.0	1%	− 1.2	0%	2.6	1%	1.2	0%
E2A	0.3	3%	0.3	2%	18.0	12%	− 1.1	0%	49.0	11%	11.6	4%
E3A	0.3	4%	0.8	5%	3.7	2%	− 1.1	0%	13.8	3%	0.7	0%
signalB	7.1		11.0		154.7		− 242.7		454.8		− 288.7	
E1B	7.3	104%	25.5	231%	7.7	5%	− 16.7	7%	17.3	4%	12.7	4%
E2B	7.1	100%	20.2	184%	19.2	12%	− 25.2	10%	52.3	11%	27.0	9%
E3B	7.3	103%	24.8	225%	11.9	8%	− 17.3	7%	30.7	7%	14.3	5%
Antarctic ice sheet												
signalA	8.9		98.8		55.5		− 114.7		27.1		− 10.0	
E1A	1.1	13%	5.4	5%	0.9	2%	− 5.9	5%	1.6	6%	5.8	58%
E2A	7.4	83%	− 16.7	17%	8.6	16%	22.5	20%	12.3	46%	− 15.3	153%
E3A	2.8	31%	7.6	8%	2.3	4%	− 8.9	8%	10.8	40%	6.9	69%
signalB	7.9		117.8		55.5		− 114.7		27.1		− 10.0	
E1B	1.3	17%	13.3	11%	1.0	2%	− 7.5	7%	1.4	5%	5.7	57%
E2B	8.8	111%	− 36.2	31%	8.7	16%	55.7	49%	12.6	47%	− 23.5	235%
E3B	4.0	51%	6.3	5%	3.5	6%	3.5	3%	11.1	41%	− 2.2	22%

The root mean square (RMS) values refer either to the synthetic signal (Eq. 22, lines marked as 'signalA', 'signalB') or to the RMS error (ΔRMS, Eq. 23, lines marked as E1A, E2A, E3A, E1B, E2B, E3B). The RMS ratio is the RMS error divided by the RMS signal. $\dot{M}$ and $\dot{V}$ (Eqs. 24, 26) are integrated values over the indicated ice sheet either of the synthetic signals (lines marked as 'signalA', 'signalB') or of the error of the experiments (lines marked as E1A, E2A, E3A, E1B, E2B, E3B). $\lvert\dot{M}\rvert$ and $\lvert\dot{V}\rvert$ ratios are the absolute values of the integrated error divided by the integrated synthetic signals and the integrated misfit. For example for the Antarctic GIA and FAC this is

$$\Delta \dot{M}_{\mathrm{AIS}}^{\mathrm{GIA}} = \sum_{i=1}^{v} (\dot{\kappa}_i^{\mathrm{GIA}} - \hat{\dot{\kappa}}_i^{\mathrm{GIA}}) A_i \tag{26}$$

$$\Delta \dot{V}_{\mathrm{AIS}}^{\mathrm{FAC}} = \sum_{i=1}^{v} (\dot{h}_i^{\mathrm{FAC}} - \hat{\dot{h}}_i^{\mathrm{FAC}}) A_i . \tag{27}$$

4 Results

Table 1 presents the results of the experiments conducted with the two variants of observations (variants A and B) in context to the original signals (Sect. 3.3). We list RMS values (Eq. 22) and the integrated mass and volume changes (Eq. 24) of the original GIA, IMC, and FAC for the AIS and GIS. Additionally, we show the misfit in terms of ΔRMS (Eq. 23) and the integrated misfit (Eq. 26) from each experiment. The ratio of the RMS of the misfit (RMS error) and the RMS of the signals indicates the relative noise level of the results. The ratio of the integrated difference and the integrated signals ($|\dot{M}|$ ratio and $|\dot{V}|$ ratio in Table 1) reveal the deviation of the results from the original signal. Figures 4, 5, 6 and S8–10 show maps of the estimated signals for GIS (a–c in each figure) and AIS (g–i in each figure), along with the misfit in Greenland (d–f in each figure) and in Antarctica (j–l in each figure). In Figure S11, we compare degree amplitudes of the original GIA signal, the Antarctic GIA signal, and the misfit from E2A and E3A.

In case of variant A experiments deviations of integrated results are only 6% at maximum (Table 1) in Greenland. Moreover, results from E1A and E3A in Greenland have only a small IMC and FAC misfit, reflected by small ΔRMS values (Table 1); however, results from E2A have a noticeable misfit. The misfit is mainly present in coastal regions in addition to some random inland oscillations (Fig. 4e+f). For the results of the variant B experiments, these statements also generally apply to estimates of IMC and FAC in Greenland. In contrast, the deviations in the estimated GIA are very large. The RMS ratio is approximately 100% in all three variant B experiments. Note that the deviation ratio of integrated results is very large because the original integrated GIA effect from Caron et al. (2018) over Greenland is small (the original GIA effect is 11 Gt a^{-1} and the estimate from E3B is 25 Gt a^{-1}). In Antarctica deviations of integrated results are in the range of 3–11% in case of GIA and IMC from E1A, E1B, E3A, and E3B results (Table 1). The E2A and E2B results differ from the synthetic truth by 17% and 31%, respectively (integrated GIA signal) and by 20% and 49%, respectively (integrated IMC signal). FAC results in Antarctica deviate considerably from the synthetic truth. In E2A and E2B, the integrated FAC volume change of the AIS deviates most by −15.2 km^{3}a^{-1} and −23.5 km^{3}a^{-1}, respectively, from the −10.0 km^{3}a^{-1} true signal (Table 1). Note that the integrated FAC signal in Antarctica is relatively small compared to the other signals.

Despite the fact that E1A and E1B do not include any observational errors, the errors of retrieved signals from those experiments are not negligible. The ΔRMS values are between one third and one half of the magnitude of ΔRMS values from E3A and E3B for AIS GIA and AIS IMC. For GIS GIA and GIS IMC, E1A ΔRMS is equal to E3A ΔRMS and E1B ΔRMS is equal to E3B ΔRMS. Except for GIS GIA, the E3A/E3B results deviate less than the E2A/E2B results from the synthetic truth, in terms of both ΔRMS values and integrated differences (Table 1). Notably, the RMS ratio of AIS GIA is 31% in E3A compared to 83% in E2A; and 51% in E3B compared to 111% in E2B. But also, for example, the RMS ratio of GIS IMC is 2% in E3A compared to 12% in E2A; and 8% in E3B compared to 12% in E2B. For Greenland, the misfit maps for IMC and FAC show a significant discrepancy for E2A/E2B (Fig. 4e+f, S10e+f), and somewhat less for E3B (Fig. 6). In Antarctica differential maps (Fig. 4j–l, 5j–l, S10j–l, and 6j–l) further illustrate that E3A/E3B results deviate less from the synthetic truth than E2A/E2B results. In Antarctica spatial correlations (Fig. 3j+k) are less present in E3A/E3B results than in E2A/E2B results. This is visible by IMC estimates from E2A/E2B (Fig. 4k, S10k) and E3 (Fig. 5k, 6k). The spatial patterns of the Antarctic GIA misfit (Fig. 4j, S10j) and the IMC misfit (Fig. 4k, S10k) are opposed to some degree.

The GIA signal we used for variant A observations is consistent to GIA parametrization with respect of their modelling environment. The integrated misfit of the GIA signal in Greenland is 1 Gt a^{-1} at maximum in all A experiments. Differences are small (Fig. 4d, 5d). Regarding the Antarctic GIA estimate, the misfit is considerably larger in E2A/E2B than in E3A/E3B (Fig. 5j, 6j, Fig. 4j, S10j), although typical GRACE error patterns are still visible for E3A/E3B. The E2A ΔRMS of the Antarctic GIA signal is 7.4 kg m^{-2} a^{-1} (Table 1), which is close to the RMS of the original GIA signal of 8.9 kg m^{-2} a^{-1} (8.8 kg m^{-2} a^{-1} and 7.9 kg m^{-2} a^{-1} in case of E2B). When we consider the full spatial covariance information (E3A/E3B), the ΔRMS decreases to 3.0 kg m^{-2} a^{-1}/4.0 kg m^{-2} a^{-1}. In the spectral domain, the GIA misfit of E2A and its excess over the GIA misfit of E3A are mainly present between degree 10 and 80 (Fig. S11a).

For the results from variant B experiments, we can summarize for the estimated GIA: In Greenland, the error of the GIA estimate from E1B–E3B is as large as the original GIA signal. Taking the spatial correlations into account does not improve the GIA result in Greenland. This is different in Antarctica where the integrated GIA misfit of the E3B result deviates by 5% from the original GIA signal which is close to the 8% deviation of the E3A result. However, the RMS ratio of the estimated GIA effect is larger for E3B than for E3A (51% vs. 31%). The error degree amplitudes of the estimated GIA (Fig. S6) are also larger for the E3B GIA result than for the E3A result in the degree range from 12 to 32. This is mainly due to the misfit of the variant B experiments outside Antarctica.

5 Discussion

5.1 Conceptual assumptions

Six conceptual assumptions are paramount in our synthetic experiments.

(1) We assume that we have full knowledge of observational uncertainties (Sect. 3.4). We compute the covariance information from real data and synthesize the errors from it. Thus, the weighting in the parameter estimation is consistent to the errors present in the synthetic observations. In reality, knowledge about uncertainties is incomplete so that the error characterization may deviate from the actual error characteristics.

(2) We assume that altimetry observations are available with full spatial coverage. The orbit design (inclination) of altimetry missions and steep slope topography limit spatial sampling and lead to a polar gap and unobserved regions (e.g. valleys). In our experiments, we do not directly investigate effects due to sampling issues. However, we use the spread between the results of different interpolation methods in the altimetry ensemble to characterize errors in the altimetry products (Sect. 3.4).

(3) We base the experiments on a period of 10 years. This is motivated by the period of availability of CryoSat-2 observations. For CryoSat-2, limitations addressed by point (2) are less severe than for other missions (Schröder et al. 2019). Obviously, errors in the calculated rates would be smaller over longer periods of time, with the restriction that correlated errors decrease less with a longer observation period than uncorrelated errors do. However, we do not quantify the error reduction with longer periods here, because analytical error models are not available and we estimate uncertainties empirically based on the chosen time period (Sect. 3.4).

(4) In the synthetic experiments, we incorporate mean rates of IMC and FAC only. We did not yet generalize the approach to analyse interannual variations of IMC and FAC or to analyse time-variable rates of the ice dynamic contribution to the mass balance which are in particular present in the West Antarctic Ice Sheet (Willen et al. 2021).

(5) We generate the GIA parametrization with the GIA modelling software SELEN (Spada and Melini 2019), which is publicly available. The modelling results generated with SELEN determine the relationship between GIA-induced gravity changes and geometry changes. We do not use an effective density to define the ratio of GIA-induced gravity change and the GIA-induced geometry change (e.g. Riva et al. 2009; Gunter et al. 2014; Engels et al. 2018). Furthermore, by the assumptions on generating the Antarctic GIA patterns (Sect. 3.2), we essentially specify a formal spatial GIA resolution of ~250 km. Thus, the chosen Antarctic GIA parametrization can only hardly reproduce GIA changes at smaller spatial scales, e.g. as the GIA effect found by Barletta et al. (2018) (Fig. S5).

(6) We do not investigate other signals in addition to IMC of ice sheets and GIA ($\dot{\kappa}^{\mathrm{OTHER}}$ in Eq. 3), e.g. terrestrial water redistributions, which we expect to be small over GIS and AIS.

5.2 Capabilities and limitations of the approach

In Greenland, we parametrize GIA with a single regional fingerprint which exactly matches the GIA signal to be estimated in terms of assumed ice history and rheology in variant A observations. Results from all experiments demonstrate that the estimate of the GIA signal in Greenland is robust against observational errors. This emphasizes that the fingerprint parametrization is a globally consistent and robust method. In addition, the relatively small magnitude of the integrated GIA signal in Greenland (Table 1) means that errors in the Greenland GIA recovery do not crucially affect the global inversion results. For example, Rietbroek et al. (2016) obtained a difference between the estimated Greenland fingerprint and the modelled Greenland fingerprint equivalent to only $-0.003\,\mathrm{mm\,a^{-1}}$ global mean sea level. In general, the chosen parametrization strategy relies on knowledge of the ice history and the solid-Earth rheology. With the variant A experiments, we investigate the ideal case. With variant B simulated observations, we investigate the case when deviations between the modelled GIA fingerprints and the synthetic true GIA signal exist. We find that the fingerprint for Greenland created with SELEN and the ICE-6G glacial history restricted to Greenland is hardly able to resolve the present-day GIA effect predicted from Caron et al. (2018). Because the fingerprint can only be scaled as a whole, deviations affect the entire GIA signal represented by the fingerprint. This is especially problematic if the dominating spatial scale of errors in ice history and rheology are regional or local, as shown by Kappelsberger et al. (2021) and Adhikari et al. (2021). We confirm that large continental-scale fingerprints are inappropriate for the regional or local improvement of the GIA information.

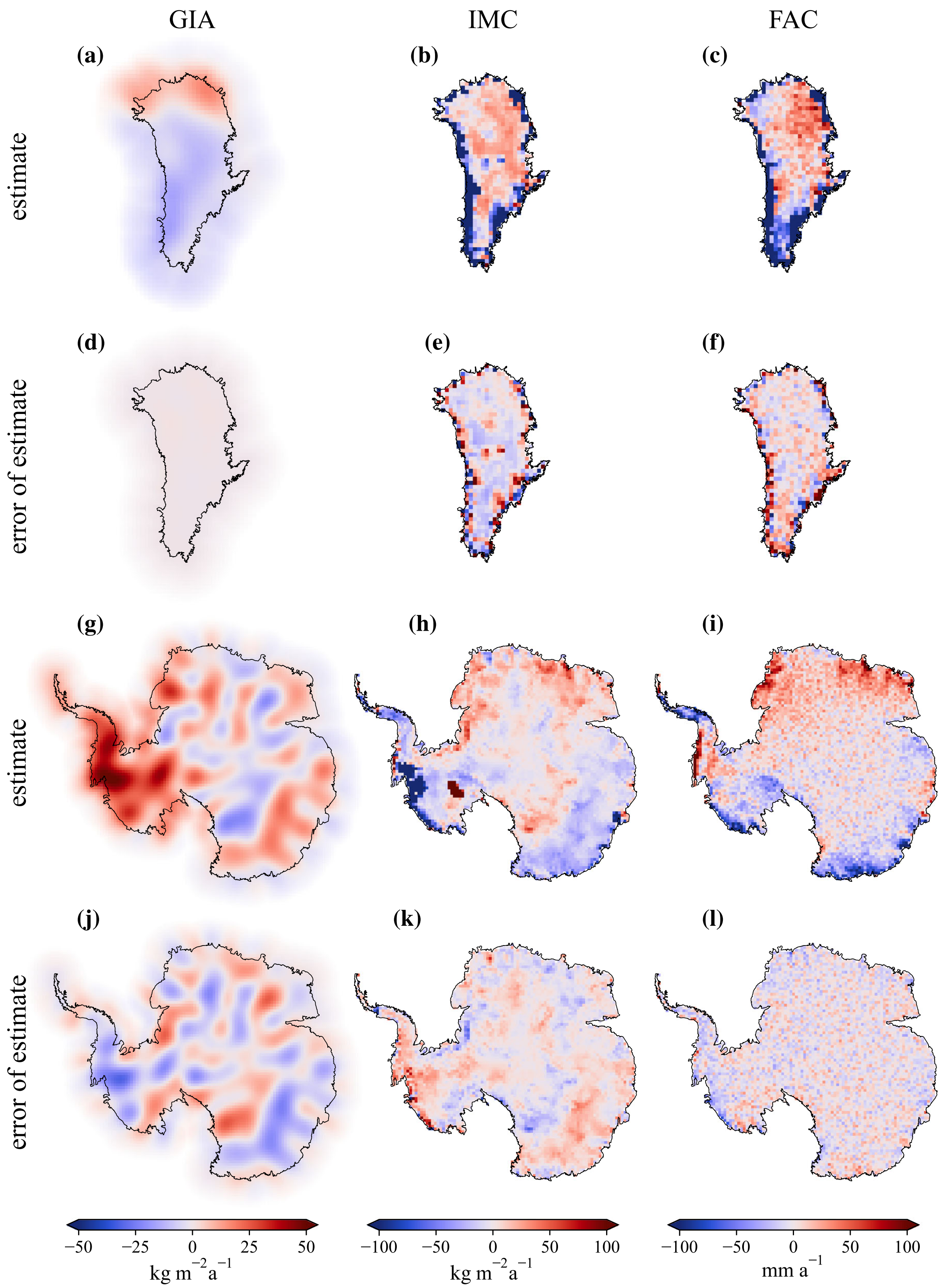

Fig. 4 Results from Experiment 2A (E2A): estimated signals (**a–c** and **g–i**) and the difference to the original signals (**d–f** and **j–l**) for GIA-induced bedrock motion (first column), IMC-induced surface density change (second column), and FAC change (third column). The observations contain correlated errors and any correlations are neglected during the parameter estimation

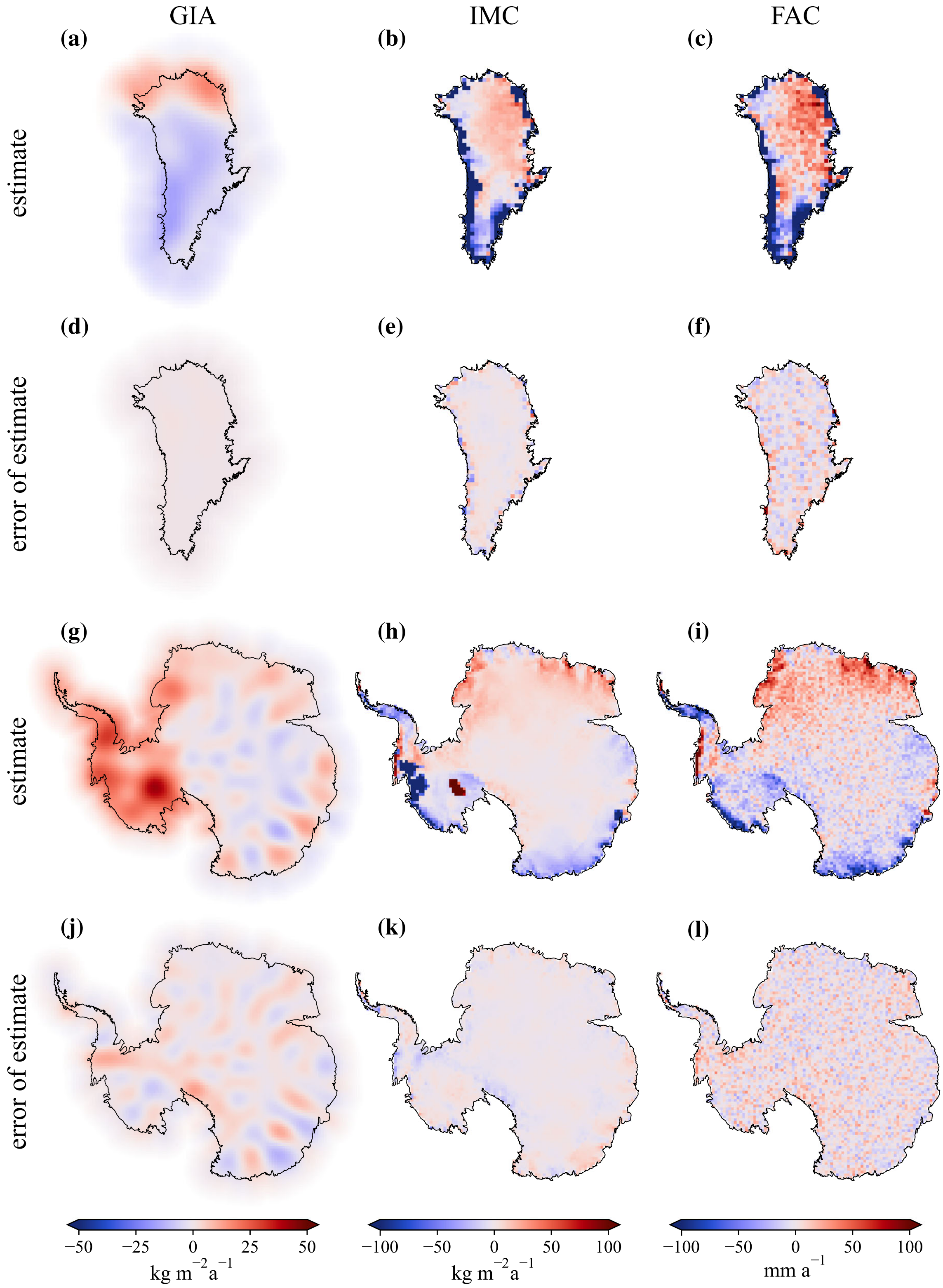

Fig. 5 Results from Experiment 3A (E3A): estimated signals (**a–c** and **g–i**) and the difference to the original signals (**d–f** and **j–l**) of GIA-induced bedrock motion (first column), IMC-induced surface density change (second column), and FAC change (third column). The observations contain correlated errors, and the covariance information is used during the parameter estimation

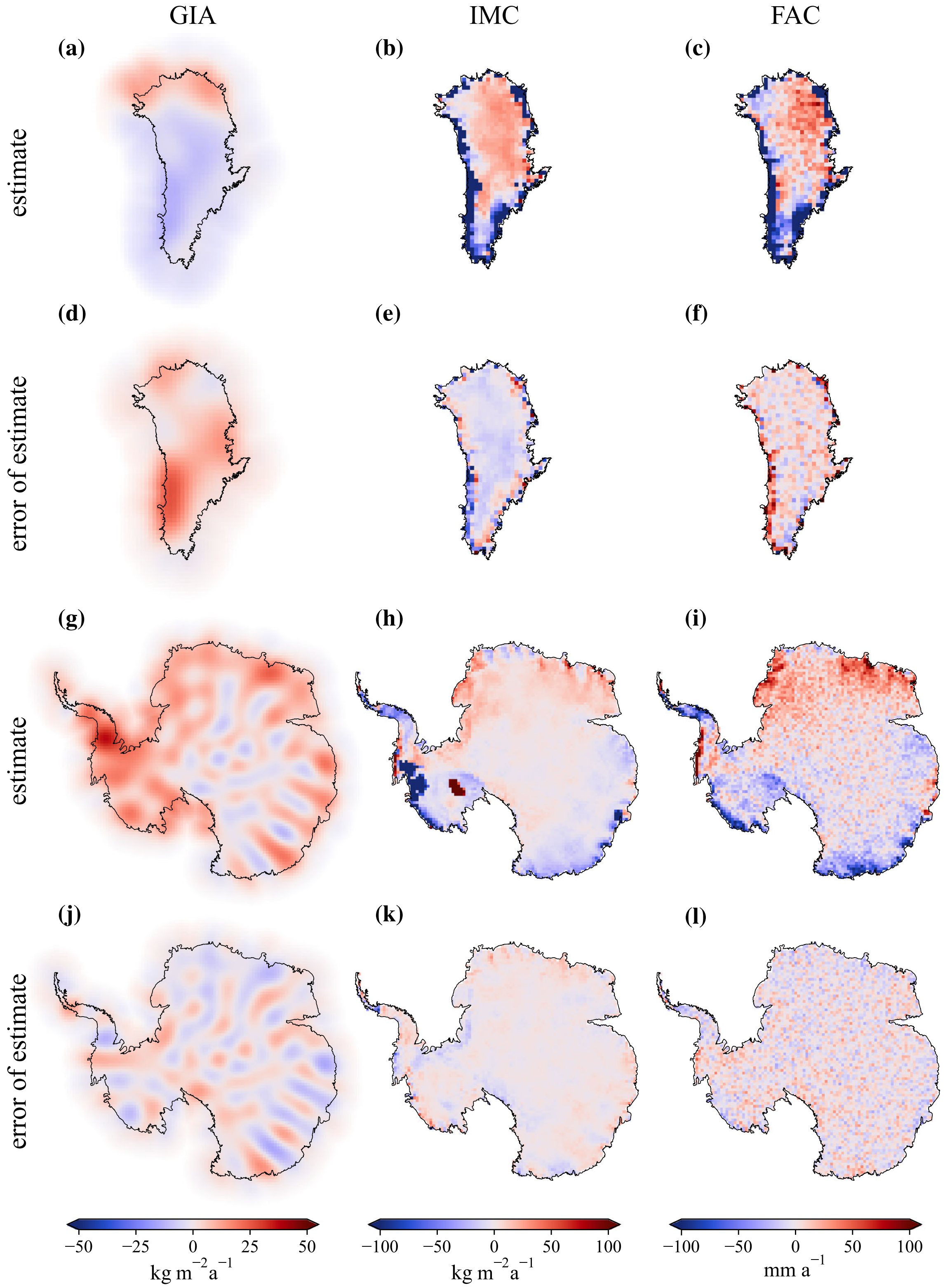

Fig. 6 Results from Experiment 3B (E3B): estimated signals (**a–c** and **g–i**) and the difference to the original signals (**d–f** and **j–l**) for GIA-induced surface density change (first column), IMC-induced surface density change (second column), and FAC change (third column). The observations contain correlated errors and the covariance information is used during the parameter estimation

In Antarctica, we apply a different strategy for the GIA parametrization, because we assume that spatial GIA patterns from geophysical modelling may have substantial errors (Sect. 1). The Antarctic GIA parametrization is consistent to geophysical GIA modelling by using the local deglaciation impulses to create the globally consistent GIA patterns, but remains independent from any full GIA modelling based on a prescribed glaciation history. This model-independent parametrization is less robust against observational errors. For degrees larger than 30, the effect of GRACE errors on the GIA retrieval is larger than the GIA signal itself (Fig. S6). If error covariances of the observations are not addressed (E2A and E2B), the integrated GIA signal will be still relatively close to the truth, but the noise level of the estimated signal will be similar to that of the signal itself (Table 1). In that case, the Antarctic GIA RMS error (ΔRMS) is 83%/111% (E2A/E2B) of the RMS of the Antarctic GIA signal. This can be considerably improved by including the covariance information in the parameter estimation. In this case the RMS error is 31%/51% of the RMS signal (E3A/E3B). The incorporation of the full covariance information also improves the estimates for IMC and FAC. We thus caution that any real data analysis, using the localized GIA parametrization in a global inversion, will only provide meaningful results if the error covariance information is available and utilized.

The formal spatial resolution of our AIS GIA parametrization is determined by the spacing between the local deglaciation discs, that is, ~250 km. This spacing is guided by the autocorrelation of the addressed GIA signal. To further justify our choice of spacing, we made GIA parametrization test experiments (Sect. A in the SM) and found that our parametrization recovers the ICE-6G(VM5a) GIA signal with only small misfits.

The effective spatial resolution of the AIS GIA retrieval may be assessed through comparing signal and error per spherical harmonic degree (Fig. S11a). For E3A, the amplitude of the Antarctic GIA signal exceeds the GIA error amplitude below degree 45, indicating an effective resolution of ~450 km. Note that the GIA errors of the inversion are dominated by Antarctic GIA errors in the variant A experiments. This is different in variant B results, where the GIA misfit is dominated by misfits due to the incompatible fingerprints outside of Antarctica (Fig. S11b).

There are some degrees of freedom in the generation of the GIA patterns from deglaciation impulses. The shape of the response (Fig. 1) depends on the choice of the generic ice loading history and the assumed rheology. For example, shifting the time of the instantaneous deglaciation step further to the past (or to the present) would lead to wider (or, respectively, narrower) GIA patterns.

A present-day GIA signal resulting from ice loading changes during the last centuries and a comparatively low mantle viscosity, as the GIA signal Barletta et al. (2018) found in West Antarctica (Fig. S5), involves smaller spatial scales than the GIA signals predicted by, e.g. Caron et al. (2018). Other inversion frameworks aim to account for GIA signals resulting from the centennial ice loading changes and a low viscosity (Jiang et al. 2021), whereby their results show present-day GIA effects mainly on long spatial wavelengths (Fig. 7 in Jiang et al. (2021)). The smaller spatial scales of the modelled signal from Barletta et al. (2018) would require gravity fields with higher spatial resolution, preferably up to degree ~200 (~100 km is the approximate half width of the found GIA feature). In that case, our approach could be adapted by using a localized GIA parametrization that captures the expected spatial scales. For this purpose, the time of the deglaciation impulse could be modified as well as the distance between the patterns and thus the number of parameters to be estimated. Likewise, the viscosity could be adjusted. Further test experiments with GIA models that include heterogeneity of the viscosity and ice loading history during the last centuries may help to find an appropriate GIA parametrization for a GIA signal on short spatial wavelengths. However, the applied parametrization strategy does not allow to invert for the glacial history or rheological parameters. Attributing the GIA signal inherent in satellite gravimetry observations to an ice history and rheological parameters is ambiguous and needs further boundary information.

We completely avoid filtering or regularization in the experiments and only apply the covariance information to account for errors. However, results from E1A and E1B (the error-free experiments) demonstrate that the incorporation of error correlations in the stochastic model may entail patterns of signal misattribution that are correspondingly correlated. That is, the separation of error patterns and signal patterns is imperfect. Besides, it should be noted that the uncertainty characterization we present here is an assumption on the observational covariance information based on available data sets.

Gunter et al. (2014) linked the surface density rate due to SMB and the firn thickness rate by a firn density (Eq. 7). This density is subject to large uncertainties (Willen et al. 2020), especially if the volume and mass rates are small and need further constraints. We link mass and volume changes by parametrizing FAC changes in addition to IMC. This allows to avoid the firn density (Eq. 7). FAC has the important advantage that it is linearly related to altimetry observations and can thus be directly implemented in the general linear model (Sect. 3.1) without linearization, as would be the case using a firn density.

By the study design, we neglect far-field effects due to hydrological or glacier mass changes ($\dot{\kappa}^{\mathrm{OTHER}}$ in Eq. 3), which is a limitation in our simulation setup and potentially leads to too optimistic results. We quantified the effect of mass changes originating outside of Antarctica and Greenland from Jan 2003 until Dec 2012 using a global inversion for all sea level contributions (Rietbroek et al. 2016; Uebbing et al. 2019). Hydrological mass changes have an integrated effect of 0.4 Gt a^{-1} and -1.0 Gt a^{-1} within in the grounding line of the GIS and AIS, respectively. Glacier mass changes have an effect of 1.4 Gt a^{-1} (GIS) and 10.5 Gt a^{-1} (AIS). We conclude that these effects are relatively small and justify neglecting them in this simulation study.

As discussed in Sect. 1, uncertainties of GIA forward models for the AIS are on the order of tens of Gt a^{-1} in terms of the integral mass effect. If GIA forward models are used to correct for GIA in GRACE IMC estimates, GIA model errors directly map (with opposite sign) into the IMC errors. For E3A and E3B, the AIS GIA error is below 10 Gt a^{-1} (Table 1), significantly lower than the uncertainty of GIA forward models. This low GIA error is reflected in an accordingly low IMC error for E3A and E3B. Its sign is opposite to that of the GIA error and is below 10 Gt a^{-1}, too. Hence, the inversion is a promising approach to significantly reduce the uncertainty of GRACE AIS IMC inferences, previously related to GIA uncertainties.

5.3 Outlook

The next step will be obviously to implement the presented approach in a framework to process real-world data. The synthetic experiments demonstrate that the GIA parametrization presented here is appropriate to resolve GIA. In our ongoing research, we will incorporate the obtained findings into a global framework which is able to estimate all sea level contributions (Rietbroek et al. 2016; Uebbing et al. 2019). It will be investigated how the new GIA parametrization affects the GIA-related uncertainty in IMC and ocean mass change estimates and in sea level budget assessments under the conditions of the full global inversion.

We see potential for extending the approach by enabling the investigation of temporal variations of IMC and FAC rather than constant rates. For this purpose, the approach can be adapted so that time series with monthly resolution can be evaluated and, in line width Rietbroek et al. (2016), monthly IMC, monthly changes in FAC and a linear GIA effect can be estimated. However, this requires further investigation of the spatial and temporal covariance of both the involved signals and the observation errors.

Furthermore, real data results on the present-day GIA effect derived with the approach might hold some potential for investigation of the glacial history or lateral rheology heterogeneity. This might requires further development of the GIA patterns, i.e. the parametrization of GIA, beyond the 1-D rheology and the deglaciation impulses.

6 Conclusions

The inversion that we propose here uses a globally consistent parametrization of GIA and allows a co-estimation of GIA together with changes of the ice mass and the firn air content in Greenland and Antarctica. It enables to process, in a global framework, three types of observations available as five datasets: satellite gravimetry, satellite altimetry over GIS and AIS, as well as modelled firn air content over GIS and AIS in a single least-squares parameter estimation step. Loosening the dependence on geophysical GIA models of previous GIA parametrizations is paramount to our approach. The use of a set of 'local GIA patterns' (more precisely, global GIA patterns based on local deglaciation impulses) holds promise to spatially resolve GIA patterns that are not identified by geophysical GIA modelling and therefore not part of modelled regional GIA fingerprints.

In turn, a GIA parametrization through a large number of local GIA patterns is less robust and therefore more sensitive to the details of error covariance information of the input data. We assessed this covariance information from real observations of the five data sets and demonstrated that the set of GIA patterns is able to spatially resolve a physically meaningful present-day GIA effect in Antarctica that results from ICE-6G ice history and VM5a rheology. In this case the RMS error of the spatially resolved Antarctic GIA signal is about one third of the RMS of the GIA signal over an observation period of 10 years assuming ideal observing conditions and full knowledge of the covariance information. This RMS error increases up to half of the RMS of the GIA signal in Antarctica when we aim to resolve the GIA signal predicted by an alternative GIA model. Longer observation periods would lead to smaller errors of the mean rate, which we do not quantify here, because we characterize errors empirically over the 10-year observation period. From the experiments we conclude: If errors of the input data sets are thoroughly characterized, a GIA parametrization by local GIA patterns can plausibly resolve the GIA-induced deformation from satellite observations in a global framework. On the other hand, if the error covariances are unknown, error and signal cannot be clearly distinguished in the GIA result. In this feasibility study, we limit the investigations to one realization of the GIA parametrization. As a caveat, we neglect for hydrological and glacier mass changes outside of the ice sheets in our simulation study, but which need to be accounted for when evaluating real world data. However, global inversion results according to Rietbroek et al. (2016); Uebbing et al. (2019) show rather small far-field effects over ice sheets.

Supplementary Information The online version contains supplementary material available at https://doi.org/10.1007/s00190-022-01651-8.

Acknowledgements M. O. Willen and B. Uebbing were funded through grant HO 4232/4-2 and KU 1207/22-2, respectively, "Reconciling ocean mass change and GIA from satellite gravity and altimetry (OMCG)" from the Deutsche Forschungsgemeinschaft (DFG) as part of the Special Priority Program (SPP) 1889 "Regional Sea Level Change and Society" (SeaLevel). We thank Valentina Barletta and Lambert Caron for providing GIA modelling results. We thank Matt King, the two anonymous reviewers and the Associate Editor Brian Gunter for their helpful comments which improved the manuscript.

Author Contributions CRediT taxonomy: Matthias Willen and Martin Horwath were involved in the conceptualization, methodology, and writing—original draft; Matthias Willen contributed to the formal analysis, investigation, and visualization; Veit Helm, Andreas Groh, and Matthias Willen helped in the data curation; Martin Horwath and Jürgen Kusche contributed to the funding acquisition; Matthias Willen and Andreas Groh contributed to software; Martin Horwath contributed to the supervision; Martin Horwath, Jürgen Kusche, Andreas Groh, Bernd Uebbing, Veit Helm, and Matthias Willen were involved in writing—review and editing.

Funding Open Access funding enabled and organized by Projekt DEAL.

Data availability The datasets generated during and/or analysed during the current study are available from the corresponding author on reasonable request.

Declarations

Conflict of interest The authors declare that they have no conflict of interest.

References

A G, Wahr J, Zhong S (2013) Computations of the viscoelastic response of a 3-D compressible Earth to surface loading: an application to Glacial Isostatic Adjustment in Antarctica and Canada. Geophys J Int 192(2):557–572. https://doi.org/10.1093/gji/ggs030

Adhikari S, Milne G, Caron L, Khan S, Kjeldsen K, Nilsson J, Larour E, Ivins E (2021) Decadal to centennial timescale mantle viscosity inferred from modern crustal uplift rates in Greenland. Geophys Res Lett 48(19):e2021GL094040. https://doi.org/10.1029/2021GL094040

Agosta C, Amory C, Kittel C, Orsi A, Favier V, Gallée H, van den Broeke MR, Lenaerts JTM, van Wessem JM, van de Berg WJ, Fettweis X (2019) Estimation of the Antarctic surface mass balance using the regional climate model MAR (1979–2015) and identification of dominant processes. Cryosphere 13(1):281–296. https://doi.org/10.5194/tc-13-281-2019

Barletta VR, Bevis M, Smith BE, Wilson T, Brown A, Bordoni A, Willis M, Khan SA, Rovira-Navarro M, Dalziel I, Smalley R Jr, Kendrick E, Konfal S, Caccamise DJ II, Aster RC, Nyblade A, Wiens DA (2018) Observed rapid bedrock uplift in Amundsen Sea Embayment promotes ice-sheet stability. Science 360(6395):1335–1339. https://doi.org/10.1126/science.aao1447

Bettadpur S (2018) GRACE geopotential coefficients CSR release 6.0. University of Texas Center For Space Research (UTCSR). https://doi.org/10.5067/GRGSM-20C06

Bevis M, Wahr J, Khan SA, Madsen FB, Brown A, Willis M, Kendrick E, Knudsen P, Box JE, van Dam T, Caccamise DJ, Johns B, Nylen T, Abbott R, White S, Miner J, Forsberg R, Zhou H, Wang J, Wilson T, Bromwich D, Francis O (2012) Bedrock displacements in Greenland manifest ice mass variations, climate cycles and climate change. Proc Natl Acad Sci USA 109(30):11944–11948. https://doi.org/10.1073/pnas.1204664109

Caron L, Ivins E, Larour E, Adhikari S, Nilsson J, Blewitt G (2018) GIA model statistics for GRACE hydrology, cryosphere, and ocean science. Geophys Res Lett 45:2203–2212. https://doi.org/10.1002/2017GL076644

Dahle C, Flechtner F, Murböck M, Michalak G, Neumayer H, Abrykosov O, Reinhold A, König R (2018) GRACE geopotential GSM coefficients GFZ RL06. V. 6.0. GFZ Data Services. https://doi.org/10.5880/GFZ.GRACE_06_GSM

Dah-Ning Y (2018) GRACE geopotential coefficients JPL release 6.0. NASA Jet Propulsion Laboratory (JPL). https://doi.org/10.5067/GRGSM-20J06

Engels O, Gunter B, Riva REM, Klees R (2018) Separating geophysical signals using GRACE and high-resolution data: a case study in Antarctica. Geophys Res Lett 45(22):12,340-12,349. https://doi.org/10.1029/2018GL079670

Farrell WE, Clark JA (1976) On postglacial sea level. Geophys J R Astr Soc 46(3):647–667. https://doi.org/10.1111/j.1365-46X.1976.tb01252.x

Fettweis X, Box JE, Agosta C, Amory C, Kittel C, Lang C, van As D, Machguth H, Gallée H (2017) Reconstructions of the 1900–2015 Greenland ice sheet surface mass balance using the regional climate MAR model. Cryosphere 11(2):1015–1033. https://doi.org/10.5194/tc-11-1015-2017

Groh A, Horwath M (2021) Antarctic ice mass change products from GRACE/GRACE-FO using tailored sensitivity kernels. Remote Sens 13(9):1736. https://doi.org/10.3390/rs13091736

Gunter BC, Didova O, Riva REM, Ligtenberg SRM, Lenaerts JTM, King MA, van den Broeke MR, Urban T (2014) Empirical estimation of present-day Antarctic glacial isostatic adjustment and ice mass change. Cryosphere 8(2):743–760. https://doi.org/10.5194/tc-8-743-2014

Jiang Y, Wu X, van den Broeke MR, Kuipers Munneke P, Simonsen SB, van der Wal W, Vermeersen BL (2021) Assessing global present-day surface mass transport and glacial isostatic adjustment from inversion of geodetic observations. J Geophys Res Solid Earth 126(5). https://doi.org/10.1029/2020JB020713

Joughin I, Smith B, Howat I, Scambos T (2018) MEaSUREs Greenland ice sheet velocity map from InSAR data, version 2. NASA National Snow and Ice Data Center Distributed Active Archive Center, Boulder, Colorado, USA. https://doi.org/10.5067/OC7B04ZM9G6Q

Kappelsberger MT, Strößenreuther U, Scheinert M, Horwath M, Groh A, Knöfel C, Lunz S, Khan SA (2021) Modeled and observed bedrock displacements in North-East Greenland using refined estimates of present-day ice-mass changes and densified GNSS measurements. J Geophys Res Earth Surf 126(4):e2020JF005860. https://doi.org/10.1029/2020JF005860

Klemann V, Martinec Z (2011) Contribution of glacial-isostatic adjustment to the geocenter motion. Tectonophysics 511(3–4):99–108

Koch KR (1999) Parameter estimation and hypothesis testing in linear models, 2nd edn. Springer, Berlin. https://doi.org/10.1007/978-3-662-03976-2

Kvas A, Mayer-Gürr T (2019) GRACE gravity field recovery with background model uncertainties. J Geod 93(12):2543–2552. https://doi.org/10.1007/s00190-019-01314-1

Kvas A, Behzadpour S, Ellmer M, Klinger B, Strasser S, Zehentner N, Mayer-Gürr T (2019) ITSG-Grace2018: overview and evaluation of a new GRACE-only gravity field time series. J Geophys Res Solid Earth 124(8):9332–9344. https://doi.org/10.1029/2019JB017415

Ligtenberg SRM, Helsen MM, van den Broeke MR (2011) An improved semi-empirical model for the densification of Antarctic firn. Cryosphere 5(4):809–819. https://doi.org/10.5194/tc-5-809-2011

Ligtenberg SRM, Kuipers Munneke P, van den Broeke MR (2014) Present and future variations in Antarctic firn air content. Cryosphere 8(5):1711–1723. https://doi.org/10.5194/tc-8-1711-2014

Loomis BD, Rachlin KE, Wiese DN, Landerer FW, Luthcke SB (2020) Replacing GRACE/GRACE-FO C_30 with satellite laser ranging: impacts on Antarctic Ice Sheet mass change. Geophys Res Lett 47(3) 47(3):e2019GL085488. https://doi.org/10.1029/2019GL085488

Martín-Español A, King MA, Zammit-Mangion A, Andrews SB, Moore P, Bamber JL (2016a) An assessment of forward and inverse GIA solutions for Antarctica. J Geophys Res Solid Earth 121(9):6947–6965. https://doi.org/10.1002/2016JB013154

Martín-Español A, Zammit-Mangion A, Clarke PJ, Flament T, Helm V, King MA, Luthcke SB, Petrie E, Rémy F, Schön N, Wouters B, Bamber JL (2016b) Spatial and temporal Antarctic Ice Sheet mass trends, glacio-isostatic adjustment and surface processes from a joint inversion of satellite altimeter, gravity and GPS data. J Geophys Res Earth Surf 121(2):182–200. https://doi.org/10.1002/2015JF003550

Matsumoto M, Nishimura T (1998) Mersenne twister: a 623-dimensionally equidistributed uniform pseudo-random number generator. ACM Trans Model Comput Simul 8(1):3–30. https://doi.org/10.1145/272991.272995

Mayer-Gürr T, Behzadpur S, Ellmer M, Kvas A, Klinger B, Strasser S, Zehentner N (2018) ITSG-Grace2018 - Monthly. Daily and static gravity field solutions from GRACE, GFZ data services. https://doi.org/10.5880/ICGEM.2018.003

McMillan M, Shepherd A, Sundal A, Briggs K, Muir A, Ridout A, Hogg A, Wingham D (2014) Increased ice losses from Antarctica detected by CryoSat-2. Geophys Res Lett 41(11):3899–3905. https://doi.org/10.1002/2014GL060111

Noël B, van de Berg WJ, van Wessem JM, van Meijgaard E, van As D, Lenaerts JTM, Lhermitte S, Kuipers Munneke P, Smeets CJPP, van Ulft LH, van de Wal RSW, van den Broeke RM (2018) Modelling the climate and surface mass balance of polar ice sheets using RACMO2–Part 1: Greenland (1958–2016). Cryosphere 12(3):811–831. https://doi.org/10.5194/tc-12-811-2018

Peltier WR, Argus DF, Drummond R (2015) Space geodesy constrains ice age terminal deglaciation: the global ICE-6G_C (VM5a) model: global glacial isostatic adjustment. J Geophys Res Solid Earth 120(1):450–487. https://doi.org/10.1002/2014JB011176

Pollack NH (1973) Spherical harmonic representation of the gravitational potential of a point mass, a spherical cap, and a spherical rectangle. J Geophys Res 78(11):1760–1768. https://doi.org/10.1029/JB078i011p01760

Purcell A, Tregoning P, Dehecq A (2016) An assessment of the ICE6G_C(VM5a) glacial isostatic adjustment model. J Geophys Res Solid Earth 121(5):3939–3950. https://doi.org/10.1002/2015JB012742

Rietbroek R, Brunnabend S-E, Kusche J, Schröter J, Dahle C (2016) Revisiting the contemporary sea-level budget on global and regional scales. Proc Natl Acad Sci USA 113(6):1504–1509. https://doi.org/10.1073/pnas.1519132113

Riva REM, Gunter BC, Urban TJ, Vermeersen BLA, Lindenbergh RC, Helsen MM, Bamber JL, van de Wal RSW, van den Broeke MR, Schutz BE (2009) Glacial Isostatic Adjustment over Antarctica from combined ICESat and GRACE satellite data. Earth Planet Sci Lett 288(3–4):516–523. https://doi.org/10.1016/j.epsl.2009.10.013

Sasgen I, Martín-Español A, Horvath A, Klemann V, Petrie EJ, Wouters B, Horwath M, Pail R, Bamber JL, Clarke PJ, Konrad H, Drinkwater MR (2017) Joint inversion estimate of regional glacial isostatic adjustment in Antarctica considering a lateral varying Earth structure (ESA STSE Project REGINA). Geophys J Int 211(3):1534–1553. https://doi.org/10.1093/gji/ggx368

Schröder L, Horwath M, Dietrich R, Helm V, van den Broeke MR, Ligtenberg SRM (2019) Four decades of Antarctic surface elevation changes from multi-mission satellite altimetry. Cryosphere 13(2):427–449. https://doi.org/10.5194/tc-13-427-2019

Shepherd, A, Ivins E, Rignot E, Smith B, van den Broeke M, Velicogna I, Whitehouse P, Briggs K, Joughin I, Krinner G, Nowicki S, Payne T, Scambos T, Schlegel N, A G, Agosta C, Ahlstrøm A, Babonis G, Barletta V, Blazquez A, Bonin J, Csatho B, Cullather R, Felikson D, Fettweis X, Forsberg R, Gallee H, Gardner A, Gilbert L, Groh A, Gunter B, Hanna E, Harig C, Helm V, Horvath A, Horwath M, Khan S, Kjeldsen KK, Konrad H, Langen P, Lecavalier B, Loomis B, Luthcke S, McMillan M, Melini D, Mernild S, Mohajerani Y, Moore P, Mouginot J, Moyano G, Muir A, Nagler T, Nield G, Nilsson J, Noel B, Otosaka I, Pattle ME, Peltier WR, Pie N, Rietbroek R, Rott H, Sandberg-Sørensen L, Sasgen I, Save H, Scheuchl B, Schrama E, Schröder L, Seo K-W, Simonsen S, Slater T, Spada G, Sutterley T, Talpe M, Tarasov L, van de Berg WJ, van der Wal W, van Wessem JM, Vishwakarma BD, Wiese D, Wouters B (2018) Mass balance of the Antarctic Ice Sheet from 1992 to 2017. Nature 558(7709):219–222. https://doi.org/10.1038/s41586-018-0179-y

Shepherd A, Ivins E, Rignot E, Smith B, van den Broeke M, Velicogna I, Whitehouse P, Briggs K, Joughin I, Krinner G, Nowicki S, Payne T, Scambos T, Schlegel N, Agosta GAC, Ahlstrøm A, Babonis G, Barletta V, Bjørk A, Blazquez A, Bonin J, Colgan W, Csatho B, Cullather R, Engdahl M, Felikson D, Fettweis X, Forsberg R, Hogg A, Gallee H, Gardner A, Gilbert L, Gourmelen N, Groh A, Gunter B, Hanna E, Harig C, Helm V, Horvath A, Horwath M, Khan S, Kjeldsen K, Konrad H, Langen P, Lecavalier B, Loomis B, Luthcke S, McMillan M, Melini D, Mernild S, Mohajerani Y, Moore P, Mottram R, Mouginot J, Moyano G, Muir A, Nagler T, Nield G, Nilsson J, Noël B, Otosaka I, Pattle M, Peltier W, Pie N, Rietbroek R, Rott H, Sørensen L, Sasgen I, Save H, Scheuchl B, Schrama E, Schröder L, Seo K-W, Simonsen S, Slater T, Spada G, Sutterley T, Talpe M, Tarasov L, Jan van de Berg W, van der Wal W, van Wessem J, Vishwakarma B, Wiese D, Wilton D, Wagner T, Wouters B, Wuite J (2019) Mass balance of the Greenland Ice Sheet from 1992 to 2018. Nature. https://doi.org/10.1038/s41586-019-1855-2

Spada G, Melini D (2019) SELEN^4 (SELEN version 4.0): a Fortran program for solving the gravitationally and topographically self-consistent sea-level equation in glacial isostatic adjustment modeling. Geosci Model Dev 12(12):5055–5075. https://doi.org/10.5194/gmd-12-5055-2019

Strößenreuther U, Horwath M, Schröder L (2020) How different analysis and interpolation methods affect the accuracy of ice surface elevation changes inferred from satellite altimetry. Math Geosci https://doi.org/10.1007/s11004-019-09851-3

Stuhne GR, Peltier WR (2015) Reconciling the ICE-6G_C reconstruction of glacial chronology with ice sheet dynamics: the cases of Greenland and Antarctica. J Geophys Res Earth Surf. https://doi.org/10.1002/2015JF003580

Sun Y, Riva REM (2020) A global semi-empirical glacial isostatic adjustment (GIA) model based on Gravity Recovery and Climate Experiment (GRACE) data. Earth Syst Dyn 11(1):129–137. https://doi.org/10.5194/esd-11-129-2020

Swenson S, Chambers D, Wahr J (2008) Estimating geocenter variations from a combination of GRACE and ocean model output. J Geophys Res B 113:B08410. https://doi.org/10.1029/2007JB005338

Tegmark M (1996) An Icosahedron-based Method for Pixelizing the Celestial Sphere. Astrophys J 470(2):L81–L84. https://doi.org/10.1086/310310

Thomas ID, King MA, Bentley MJ, Whitehouse PL, Penna NT, Williams SDP, Riva REM, Lavallee DA, Clarke PJ, King EC, Hindmarsh RCA, Koivula H (2011) Widespread low rates of Antarctic glacial isostatic adjustment revealed by GPS observations. Geophys Res Lett 38(22):L22302. https://doi.org/10.1029/2011GL049277

Uebbing B, Kusche J, Rietbroek R, Landerer F (2019) Processing choices affect ocean mass estimates from GRACE. J Geophys Res Oceans 124:1029–1044. https://doi.org/10.1029/2018JC014341

van Wessem JM, van de Berg WJ, Noël BPY, van Meijgaard E, Amory C, Birnbaum G, Jakobs C, Krüger K, Lenaerts JTM, Lhermitte S, Ligtenberg SRM, Medley B, Reijmer CH, van Tricht K, Trusel L, van Ulft LH, Wouters B, Wuite J, van den Broeke MR (2018) Modelling the climate and surface mass balance of polar ice sheets using RACMO2—Part 2: Antarctica (1979–2016). Cryosphere 12(4):1479–1498. https://doi.org/10.5194/tc-12-1479-2018

Verjans V, Leeson AM, Stevens C, van Wessem JM, van de Berg W, van den Broeke, C. Kittel, C. Amory, X. Fettweis, N. Hansen, F. Boberg, and R. Mottram, M (2021) Uncertainty in East Antarctic firn thickness constrained using a model ensemble approach. Geophys Res Lett 48(7):e2020GL092060. https://doi.org/10.1029/2020GL092060

Wahr J, Molenaar M, Bryan F (1998) Time variability of the Earth's gravity field: hydrological and oceanic effects and their possible detection using GRACE. J Geophys Res 103(B12):30205–30229. https://doi.org/10.1029/98JB02844

Whitehouse P, Gomez N, King M, Wiens D (2019) Solid Earth change and the evolution of the Antarctic Ice Sheet. Nat Commun 10(1):503. https://doi.org/10.1038/s41467-018-08068-y

Willen MO, Horwath M, Schröder L, Groh A, Ligtenberg SRM, Kuipers Munneke P, van den Broeke MR (2020) Sensitivity of inverse glacial isostatic adjustment estimates over Antarctica. Cryosphere 14(1):349–366. https://doi.org/10.5194/tc-14-349-2020

Willen MO, Broerse T, Groh A, Wouters B, Kuipers Munneke P, Horwath M, van den Broeke M, Schröder L (2021) Separating long-term and short-term mass changes of Antarctic ice drainage basins: a coupled state space analysis of satellite observations and model products. J Geophys Res Earth Surf 126(6):e2020JF005966. https://doi.org/10.1029/2020JF005966

Wu X, Heflin MB, Schotman H, Vermeersen BLA, Dong D, Gross RS, Ivins ER, Moore AW, Owen SE (2010) Simultaneous estimation of global present-day water transport and glacial isostatic adjustment. Nat Geosci 3(9):642–646. https://doi.org/10.1038/ngeo938

6 Inversion of real data for glacial isostatic adjustment and ice mass changes in Antarctica

The simulation study of the approach presented in P3 was subject to some simplifications, but P3 proved the feasibility of the inversion method. The next step is to apply the approach to real data. This chapter shows results of a first experiment with a focus on Antarctica where real-world data was combined. Note that this experiment focuses only on mass redistributions without considering steric sea level changes. The implementation in the full inversion for all sea level components should be the task of future work (Chapter 7).

With the focus on Antarctica, the parametrization and choice of observations are modified here. The experiment here restricts to the following data sets: (1) global gravity fields, $\boldsymbol{d}^{\text{GRAV}}$, (2) surface elevation changes of the AIS, $\boldsymbol{d}^{\text{AIS-ALT}}$, and (3) changes of the FAC of the AIS, $\boldsymbol{d}^{\text{AIS-FAC}}$. Here, satellite altimetry and FAC changes of the GIS are not explicitly implemented. Furthermore, glaciers and hydrology are parametrized, because, when using real-world global gravity fields, mass changes of glaciers and hydrology reservoirs cannot be neglected. The observation equation (Eq. 16 in P3) is adjusted to the specific case here as follows:

$$\begin{pmatrix} \boldsymbol{d}^{\text{GRAV}} \\ \boldsymbol{d}^{\text{AIS-ALT}} \\ \boldsymbol{d}^{\text{AIS-FAC}} \end{pmatrix} + \boldsymbol{e} = \begin{pmatrix} \boldsymbol{X}^{\text{GRAV}}_{\text{GIA}} & \boldsymbol{X}^{\text{GRAV}}_{\text{AIS-IMC}} & \boldsymbol{0} & \boldsymbol{X}^{\text{GRAV}}_{\text{GIS-IMC}} & \boldsymbol{X}^{\text{GRAV}}_{\text{GLAC}} & \boldsymbol{X}^{\text{GRAV}}_{\text{HYD}} \\ \boldsymbol{X}^{\text{AIS-ALT}}_{\text{GIA}} & \boldsymbol{X}^{\text{AIS-ALT}}_{\text{AIS-IMC}} & \boldsymbol{X}^{\text{AIS-ALT}}_{\text{AIS-FAC}} & \boldsymbol{0} & \boldsymbol{0} & \boldsymbol{0} \\ \boldsymbol{0} & \boldsymbol{0} & \boldsymbol{X}^{\text{AIS-FAC}}_{\text{AIS-FAC}} & \boldsymbol{0} & \boldsymbol{0} & \boldsymbol{0} \end{pmatrix} \begin{pmatrix} \boldsymbol{\beta}_{\text{GIA}} \\ \boldsymbol{\beta}_{\text{AIS-IMC}} \\ \boldsymbol{\beta}_{\text{AIS-FAC}} \\ \boldsymbol{\beta}_{\text{GIS-IMC}} \\ \boldsymbol{\beta}_{\text{GLAC}} \\ \boldsymbol{\beta}_{\text{HYD}} \end{pmatrix}. \quad (6.1)$$

P3 did not include the parameters for glacier mass changes, $\boldsymbol{\beta}_{\text{GLAC}}$, and continental hydrology mass changes, $\boldsymbol{\beta}_{\text{HYD}}$. The matrices $\boldsymbol{X}^{\text{GRAV}}_{\text{GIS-IMC}}$, $\boldsymbol{X}^{\text{GRAV}}_{\text{GLAC}}$, and $\boldsymbol{X}^{\text{GRAV}}_{\text{HYD}}$ link gravity field changes associated with IMC of the GIS, glaciers, and hydrology, respectively. Glacier mass changes and continental hydrology mass changes are parametrized with 68 and 60 globally consistent fingerprints, respectively, from Rietbroek et al. (2016) and Uebbing et al. (2019). In contrast to P3, the parametrization of IMC in Greenland applies 16 fingerprints for the 8 drainage basins of the GIS (Zwally et al., 2012). For this purpose, each basin is divided into a part below and above 2000 m surface elevation, i.e. in total 16 sub-basins of the GIS. The mass change of each sub-basin is not assumed to be uniform. Instead, a more realistic mass change pattern within each sub-basin is chosen based on mean rates of surface elevation changes derived from CryoSat-2 satellite altimetry (updated according to Helm et al., 2014). The mass change pattern of each sub-basin is then used to create a globally consistent fingerprint (cf. Sect. 3.2 in P3). The remaining parameters, $\boldsymbol{\beta}$, and design matrices, $\boldsymbol{X}$, are chosen analogously to P3.

The observations, $\boldsymbol{d}$, are mean rates according to the time period from Jan 2011 until Dec 2020. The mean rate of gravity changes is derived from ITSG-Grace2018 (Mayer-Gürr et al., 2018) products which are based on GRACE and GRACE-FO observations. These level-2 products have a low noise level compared to other products, with retaining almost completely the signal (Ditmar, 2022). The gravity fields are complemented with degree-1 products derived according to Swenson et al. (2008), Bergmann-Wolf et al. (2014), and Sun et al. (2016). c_{20} coefficients, and c_{30} coefficients in case of GRACE-FO and GRACE accelerometer failures, are replaced with Satellite Laser Ranging products (Loomis et al., 2020). The surface elevation changes are derived from updated CryoSat-2 products according to Helm et al. (2014). The variant used here is the median of the altimetry ensemble in P3. Finally, the FAC changes are derived from the RACMO2.3p2 SMB product (Wessem et al., 2018) and the IMAU-FDM v1.2A firn-thickness change product (Veldhuijsen et al., 2022). Surface elevation and FAC changes are resampled to a grid of 50 km × 50 km by calculating the mean of all observations within a grid cell.

The error covariance information utilized in $\boldsymbol{P}$ is the same as implemented in Experiment 3 in P3. Furthermore, variance components for the three observational groups gravimetry, altimetry, and FAC changes are introduced and iteratively adjusted via variance component estimation (Koch, 1999).

Initial tests showed strong spatial oscillations of the GIA result in Antarctica. This is reduced using a Tikhonov regularization (Tikhonov et al., 1995) by extending the normal equation (cf. Eq. 12 in P3) with a regularization matrix, $\boldsymbol{\Psi}$:

$$\hat{\boldsymbol{\beta}} = (\boldsymbol{N} + \boldsymbol{\Psi}^{\mathrm{T}}\boldsymbol{\Psi})^{-1}\boldsymbol{n} \tag{6.2}$$

$$\boldsymbol{N} = \boldsymbol{X}^{\mathrm{T}}\boldsymbol{P}\boldsymbol{X} \tag{6.3}$$

$$\boldsymbol{n} = \boldsymbol{X}^{\mathrm{T}}\boldsymbol{P}\boldsymbol{d}. \tag{6.4}$$

Here, $\boldsymbol{\Psi}$ is designed to only regularize the Antarctic GIA parameters, $\boldsymbol{\beta}_{\mathrm{GIA,ANT}}$. $\boldsymbol{\Psi}$ is a square matrix with the two dimensions equal to the total amount of parameters. The non-zero elements are

$$\psi_{ij} = \varepsilon\delta_{ij}, \qquad i, j = 1, ..., 189. \tag{6.5}$$

189 is the number of Antarctic GIA parameters and ε is the regularization factor. This factor is chosen according to a trade-off between minimizing the norm of the residuals, $\|\boldsymbol{e}\|_2 = \sqrt{\boldsymbol{e}^{\mathrm{T}}\boldsymbol{e}}$, and minimizing the norm of the parameters, $\|\boldsymbol{\beta}_{\mathrm{GIA,ANT}}\|_2$. This trade-off between a best-fit solution and a short solution vector, i.e. a simple solution in terms of Occam's razor, can be determined using the L-curve criterion (Hansen,

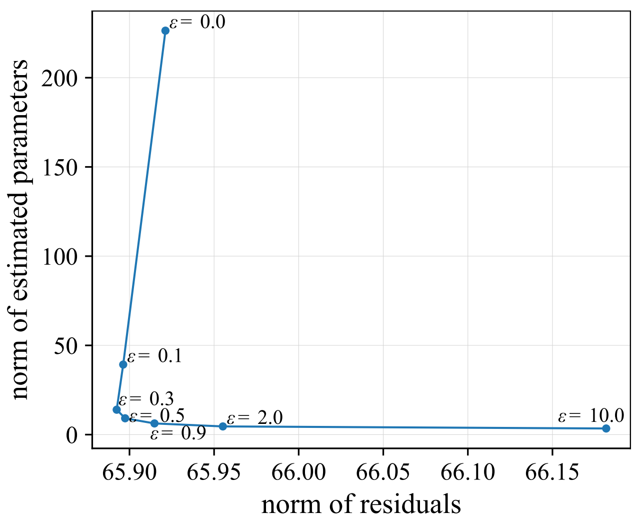

Figure 6.1: The L-curve illustrating the trade-off between the norm of residuals and the norm of estimated Antarctic GIA parameters depending on the regularization factor ε.

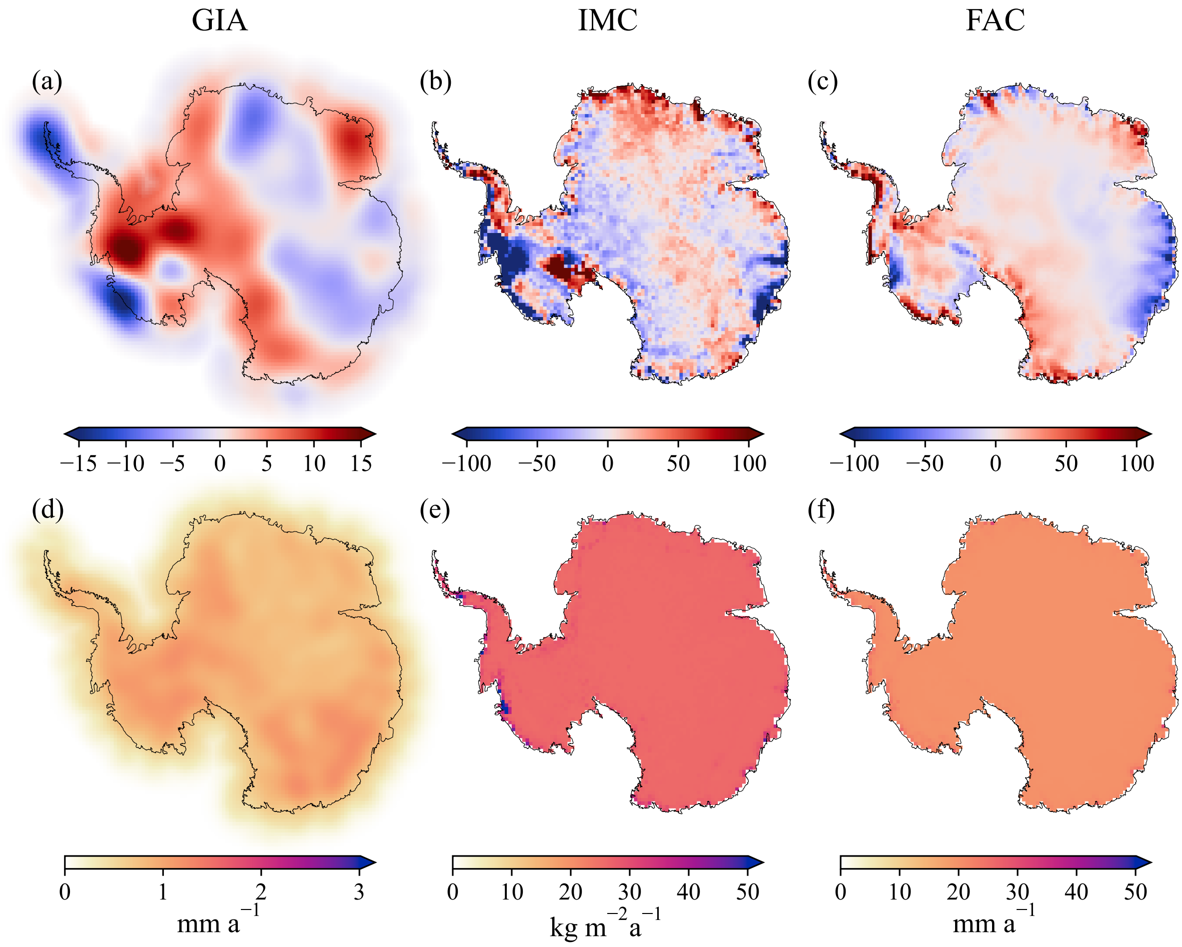

Figure 6.2: The results (a–c) and their formal uncertainties (d–f) of the inversion experiment using real-world data from Jan 2011 to Dec 2020. a+d, b+e, and c+f illustrate GIA-induced bedrock motion, IMC-induced surface density change, and FAC changes, respectively. The uncertainties are two times of the standard deviation from error-covariance propagation.

2001). Figure 6.1 illustrates the relation between the norm of residuals and the norm of parameters in dependence on the regularization factor of the real-data example. Based on the L-curve test (Figure 6.1), a regularization factor of $\varepsilon = 0.5$ is chosen.

The results of the experiment, which are in focus here, are estimates of GIA bedrock motion in Antarctica, AIS IMC, and AIS FAC changes (Figure 6.2a–c). Figure 6.2d–f show the formal uncertainties. The uncertainties of the parameters are derived from the propagated error covariance information of the observations (e.g. Menke, 2012). Integrated over the grounded AIS the IMC is $(-150 \pm 5)\,\mathrm{Gt\,a^{-1}}$, and the change of FAC is $(40 \pm 5)\,\mathrm{km^3\,a^{-1}}$. The Antarctic GIA mass effect integrated over the AIS with a buffer zone amounts to $(72 \pm 4)\,\mathrm{Gt\,a^{-1}}$. The indicated uncertainties are two times of the formally propagated standard deviation.

The inversion experiment using real-world data leads to integrated quantities similar to estimates of IMC and the GIA effect published elsewhere (Shepherd et al., 2018). The integrated GIA mass effect is within the range of GIA predictions presented by Whitehouse et al. (2019). Notably, this result is estimated in a globally consistent framework without applying any conventional filtering strategies like Gaussian smoothing or a decorrelation filter. The spatial pattern is comparable to other inverse GIA estimates (Riva et al., 2009; Gunter et al., 2014; Engels et al., 2018; Martín-Español et al., 2016b). Main differences to these GIA estimates exist in East Antarctica, where in particular Engels et al. (2018) (Figure 6.3) and Sasgen et al.

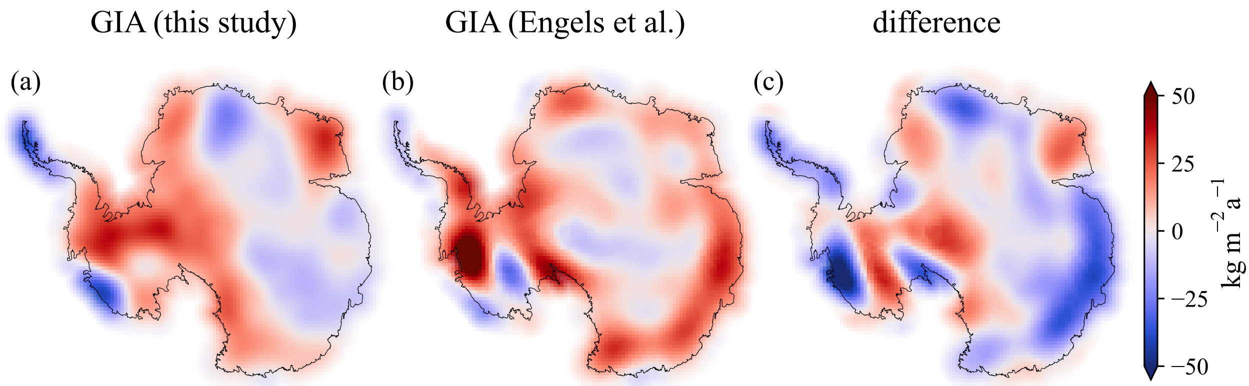

Figure 6.3: The estimated GIA-induced surface density change from an inverse approach applied in this this study shown in (a) and from an alternative inverse approach applied in Engels et al. (2018) shown in (b). (c) illustrate the difference of both estimates (a−b). The results in (a) and (b) are based on different data sets over different time intervals: Jan 2011 to Dec 2020 (a) and Feb 2003 to Oct 2009 (b).

(2017) found significant uplift rates. Additionally in West Antarctica there is disagreement in the southern part of the Ross Ice Shelf. Further, the magnitude and location of the maximum uplift in the Amundsen Sea Embayment differs (Figure 6.3). Interestingly, the results indicate a negative bedrock motion in the Getz Ice Shelf region (∼120°–130°W). This anomaly ("Getz bubble") is not predicted by forward models (Whitehouse et al., 2019), but is apparent in the GIA estimates according to Sasgen et al. (2017), Engels et al. (2018) (somewhat offshore in Figure 6.3), and Riva et al. (2009) (clipped in Fig. 3a in Riva et al. (2009), but visible in Fig. 2f in Martín-Español et al. (2016a)). Part of this anomaly may be explained by a missing signal content in the altimetry observations compared to gravity fields from GRACE and GRACE-FO (Sasgen et al., 2019). Radar altimetry measurements only capture points with the highest surface elevation within the footprint. This leads to an incomplete sampling of surface elevation changes especially in steep-slope topography regions. For example, surface elevation changes due to changing IFD in narrow valleys may remain unobserved (Schröder et al., 2019). The inversion attributes this systematic difference in the signal content due to sampling issues to an artificial GIA effect. As another reason, the parametrization is limited to the grounded AIS. This parametrization misses the peripheral glaciers, e.g. on the islands offshore Getz Ice Shelf. Potentially, this is a region of interest for further investigation.

A task of future work is to validate the preliminary results presented here with GNSS measurements and geophysical modelling results. Further, the sensitivity of the inversion results towards applying alternative data products should be investigated, e.g. with newly available altimetry time series (e.g. Nilsson et al., 2022) and alternative GRACE/GRACE-FO level-2 products. Additional methodological developments hold promise to further improve the results, e.g. the regularization (Equation 6.5) can be tuned to fit GIA-induced bedrock motion from GNSS observations or other external information. Also the IMC parametrization will be extended in future work to include peripheral glaciers. Furthermore, future investigations may find a strategy to tackle the systematic differences between satellite gravimetry and altimetry products in regions with steep-slope topography, e.g. the regions of outlet glaciers. And, of course, another upcoming task is to implement this Antarctica-focused estimation strategy in the global inversion framework allowing to estimate all contributions to sea level change (Chapter 7).

7 Outlook

The methodology presented in P3 (Willen et al., 2022) and findings from Chapter 6 should be utilized in a global inversion framework allowing to estimate all contributions to sea level change. For this purpose, the approach according to Rietbroek et al. (2016) needs to be extended by implementing additional parameters for IMC and GIA. In the case of Antarctic IMC, the framework from Rietbroek et al. (2016) is originally designed to monthly estimate 27 scale factors for 27 drainage basins (Zwally et al., 2012). Rietbroek et al. (2016) parametrized the present-day GIA effect using five regional GIA patterns, including one pattern for the Antarctic GIA signal. To spatially resolve GIA in Antarctica, the single Antarctic GIA pattern could be replaced by 189 local patterns as demonstrated in P3. The co-estimation of the additional GIA parameters could be enabled by implementing additional observational information from satellite altimetry over ice sheets. But, the parametrization of IMC with 27 fingerprints would be too coarse to allow a joint estimation of IMC and GIA. According to P3, Antarctic IMC could be parametrized on a grid of $50\,\text{km} \times 50\,\text{km}$, i.e. with 4755 parameters. As in Rietbroek et al. (2016), GIA could be parametrized as a linear trend with constant rate over time, whereby IMC and other parameters will be resolved monthly. This assumption of linearity over time in case of GIA would allow to computationally simplify the estimation strategy by applying a linear parameter transformation (e.g. Section C.5 in Rietbroek, 2014).

The determination of the present-day GIA effect using geodetic observation methods (inverse GIA estimation), as it is also the subject of this work, serves primarily to reduce the GIA-related uncertainty in gravimetric mass balance estimates. As stated in Chapter 1, different GIA modelling results vary significantly, especially in Antarctica, since the assumptions about ice history and solid-Earth rheology deviate extensively (Argus et al., 2014). Thus, the measurement of bedrock motion by GNSS and the combination of satellite gravimetry and satellite altimetry were able to reveal GIA-induced changes of the solid Earth which were hardly included in GIA modelling results, e.g. in the Amundsen Sea Embayment (Groh et al., 2012). This raises questions for the geophysical models to represent the local and regional settings of rheology as well as all parts of the rheology-relevant ice history. For example, the late Holocene ice loading history is not included in the ice history so far (Whitehouse et al., 2019). But this Holocene ice history is particularly relevant to explain the solid-Earth response in the Amundsen Sea Embayment which is on decadal to centennial, and not millennial, time scales. This is because of the postulated low viscosities in this region (Barletta et al., 2018). Geodetic observational methods may also help to constrain and extend the geophysical models in future work, e.g. as done by incorporating information from GNSS in GIA modelling in the Amundsen Sea Embayment (Barletta et al., 2018), in Greenland (Adhikari et al., 2021), and in global GIA models (Caron et al., 2018). Argus et al. (2021) even constrained the solid-Earth rheology with GRACE and GNSS observations. The continuous observation of Earth's gravity and geometry changes as well as estimated rheological properties from seismological measurements (Ivins et al., 2021) may further improve GIA modelling results in the near future and hold promise to enhance the understanding of GIA beyond *medium confidence* (Fox-Kemper et al., 2021).

Moreover, the causal processes that lead to IMC require further investigation. In future work investigations on sources of IMC from data combinations may be helpful in understanding the more Greenland-specific processes, such as surface melting, seasonal variations of IFD, and adjustment processes of the GIS to climate change. In Antarctica a major uncertainty is the dynamic stability of the APIS and the WAIS in the future. Diener et al. (2021) quantified the acceleration in the AIS ice discharge which significantly matters in projecting Antarctica's contribution to sea level change. Further, Barletta et al. (2018) predicted also stabilizing effects due to the bedrock uplift in the Amundsen Sea Embayment which could somewhat counteract an accelerating IFD contribution to the mass balance. Another major uncertainty in the AIS mass balance originates from the uncertainty of the mass balance of the EAIS (Fig. 2 in Shepherd et al., 2018). Firstly, this is due to the mentioned uncertainty of the present-day GIA effect. Geophysical models even predict the present-day GIA effect with different signs in East Antarctica (Whitehouse et al., 2019). Furthermore, the most part of the East Antarctic bedrock is inaccessible for a direct observation of the bedrock motion. Secondly, different SMB modelling results (Mottram et al., 2021) and firn modelling results (Verjans et al., 2021) show significant differences in the EAIS. Possible climate trends in the SMB and firn thickness change may have been neglected so far. Thirdly, there is ambiguity of a potential ongoing adjustment of IFD in East Antarctica to climate changes in the past (Zwally et al., 2015; Richter et al., 2016). As shown in P2, separating these three long-term changes is a key challenge in the evaluation of satellite observations. The understanding of GIA in East Antarctica would benefit from a possibility to observe the GIA-induced solid-Earth deformation independent from gravimetry and altimetry. For the second point, climate trends in East Antarctica, investigations of large-scale variations observed by satellite gravimetry and altimetry may further contribute to understanding the climate variability of the (E)AIS. These large-scale variations are related to atmospheric interannual variability, e.g. the El Niño-Southern Oscillation (ENSO), the Southern Annular Mode (SAM), or the Antarctic Circumpolar Wave (ACW). Investigations of interannual patterns and their causes with satellite methods were pursued by Horwath et al. (2012), Mémin et al. (2015), Kaitheri et al. (2021), and Shi et al. (2022). Last but not least, trends in the basal mass balance of the grounded ice sheet are an open question that remains unconsidered in ice mass balance studies so far.

Satellite missions launched a few years ago and future missions will provide data products with improved quality of gravity field changes (e.g. Pail et al., 2019) as well as of surface elevation changes over ice sheets (e.g. Nilsson et al., 2022). They will continuously extend the time period in which observational data sets are available. The improved product quality is expected to increase both the precision and accuracy of IMC estimates. Further, a longer total observation period and a higher spatial resolution will potentially allow to extent the temporal and spatial parametrization applied in P2 and P3. Beyond data combination approaches, data assimilations of observational data from gravimetry, altimetry, and GNSS into ice sheet models and GIA models could help to answer questions about the process implementations in these models. Another step further beyond, it may be possible in the future that global inversion approaches allow to determine surface mass changes in such a precise way that other solid-Earth signals, e.g. from core dynamics, can be estimated (Dumberry and Mandea, 2022). Nevertheless the following challenges will remain in future work when combining multiple observational and model data: (i) Justify assumptions when parametrizing the geophysical processes, (ii) account for quality limitations due to errors and sampling of the observational data, (iii) characterize the uncertainty of modelling results, and (iv) find appropriate observation(s) independent of the estimate to assess the results.

8 Conclusions

Products derived from satellite gravimetry and satellite altimetry as well as regional climate and firn modelling reveal high agreement over the ice sheets in Greenland and Antarctica (Figure 3.2). This work examines, how these products can be combined to attribute mass as well as volume changes, inherent in observed gravity and geometry changes, to their sources. Within the three publications combination methods have been investigated and developed with a focus on resolving the present-day GIA effect in Antarctica. This has been pursued to improve estimates of the contribution of the ice sheets to global sea level change.

In P1 it was demonstrated that an inverse approach to resolve GIA according to Gunter et al. (2014) in Antarctica is highly sensitive to input data sets. It was shown, that a major source of uncertainties are degree-1 and c_{20} products used to complement GRACE monthly gravity fields. There is a practical strategy to remove the bias introduced by degree-1 and c_{20} products. This bias correction and filtering applied during data processing leads to robust results, but regionally constraints the estimate and revokes global consistency. This disables to utilize this inverse approach in a global inversion framework, e.g. the one presented by Rietbroek et al. (2016). Further, the approach hardly allows to account for the temporal and spatial sampling characteristics of the used sensors. A side investigation from Kappelsberger et al. (2021), applying this approach to Greenland, demonstrated that it was not possible to extract a meaningful GIA estimate for Greenland so far. The uncertainty characterization of the SMB and the firn thickness products revealed the challenges of the signal separation on trend level between sources of mass and volume changes in the firn or ice layer of the ice sheet.

This challenge was explored in P2 by utilizing a state space approach for time series of Antarctic drainage basins. To separate the sources of mass and volume changes, they were parametrized by their temporal characteristic. It is distinguished between (i) long-term changes observed commonly by altimetry and gravimetry which are likely induced by changes of IFD, an (ii) short-term changes resulting from SMB/firn fluctuations and (correlated) errors. It was possible to fit the accelerated ice-dynamical loss in West Antarctica without the artificial selection of separate periods with constant trends such as deterministic models may use, e.g. several mean rates for various time periods. The found long-term variability of the ice-dynamic signal is low in East Antarctica. Remarkably, a positive long-term contribution at almost a constant rate was found e.g. in Dronning Maud Land and Enderby Land of the EAIS. This raises questions upon interpretation of long-term errors or potential long-term thickening. So far, it was not attainable to attribute all of the separated short-term signals to specific sources.

The feasibility of a methodology that enables to spatially resolve the present-day GIA effect in Antarctica in a global inversion framework was investigated in P3. It was shown that it is possible to co-estimate present-day GIA, IMC, and FAC over both ice sheets in this global framework by the integrated use of information from satellite gravimetry, satellite altimetry, regional climate modelling, and firn modelling. With the presented methodology, it is possible to resolve GIA patterns in Antarctica that are not predicted by geophysical GIA modelling. In the study, the input-data uncertainty was characterized using real world observations. Further, it was concluded that the uncertainty characterization accounting for spatially correlated errors is essential to obtain sound results. Otherwise, the detected signals may vanish in the noise of the estimate. In a regional application of the methodology from P3 to Antarctica (Chapter 6), over the time interval from Jan 2011 to Dec 2020, an IMC of $(-150 \pm 5)\,\mathrm{Gt\,a^{-1}}$ and a GIA-induced mass effect of

$(72 \pm 4)\,\mathrm{Gt\,a^{-1}}$ is estimated.

For Antarctica the findings presented here confirm the different spatio-temporal characteristic of IMC between the West and the East Antarctic Ice Sheet. A promising methodology has been found to co-estimate the present-day GIA effect by combining data sets in the presence of realistic data quality limitations. This provides the possibility to determine the present-day GIA effect as an alternative to GIA modelling results, which differ strongly in Antarctica (Whitehouse et al., 2019). It can be expected that future GIA modelling results will further improve by accounting for the broader range of the ice history on decadal to millennial time scales. In addition to that local and regional specific settings of the Earth structure, such as distinguishing between East and West Antarctica (Coulon et al., 2021) and implementing 3-D Earth models (Wal et al., 2015; Bagge et al., 2021) will improve GIA modelling results. In Greenland, the integrated GIA mass effect is small compared to the IMC, i.e. GIA modelling errors are a smaller issue in gravimetric mass balance estimates compared to Antarctica. Nevertheless, GIA modelling results disagree in Greenland, too (Figure 2.3). But compared to Antarctica, smaller improvements in the IMC can be expected here by co-estimating the present-day GIA with a gravimetry-altimetry combination.

Finally, it is worth noting that the quantification of the present-day GIA effect from satellite geodetic observations is very relevant to geodynamic questions, in addition to questions about the mass balance of the ice sheets. Observations allow the detection of mismatches that are not predicted by GIA modelling. However, it remains the task of GIA modelling to reconcile the rheology of Earth materials and the loading history, but probably with the aid of (future) geodetic satellite observations. From the observational perspective, combining satellite gravimetry and satellite altimetry data is so far the only access to solid-Earth deformation of regions covered with ice, since in these areas there is no direct observation of bedrock motion.

References

Adhikari, S., L. Milne G.A.and Caron, S.A. Khan, K.K. Kjeldsen, J. Nilsson, E. Larour, and E.R. Ivins (2021). “Decadal to Centennial Timescale Mantle Viscosity Inferred from Modern Crustal Uplift Rates in Greenland”. In: *Geophys. Res. Lett.* 48.19, e2021GL094040. DOI: 10.1029/2021GL094040.

Agosta, C., C. Amory, C. Kittel, A. Orsi, V. Favier, H. Gallée, M. R. van den Broeke, J. T. M. Lenaerts, J. M. van Wessem, W. J. van de Berg, and X. Fettweis (2019). “Estimation of the Antarctic surface mass balance using the regional climate model MAR (1979–2015) and identification of dominant processes”. In: *The Cryosphere* 13.1, pp. 281–296. ISSN: 1994-0424. DOI: 10.5194/tc-13-281-2019.

Argus, D.F., W.R. Peltier, G. Blewitt, and C. Kreemer (2021). “The Viscosity of the Top Third of the Lower Mantle Estimated Using GPS, GRACE, and Relative Sea Level Measurements of Glacial Isostatic Adjustment”. In: *J. Geophys. Res. Solid Earth* 126.5. ISSN: 2169-9313. DOI: 10.1029/2020JB021537.

Argus, D.F., W.R. Peltier, R. Drummond, and A.W. Moore (2014). “The Antarctica component of postglacial rebound model ICE-6G_C (VM5a) based on GPS positioning, exposure age dating of ice thicknesses, and relative sea level histories”. In: *Geophys. J. Int.* 198.1, pp. 537–563. ISSN: 0956-540X. DOI: 10.1093/gji/ggu140.

Bagge, M., V. Klemann, B. Steinberger, M. Latinović, and M. Thomas (2021). “Glacial-Isostatic Adjustment Models Using Geodynamically Constrained 3D Earth Structures”. In: *Geochemistry, Geophysics, Geosystems* 22.11. ISSN: 1525-2027. DOI: 10.1029/2021GC009853.

Barletta, V.R., M. Bevis, B.E. Smith, T. Wilson, A. Brown, A. Bordoni, M. Willis, S.A. Khan, M. Rovira-Navarro, I. Dalziel, R. Smalley Jr., E. Kendrick, S. Konfal, D.J. Caccamise II, R.C. Aster, A. Nyblade, and D.A. Wiens (2018). “Observed rapid bedrock uplift in Amundsen Sea Embayment promotes ice-sheet stability”. In: *Science* 360.6395, pp. 1335–1339. ISSN: 0036-8075. DOI: 10.1126/science.aao1447.

Bergmann-Wolf, I., L. Zhang, and H. Dobslaw (2014). “Global Eustatic Sea-Level Variations for the Approximation of Geocenter Motion from Grace”. In: *Journal of Geodetic Science* 4.1. ISSN: 2081-9943. DOI: 10.2478/jogs-2014-0006.

Beutler, G. and A. Jäggi (2016). “Bahn- und Gravitationsfeldbestimmung aus den Positionen tief fliegender Satelliten”. In: *Handbuch der Geodäsie*. Ed. by W. Freeden and R. Rummel. Springer Reference Naturwissenschaften. Berlin, Heidelberg: Springer Spektrum, pp. 1–62. ISBN: 978-3-662-46900-2. DOI: 10.1007/978-3-662-46900-2_4-2.

Blewitt, G. (2003). “Self-consistency in reference frames, geocenter definition, and surface loading of the solid Earth”. In: *J. Geophys. Res.* 108.B2, p. 2103. DOI: 10.1029/2002JB002082.

Blewitt, G. and P. Clarke (2003). “Inversion of Earth’s changing shape to weigh sea level in static equilibrium with surface mass redistribution”. In: *J. Geophys. Res.* 108.B6, p. 2311. DOI: 10.1029/2002JB002290.

Borreggine, M., E. Powell, T. Pico, J.X. Mitrovica, R. Meadow, and C. Tryon (2022). “Not a bathtub: A consideration of sea-level physics for archaeological models of human migration”. In: *Journal of Archaeological Science* 137, p. 105507. ISSN: 0305-4403. DOI: 10.1016/j.jas.2021.105507.

Brils, M., P. Kuipers Munneke, W.J. van de Berg, and M. van den Broeke (2022). “Improved representation of the contemporary Greenland ice sheet firn layer by IMAU-FDM v1.2G”. In: *Geoscientific Model Development* 15.18, pp. 7121–7138. ISSN: 1991-9603. DOI: 10.5194/gmd-15-7121-2022.

Caron, L., E.R. Ivins, E. Larour, S. Adhikari, J. Nilsson, and G. Blewitt (2018). “GIA Model Statistics for GRACE Hydrology, Cryosphere, and Ocean Science”. In: *Geophys. Res. Lett.* 45. DOI: 10.1002/2017GL076644.

Chen, J.L., A. Cazenave, C. Dahle, W. Llovel, I. Panet, J. Pfeffer, and L. Moreira (2022). “Applications and Challenges of GRACE and GRACE Follow-On Satellite Gravimetry”. In: *Surv. Geophys.*, 41 pp. ISSN: 0169-3298. DOI: 10.1007/s10712-021-09685-x.

Cheng, M.K., J.C. Ries, and B.D. Tapley (2013). “Reference Frames for Applications in Geosciences”. In: vol. 138. International Association of Geodesy Symposia. Springer Berlin Heidelberg. Chap. Geocenter Variations from Analysis of SLR Data, pp. 19–25. ISBN: 978-3-642-32997-5. DOI: 10.1007/978-3-642-32998-2_4.

Clarke, P.J., D.A. Lavallée, G. Blewitt, T.M. van Dam, and J.M. Wahr (2005). “Effect of gravitational consistency and mass conservation on seasonal surface mass loading models”. In: *Geophys. Res. Lett.* 32, p. L08306. DOI: 10.1029/2005GL022441.

Coulon, V., K. Bulthuis, P.L. Whitehouse, S. Sun, K. Haubner, L. Zipf, and F. Pattyn (2021). "Contrasting response of West and East Antarctic ice sheets to Glacial Isostatic Adjustment". In: *J. Geophys. Res. Earth Surf.* n/a.n/a. e2020JF006003 2020JF006003, p. 2020.

Dahlen, F.A. (1976). "The Passive Influence of the Oceans upon the Rotation of the Earth". In: *Geophys. J. Int.* 46 (2), pp. 363–406. DOI: 10.1111/j.1365-246X.1976.tb04163.x.

Davis, J. L., B. P. Wernicke, and M. E. Tamisiea (2012). "On seasonal signals in geodetic time series". In: *Journal of Geophysical Research: Solid Earth* 117.B1.

Didova, O., B. Gunter, R.E.M. Riva, R. Klees, and L. Roese-Koerner (2016). "An approach for estimating time-variable rates from geodetic time series". In: *J. Geod.* 90.11, pp. 1207–1221. ISSN: 0949-7714. DOI: 10.1007/s00190-016-0918-5.

Diener, T., I. Sasgen, C. Agosta, J.J. Fürst, M.H. Braun, H. Konrad, and X. Fettweis (2021). "Acceleration of Dynamic Ice Loss in Antarctica From Satellite Gravimetry". In: *Front. Earth Sci.* 9. ISSN: 2296-6463. DOI: 10.3389/feart.2021.741789.

Ditmar, P. (2022). "How to quantify the accuracy of mass anomaly time-series based on GRACE data in the absence of knowledge about true signal?" In: *J. Geod.* 96.8. ISSN: 0949-7714. DOI: 10.1007/s00190-022-01640-x.

Dumberry, M. and M. Mandea (2022). "Gravity Variations and Ground Deformations Resulting from Core Dynamics". In: *Surv. Geophys.* 43.1, pp. 5–39. ISSN: 0169-3298. DOI: 10.1007/s10712-021-09656-2.

Dupont, T.K. and R.B. Alley (2005). "Assessment of the importance of ice-shelf buttressing to ice-sheet flow". In: *Geophys. Res. Lett.* 32.4. ISSN: 0094-8276. DOI: 10.1029/2004GL022024.

Durbin, J. and S. J. Koopman (2012). *Time series analysis by state space methods*. Oxford University Press.

Dziadek, R., F. Ferraccioli, and K. Gohl (2021). "High geothermal heat flow beneath Thwaites Glacier in West Antarctica inferred from aeromagnetic data". In: *Commun. Earth Environ.* 2.1. ISSN: 2662-4435. DOI: 10.1038/s43247-021-00242-3.

Ellmer, M. and T. Mayer-Gürr (2017). "High precision dynamic orbit integration for spaceborne gravimetry in view of GRACE Follow-on". In: *Adv. Space Res.* 60.1, pp. 1–13. ISSN: 0273-1177. DOI: 10.1016/j.asr.2017.04.015.

Engels, O., B. Gunter, R.E.M. Riva, and R. Klees (2018). "Separating Geophysical Signals Using GRACE and High-Resolution Data: A Case Study in Antarctica". In: *Geophys. Res. Lett.* 45.22, pp. 12, 340–12, 349. ISSN: 0094-8276. DOI: 10.1029/2018GL079670.

Ewert, H., A. Groh, and R. Dietrich (2012). "Volume and mass changes of the Greenland ice sheet inferred from ICESat and GRACE". In: *J. Geodyn.* 59–60, pp. 111–123. ISSN: 0264-3707. DOI: 10.1016/j.jog.2011.06.003.

Farrell, W.E. (1972). "Deformation of the Earth by Surface Loads". In: *Rev. Geophys. Space Phys.* 10.3, pp. 761–797. DOI: 10.1029/RG010i003p00761.

— (1973). "Earth Tides, Ocean Tides and Tidal Loading". In: *Phil. Trans. R. Soc. Lond. A* 274.1239, pp. 253–259. ISSN: 1364-503X. DOI: 10.1098/rsta.1973.0050.

Farrell, W.E. and J.A. Clark (1976). "On Postglacial Sea Level". In: *Geophys. J. R. Astr. Soc.* 46.3, pp. 647–667. ISSN: 1365-246X. DOI: 10.1111/j.1365-246X.1976.tb01252.x.

Fettweis, X., J.E. Box, C. Agosta, C. Amory, C. Kittel, C. Lang, D. van As, H. Machguth, and H. Gallée (2017). "Reconstructions of the 1900–2015 Greenland ice sheet surface mass balance using the regional climate MAR model". In: *The Cryosphere* 11.2, pp. 1015–1033. ISSN: 1994-0424. DOI: 10.5194/tc-11-1015-2017.

Forsberg, R., L. Sørensen, and S. Simonsen (2017). "Greenland and Antarctica Ice Sheet Mass Changes and Effects on Global Sea Level". In: *Surv. Geophys.* 38.1, pp. 89–104. ISSN: 1573-0956. DOI: 10.1007/s10712-016-9398-7.

Fox-Kemper, B., H.T. Hewitt, C. Xiao, G. Aðalgeirsdóttir, S.S. Drijfhout, T.L. Edwards, N.R. Golledge, M. Hemer, R.E. Kopp, G. Krinner, A. Mix, D. Notz, S. Nowicki, I.S. Nurhati, L. Ruiz, J.-B. Sallée, A.B.A. Slangen, and Y. Yu (2021). "Chapter 9: Ocean, Cryosphere and Sea Level Change". In: *Climate Change 2021: The Physical Science Basis. Contribution of Working Group I to the Sixth Assessment Report of the Intergovernmental Panel on Climate Change*. Ed. by V. Masson-Delmotte, P. Zhai, A. Pirani, S.L. Connors, C. Péan, S. Berger, N. Caud, Y. Chen, L. Goldfarb, M.I. Gomis, M. Huang, K. Leitzell, E. Lonnoy, J.B.R. Matthews, T.K. Maycock, T. Waterfield, O. Yelekçi, R. Yu, and B. Zhou. Cambridge University Press, pp. 1211–1362. DOI: 10.1017/9781009157896.011.

Frederikse, T., R. Riva, C. Slobbe, T. Broerse, and M. Verlaan (2016). “Estimating decadal variability in sea level from tide gauge records: An application to the North Sea”. In: *Journal of Geophysical Research: Oceans* 121.3, pp. 1529–1545. ISSN: 2169-9275. DOI: 10.1002/2015JC011174.

Gao, C., Y. Lu, Z. Zhang, and H. Shi (2019). “A Joint Inversion Estimate of Antarctic Ice Sheet Mass Balance Using Multi-Geodetic Data Sets”. In: *MDPI Remote Sens.* 11.6, p. 653. ISSN: 2072-4292. DOI: 10.3390/rs11060653.

Ghobadi-Far, K., S.-C. Han, C.M. McCullough, D.N. Wiese, R.D. Ray, J. Sauber, L. Shihora, and H. Dobslaw (2022). “Along-Orbit Analysis of GRACE Follow-On Inter-Satellite Laser Ranging Measurements for Sub-Monthly Surface Mass Variations”. In: *J. Geophys. Res. Solid Earth* 127.2. ISSN: 2169-9313. DOI: 10.1029/2021JB022983.

Göttl, F., A. Groh, M. Schmidt, L. Schröder, and F. Seitz (2021). “The influence of Antarctic ice loss on polar motion: an assessment based on GRACE and multi-mission satellite altimetry”. In: *Earth, Planets and Space* 73.1. ISSN: 1880-5981. DOI: 10.1186/s40623-021-01403-6.

Groh, A. (2014). “Zur Bestimmung eisinduzierter Massensignale aus der Kombination geodätischer Daten”. PhD thesis. Technische Universität Dresden.

Groh, A., H. Ewert, M. Scheinert, M. Fritsche, A. Rülke, A. Richter, R. Rosenau, and R. Dietrich (2012). “An Investigation of Glacial Isostatic Adjustment over the Amundsen Sea sector, West Antarctica”. In: *Global Planet. Change* 98–99, pp. 45–53. ISSN: 0921-8181. DOI: 10.1016/j.gloplacha.2012.08.001.

Groh, A. and M. Horwath (2021). “Antarctic Ice Mass Change Products from GRACE/GRACE-FO Using Tailored Sensitivity Kernels”. In: *MDPI Remote Sens.* 13.9. ISSN: 2072-4292. DOI: 10.3390/rs13091736.

Gunter, B.C., O. Didova, R.E.M. Riva, S.R.M. Ligtenberg, J.T.M. Lenaerts, M.A. King, M.R. van den Broeke, and T. Urban (2014). “Empirical estimation of present-day Antarctic glacial isostatic adjustment and ice mass change”. In: *The Cryosphere* 8.2, pp. 743–760. ISSN: 1994-0424. DOI: 10.5194/tc-8-743-2014.

Hanna, E., F. Pattyn, F. Navarro, V. Favier, H. Goelzer, M.R. van den Broeke, M. Vizcaino, P.L. Whitehouse, C. Ritz, K. Bulthuis, and B. Smith (2020). “Mass balance of the ice sheets and glaciers – Progress since AR5 and challenges”. In: *Earth-Science Reviews* 201, p. 102976. ISSN: 0012-8252. DOI: 10.1016/j.earscirev.2019.102976.

Hansen, P. C. (2001). “Computational Inverse Problems in Electrocardiology”. In: vol. 4. WIT Press. Chap. The L-curve and its use in the numerical treatment of inverse problems.

Hardy, R.A. (2019). “Combination of Geodetic Data over the Antarctic Ice Sheet for Monthly Mass Variation Solutions”. PhD thesis. URL: https://scholar.colorado.edu/concern/graduate_thesis_or_dissertations/5425k986q.

Heiskanen, W.A. and H. Moritz (1967). *Physical Geodesy*. San Francisco: W.H. Freeman.

Helm, V., A. Humbert, and H. Miller (2014). “Elevation and elevation change of Greenland and Antarctica derived from CryoSat-2”. In: *The Cryosphere* 8.4, pp. 1539–1559. ISSN: 1994-0424. DOI: 10.5194/tc-8-1539-2014.

Horwath, M., B.D. Gutknecht, A. Cazenave, H.K. Palanisamy, F. Marti, B. Marzeion, F. Paul, R. Le Bris, A.E. Hogg, I. Otosaka, A. Shepherd, P. Döll, D. Cáceres, H. Müller Schmied, J.A. Johannessen, J.E.Ø. Nilsen, R.P. Raj, R. Forsberg, L. Sandberg Sørensen, V.R. Barletta, S.B. Simonsen, P. Knudsen, O.B. Andersen, H. Ranndal, S.K. Rose, C.J. Merchant, C.R. Macintosh, K. von Schuckmann, K. Novotny, A. Groh, M. Restano, and J. Benveniste (2022). “Global sea-level budget and ocean-mass budget, with a focus on advanced data products and uncertainty characterisation”. In: *Earth System Science Data* 14.2, pp. 411–447. ISSN: 1866-3516. DOI: 10.5194/essd-14-411-2022.

Horwath, M., B. Legrésy, F. Rémy, F. Blarel, and J.-M. Lemoine (2012). “Consistent patterns of Antarctic ice sheet interannual variations from ENVISAT radar altimetry and GRACE satellite gravimetry”. In: *Geophys. J. Int.* 189.2, pp. 863–876. ISSN: 1365-246X. DOI: 10.1111/j.1365-246X.2012.05401.x.

Ince, E.S., F. Barthelmes, S. Reißland, K. Elger, C. Förste, F. Flechtner, and H. Schuh (2019). “ICGEM – 15 years of successful collection and distribution of global gravitational models, associated services, and future plans”. In: *Earth System Science Data* 11.2, pp. 647–674. ISSN: 1866-3516. DOI: 10.5194/essd-11-647-2019.

Ivins, E. R., T. S. James, J. Wahr, E. J. O. Schrama, F. W. Landerer, and K. M. Simon (2013). “Antarctic contribution to sea level rise observed by GRACE with improved GIA correction”. In: *J. Geophys. Res. Solid Earth* 118.6, pp. 3126–3141. ISSN: 2169-9356. DOI: 10.1002/jgrb.50208.

Ivins, E.R., L. Caron, S. Adhikari, E. Larour, and M. Scheinert (2020). “A Linear Viscoelasticity for Decadal to Centennial Time Scale Mantle Deformation”. In: *Reports on Progress in Physics* 83.10. Ed. by M. Bevis, p. 27. DOI: 10.1088/1361-6633/aba346.

Ivins, E.R., W. van der Wal, D.A. Wiens, A.J. Lloyd, and L. Caron (2021). “Antarctic upper mantle rheology”. In: *Geological Society, London, Memoirs* 56, pp. M56–2020. DOI: 10.1144/M56-2020-19.

Jiang, Y., X. Wu, M.R. van den Broeke, P. Kuipers Munneke, S.B. Simonsen, W. van der Wal, and B.L. Vermeersen (2021). “Assessing Global Present-Day Surface Mass Transport and Glacial Isostatic Adjustment From Inversion of Geodetic Observations”. In: *J. Geophys. Res. Solid Earth* 126.5. ISSN: 2169-9313. DOI: 10.1029/2020JB020713.

Kaitheri, A., A. Mémin, and F. Rémy (2021). “Inter-Annual Variability in the Antarctic Ice Sheets Using Geodetic Observations and a Climate Model”. In: *MDPI Remote Sens.* 13.11, p. 2199. ISSN: 2072-4292. DOI: 10.3390/rs13112199.

Kallenberg, B., P. Tregoning, J.F. Hoffmann, R. Hawkins, A. Purcell, and S. Allgeyer (2017). “A new approach to estimate ice dynamic rates using satellite observations in East Antarctica”. In: *The Cryosphere* 11.3, pp. 1235–1245. ISSN: 1994-0424. DOI: 10.5194/tc-11-1235-2017.

Kang, K., S. Zhong, A. Geruo, and W. Mao (2021). “The effects of non-Newtonian rheology in the upper mantle on relative sea level change and geodetic observables induced by glacial isostatic adjustment process”. In: *Geophys. J. Int.* 228.3, pp. 1887–1906. ISSN: 0956-540X. DOI: 10.1093/gji/ggab428.

Kappelsberger, M.T., U. Strößenreuther, M. Scheinert, M. Horwath, A. Groh, C. Knöfel, S. Lunz, and S.A. Khan (2021). “Modeled and Observed Bedrock Displacements in North-East Greenland Using Refined Estimates of Present-Day Ice-Mass Changes and Densified GNSS Measurements”. In: *J. Geophys. Res. Earth Surf.* 126.4, e2020JF005860. ISSN: 2169-9003. DOI: 10.1029/2020JF005860.

Karato, S.-I. (2008). *Deformation of Earth Materials: An Introduction to the Rheology of Solid Earth*. Cambridge University Press. ISBN: 978-05-118-0489-2. DOI: 10.1017/CBO9780511804892.

Keenan, E., N. Wever, M. Dattler, J.T.M. Lenaerts, B. Medley, P. Kuipers Munneke, and C. Reijmer (2021). “Physics-based SNOWPACK model improves representation of near-surface Antarctic snow and firn density”. In: *The Cryosphere* 15.2, pp. 1065–1085. ISSN: 1994-0424. DOI: 10.5194/tc-15-1065-2021.

Kim, J.-S., K.-W. Seo, J. Chen, and C. Wilson (2022). “Uncertainty in GRACE/GRACE-follow on global ocean mass change estimates due to mis-modeled glacial isostatic adjustment and geocenter motion”. In: *Scientific Reports* 12.1. ISSN: 2045-2322. DOI: 10.1038/s41598-022-10628-8.

King, M.A., Z. Altamimi, J. Boehm, M. Bos, R. Dach, P. Elosegui, F. Fund, M. Hernández-Pajares, D. Lavallee, P.J. Mendes Cerveira, N. Penna, R.E.M. Riva, P. Steigenberger, T. Dam, L. Vittuari, S. Williams, and P. Willis (2010). “Improved Constraints on Models of Glacial Isostatic Adjustment: A Review of the Contribution of Ground-Based Geodetic Observations”. In: *Surv. Geophys.* 31.5, pp. 465–507. ISSN: 0169-3298. DOI: 10.1007/s10712-010-9100-4.

Koch, K.R. (1999). *Parameter Estimation and Hypothesis Testing in Linear Models*. 2nd. Springer, Berlin, Heidelberg. ISBN: 978-3-662-03976-2. DOI: 10.1007/978-3-662-03976-2. URL: https://link.springer.com/book/10.1007/978-3-662-03976-2.

Kuipers Munneke, P., S.R.M. Ligtenberg, B.P.Y. Noël, I.M. Howat, J.E. Box, E. Mosley-Thompson, J.R. McConnell, K. Steffen, J.T. Harper, S.B. Das, and M.R. van den Broeke (2015). “Elevation change of the Greenland Ice Sheet due to surface mass balance and firn processes, 1960–2014”. In: *The Cryosphere* 9.6, pp. 2009–2025. DOI: 10.5194/tc-9-2009-2015.

Kvas, A., S. Behzadpour, M. Ellmer, B. Klinger, S. Strasser, N. Zehentner, and T. Mayer-Gürr (2019). “ITSG-Grace2018: Overview and Evaluation of a New GRACE-Only Gravity Field Time Series”. In: *J. Geophys. Res. Solid Earth* 124.8, pp. 9332–9344. ISSN: 2169-9313. DOI: 10.1029/2019JB017415.

Lambeck, K. (1988). *Geophysical Geodesy – The Slow Deformations of the Earth*. Clarendon Press, Oxford University Press. ISBN: 0-19-854438-3.

Lambeck, K., H. Rouby, A. Purcell, Y. Sun, and M. Sambridge (2014). “Sea level and global ice volumes from the Last Glacial Maximum to the Holocene”. In: *Proc. Natl. Acad. Sci. USA* 111.43, pp. 15296–15303. ISSN: 0027-8424. DOI: 10.1073/pnas.1411762111.

Lau, H.C.P., J. Austermann, B.K. Holtzman, C. Havlin, A.J. Lloyd, C. Book, and E. Hopper (2021). “Frequency Dependent Mantle Viscoelasticity via the Complex Viscosity: Cases From Antarctica”. In: *J. Geophys. Res. Solid Earth* 126.11. ISSN: 2169-9313. DOI: 10.1029/2021JB022622.

Legrésy, B. and F. Rémy (1997). "Altimetric observations of surface characteristics of the Antarctic ice sheet". In: *J. Glac.* 43.144, pp. 265–276.

Lenaerts, J.T.M., B. Medley, M.R. Broeke, and B. Wouters (2019). "Observing and Modeling Ice Sheet Surface Mass Balance". In: *Rev. Geophys.* 57. ISSN: 8755-1209. DOI: 10.1029/2018RG000622.

Ligtenberg, S.R.M., M.M. Helsen, and M.R. van den Broeke (2011). "An improved semi-empirical model for the densification of Antarctic firn". In: *The Cryosphere* 5.4, pp. 809–819. ISSN: 1994-0424. DOI: 10.5194/tc-5-809-2011.

Ligtenberg, S.R.M., P. Kuipers Munneke, and M.R. van den Broeke (2014). "Present and future variations in Antarctic firn air content". In: *The Cryosphere* 8.5, pp. 1711–1723. ISSN: 1994-0424. DOI: 10.5194/tc-8-1711-2014.

Lipzig, N.P.M. van, E. van Meijgaard, and J. Oerlemans (2002). "The spatial and temporal variability of the surface mass balance in Antarctica: results from a regional atmospheric climate model". In: *Int. J. Climatol.* 22, pp. 1197–1217. DOI: 10.1002/joc.798.

Loomis, B.D., K.E. Rachlin, D.N. Wiese, F.W. Landerer, and S.B. Luthcke (2020). "Replacing GRACE/GRACE-FO C30 with satellite laser ranging: Impacts on Antarctic Ice Sheet mass change". In: *Geophys. Res. Lett.* 47, e2020GL088306. ISSN: 0094-8276. DOI: 10.1029/2019GL085488.

Love, A. (1909). "The yielding of the earth to disturbing forces". In: *Proceedings of the Royal Society of London. Series A, Containing Papers of a Mathematical and Physical Character* 82.551, pp. 73–88. ISSN: 0950-1207. DOI: 10.1098/rspa.1909.0008.

Lundin, J.M.D., C.M. Stevens, R. Arthern, C. Buizert, A. Orsi, S.R.M. Ligtenberg, S.B. Simonsen, E. Cummings, R. Essery, W. Leahy, P. Harris, M.M. Helsen, and E.D. Waddington (2017). "Firn Model Intercomparison Experiment (FirnMICE)". In: *J. Glac.* 63.239, pp. 401–422. ISSN: 0022-1430. DOI: 10.1017/jog.2016.114.

Martín-Español, A., M.A. King, A. Zammit-Mangion, S.B. Andrews, P. Moore, and J.L. Bamber (2016a). "An assessment of forward and inverse GIA solutions for Antarctica". In: *J. Geophys. Res. Solid Earth* 121.9, pp. 6947–6965. ISSN: 2169-9313. DOI: 10.1002/2016JB013154.

Martín-Español, A., A. Zammit-Mangion, P.J. Clarke, T. Flament, V. Helm, M. A. King, S. B. Luthcke, E. Petrie, F. Rémy, N. Schön, B. Wouters, and J.L. Bamber (2016b). "Spatial and temporal Antarctic Ice Sheet mass trends, glacio-isostatic adjustment and surface processes from a joint inversion of satellite altimeter, gravity and GPS data". In: *J. Geophys. Res. Earth Surf.* 121.2, pp. 182–200. ISSN: 2169-9003. DOI: 10.1002/2015JF003550.

Mayer-Gürr, T., S. Behzadpur, M. Ellmer, A. Kvas, B. Klinger, S. Strasser, and N. Zehentner (2018). "ITSG-Grace2018 – Monthly, Daily and Static Gravity Field Solutions from GRACE". In: *GFZ Data Services*. DOI: http://doi.org/10.5880/ICGEM.2018.003.

Mémin, A., T. Flament, B. Alizier, C. Watson, and F. Rémy (2015). "Interannual variation of the Antarctic Ice Sheet from a combined analysis of satellite gravimetry and altimetry data". In: *Earth Planet. Sci. Lett.* 422, pp. 150–156. ISSN: 0012821X. DOI: 10.1016/j.epsl.2015.03.045.

Mémin, A., T. Flament, F. Rémy, and M. Llubes (2014). "Snow- and ice-height change in Antarctica from satellite gravimetry and altimetry data". In: *Earth Planet. Sci. Lett.* 404, pp. 344–353. ISSN: 0012821X. DOI: 10.1016/j.epsl.2014.08.008.

Menke, W. (2012). *Geophysical Data Analysis: Discrete Inverse Theory: MATLAB Edition*. 3rd ed. International Geophysics. Elsevier Science. ISBN: 9780123977847.

Mitrovica, J.X. and J. Wahr (2011). "Ice Age Earth Rotation". In: *Annu. Rev. Earth Planet. Sci.* 39.1, pp. 577–616. ISSN: 0084-6597. DOI: 10.1146/annurev-earth-040610-133404.

Mottram, R., N. Hansen, C. Kittel, J.M. van Wessem, C. Agosta, C. Amory, F. Boberg, W.J. van de Berg, X. Fettweis, A. Gossart, N.P.M. van Lipzig, E. van Meijgaard, A. Orr, T. Phillips, S. Webster, S.B. Simonsen, and N. Souverijns (2021). "What is the surface mass balance of Antarctica? An intercomparison of regional climate model estimates". In: *The Cryosphere* 15.8, pp. 3751–3784. ISSN: 1994-0424. DOI: 10.5194/tc-15-3751-2021.

Mouginot, J., E. Rignot, A.A. Bjørk, M. van den Broeke, R. Millan, M. Morlighem, B. Noël, B. Scheuchl, and M. Wood (2019). "Forty-six years of Greenland Ice Sheet mass balance from 1972 to 2018". In: *Proc. Natl. Acad. Sci. USA* 116.19, pp. 9239–9244. DOI: 10.1073/pnas.1904242116.

Müller, L., M. Horwath, M. Scheinert, C. Mayer, B. Ebermann, D. Floricioiu, L. Krieger, R. Rosenau, and S. Vijay (2021). "Surges of Harald Moltke Bræ, north-western Greenland: seasonal modulation and initiation at the terminus". In: *The Cryosphere* 15.7, pp. 3355–3375. ISSN: 1994-0424. DOI: 10.5194/tc-15-3355-2021.

Nilsson, J., A.S. Gardner, and F.S. Paolo (2022). “Elevation change of the Antarctic Ice Sheet: 1985 to 2020”. In: *Earth System Science Data* 14.8, pp. 3573–3598. ISSN: 1866-3516. DOI: 10.5194/essd-14-3573-2022.

Noël, B., W.J. van de Berg, J.M. van Wessem, E. van Meijgaard, D. van As, J.T.M. Lenaerts, S. Lhermitte, P. Kuipers Munneke, C.J.P.P. Smeets, L.H. van Ulft, R.S.W. van de Wal, and M.R. van den Broeke (2018). “Modelling the climate and surface mass balance of polar ice sheets using RACMO2 – Part 1: Greenland (1958–2016)”. In: *The Cryosphere* 12.3, pp. 811–831. ISSN: 1994-0424. DOI: 10.5194/tc-12-811-2018.

Pail, R., J. Bamber, R. Biancale, R. Bingham, C. Braitenberg, A. Eicker, F. Flechtner, T. Gruber, A. Güntner, G. Heinzel, M. Horwath, L. Longuevergne, J. Müller, I. Panet, H. Savenije, S. Seneviratne, N. Sneeuw, T. van Dam, and B. Wouters (2019). “Mass variation observing system by high low inter-satellite links (MOBILE) – a new concept for sustained observation of mass transport from space”. In: *Journal of Geodetic Science* 9.1, pp. 48–58. ISSN: 2081-9943. DOI: 10.1515/jogs-2019-0006.

Palmer, M.D., J.M. Gregory, M. Bagge, D. Calvert, J.M. Hagedoorn, T. Howard, V. Klemann, J.A. Lowe, C.D. Roberts, A.B.A. Slangen, and G. Spada (2020). “Exploring the Drivers of Global and Local Sea-Level Change Over the 21st Century and Beyond”. In: *Earth’s Future* 8.9. ISSN: 2328-4277. DOI: 10.1029/2019EF001413.

Patterson, T. and N.V. Kelso et al. (2022). *Natural Earth*. URL: https://www.naturalearthdata.com/ (visited on 2022-06-02).

Pattyn, F. (2010). “Antarctic subglacial conditions inferred from a hybrid ice sheet/ice stream model”. In: *Earth Planet. Sci. Lett.* 295.3-4, pp. 451–461. ISSN: 0012821X. DOI: 10.1016/j.epsl.2010.04.025.

Pritchard, H.D., S.R.M. Ligtenberg, H.A. Fricker, D.G. Vaughan, M.R. van den Broeke, and L. Padman (2012). “Antarctic ice-sheet loss driven by basal melting of ice shelves”. In: *Nature* 484.7395, pp. 502–505. ISSN: 0028-0836. DOI: 10.1038/nature10968.

Richter, A., A.A. Ekaykin, M.O. Willen, V.Y. Lipenkov, A. Groh, S.V. Popov, M. Scheinert, M. Horwath, and R. Dietrich (2021). “Surface Mass Balance Models Vs. Stake Observations: A Comparison in the Lake Vostok Region, Central East Antarctica”. In: *Front. Earth Sci.* 9, p. 388. ISSN: 2296-6463. DOI: 10.3389/feart.2021.669977.

Richter, A., M. Horwath, and R. Dietrich (2016). “Comment on Zwally and others (2015)-Mass gains of the Antarctic ice sheet exceed losses”. In: *J. Glac.* 62.223, pp. 604–606. ISSN: 1727-5652. DOI: 10.1017/jog.2016.60.

Richter, A., L. Schröder, M. Scheinert, S.V. Popov, A. Groh, M.O. Willen, M. Horwath, and R. Dietrich (2022). “The hydrostatic control of load-induced height changes above subglacial Lake Vostok”. In: *J. Glac.*, pp. 1–18. ISSN: 0022-1430. DOI: 10.1017/jog.2022.2.

Rietbroek, R. (2014). “Retrieval of Sea Level and Surface Loading Variations from Geodetic Observations and Model Simulations: an Integrated Approach”. PhD thesis. Rheinische Friedrich-Wilhelms-Universität Bonn.

Rietbroek, R., S.-E. Brunnabend, J. Kusche, and J. Schröter (2012). “Resolving sea level contributions by identifying fingerprints in time-variable gravity and altimetry”. In: *J. Geodyn.* 59-60, pp. 72–81. ISSN: 0264-3707. DOI: 10.1016/j.jog.2011.06.007.

Rietbroek, R., S.-E. Brunnabend, J. Kusche, J. Schröter, and C. Dahle (2016). “Revisiting the contemporary sea-level budget on global and regional scales”. In: *Proc. Natl. Acad. Sci. USA* 113.6, pp. 1504–1509. ISSN: 0027-8424. DOI: 10.1073/pnas.1519132113.

Rignot, E., J. Mouginot, B. Scheuchl, M. van den Broeke, J.M. Van Wessem, and M. Morlighem (2019). “Four decades of Antarctic Ice Sheet mass balance from 1979–2017”. In: *Proc. Natl. Acad. Sci. USA* 116.4, pp. 1095–1103. ISSN: 0027-8424. DOI: 10.1073/pnas.1812883116.

Riva, R.E.M., B.C. Gunter, T.J. Urban, B.L.A. Vermeersen, R.C. Lindenbergh, M.M. Helsen, J.L. Bamber, R.S.W. van de Wal, M.R. van den Broeke, and B.E. Schutz (2009). “Glacial Isostatic Adjustment over Antarctica from combined ICESat and GRACE satellite data”. In: *Earth Planet. Sci. Lett.* 288.3-4, pp. 516–523. ISSN: 0012-821X. DOI: 10.1016/j.epsl.2009.10.013.

Saito, M. (1978). “Relationship between tidal and load Love numbers”. In: *Journal of Physics of the Earth* 26.1, pp. 13–16. ISSN: 0022-3743. DOI: 10.4294/jpe1952.26.13.

Sasgen, I., H. Konrad, V. Helm, and K. Grosfeld (2019). “High-Resolution Mass Trends of the Antarctic Ice Sheet through a Spectral Combination of Satellite Gravimetry and Radar Altimetry Observations”. In: *MDPI Remote Sens.* 11.2, p. 144. ISSN: 2072-4292. DOI: 10.3390/rs11020144.

Sasgen, I., A. Martín-Español, A. Horvath, V. Klemann, E.J. Petrie, B. Wouters, M. Horwath, R. Pail, J.L. Bamber, P.J. Clarke, H. Konrad, and M.R. Drinkwater (2017). “Joint inversion estimate of regional glacial isostatic adjustment in Antarctica considering a lateral varying Earth structure (ESA STSE Project REGINA)". In: *Geophys. J. Int.* 211.3, pp. 1534–1553. ISSN: 0956-540X. DOI: 10.1093/gji/ggx368.

Sasgen, I., A. Martín-Español, A. Horvath, V. Klemann, E.J. Petrie, B. Wouters, M. Horwath, R. Pail, J.L. Bamber, P.J. Clarke, H. Konrad, T. Wilson, and M.R. Drinkwater (2018). "Altimetry, gravimetry, GPS and viscoelastic modeling data for the joint inversion for glacial isostatic adjustment in Antarctica (ESA STSE Project REGINA)". In: *Earth System Science Data* 10.1, pp. 493–523. ISSN: 1866-3516. DOI: 10.5194/essd-10-493-2018.

Schröder, L., M. Horwath, R. Dietrich, V. Helm, M.R. van den Broeke, and S.R.M. Ligtenberg (2019). "Four decades of Antarctic surface elevation changes from multi-mission satellite altimetry". In: *The Cryosphere* 13.2, pp. 427–449. ISSN: 1994-0424. DOI: 10.5194/tc-13-427-2019.

Seeber, G. (2003). *Satellite Geodesy*. 2nd ed. Berlin – New York: Walter de Gruyter. ISBN: 3-11-017549-5.

Sha, Z., J.C. Rougier, M. Schumacher, and J.L. Bamber (2018). "Bayesian model–data synthesis with an application to global glacio-isostatic adjustment". In: *Environmetrics*. e2530 env.2530, p. 2530. DOI: 10.1002/env.2530.

Shepherd, A., E. Ivins, E. Rignot, B. Smith, M. van den Broeke, I. Velicogna, P. Whitehouse, K. Briggs, I. Joughin, G. Krinner, S. Nowicki, T. Payne, T. Scambos, N. Schlegel, G. A, C. Agosta, A. Ahlstrøm, G. Babonis, V. Barletta, A. Blazquez, J. Bonin, B. Csatho, R. Cullather, D. Felikson, X. Fettweis, R. Forsberg, H. Gallee, A. Gardner, L. Gilbert, A. Groh, B. Gunter, E. Hanna, C. Harig, V. Helm, A. Horvath, M. Horwath, S. Khan, K.K. Kjeldsen, H. Konrad, P. Langen, B. Lecavalier, B. Loomis, S. Luthcke, M. McMillan, D. Melini, S. Mernild, Y. Mohajerani, P. Moore, J. Mouginot, G. Moyano, A. Muir, T. Nagler, G. Nield, J. Nilsson, B. Noel, I. Otosaka, M.E. Pattle, W.R. Peltier, N. Pie, R. Rietbroek, H. Rott, L. Sandberg-Sørensen, I. Sasgen, H. Save, B. Scheuchl, E. Schrama, L. Schröder, K.-W. Seo, S. Simonsen, T. Slater, G. Spada, T. Sutterley, M. Talpe, L. Tarasov, W.J. van de Berg, W. van der Wal, J.M. van Wessem, B.D. Vishwakarma, D. Wiese, and B. Wouters (2018). "Mass balance of the Antarctic Ice Sheet from 1992 to 2017". In: *Nature* 558.7709, pp. 219–222. ISSN: 0028-0836. DOI: 10.1038/s41586-018-0179-y.

Shepherd, A., E. Ivins, E. Rignot, B. Smith, M. van den Broeke, I. Velicogna, P. Whitehouse, K. Briggs, I. Joughin, G. Krinner, S. Nowicki, T. Payne, T. Scambos, N. Schlegel, G. A, C. Agosta, A. Ahlstrøm, G. Babonis, V.R. Barletta, A.A. Bjørk, A. Blazquez, J. Bonin, W. Colgan, B. Csatho, R. Cullather, M.E. Engdahl, D. Felikson, X. Fettweis, R. Forsberg, A.E. Hogg, H. Gallee, A. Gardner, L. Gilbert, N. Gourmelen, A. Groh, B. Gunter, E. Hanna, C. Harig, V. Helm, A. Horvath, M. Horwath, S. Khan, K.K. Kjeldsen, H. Konrad, P.L. Langen, B. Lecavalier, B. Loomis, S. Luthcke, M. McMillan, D. Melini, S. Mernild, Y. Mohajerani, P. Moore, R. Mottram, J. Mouginot, G. Moyano, A. Muir, T. Nagler, G. Nield, J. Nilsson, B. Noël, I. Otosaka, M.E. Pattle, W.R. Peltier, N. Pie, R. Rietbroek, H. Rott, L.S. Sørensen, I. Sasgen, H. Save, B. Scheuchl, E. Schrama, L. Schröder, K.-W. Seo, S.B. Simonsen, T. Slater, G. Spada, T. Sutterley, M. Talpe, L. Tarasov, W. Jan van de Berg, W. van der Wal, J.M. van Wessem, B.D. Vishwakarma, D. Wiese, D. Wilton, T. Wagner, B. Wouters, and J. Wuite (2019). "Mass balance of the Greenland Ice Sheet from 1992 to 2018". In: *Nature*. ISSN: 1476-4687. DOI: 10.1038/s41586-019-1855-2.

Shi, T., Y. Fukuda, K. Doi, and J. Okuno (2022). "Extraction of GRACE/GRACE-FO observed mass change patterns across Antarctica via independent component analysis (ICA)". In: *Geophys. J. Int.* 229.3, pp. 1914–1926. ISSN: 0956-540X. DOI: 10.1093/gji/ggac033.

Sigmundsson, F., V. Pinel, B. Lund, F. Albino, C. Pagli, H. Geirsson, and E. Sturkell (2010). "Climate effects on volcanism: influence on magmatic systems of loading and unloading from ice mass variations, with examples from Iceland". In: *Phil. Trans. R. Soc. Lond. A* 368.1919, pp. 2519–2534. ISSN: 1364-503X. DOI: 10.1098/rsta.2010.0042.

Singh, V.P, P. Singh, and U.K Haritashya (2011). *Encyclopedia of Snow, Ice and Glaciers*. Springer. ISBN: 978-90-481-2641-5.

Slobbe, D.C., P. Ditmar, and R.C. Lindenbergh (2009). "Estimating the rates of mass change, ice volume change and snow volume change in Greenland from ICESat and GRACE data". In: *Geophys. J. Int.* 176, pp. 95–106. DOI: 10.1111/j.1365-246X.2008.03978.x.

Spada, G. (2017). "Glacial Isostatic Adjustment and Contemporary Sea Level Rise: An Overview". In: *Surv. Geophys.* 38.1, pp. 153–185. ISSN: 0169-3298. DOI: 10.1007/s10712-016-9379-x.

Spada, G. and D. Melini (2019). "SELEN^4 (SELEN version 4.0): a Fortran program for solving the gravitationally and topographically self-consistent sea-level equation in glacial isostatic adjustment modeling". In: *Geoscientific Model Development* 12.12, pp. 5055–5075. ISSN: 1991-9603. DOI: 10.5194/gmd-12-5055-2019.

Steffen, R., H. Steffen, P. Wu, and D.W. Eaton (2014). "Stress and fault parameters affecting fault slip magnitude and activation time during a glacial cycle". In: *Tectonics* 33.7, pp. 1461–1476. ISSN: 0278-7407. DOI: 10.1002/2013TC003450.

Sun, Y. and R.E.M. Riva (2020). “A global semi-empirical glacial isostatic adjustment (GIA) model based on Gravity Recovery and Climate Experiment (GRACE) data”. In: *Earth Syst. Dynam.* 11.1, pp. 129–137. ISSN: 2190-4987. DOI: 10.5194/esd-11-129-2020.

Sun, Y., R.E.M. Riva, and P. Ditmar (2016). “Optimizing estimates of annual variations and trends in geocenter motion and J_2 from a combination of GRACE data and geophysical models”. In: *J. Geophys. Res. Solid Earth* 121.11, pp. 8352–8370. ISSN: 2169-9313. DOI: 10.1002/2016JB013073.

Swenson, S., D. Chambers, and J. Wahr (2008). “Estimating geocenter variations from a combination of GRACE and ocean model output”. In: *J. Geophys. Res.* B113, B08410. DOI: 10.1029/2007JB005338.

Tapley, B.D., S. Bettadpur, M. Watkins, and C. Reigber (2004). “The gravity recovery and climate experiment: Mission overview and early results”. In: *Geophys. Res. Lett.* 31, p. L09607. DOI: 10.1029/2004GL019920.

Tarantola, A. (2005). *Inverse Problem Theory and Methods for Model Parameter Estimation*. Society for Industrial and Applied Mathematics. DOI: 10.1137/1.9780898717921.

Thomas, E.R., J.M. van Wessem, J. Roberts, E. Isaksson, E. Schlosser, T.J. Fudge, P. Vallelonga, B. Medley, J. Lenaerts, N. Bertler, M.R. van den Broeke, D.A. Dixon, M. Frezzotti, B. Stenni, M. Curran, and A.A. Ekaykin (2017). “Regional Antarctic snow accumulation over the past 1000 years”. In: *Climate of the Past* 13.11, pp. 1491–1513. ISSN: 1814-9332. DOI: 10.5194/cp-13-1491-2017.

Thomas, I.D., M.A. King, M.J. Bentley, P.L. Whitehouse, N.T. Penna, S.D.P. Williams, R.E.M. Riva, D.A. Lavallee, P.J. Clarke, E.C. King, R.C.A. Hindmarsh, and H. Koivula (2011). “Widespread low rates of Antarctic glacial isostatic adjustment revealed by GPS observations”. In: *Geophys. Res. Lett.* 38.22, p. L22302. ISSN: 0094-8276. DOI: 10.1029/2011GL049277.

Tikhonov, A. N., A. V. Goncharsky, V. V. Stepanov, and A. G. Yagola (1995). *Numerical Methods for the Solution of Ill-Posed Problems*. Kluwer Academic Publishers. ISBN: 978-90-481-4583-6. DOI: 10.1007/978-94-015-8480-7.

Torge, W. and J. Müller (2012). *Geodesy*. 4th ed. Berlin, Boston: De Gruyter. ISBN: 978-3-11-020718-7.

Uebbing, B., J. Kusche, R. Rietbroek, and F.W. Landerer (2019). “Processing choices affect ocean mass estimates from GRACE”. In: *Journal of Geophysical Research: Oceans* 124. Supplementary. ISSN: 2169-9275. DOI: 10.1029/2018JC014341.

Veldhuijsen, S.B.M., W.J. van de Berg, M. Brils, P. Kuipers Munneke, and M.R. van den Broeke (2022). “Characteristics of the contemporary Antarctic firn layer simulated with IMAU-FDM v1.2A (1979–2020)”. In: *The Cryosphere Discuss.* 2022, pp. 1–26. DOI: 10.5194/tc-2022-118.

Velicogna, I. and J. Wahr (2002). “A method for separating Antarctic postglacial rebound and ice mass balance using future ICESat Geosience Laser Altimeter System, Gravity Recovery and Climate Experiment, and GPS satellite data”. In: *J. Geophys. Res.* 107.B10, p. 2263. DOI: 10.1029/2001JB000708.

Verjans, V., A.A.: McMillan Leeson, C.M. Stevens, J. M. van Wessem, W.J. van de Berg, M.R. van den Broeke, C. Kittel, C. Amory, X. Fettweis, N. Hansen, F. Boberg, and R. Mottram (2021). “Uncertainty in East Antarctic Firn Thickness Constrained Using a Model Ensemble Approach”. In: *Geophys. Res. Lett.* 48.7. e2020GL092060 2020GL092060, e2020GL092060. DOI: https://doi.org/10.1029/2020GL092060.

Vernon, C.L., J.L. Bamber, J.E. Box, M.R. van den Broeke, X. Fettweis, E. Hanna, and P. Huybrechts (2013). “Surface mass balance model intercomparison for the Greenland ice sheet”. In: *The Cryosphere* 7.2, pp. 599–614. ISSN: 1994-0424. DOI: 10.5194/tc-7-599-2013.

Wahr, J., M. Molenaar, and F. Bryan (1998). “Time variability of the Earth’s gravity field: Hydrological and oceanic effects and their possible detection using GRACE”. In: *J. Geophys. Res.* 103.B12, pp. 30205–30229. ISSN: 0148-0227. DOI: 10.1029/98JB02844.

Wahr, J., D. Wingham, and C. Bentley (2000). “A method of combining ICESat and GRACE satellite data to constrain Antarctic mass balance”. In: *J. Geophys. Res.* 105.B7, pp. 16279–16294. DOI: 10.1029/2000JB900113.

Wal, W. van der, P.L. Whitehouse, and E.J.O. Schrama (2015). “Effect of GIA models with 3D composite mantle viscosity on GRACE mass balance estimates for Antarctica”. In: *Earth Planet. Sci. Lett.* 414, pp. 134–143. ISSN: 0012821X. DOI: 10.1016/j.epsl.2015.01.001.

Wan, J.X.W., N. Gomez, K. Latychev, and H.K. Han (2022). “Resolving glacial isostatic adjustment (GIA) in response to modern and future ice loss at marine grounding lines in West Antarctica”. In: *The Cryosphere* 16.6, pp. 2203–2223. ISSN: 1994-0424. DOI: 10.5194/tc-16-2203-2022.

Wang, L., J.L. Davis, and I.M. Howat (2021). "Complex Patterns of Antarctic Ice Sheet Mass Change Resolved by Time-Dependent Rate Modeling of GRACE and GRACE Follow-On Observations". In: *Geophys. Res. Lett.* 48.1. ISSN: 0094-8276. DOI: 10.1029/2020GL090961.

WCRP Global Sea Level Budget Group (2018). "Global Sea Level Budget 1993–Present". In: *Earth System Science Data* 10.3, pp. 1551–1590. DOI: 10.5194/essd-10-1551-2018.

Wessem, J.M. van, W.J. van de Berg, B.P.Y. Noël, E. van Meijgaard, C. Amory, G. Birnbaum, C.L. Jakobs, K. Krüger, J.T.M. Lenaerts, S. Lhermitte, S.R.M. Ligtenberg, B. Medley, C.H. Reijmer, K. van Tricht, L.D. Trusel, L.H. van Ulft, B. Wouters, J. Wuite, and M.R. van den Broeke (2018). "Modelling the climate and surface mass balance of polar ice sheets using RACMO2 – Part 2: Antarctica (1979–2016)". In: *The Cryosphere* 12.4, pp. 1479–1498. ISSN: 1994-0424. DOI: 10.5194/tc-12-1479-2018.

Whitehouse, P.L. (2018). "Glacial isostatic adjustment modelling: historical perspectives, recent advances, and future directions". In: *Earth Surface Dynamics* 6.2, pp. 401–429. ISSN: 2196-632X. DOI: 10.5194/esurf-6-401-2018.

Whitehouse, P.L., M.J. Bentley, G.A. Milne, M.A. King, and I.D. Thomas (2012). "A new glacial isostatic adjustment model for Antarctica: calibrated and tested using observations of relative sea-level change and present-day uplift rates". In: *Geophys. J. Int.* 190.3, pp. 1464–1482. DOI: 10.1111/j.1365-246X.2012.05557.x.

Whitehouse, P.L., N. Gomez, M.A. King, and D.A. Wiens (2019). "Solid Earth change and the evolution of the Antarctic Ice Sheet". In: *Nature Communications* 10.1. ISSN: 2041-1723. DOI: 10.1038/s41467-018-08068-y.

Willen, M.O., T. Broerse, A. Groh, B. Wouters, P. Kuipers Munneke, M. Horwath, M.R. van den Broeke, and L. Schröder (2021). "Separating Long-Term and Short-Term Mass Changes of Antarctic Ice Drainage Basins: A Coupled State Space Analysis of Satellite Observations and Model Products". In: *J. Geophys. Res. Earth Surf.* 126.6, e2020JF005966. DOI: 10.1029/2020JF005966.

Willen, M.O., M. Horwath, A. Groh, V. Helm, B. Uebbing, and J. Kusche (2022). "Feasibility of a global inversion for spatially resolved glacial isostatic adjustment and ice sheet mass changes proven in simulation experiments". In: *J. Geod.* 96.10, pp. 1–21. ISSN: 0949-7714. DOI: 10.1007/s00190-022-01651-8.

Willen, M.O., M. Horwath, L. Schröder, A. Groh, S.R.M. Ligtenberg, P. Kuipers Munneke, and M.R. van den Broeke (2020). "Sensitivity of inverse glacial isostatic adjustment estimates over Antarctica". In: *The Cryosphere* 14.1, pp. 349–366. DOI: 10.5194/tc-14-349-2020.

Wu, X., M.B. Heflin, H. Schotman, B.L.A. Vermeersen, D. Dong, R.S. Gross, E.R. Ivins, A.W. Moore, and S.E. Owen (2010). "Simultaneous estimation of global present-day water transport and glacial isostatic adjustment". In: *Nature Geosci.* 3.9, pp. 642–646. ISSN: 1752-0894. DOI: 10.1038/ngeo938.

Yang, Y., F. Li, C. Hwang, M. Ding, and J. Ran (2019). "Space-Time Evolution of Greenland Ice Sheet Elevation and Mass From Envisat and GRACE Data". In: *J. Geophys. Res. Earth Surf.* 124.8, pp. 2079–2100. ISSN: 2169-9003. DOI: 10.1029/2018JF004765.

Zammit-Mangion, A., J. Rougier, N. Schön, F. Lindgren, and J. Bamber (2015). "Multivariate spatio-temporal modelling for assessing Antarctica's present-day contribution to sea-level rise". In: *Environmetrics* 26.3, pp. 159–177. ISSN: 1180-4009. DOI: 10.1002/env.2323.

Zhang, B., Z. Wang, J. An, T. Liu, and H. Geng (2022). "A 30-year monthly 5 km gridded surface elevation time series for the Greenland Ice Sheet from multiple satellite radar altimeters". In: *Earth System Science Data* 14.2, pp. 973–989. ISSN: 1866-3516. DOI: 10.5194/essd-14-973-2022.

Zhang, B., Z. Wang, F. Li, J. An, Y. Yang, and J. Liu (2017). "Estimation of present-day glacial isostatic adjustment, ice mass change and elastic vertical crustal deformation over the Antarctic ice sheet". In: *J. Glac.* 63.240, pp. 703–715. ISSN: 0022-1430. DOI: 10.1017/jog.2017.37.

Zwally, H.J., Mario B.G., Matthew A.B., and Jack L.S. (2012). *Antarctic and Greenland Drainage Systems*. GSFC Cryospheric Sciences Laboratory. URL: https://earth.gsfc.nasa.gov/cryo/data/polar-altimetry/antarctic-and-greenland-drainage-systems.

Zwally, H.J., J. Li, J.W. Robbins, J.L. Saba, D. Yi, and A.C. Brenner (2015). "Mass gains of the Antarctic ice sheet exceed losses". In: *J. Glac.* 61.230, pp. 1019–1936. DOI: 10.3189/2015JoG15J071.

Zwally, H.J., J.W. Robbins, S.B. Luthcke, B.D. Loomis, and F. Rémy (2021). "Mass balance of the Antarctic ice sheet 1992–2016: reconciling results from GRACE gravimetry with ICESat, ERS1/2 and Envisat altimetry". In: *J. Glac.* 67.263, pp. 533–559. ISSN: 0022-1430. DOI: 10.1017/jog.2021.8.

Acknowledgements

I am very grateful to all people creating the framework conditions that have enabled me to finish this dissertation and that have allowed me to learn so much.
I am very grateful to my Doktorvater Martin Horwath for his immensely esteeming supervision as well as trustful support during the long path I came until the end of this thesis.
I am very grateful to the reviewers of this thesis—Roland Pail and Ingo Sasgen—for their efforts and time on evaluation as well as their very useful comments.
I am very grateful to Andreas Groh particularly for the broad support at the very beginning of my doctorate and for the very helpful discussions.
I am very grateful to Benjamin Gutknecht and Andreas Groh for accompanying me as my office mates with scientific but also non-scientific discussions and thus creating a well-being working atmosphere.
I am very grateful to the co-authors for their support during the publications; especially to Taco Broerse, for his efforts and time he invested in Publication 2.
I am very grateful to Thorben Döhne for proofreading and the very helpful suggestions which improved the framework paper.
I am very grateful to my colleagues of the Chair of Geodetic Earth System Research for the incomparably friendly atmosphere, also apart from the working hours, which for me has meant that I always felt welcome and very happy to be present.
I am very grateful for having had the opportunity to participate in interesting meetings, summer schools, and exciting expeditions.
I am very grateful to Lutz Eberlein for the intriguing insights to fieldwork.
I am very grateful for having had the opportunity to give lectures and exercises, as I really enjoy teaching.
I am very grateful to Jürgen Kusche and Bernd Uebbing for the collaboration in the two OMCG projects and the very warm atmosphere during my visits in Bonn.
I am very grateful to the scientists at IMAU for the very gainful stay I had in Utrecht.
I am very grateful to the Deutsche Forschungsgemeinschaft for the financial funding within the SPP "SeaLevel", which was a highly inspiring framework for me.
I am very grateful to my children—Albin and Nathan—for the necessary distraction and all the fun we have together.
I am very grateful to my wife Luzia for the many, many support with our children especially during the "Corona-Lockdown" and my absences.
I am very grateful to her for accompanying me on this—unfortunately quite uncertain—path and for being with me.

List of Abbreviations and Symbols[1]

Abbreviations

ACW	Antarctic Circumpolar Wave
AIS	Antarctic Ice Sheet
APIS	Antarctic Peninsula
CE	centre of mass of the solid Earth
CF	centre of the Earth's surface figure
CM	centre of mass of the Earth system
DFG	Deutsche Forschungsgemeinschaft (English: German Research Foundation)
EAIS	East Antarctic Ice Sheet
ECMWF	European Centre for Medium Range Weather Forecast
EL	equilibrium line
ENSO	El Niño-Southern Oscillation
Envisat	Environmental Satellite
ERA	ECMWF re-analysis
ERS	European Remote Sensing Satellite
ESA	European Space Agency
EWH	equivalent water height
FAC	firn air content
FDM	firn densification model
GIA	glacial isostatic adjustment
GIS	Greenland Ice Sheet
GL	grounding line
GNSS	Global Navigation Satellite System
GRACE	Gravity Record And Climate Experiment
GRACE-FO	GRACE-Follow-On
ICESat	Ice, Cloud and Land Elevation Satellite
ICGEM	International Centre for Global Gravity Field Models
IFD	ice flow dynamics
IMAU	Institute for Marine and Atmospheric Research Utrecht
IMBIE	Ice sheet Mass Balance Inter-comparison Exercise
IMC	ice mass change
IPCC	Intergovernmental Panel on Climate Change
ITSG	Institute of Geodesy Graz
MAR	Modèle Atmosphérique Régional (English: Regional Atmosphere Model)
OMCG	Reconciling ocean mass change and GIA from satellite gravity and altimetry
P	publication
RACMO	Regional Atmospheric Climate Model
SAM	Southern Annular Mode
SARIn	Synthetic Aperture Radar Interferometric
SELEN	sea level equation solver
SM	supplemental material
SMB	surface mass balance
SPP	special priority programme
WAIS	West Antarctic Ice Sheet
WCRP	World Climate Research Programme

[1]This list refers to abbreviations and symbols used in the framework paper only. Abbreviations and symbols used in the publications (Chapter 5) are explained therein.

Symbols

$\boldsymbol{\beta}$	parameter vector
Γ	Green's function
Δ	difference
δ_{ij}	Kronecker delta
$\boldsymbol{\epsilon}$	unit vector
ε	regularization factor
θ	colatitude
κ	surface density
λ	latitude
ρ	mass density
Φ	centrifugal potential
$\boldsymbol{\Psi}$	regularization matrix
$\boldsymbol{\omega}$	Earth's rotation vector
a	normalization factor
C^{RSL}	uniform shift of the relative sea level
c	Stokes coefficient
D	region or Domain
$\boldsymbol{d}$	data or observation vector
$\boldsymbol{e}$	residual vector
G	gravitational constant
$\boldsymbol{g}$	gravity field
g	gravity
$\operatorname{grad} V$ or ∇V	gradient of V, V is an example of a scalar field
h	surface elevation or height
h', k', l'	load Love numbers
I	function of ice thickness variation
i, j	indices
l	distance between mass element, $\mathrm{d}M$, and $\boldsymbol{x}$
M	mass
$\boldsymbol{N}$	normal equation matrix
N	geoid height
$\boldsymbol{n}$	right side of the normal equation
n, m	degree and order
$\mathcal{O}$	ocean function
$\boldsymbol{P}$	weighting matrix
P	Legendre function
$\mathbb{R}$	real space
R	earth radius or semi-major axis of reference ellipsoid
r	distance to geocentre
S	relative sea level
t	time
V	gravitational potential
$\mathcal{V}$	volume
W	gravity potential
$\boldsymbol{X}$	design matrix
$\boldsymbol{x}$	position vector
Y	spherical harmonic basis function

List of Figures

Appendix

Supplement of The Cryosphere, 14, 349–366, 2020
https://doi.org/10.5194/tc-14-349-2020-supplement

Supplement of

Sensitivity of inverse glacial isostatic adjustment estimates over Antarctica

Matthias O. Willen et al.

Correspondence to: Matthias O. Willen (matthias.willen@tu-dresden.de)

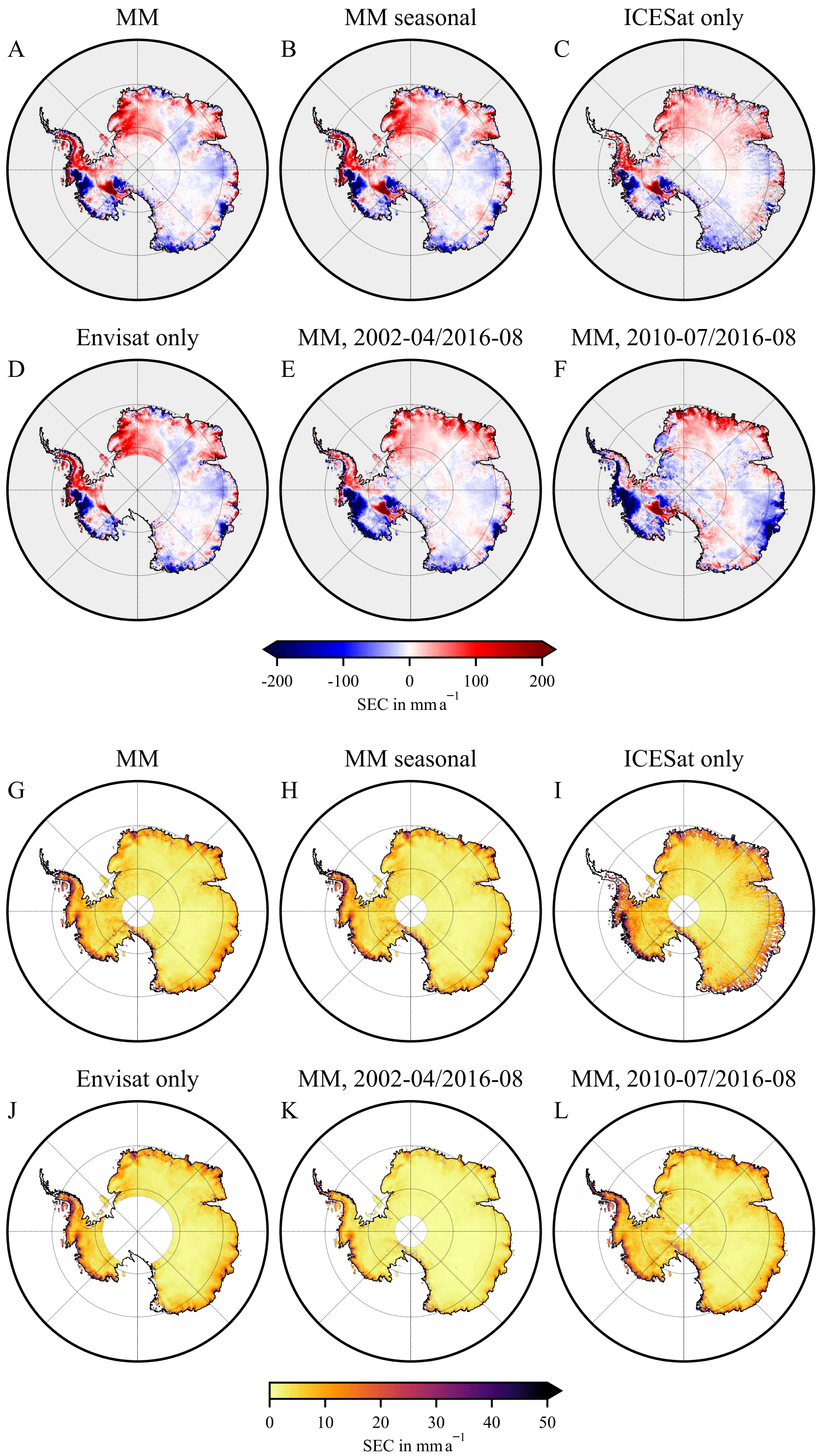

Figure S1: A–D: Estimated altimetry-derived surface elevation change (SEC) from Multi-Mission-Altimetry (MM) and analogous Single-Mission-Processing. Estimation period: 2003-03/2009-09. E, F: MM altimetry for periods specified in the title. G–L: Corresponding uncertainties to A–F from least-squares estimation.

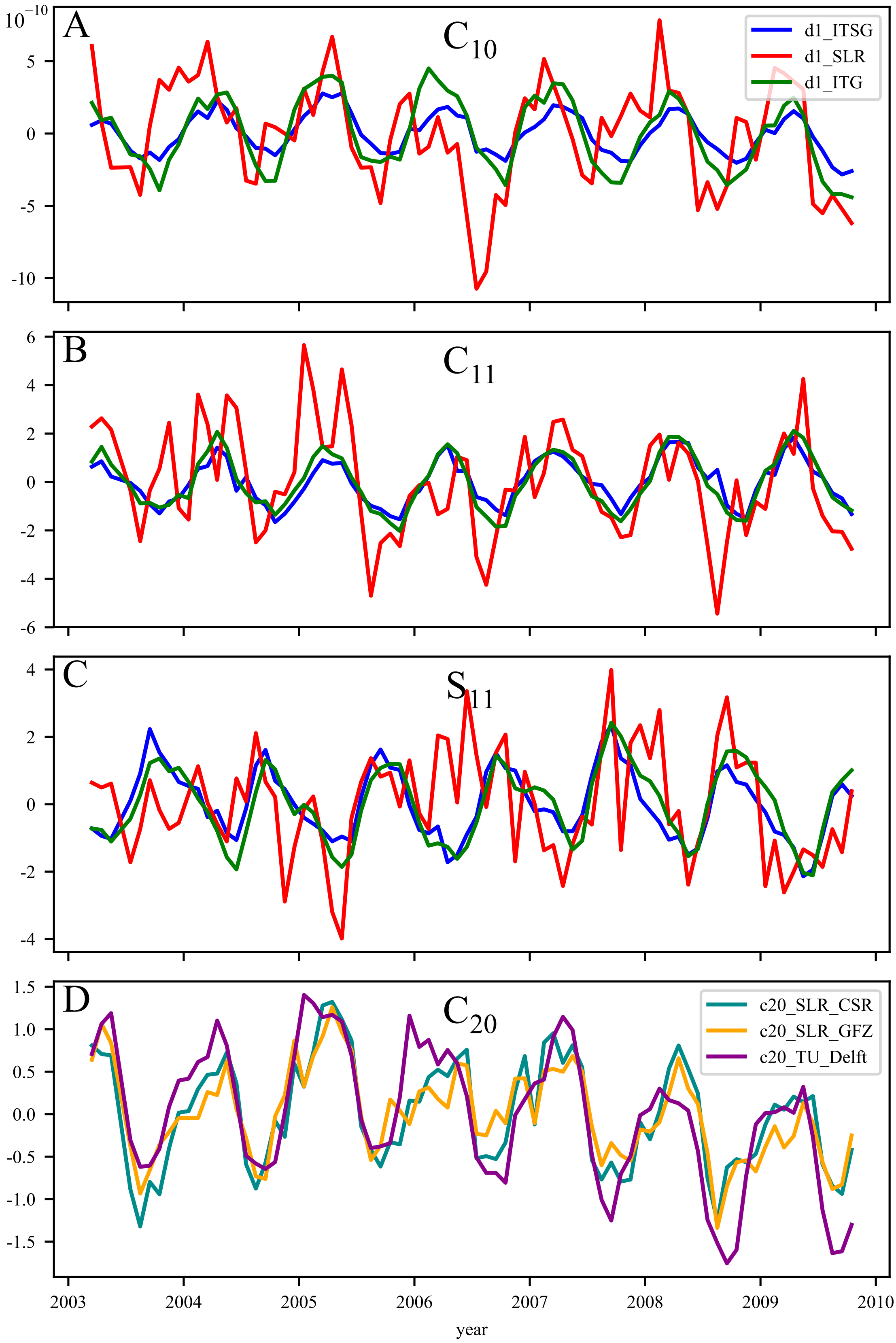

Figure S2: Degree-1 and C_{20} time series (2003-03/2009-09) of products used for replacement in GRACE gravity field solutions.

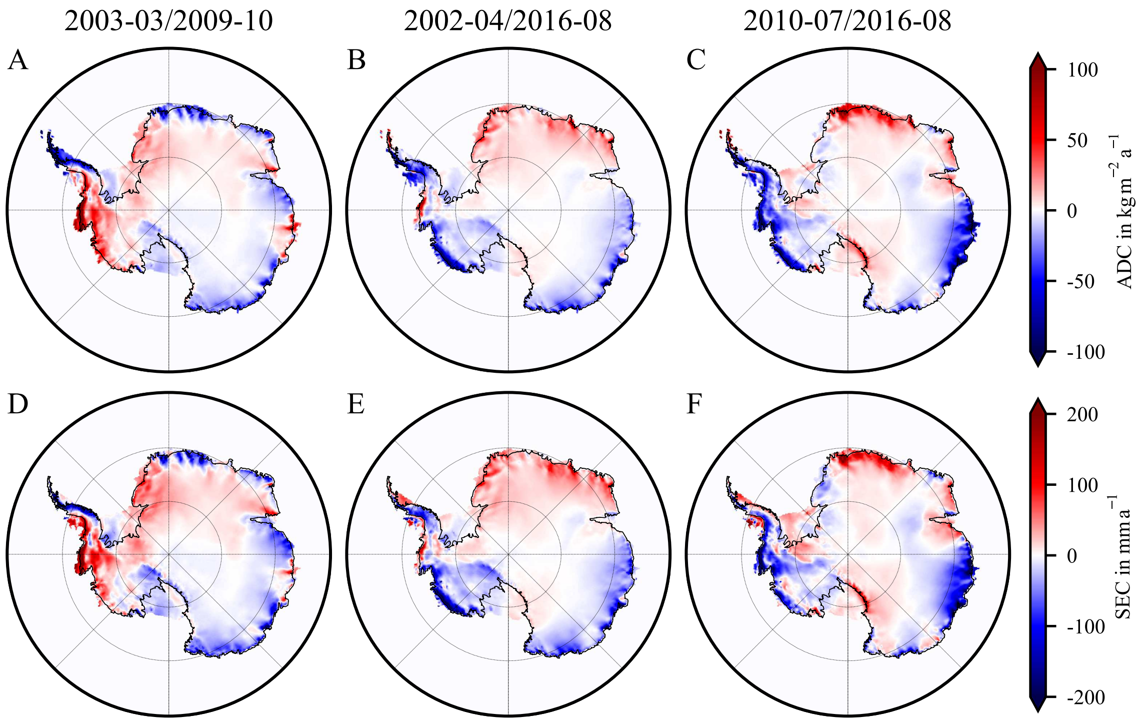

Figure S3: A–C: Estimated area-density change (ADC) of cumulated surface mass balance anomalies (cSMBA) and D–F: the firn densification model derived surface elevation change (SEC) for the used time periods.

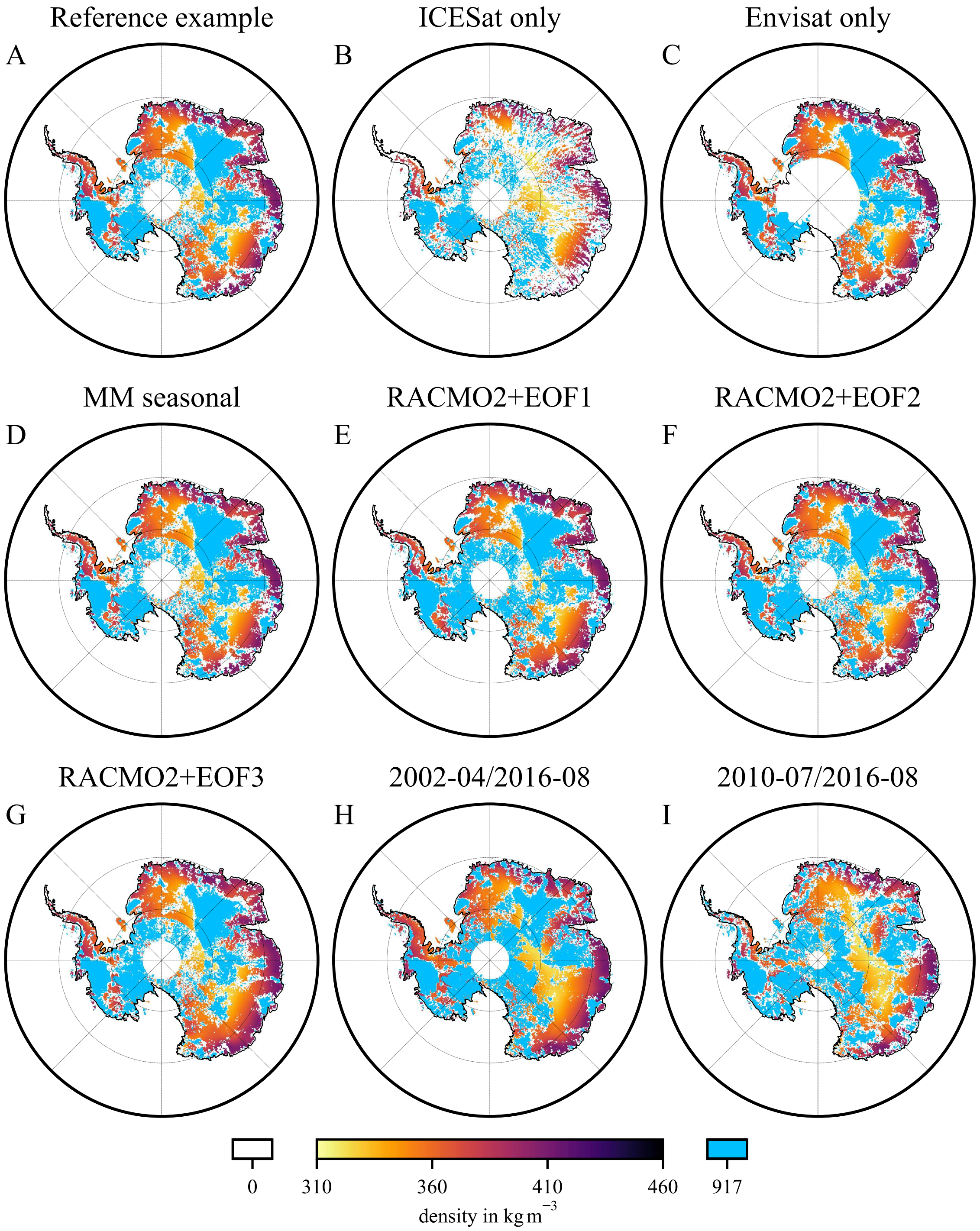

Figure S4: The density ρ_α as determined by Eq. 10 for the different sensitivity experiments (cf. subfigure captions and Table 1).

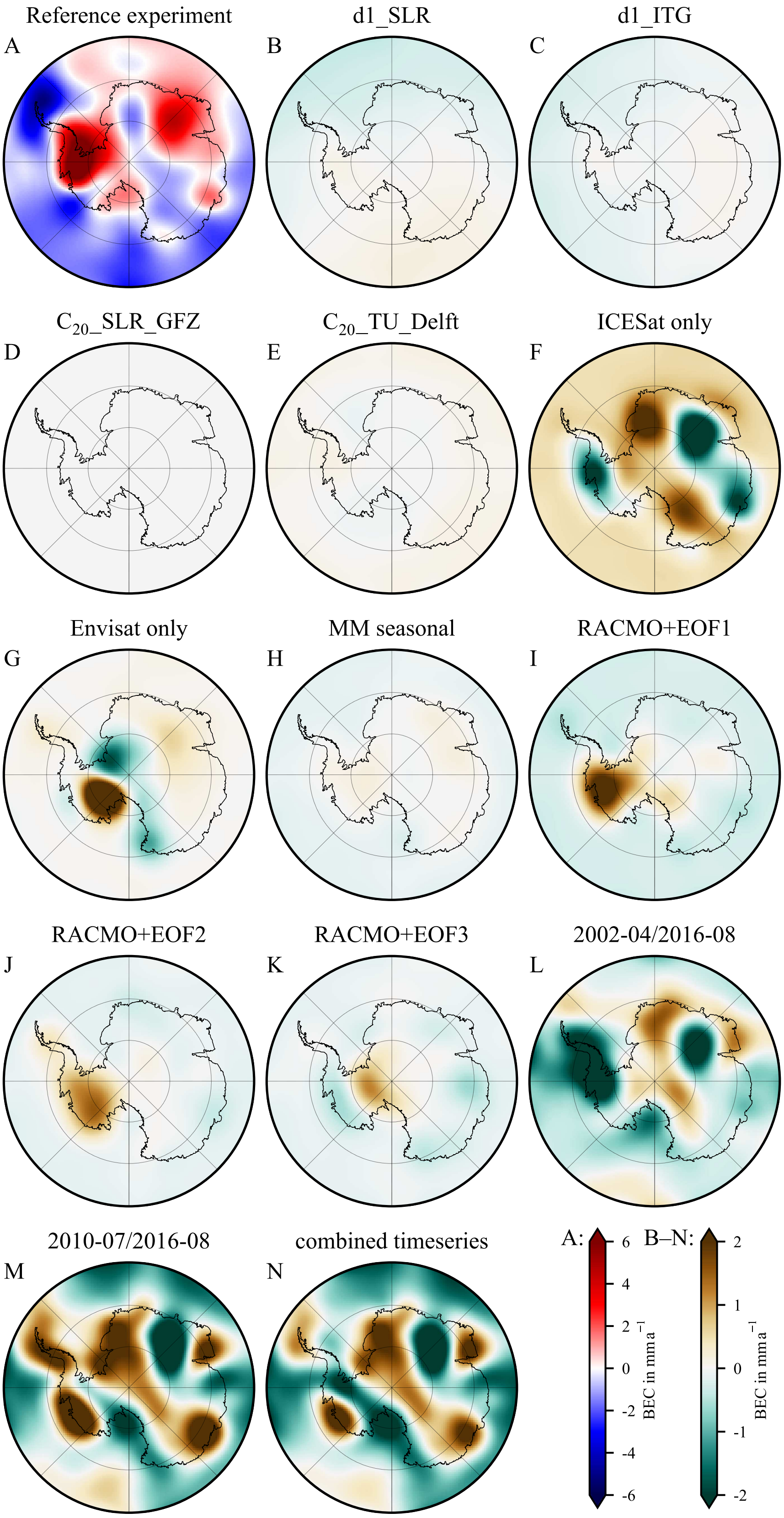

Figure S5: All GIA inverse estimates of bedrock elevation change (BEC) with LPZ-based bias correction obtained in the sensitivity analysis (Sect. 4.2). Subplots B–N show differences with regard to the reference experiment (A).

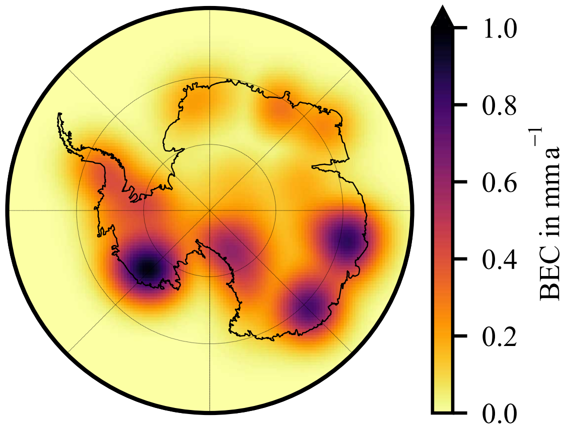

Figure S6: The single standard deviation of the 32 biased estimates of GIA-induced bedrock elevation change (BEC) from propagating the trend differences between RACMO2.3p2 and MAR. The mass change integrated for AIS is 19 Gt a^{-1}.

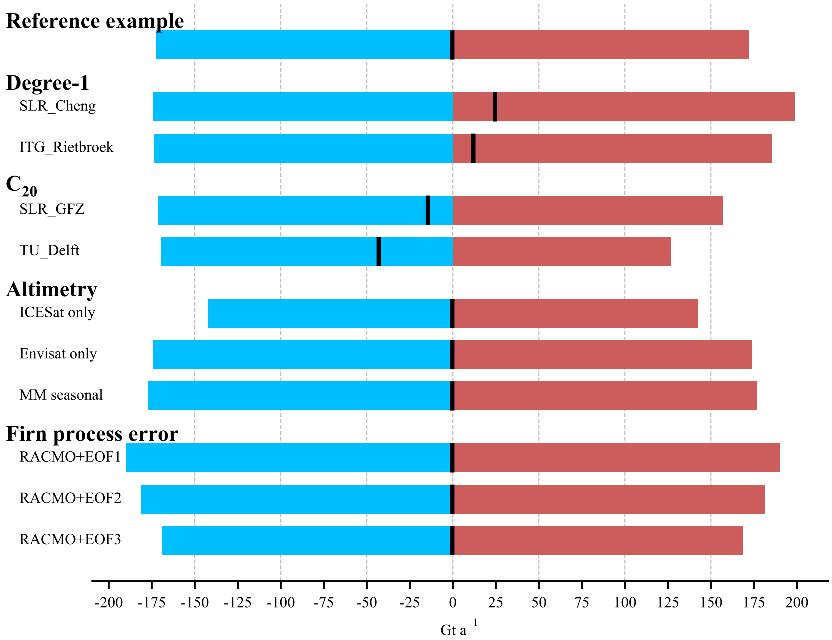

Figure S7: Biased mass change results of the sensitivity study (cf. Fig. 6). Biased total-mass change (solid black lines) is separated into biased GIA-related mass change (red) and ice-mass change (blue). Note that total-mass change of 0 Gt a^{-1} arises coincidentally by used input data.

Supporting Information for:

Separating long-term and short-term mass changes of Antarctic ice drainage basins: a coupled state space analysis of satellite observations and model products

M. O. Willen[1], T. Broerse[2], A. Groh[1], B. Wouters[3,4], P. Kuipers Munneke[3], M. Horwath[1], M. R. van den Broeke[3], and L. Schröder[5]

[1]Institut für Planetare Geodäsie, Technische Universität Dresden, Dresden, Germany
[2]Department of Geosciences, Utrecht University, Utrecht, The Netherlands
[3]Institute for Marine and Atmospheric research Utrecht (IMAU), Utrecht University, Utrecht, The Netherlands
[4]Faculty of Civil Engineering and Geosciences, Delft University of Technology, Delft, The Netherlands
[5]Federal Agency for Cartography and Geodesy, Leipzig, Germany

Contents

A State space vectors and matrices

Here we provide details on the contents of the vectors and matrices that we use to setup our state space model. We use the following dimensions in our models: the state coefficient dimension $m = 14$, the number of time series $p = 2$ and the number of epochs n. The $[m \times 1]$ state vector $\boldsymbol{\alpha}_i$ contains the time variable model coefficients $\boldsymbol{\alpha}_i$ for times $t_i, i = 1, ..., n$, and it reads in our case:

$$\boldsymbol{\alpha}_i = [\mu_i^{\mathrm{v}}\ \nu_i^{\mathrm{v}}\ c_{i,1}^{\mathrm{v}}\ c_{i,1}^{*\mathrm{v}}\ c_{i,2}^{\mathrm{v}}\ c_{i,2}^{*\mathrm{v}}\ \zeta_i^{\mathrm{v}}\ \mu_i^{\mathrm{m}}\ \nu_i^{\mathrm{m}}\ c_{i,1}^{\mathrm{m}}\ c_{i,1}^{*\mathrm{m}}\ c_{i,2}^{\mathrm{m}}\ c_{i,2}^{*\mathrm{m}}\ \zeta_i^{\mathrm{m}}] \tag{S1}$$

with trend $\boldsymbol{\mu}_i$ and rate $\boldsymbol{\nu}_i$; cycle (seasonal harmonic) terms $\boldsymbol{c}_i$ and $\boldsymbol{c}_i^*$ with subscripts 1 and 2 for annual and half-annual cycles, respectively; AR(1) process component $\boldsymbol{\zeta}_i$, and superscripts v denoting the volume time series from the ALT–FDM combination and m denoting the mass time series from GRACE–cSMBA. The accompanying disturbances can be put in the vector $\boldsymbol{\eta}_i$:

$$\boldsymbol{\eta}_i = [0\ \xi_i^{\mathrm{v}}\ \omega_{i,1}^{\mathrm{v}}\ \omega_{i,1}^{*\mathrm{v}}\ \omega_{i,2}^{\mathrm{v}}\ \omega_{i,2}^{*\mathrm{v}}\ \psi_i^{\mathrm{v}}\ 0\ \xi_i^{\mathrm{m}}\ \omega_{i,1}^{\mathrm{m}}\ \omega_{i,1}^{*\mathrm{m}}\ \omega_{i,2}^{\mathrm{m}}\ \omega_{i,2}^{*\mathrm{m}}\ \psi_i^{\mathrm{m}}] \tag{S2}$$

Where in our models the trend level positions are empty as we do not include trend level disturbances, as these would add too short-term variations to the trend. Furthermore, trend level disturbance would cause model redundancy as these short-term variations are already modeled with the AR(1) process.

The $[p \times m]$ design matrix $\boldsymbol{Z}_i$ connects the state vector $\boldsymbol{\alpha}_i$ to the $[p \times 1]$ observations $\boldsymbol{y}_i$:

$$\boldsymbol{y}_i = \boldsymbol{Z}_i \boldsymbol{\alpha}_i + \boldsymbol{\epsilon}_i \tag{S3}$$

The design matrix has non-zero elements for the positions of trend levels $\boldsymbol{\mu}_i$, cycles $\boldsymbol{c}_{i,j}$ and AR(1) $\boldsymbol{\zeta}_i$ terms:

$$\boldsymbol{Z}_i = \begin{bmatrix} 1 & 0 & 1 & 0 & 1 & 0 & 1 & 0 & 0 & 0 & 0 & 0 & 0 & 0 \\ 0 & 0 & 0 & 0 & 0 & 0 & 0 & 1 & 0 & 1 & 0 & 1 & 0 & 1 \end{bmatrix} \tag{S4}$$

The $[m \times m]$ transition matrix $\boldsymbol{T}_i$ translates the state at epoch i to the state at epoch $i+1$:

$$\boldsymbol{\alpha}_{i+1} = \boldsymbol{T}_i \boldsymbol{\alpha}_i + \boldsymbol{Q}_i \tag{S5}$$

As we set up our state space model as (see main text for details on the components):

$$\boldsymbol{y}_i = \boldsymbol{\mu}_i + \sum_j \boldsymbol{c}_{i,j} + \boldsymbol{\zeta}_i + \boldsymbol{\epsilon}_i \tag{S6}$$

$\boldsymbol{T}_i$ becomes for our model:

$$\boldsymbol{T}_i = \begin{bmatrix}
1 & dt_i & 0 & 0 & 0 & 0 & 0 & \dots & \\
0 & 1 & 0 & 0 & 0 & 0 & & & \\
0 & 0 & cos(\lambda_1 dt_i) & sin(\lambda_1 dt_i) & 0 & 0 & 0 & & \\
0 & 0 & -sin(\lambda_1 dt_i) & cos(\lambda_1 dt_i) & 0 & 0 & 0 & & \\
0 & 0 & 0 & 0 & cos(\lambda_2 dt_i) & sin(\lambda_2 dt_i) & 0 & & \\
0 & 0 & 0 & 0 & -sin(\lambda_2 dt_i) & cos(\lambda_2 dt_i) & 0 & & \\
0 & 0 & 0 & 0 & 0 & 0 & \phi^{dt_i} & & \\
\vdots & & & & & & & \ddots & \\
 & \ddots & & & & & & & \vdots \\
 & & 1 & dt_i & 0 & 0 & 0 & 0 & 0 \\
 & & 0 & 1 & 0 & 0 & 0 & 0 & \\
 & & 0 & 0 & cos(\lambda_1 dt_i) & sin(\lambda_1 dt_i) & 0 & 0 & 0 \\
 & & 0 & 0 & -sin(\lambda_1 dt_i) & cos(\lambda_1 dt_i) & 0 & 0 & 0 \\
 & & 0 & 0 & 0 & 0 & cos(\lambda_2 dt_i) & sin(\lambda_2 dt_i) & 0 \\
 & & 0 & 0 & 0 & 0 & -sin(\lambda_2 dt_i) & cos(\lambda_2 dt_i) & 0 \\
 & \dots & 0 & 0 & 0 & 0 & 0 & 0 & \phi^{dt_i}
\end{bmatrix} \tag{S7}$$

Matrix $\boldsymbol{Q}_i$ $[m \times m]$ contains disturbance $\boldsymbol{\eta}$ variances and covariances:

$$\boldsymbol{Q}_i = \boldsymbol{\Sigma}_\eta dt_i \tag{S8}$$

with

$$
\boldsymbol{\Sigma}_\eta = \begin{bmatrix}
0 & 0 & 0 & 0 & 0 & 0 & 0 & 0 & 0 & 0 & 0 & 0 & 0 & 0 \\
0 & \sigma^2_{\xi^{\mathrm{v}}} & 0 & 0 & 0 & 0 & 0 & 0 & \mathrm{cov}(\xi^{\mathrm{v}}, \xi^{\mathrm{m}}) & 0 & 0 & 0 & 0 & 0 \\
0 & 0 & \sigma^2_{\omega^{\mathrm{v}}_{i,1}} & \sigma^2_{\omega^{\mathrm{v}}_{i,1}} & 0 & 0 & 0 & 0 & 0 & 0 & 0 & 0 & 0 & 0 \\
0 & 0 & \sigma^2_{\omega^{\mathrm{v}}_{i,1}} & \sigma^2_{\omega^{\mathrm{v}}_{i,1}} & 0 & 0 & 0 & 0 & 0 & 0 & 0 & 0 & 0 & 0 \\
0 & 0 & 0 & 0 & \sigma^2_{\omega^{\mathrm{v}}_{i,2}} & \sigma^2_{\omega^{\mathrm{v}}_{i,2}} & 0 & 0 & 0 & 0 & 0 & 0 & 0 & 0 \\
0 & 0 & 0 & 0 & \sigma^2_{\omega^{\mathrm{v}}_{i,2}} & \sigma^2_{\omega^{*\mathrm{v}}_{i,2}} & 0 & 0 & 0 & 0 & 0 & 0 & 0 & 0 \\
0 & 0 & 0 & 0 & 0 & 0 & \sigma^2_{\psi^{\mathrm{v}}} & 0 & 0 & 0 & 0 & 0 & 0 & \mathrm{cov}(\psi^{\mathrm{v}}, \psi^{\mathrm{m}}) \\
0 & 0 & 0 & 0 & 0 & 0 & 0 & 0 & 0 & 0 & 0 & 0 & 0 & 0 \\
0 & \mathrm{cov}(\xi^{\mathrm{v}}, \xi^{\mathrm{m}}) & 0 & 0 & 0 & 0 & 0 & 0 & \sigma^2_{\xi^{\mathrm{m}}} & 0 & 0 & 0 & 0 & 0 \\
0 & 0 & 0 & 0 & 0 & 0 & 0 & 0 & 0 & \sigma^2_{\omega^{m}_{i,1}} & \sigma^2_{\omega^{m}_{i,1}} & 0 & 0 & 0 \\
0 & 0 & 0 & 0 & 0 & 0 & 0 & 0 & 0 & \sigma^2_{\omega^{m}_{i,1}} & \sigma^2_{\omega^{m}_{i,1}} & 0 & 0 & 0 \\
0 & 0 & 0 & 0 & 0 & 0 & 0 & 0 & 0 & 0 & 0 & \sigma^2_{\omega^{m}_{i,2}} & \sigma^2_{\omega^{m}_{i,2}} & 0 \\
0 & 0 & 0 & 0 & 0 & 0 & 0 & 0 & 0 & 0 & 0 & \sigma^2_{\omega^{m}_{i,2}} & \sigma^2_{\omega^{m}_{i,2}} & 0 \\
0 & 0 & 0 & 0 & 0 & 0 & \mathrm{cov}(\psi^{\mathrm{v}}, \psi^{\mathrm{m}}) & 0 & 0 & 0 & 0 & 0 & 0 & \sigma^2_{\psi^{\mathrm{m}}}
\end{bmatrix} \tag{S9}
$$

We equate disturbance variances for $\boldsymbol{\omega}^*$ to $\boldsymbol{\omega}$ and set their correlations to 1. We do not include disturbance covariances between different type of components. Matrix $\boldsymbol{H}$ contains the irregular component variance-covariances $[p \times p]$:

$$
\boldsymbol{H}_i = \boldsymbol{\Sigma}_\epsilon dt_i = \begin{bmatrix} \sigma^2_{\epsilon^{\mathrm{v}}} & \mathrm{cov}(\epsilon^{\mathrm{v}}, \epsilon^{\mathrm{m}}) \\ \mathrm{cov}(\epsilon^{\mathrm{v}}, \epsilon^{\mathrm{m}}) & \sigma^2_{\epsilon^{\mathrm{m}}} \end{bmatrix} dt_i \tag{S10}
$$

B State estimation filters

B.1 Kalman filter

The Kalman filter estimates from $\boldsymbol{Y}_i = \boldsymbol{y}_1, .., \boldsymbol{y}_i$ (the observations up to the current epoch i) the filtered state $[m \times 1]$ $\boldsymbol{a}$:

$$
\boldsymbol{a}_{i+1} = E(\boldsymbol{\alpha}_{i+1} | \boldsymbol{Y}_i) \tag{S11}
$$

and its $[m \times m]$ error variance

$$\boldsymbol{P}_{i+1} = \mathrm{var}(\boldsymbol{\alpha}_{i+1}|\boldsymbol{Y}_i) \tag{S12}$$

in a forward iteration $i = 1,..,n$. The Kalman filter consists of the five equations (Durbin & Koopman, 2012):

$$\begin{aligned} \boldsymbol{v}_i &= \boldsymbol{y}_i - \boldsymbol{Z}_i\boldsymbol{a}_i & \boldsymbol{F}_i &= \boldsymbol{Z}_i\boldsymbol{P}_i\boldsymbol{Z}_i^{\mathrm{T}} + \boldsymbol{H}_i \\ \boldsymbol{K}_i &= \boldsymbol{T}_i\boldsymbol{P}_i\boldsymbol{Z}_i^{\mathrm{T}}(\boldsymbol{F}_i)^{-1} \\ \boldsymbol{a}_{i+1} &= \boldsymbol{T}_i\boldsymbol{a}_i + \boldsymbol{K}_i\boldsymbol{v}_i & \boldsymbol{P}_{i+1} &= \boldsymbol{T}_i\boldsymbol{P}_i(\boldsymbol{T}_i - \boldsymbol{K}_i\boldsymbol{Z}_i)^{\mathrm{T}} + \boldsymbol{R}_i\boldsymbol{Q}_i\boldsymbol{R}_i^{\mathrm{T}} \end{aligned} \tag{S13}$$

where $[p \times 1]$ $\boldsymbol{v}_i$ is the prediction error with $[p \times p]$ variance $\boldsymbol{F}_i$ and $[m \times p]$ $\boldsymbol{K}_i$ is the Kalman gain; $\boldsymbol{R}_i$ is commonly an identity matrix. We initialise the filtered state $\boldsymbol{a}_1$ with zero and its error $\boldsymbol{P}_1$ with a large number (10^4). We make an exception for the initial error variance of $\boldsymbol{\zeta}_1$ that we equate with σ^2_ψ (the AR(1) disturbance variance) to force the AR(1) process to start at zero for the first epoch.

B.2 State smoother

As the filtered estimate $\boldsymbol{a}_i$ of $\boldsymbol{\alpha}_i$ is based only on observations up to epoch i, the estimate $\boldsymbol{a}_i$ improves progressively when more observations have been filtered, i.e. with time. To estimate the state $\hat{\boldsymbol{\alpha}}_i$ and its $[m \times m]$ error variance $\boldsymbol{V}_i$ using all observations $\boldsymbol{Y}_n = y_1, ..., y_n$, we use a so-called smoother. The smoother consists of a backward loop for $t = n, ..., 1$ (chapter 4.4.4 of Durbin and Koopman (2012)). The smoothed state and its variance matrix are defined as:

$$\hat{\boldsymbol{\alpha}}_i = E(\boldsymbol{\alpha}_i|\boldsymbol{Y}_n) \tag{S14}$$

and its $[m \times m]$ error variance

$$\boldsymbol{V}_i = \mathrm{var}(\boldsymbol{\alpha}_i|\boldsymbol{Y}_n) \tag{S15}$$

The smoother equations are:

$$\begin{aligned} \boldsymbol{r}_{i-1} &= \boldsymbol{Z}_i^{\mathrm{T}}\boldsymbol{F}_i^{-1}\boldsymbol{v}_i + \boldsymbol{L}_i^{\mathrm{T}}\boldsymbol{r}_i & \boldsymbol{N}_{i-1} &= \boldsymbol{Z}_i^{\mathrm{T}}\boldsymbol{F}_i^{-1}\boldsymbol{Z}_i + \boldsymbol{L}_i^{\mathrm{T}}\boldsymbol{N}_i\boldsymbol{L}_i \\ \boldsymbol{L}_i &= \boldsymbol{T}_i - \boldsymbol{K}_i\boldsymbol{Z}_i \\ \hat{\boldsymbol{\alpha}}_i &= \boldsymbol{a}_i + \boldsymbol{P}_i\boldsymbol{r}_{i-1} & \boldsymbol{V}_i &= \boldsymbol{P}_i - \boldsymbol{P}_i\boldsymbol{N}_{i-1}\boldsymbol{P}_i \end{aligned} \tag{S16}$$

where $[m \times 1]$ vector $\boldsymbol{r}_i$ is called the weighted sum of innovations and $[m \times m]$ matrix $\boldsymbol{N}_i$ the weighted sum of the inverse variances, with $\boldsymbol{r}_n = \mathbf{0}$ and $\boldsymbol{N}_n = \mathbf{0}$.

B.3 Disturbance smoother

An alternative smoother computes smoothed estimates of disturbances $\boldsymbol{\epsilon}$ and $\boldsymbol{\eta}$ (chapter 4.5 of Durbin and Koopman (2012)):

$$\hat{\boldsymbol{\epsilon}}_i = E(\boldsymbol{\epsilon}_i|\boldsymbol{Y}_n) \qquad \hat{\boldsymbol{\eta}}_i = E(\boldsymbol{\eta}_i|\boldsymbol{Y}_n) \tag{S17}$$

These are calculated using the following recursion for $t_i = n, ..., 1$ by:

$$
\begin{aligned}
\boldsymbol{u}_i &= \boldsymbol{F}_i^{-1}\boldsymbol{v}_i - \boldsymbol{K}_i^{\mathrm{T}}\boldsymbol{r}_i & \boldsymbol{D}_i &= \boldsymbol{F}_i^{-1} + \boldsymbol{K}_i^{\mathrm{T}}\boldsymbol{N}_i\boldsymbol{K}_i \\
\boldsymbol{N}_{i-1} &= \boldsymbol{Z}_i^{\mathrm{T}}\boldsymbol{D}_i\boldsymbol{Z}_i + \boldsymbol{T}_i^{\mathrm{T}}\boldsymbol{N}_i\boldsymbol{T}_i - \boldsymbol{Z}_i^{\mathrm{T}}\boldsymbol{K}_i^{\mathrm{T}}\boldsymbol{N}_i\boldsymbol{T}_i - \boldsymbol{T}_i^{\mathrm{T}}\boldsymbol{N}_i\boldsymbol{K}_i\boldsymbol{Z}_i & \boldsymbol{r}_{i-1} &= \boldsymbol{Z}_i^{\mathrm{T}}\boldsymbol{u}_i + \boldsymbol{T}_i^{\mathrm{T}}\boldsymbol{r}_i \\
\hat{\boldsymbol{\epsilon}}_i &= \boldsymbol{H}_i\boldsymbol{u}_i & \mathrm{var}(\boldsymbol{\epsilon}_i|\boldsymbol{Y}_n) &= \boldsymbol{H}_i - \boldsymbol{H}_i\boldsymbol{D}_i\boldsymbol{H}_i \\
\hat{\boldsymbol{\eta}}_i &= \boldsymbol{Q}_i\boldsymbol{R}_i^{\mathrm{T}}\boldsymbol{r}_i & \mathrm{var}(\boldsymbol{\eta}_i|\boldsymbol{Y}_n) &= \boldsymbol{Q}_i - \boldsymbol{Q}_i\boldsymbol{R}_i^{\mathrm{T}}\boldsymbol{N}_i^{\mathrm{T}}\boldsymbol{R}_i\boldsymbol{Q}_i
\end{aligned}
\tag{S18}
$$

With additional $[p \times 1]$ smoothing error vector $\boldsymbol{u}_i$ and $[p \times p]$ variance matrix $\boldsymbol{D}_i$. We use the disturbance smoother for optimizing the disturbance variances as in that case the state itself does not need to be estimated.

B.4 Missing observations

If missing observations are present in one of the two time series, which is the case for GRACE data, we can update the state for the missing time series using an extrapolation (Durbin & Koopman, 2012). To do so, $\boldsymbol{w}_i$ are the indices of those dimensions that have observations, and we use a masking matrix $\boldsymbol{W}_i(\boldsymbol{w}_i, \boldsymbol{w}_i) = 1$ to make an alternative design matrix:

$$\boldsymbol{Z}_i^* = \boldsymbol{W}_i\boldsymbol{Z}_i \tag{S19}$$

Similarly for the irregular covariance matrix and observation we use adapted matrices and vectors:

$$
\begin{aligned}
\boldsymbol{H}_i^* &= \boldsymbol{W}_i\boldsymbol{H}_i \\
\boldsymbol{y}_i^* &= \boldsymbol{W}_i\boldsymbol{y}_i
\end{aligned}
\tag{S20}
$$

Subsequently, the matrices and vectors of $\boldsymbol{Z}_i$, $\boldsymbol{H}_i$ and $\boldsymbol{y}_i$ can be replaced by $\boldsymbol{Z}_i^*$, $\boldsymbol{H}_i^*$ and $\boldsymbol{y}_i^*$ in the equations for the Kalman filter, smoother and disturbance smoother (Eq. S13, S16, S18). The result will be that the state of the unobserved dimension is extrapolated using $\boldsymbol{T}_i$ and $\boldsymbol{a}_i$ only without an update from $\boldsymbol{K}_i$.

B.5 Estimation of additional parameters

As we do not have reliable prior information about the disturbance variances and covariances $\boldsymbol{\Sigma}_\epsilon$ and $\boldsymbol{\Sigma}_\eta$ we aim to obtain the (co)variances that lead to the best fit with the observations $\boldsymbol{Y}_n$. The same holds for the AR(1) coefficients $\boldsymbol{\phi}$. We estimate optimal values for these parameters by maximising the likelihood $\mathcal{L}(y)$.

$$\mathcal{L}(y) = p(\boldsymbol{y}_1, ..., \boldsymbol{y}_n|\boldsymbol{\Sigma}_\epsilon, \boldsymbol{\Sigma}_\eta, \boldsymbol{\phi}) \tag{S21}$$

More in specific, we maximize the log of the likelihood $\log\mathcal{L}$ instead, which equals (chapter 7.2 of Durbin and Koopman (2012)):

$$\log\mathcal{L}(\boldsymbol{Y}_n) = -\frac{n}{2}\log(2\pi) - \frac{1}{2}\sum_{i=1}^{n}\left(\log|\boldsymbol{F}_i| + \boldsymbol{v}_i^{\mathrm{T}}\boldsymbol{F}_i\boldsymbol{v}_i\right) \tag{S22}$$

The log-likelihood is thus dependent on the (forward) prediction error $\boldsymbol{v}$ and its variance $\boldsymbol{F}$, computed by equation S13. We maximise $\log\mathcal{L}$ for disturbance parameters $\boldsymbol{\Sigma}_\epsilon$ and $\boldsymbol{\Sigma}_\eta$, using the expectation-maximisation algorithm (EM-algorithm) and that should always lead to increasing log likelihood. Koopman (1993) provides equations for iterative updates of disturbance variance-covariance matrices $\boldsymbol{\Sigma}_\eta$ and $\boldsymbol{\Sigma}_\epsilon$ (with corrections from Durbin and Koopman (2012)):

$$\bar{\boldsymbol{\Sigma}}_\epsilon = \tilde{\boldsymbol{\Sigma}}_\epsilon + \frac{1}{n}\tilde{\boldsymbol{\Sigma}}_\epsilon \sum_{i=1}^{n} \left(\boldsymbol{u}_i\boldsymbol{u}_i^{\mathrm{T}} - \boldsymbol{D}_i\right)\tilde{\boldsymbol{\Sigma}}_\epsilon \tag{S23}$$

$$\bar{\boldsymbol{\Sigma}}_\eta = \tilde{\boldsymbol{\Sigma}}_\eta + \frac{1}{n-1}\tilde{\boldsymbol{\Sigma}}_\eta \sum_{i=1}^{n} \left(\boldsymbol{r}_{i-1}\boldsymbol{r}_{i-1}^{\mathrm{T}} - \boldsymbol{N}_{i-1}\right)\tilde{\boldsymbol{\Sigma}}_\eta \tag{S24}$$

with updates denoted with a bar and previous values denoted with a tilde. Smoother vectors and matrices $\boldsymbol{u}_i$, $\boldsymbol{D}_i$, $\boldsymbol{r}_i$ and $\boldsymbol{N}_i$ are determined using the disturbance filter. The EM-algorithm is applied until convergence of $\log\mathcal{L}$ has been reached. The EM-algorithm searches for a local optimum only, which means that it is important to start with an educated guess for the disturbance parameters. To find optimal values for ϕ we optimize $\log\mathcal{L}$ in a grid search in the ϕ range [0.6 1]. Notably, variances initially set to zero, will stay zero during the iteration, and correlations set to 1 will stay 1 during the application of the EM-algorithm. Correlations resulting from equation S24 between different type of disturbance components we do not preserve.

C Estimation of values for comparison

C.1 Mean time-variable rate

For comparison with the deterministic trends with a constant rate, we also compute the mean rates over the full time interval Δt:

$$\overline{\boldsymbol{\nu}} = \frac{1}{\Delta t}\sum_{i=1}^{n} \boldsymbol{\nu}_i \overline{dt_i} \tag{S25}$$

where we use a slightly different definition of the time step $\overline{dt_i}$ than before to perform the integration:

$$\overline{dt_i} = \begin{cases} (t_{i+1} - t_i)/2 & \text{if } i = 1; \\ (t_i - t_{i-1})/2 & \text{if } i = \text{n}; \\ (t_{i+1} - t_{i-1})/2 & \text{else.} \end{cases}$$

We obtain the uncertainty of the average rate $\boldsymbol{\sigma}_{\overline{\nu}}$ by propagation of smoothed error variances of the estimated time variable rate $\boldsymbol{\sigma}^2_{\nu_i}$, and the temporal auto-covariances of the estimated (smoothed) rate $\boldsymbol{\sigma}_{\nu_{ij}}$.

$$\boldsymbol{\sigma}_{\overline{\nu}} = \frac{1}{\Delta t}\sqrt{\sum_{i=1}^{n} \overline{dt_i}^2 \boldsymbol{\sigma}^2_{\nu_i} + \sum_{i=1}^{n}\sum_{j=1 (j\neq i)}^{n} \overline{dt_i dt_j}\boldsymbol{\sigma}_{\nu_{ij}}} \tag{S26}$$

The auto-covariance of the rate ($\boldsymbol{\sigma}_{\nu_{ij}}$) (i.e. the covariance of the state between different epochs) is part of the auto-covariance matrix of the smoothed state $\hat{\boldsymbol{\alpha}}_i$ as (Durbin & Koopman, 2012):

$$\mathrm{cov}(\hat{\boldsymbol{\alpha}}_i, \hat{\boldsymbol{\alpha}}_j) = \boldsymbol{P}_i\boldsymbol{L}_i^{\mathrm{T}}\boldsymbol{L}_{i+1}^{\mathrm{T}} \cdots \boldsymbol{L}_{j-1}^{\mathrm{T}}(\boldsymbol{I} - \boldsymbol{N}_{j-1}\boldsymbol{P}_j) \quad j \geq i \tag{S27}$$

as for the correlation between state component a at epoch i and b at epoch j holds:

$$\text{cov}(\hat{\boldsymbol{\alpha}}_i^a, \hat{\boldsymbol{\alpha}}_j^b) = \text{cov}(\hat{\boldsymbol{\alpha}}_j^b, \hat{\boldsymbol{\alpha}}_i^a) \tag{S28}$$

Then, it follows that the remaining auto-covariances for $j < i$ can be calculated as, using the results from Eq. S27:

$$\text{cov}(\hat{\boldsymbol{\alpha}}_i, \hat{\boldsymbol{\alpha}}_j) = \text{cov}(\hat{\boldsymbol{\alpha}}_j, \hat{\boldsymbol{\alpha}}_i)^{\mathrm{T}} \quad j < i \tag{S29}$$

C.2 Deterministic parameters

Next to the state space model we set up a deterministic model which is solved by ordinary least squares for GRACE–cSMBA and ALT–FDM time series separately from each other. We solve the following system of equations with the parameters, $\boldsymbol{\beta}$, the observations, $\boldsymbol{y}$, the design matrix, $\boldsymbol{X}$, and the residuals, $\boldsymbol{e}$

$$\boldsymbol{X}\boldsymbol{\beta} = \boldsymbol{y} + \boldsymbol{e} \tag{S30}$$

$$\boldsymbol{e} = \boldsymbol{X}\boldsymbol{\beta} - \boldsymbol{y}. \tag{S31}$$

The deterministic model is analogous to the state space model. We estimate a bias, trend, annual cycle, and semi-annual cycle terms. The design matrix is

$$\boldsymbol{X} = \begin{bmatrix} 1 & t_1 & cos\,(2\pi\, t_1) & sin\,(2\pi\, t_1) & cos\,(4\pi\, t_1) & sin\,(4\pi\, t_1) \\ 1 & t_2 & cos\,(2\pi\, t_2) & sin\,(2\pi\, t_2) & cos\,(4\pi\, t_2) & sin\,(4\pi\, t_2) \\ \vdots & \vdots & \vdots & \vdots & \vdots & \vdots \\ 1 & t_n & cos\,(2\pi\, t_n) & sin\,(2\pi\, t_n) & cos\,(4\pi\, t_n) & sin\,(4\pi\, t_n) \end{bmatrix}. \tag{S32}$$

We quantify the mean squared error (MSE) as follows

$$\text{MSE} = \frac{\boldsymbol{e}^{\mathrm{T}}\boldsymbol{e}}{n} \tag{S33}$$

The variance-covariance matrix, $\boldsymbol{\Sigma}_\beta$ can be achieved by

$$\boldsymbol{\Sigma}_\beta = \left(\boldsymbol{X}^{\mathrm{T}}\boldsymbol{X}\right)^{-1} \cdot \text{MSE}. \tag{S34}$$

The square root of the diagonal elements of $\boldsymbol{\Sigma}_\beta$ are the formal uncertainties of the estimated parameters.

C.3 Root mean square

We calculate the root mean square (RMS) of the estimated AR(1)-process as follows

$$\text{RMS}_{\text{AR(1)}} = \sqrt{\frac{1}{n}\sum_{i=1}^{n}(\zeta_i)^2} \tag{S35}$$

and the RMS of the irregular component

$$\text{RMS}_{\text{irr}} = \sqrt{\frac{1}{n}\sum_{i=1}^{n}(\epsilon_i)^2}. \tag{S36}$$

The RMS of the residuals is

$$\mathrm{RMS_{resid}} = \sqrt{\mathrm{MSE}} = \sqrt{\frac{\boldsymbol{e}^T\boldsymbol{e}}{n}} = \sqrt{\frac{1}{n}\sum_{i=1}^{n} e_i^2}. \tag{S37}$$

C.4 Auto-correlations and cross-correlations

We compute auto-correlations of a time series x for lag τ as:

$$\rho(\tau) = \frac{C(\tau)}{C(0)} \tag{S38}$$

$$C(\tau) = \frac{1}{n-\tau}\sum_{i=\tau+1}^{n}(x_i - \bar{x})(x_{i-\tau} - \bar{x}) \tag{S39}$$

$$C(0) = \frac{1}{n}\sum_{i=1}^{n}(x_i - \bar{x})^2 \tag{S40}$$

with $\bar{x}$ denoting the mean of x. Cross-correlations between component time series based on ALT–FDM (v) and GRACE–cSMBA (m) as:

$$\rho(\tau)^{\mathrm{v,m}} = \frac{C(\tau)^{\mathrm{v,m}}}{\sigma^{\mathrm{v}}\sigma^{\mathrm{m}}} \tag{S41}$$

$$C(\tau)^{\mathrm{v,m}} = \frac{1}{n-\tau}\sum_{i=\tau+1}^{n}(x_i^{\mathrm{v}} - \bar{x}^{\mathrm{v}})(x_{i-\tau}^{\mathrm{m}} - \bar{x}^{\mathrm{m}}) \tag{S42}$$

$$\sigma = \sqrt{\frac{1}{n}\sum_{i=1}^{n}(x_i - \bar{x})^2} \tag{S43}$$

C.5 Propagation of the GIA uncertainty

We propagate the GIA uncertainty to GRACE–cSMBA results. In case of mean rates we sum up the variances

$$\left(\sigma_{\overline{\nu}}^{\mathrm{m,GIA}}\right)^2 = (\sigma_{\overline{\nu}}^{\mathrm{m}})^2 + \left(\sigma^{\mathrm{GIA}}\right)^2 \tag{S44}$$

The GIA uncertainty for every time step is

$$\sigma_i^{\mathrm{GIA}} = |t_i - t_{\mathrm{ref}}|\sigma^{\mathrm{GIA}} \tag{S45}$$

ref is the chosen reference time epoch from which the GIA uncertainty linearly diverges (Apr 2002 in our case). We propagate the GIA uncertainty to the time-variable rate as follows:

$$\left(\sigma_{\nu_i}^{\mathrm{m,GIA}}\right)^2 = (\sigma_{\nu_i}^{\mathrm{m}})^2 + \left(\sigma_i^{\mathrm{GIA}}\right)^2 \tag{S46}$$

D Supplemental tables and figures

Table S1: The basin area and deterministic rates estimated from the satellite observations and model products from Apr 2002 to Aug 2016. The fourth column and fifth column are the applied GIA correction to the GRACE data including the 2-σ-uncertainty, and the spread from a GIA model ensemble (Groh & Horwath, 2021). The indicated uncertainties of the rates are the formal 2-σ-uncertanties from least-squares adjustment (Eq. S34). The mean surface mass balance (mean SMB) is estimated over the whole model period (Jan 1979–Dec 2016) and the uncertainty is 2-σ of the mean SMB values over 25, 30, and 35-year time intervals analogously to Wouters et al. (2015). The last two columns are the correlation (corr.) coefficients of detrendend GRACE and cSMBA time series and ALT and FDM time series.

	Area	GRACE rate	GIA correction	GIA spread	cSMBA rate	mean SMB	altimetry rate	FDM rate	corr. coefficient GRACE & cSMBA	corr. coefficient ALT & FDM
	in 1000 km^2	in Gt a^{-1}	in Gt a^{-1}		in Gt a^{-1}	in Gt a^{-1}	in km^{-3} a^{-1}	in km^{-3} a^{-1}		
4	245	11.0 ± 0.5	0.9 ± 2.2	3.6	4.1 ± 0.4	46.5 ± 2.0	10.4 ± 0.9	10.1 ± 1.0	0.76	0.77
5	187	6.9 ± 0.7	0.1 ± 0.8	1.3	1.7 ± 0.4	33.0 ± 1.6	8.2 ± 0.8	4.9 ± 1.0	0.79	0.95
6	605	17.3 ± 1.3	1.3 ± 1.7	2.8	7.1 ± 0.9	79.5 ± 3.9	24.5 ± 2.0	19.4 ± 2.3	0.94	0.94
7	493	16.7 ± 1.2	3.0 ± 3.6	4.8	7.2 ± 0.7	84.6 ± 3.5	23.3 ± 1.6	17.6 ± 1.8	0.82	0.94
8	160	6.7 ± 0.4	1.1 ± 1.1	1.8	2.6 ± 0.2	35.6 ± 1.3	8.6 ± 0.4	6.3 ± 0.5	0.38	0.78
9	145	1.3 ± 0.3	1.3 ± 1.3	1.7	0.3 ± 0.1	19.9 ± 0.4	1.6 ± 0.4	0.9 ± 0.3	0.41	0.60
10	919	4.0 ± 0.4	1.2 ± 5.8	11.1	0.5 ± 0.2	47.2 ± 0.7	-1.0 ± 0.5	1.2 ± 0.6	0.49	0.12
11	256	-0.2 ± 0.3	1.2 ± 2.1	2.7	0.0 ± 0.1	17.7 ± 0.3	-2.4 ± 0.5	0.5 ± 0.4	0.46	0.59
12	717	4.9 ± 1.0	2.6 ± 3.8	5.4	-6.3 ± 0.7	152.7 ± 5.5	-7.9 ± 1.3	-19.3 ± 1.3	0.84	0.87
13	1108	-12.2 ± 1.3	2.2 ± 1.5	3.0	-10.2 ± 1.0	241.0 ± 6.8	-27.1 ± 2.6	-27.5 ± 2.4	0.86	0.93
14	710	-7.4 ± 1.0	3.3 ± 3.2	4.8	-9.5 ± 0.8	140.7 ± 4.9	-11.5 ± 1.4	-21.3 ± 2.1	0.83	0.91
19	372	1.1 ± 0.4	3.7 ± 2.4	8.6	-2.1 ± 0.3	47.0 ± 1.1	-9.1 ± 0.8	-6.5 ± 0.7	0.84	0.80
20	182	-36.2 ± 1.2	1.7 ± 1.2	2.2	-8.4 ± 0.9	132.4 ± 3.4	-39.3 ± 1.8	-19.9 ± 1.9	0.96	0.96
21	217	-54.8 ± 1.2	1.8 ± 1.6	2.1	-3.2 ± 0.6	117.6 ± 2.0	-75.5 ± 1.6	-8.8 ± 1.4	0.89	0.87
22	214	-49.8 ± 1.3	2.9 ± 1.0	2.5	-1.6 ± 0.6	82.5 ± 1.8	-55.7 ± 2.1	-4.3 ± 1.6	0.93	0.95
23	75	-9.8 ± 0.6	1.3 ± 2.0	2.5	1.1 ± 0.4	62.7 ± 1.2	-5.2 ± 1.0	1.7 ± 1.0	0.87	0.96
24	100	-9.9 ± 0.9	2.3 ± 1.7	3.2	-2.4 ± 0.5	86.7 ± 1.6	-4.9 ± 1.3	-5.4 ± 1.2	0.87	0.94

Table S2: Mean rates from state space filtering GRACE–cSMBA and ALT–FDM and the corresponding deterministic results with formal 2-σ-uncertainties (Eq. S34); GRACE–cSMBA uncertainties include GIA uncertainties. Furthermore, the root mean square (RMS) of the AR(1) process and of the irregular component are compared to the RMS of the deterministic residuals (resid). In case of ALT–FDM: the mean rate and the deterministic rate are converted to mass change with an ice density (917 kg m^{-3}).

	GRACE–cSMBA					ALT–FDM				
	mean rate	det. rate	RMS			mean rate	det. rate	RMS		
			AR(1)	irr	resid			AR(1)	irr	resid
	in Gt a^{-1}	in Gt a^{-1}	in Gt	in Gt	in Gt	in Gt a^{-1}	in Gt a^{-1}	in km^3	in km^3	in km^3
4	6.9 ± 2.3	6.8 ± 2.2	2.1	6.1	8.0	2.5 ± 7.6	0.3 ± 0.6	20.9	0.5	17.5
5	5.1 ± 1.0	5.2 ± 0.9	4.9	5.5	10.2	4.4 ± 1.8	3.1 ± 0.3	11.6	0.3	8.8
6	10.1 ± 3.0	10.2 ± 1.8	11.2	9.3	11.5	8.0 ± 4.1	4.7 ± 0.6	31.7	0.1	17.4
7	9.1 ± 4.6	9.5 ± 3.7	4.1	14.8	17.3	4.9 ± 1.5	5.2 ± 0.5	15.5	0.2	15.5
8	4.2 ± 1.7	4.1 ± 1.1	5.3	8.7	9.9	3.7 ± 1.6	2.1 ± 0.3	11.0	0.1	8.8
9	0.9 ± 1.4	0.9 ± 1.3	1.0	5.3	6.2	1.9 ± 4.4	0.6 ± 0.3	17.8	0.0	8.7
10	3.1 ± 5.9	3.4 ± 5.8	2.5	6.4	8.3	0.4 ± 9.8	-2.1 ± 0.6	26.6	0.0	18.9
11	-0.4 ± 2.1	-0.3 ± 2.1	1.0	5.5	6.2	-2.6 ± 0.9	-2.6 ± 0.4	10.3	0.1	12.0
12	10.3 ± 4.0	11.0 ± 3.8	4.4	10.3	13.0	10.4 ± 1.5	10.4 ± 0.5	14.3	0.8	16.0
13	-1.9 ± 1.9	-2.2 ± 1.6	11.4	5.5	16.5	-0.4 ± 2.5	0.4 ± 0.7	21.6	1.0	22.2
14	2.3 ± 3.4	2.2 ± 3.2	5.2	10.0	13.9	9.4 ± 2.9	9.0 ± 0.9	24.8	0.1	26.1
19	3.3 ± 2.4	3.2 ± 2.4	3.0	3.1	5.6	-1.2 ± 1.9	-2.3 ± 0.4	9.8	0.1	11.2
20	-27.2 ± 4.5	-28.0 ± 1.3	16.1	2.9	9.4	-16.6 ± 1.8	-17.8 ± 0.5	14.0	3.5	14.0
21	-50.6 ± 4.0	-51.7 ± 1.7	11.9	6.5	16.1	-61.5 ± 1.4	-61.2 ± 0.7	13.3	1.6	21.8
22	-45.7 ± 1.6	-48.3 ± 1.3	2.6	4.9	18.5	-44.8 ± 1.3	-47.1 ± 0.6	8.6	0.4	19.2
23	-10.2 ± 2.9	-11.1 ± 2.1	6.5	3.8	7.1	-6.4 ± 0.7	-6.4 ± 0.2	6.0	0.3	6.9
24	-6.1 ± 4.1	-7.5 ± 1.8	8.1	6.6	12.3	0.2 ± 1.2	0.4 ± 0.4	8.5	0.1	11.4

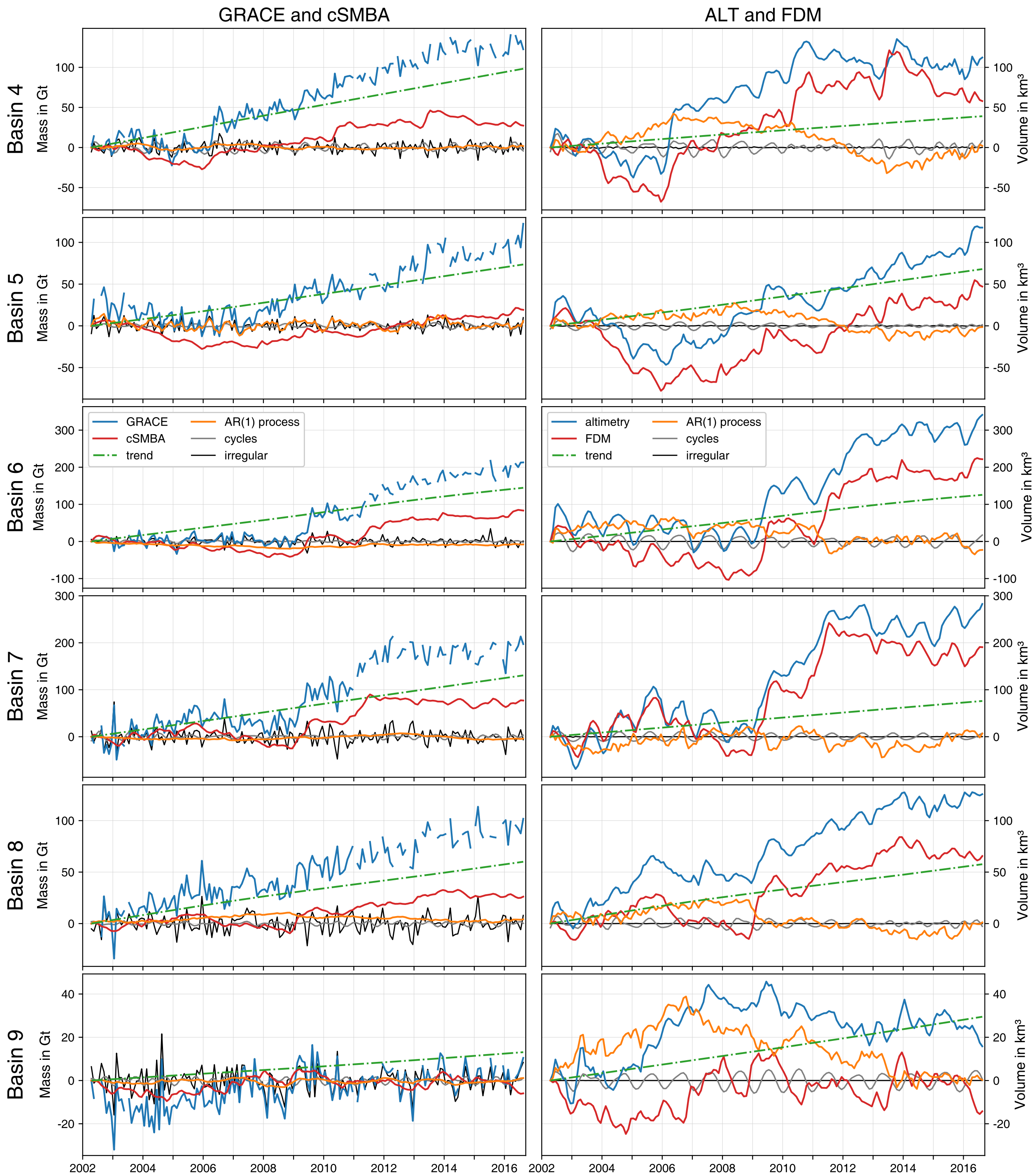
GRACE and cSMBA
ALT and FDM
Basin 4
Basin 5
Basin 6
Basin 7
Basin 8
Basin 9
Mass in Gt
Volume in km³
GRACE
cSMBA
trend
AR(1) process
cycles
irregular
altimetry
FDM
trend
AR(1) process
cycles
irregular
2002
2004
2006
2008
2010
2012
2014
2016

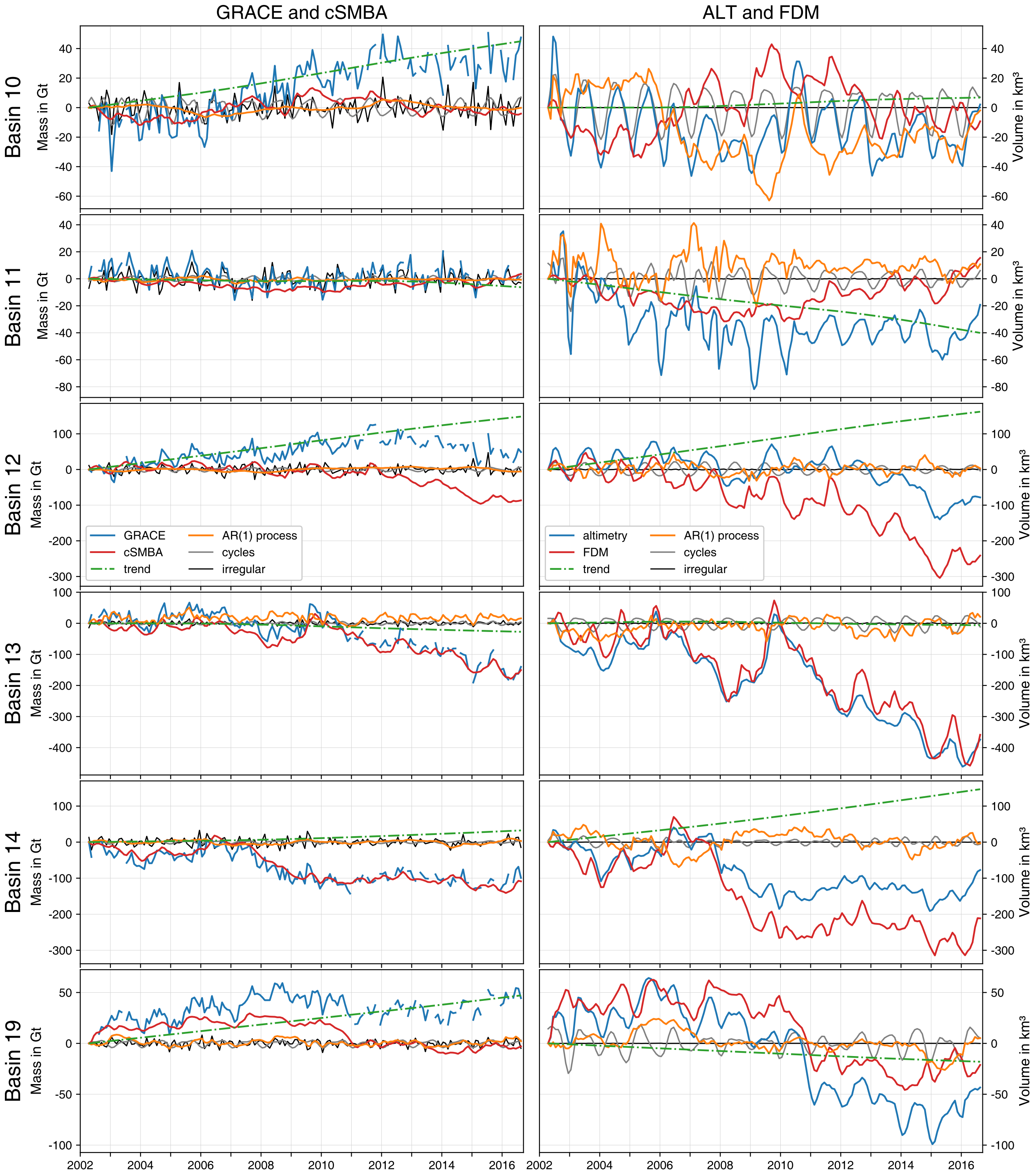

GRACE and cSMBA
ALT and FDM
Basin 10
Basin 11
Basin 12
Basin 13
Basin 14
Basin 19
Mass in Gt
Volume in km³
GRACE
cSMBA
trend
AR(1) process
cycles
irregular
altimetry
FDM

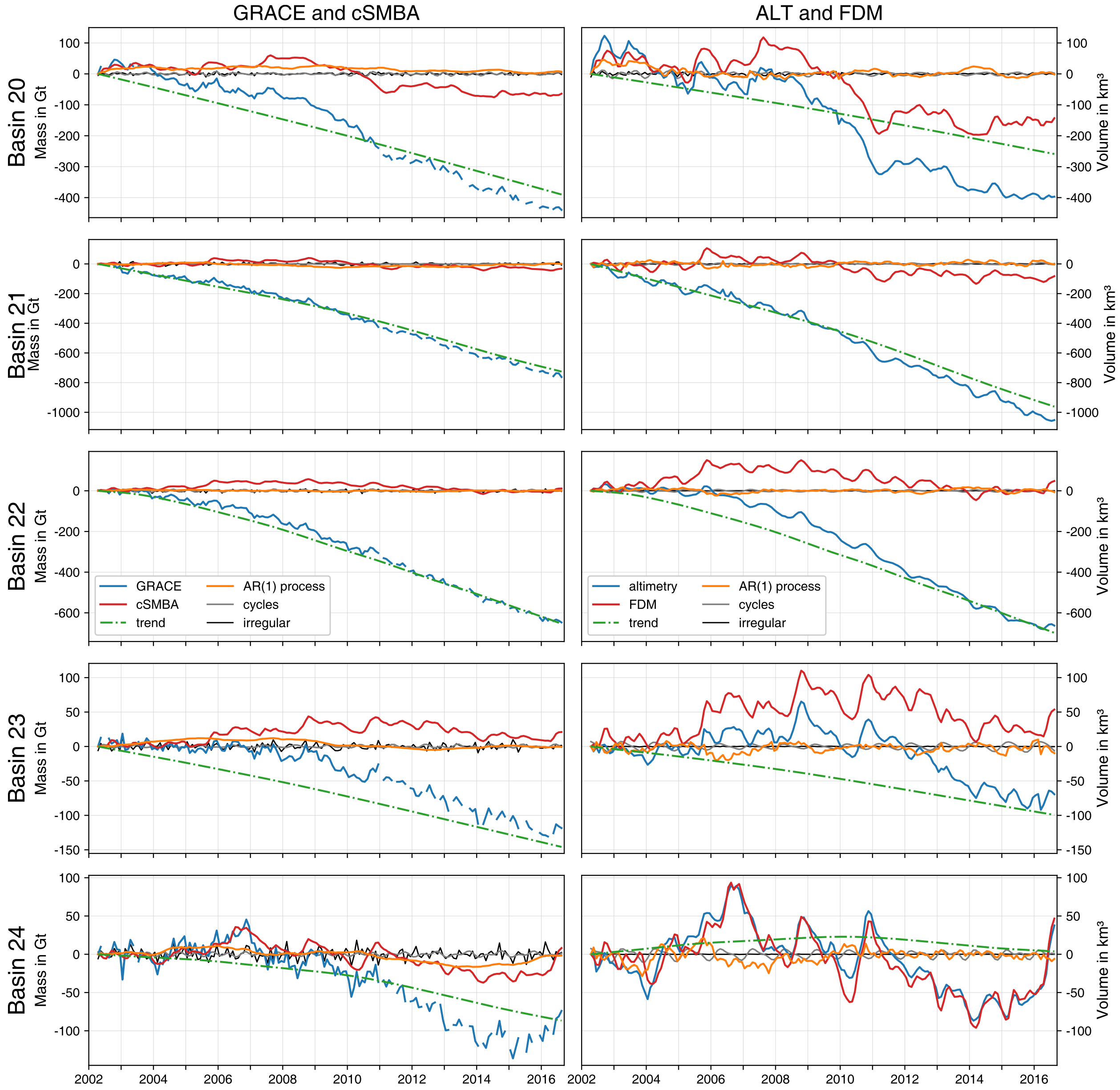

Figure S1: Time series of the satellite observations (blue), model products (red) are shown together with the estimated trend with time-variable rates (green), the AR(1) process (orange), the cycle (gray), and the irregular (black) components of all investigated basins for GRACE–cSMBA (left column) and ALT–FDM (right column).

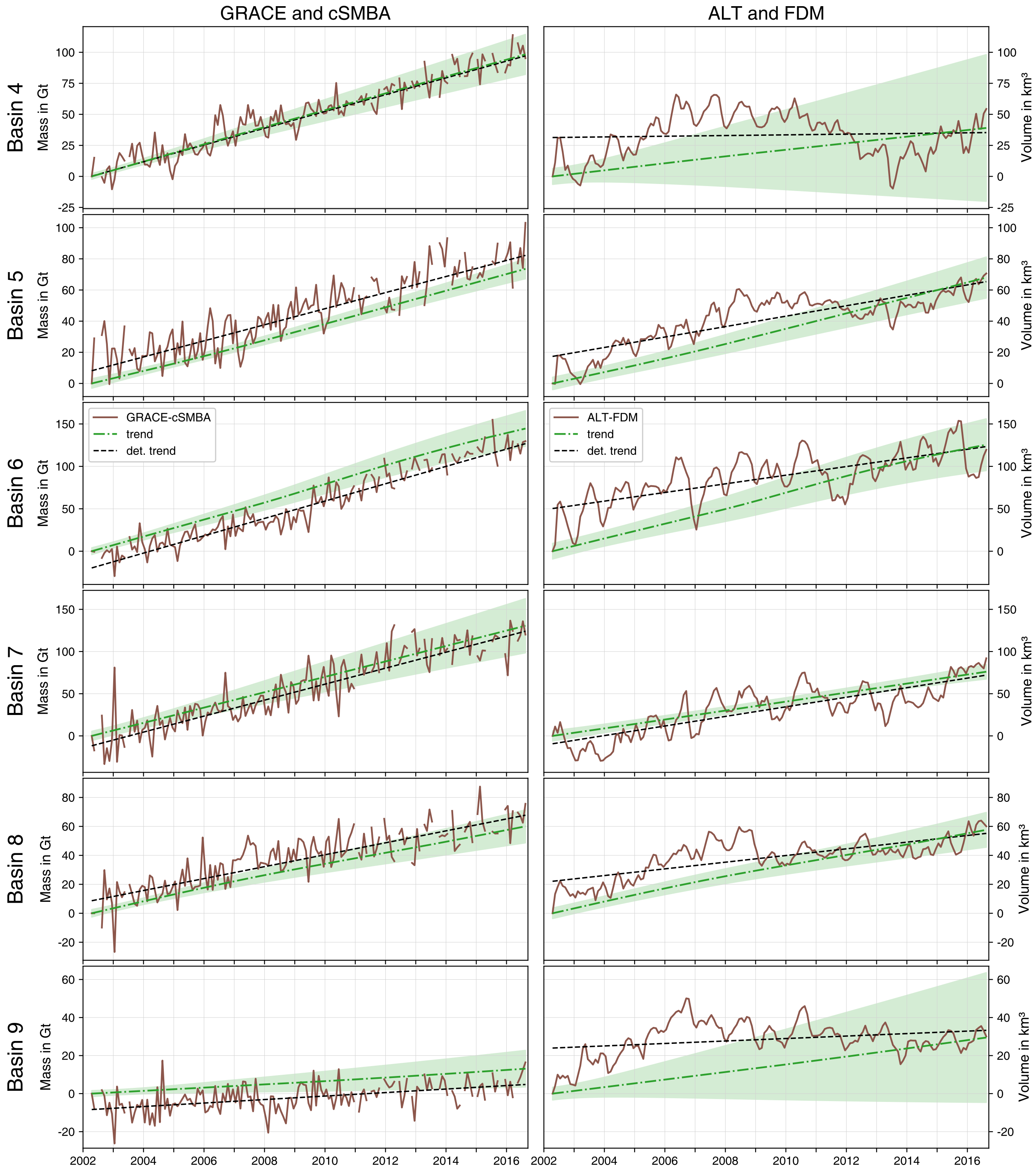
GRACE and cSMBA
ALT and FDM
Basin 4
Basin 5
Basin 6
Basin 7
Basin 8
Basin 9
Mass in Gt
Volume in km³
GRACE-cSMBA
ALT-FDM
trend
det. trend
2002
2004
2006
2008
2010
2012
2014
2016

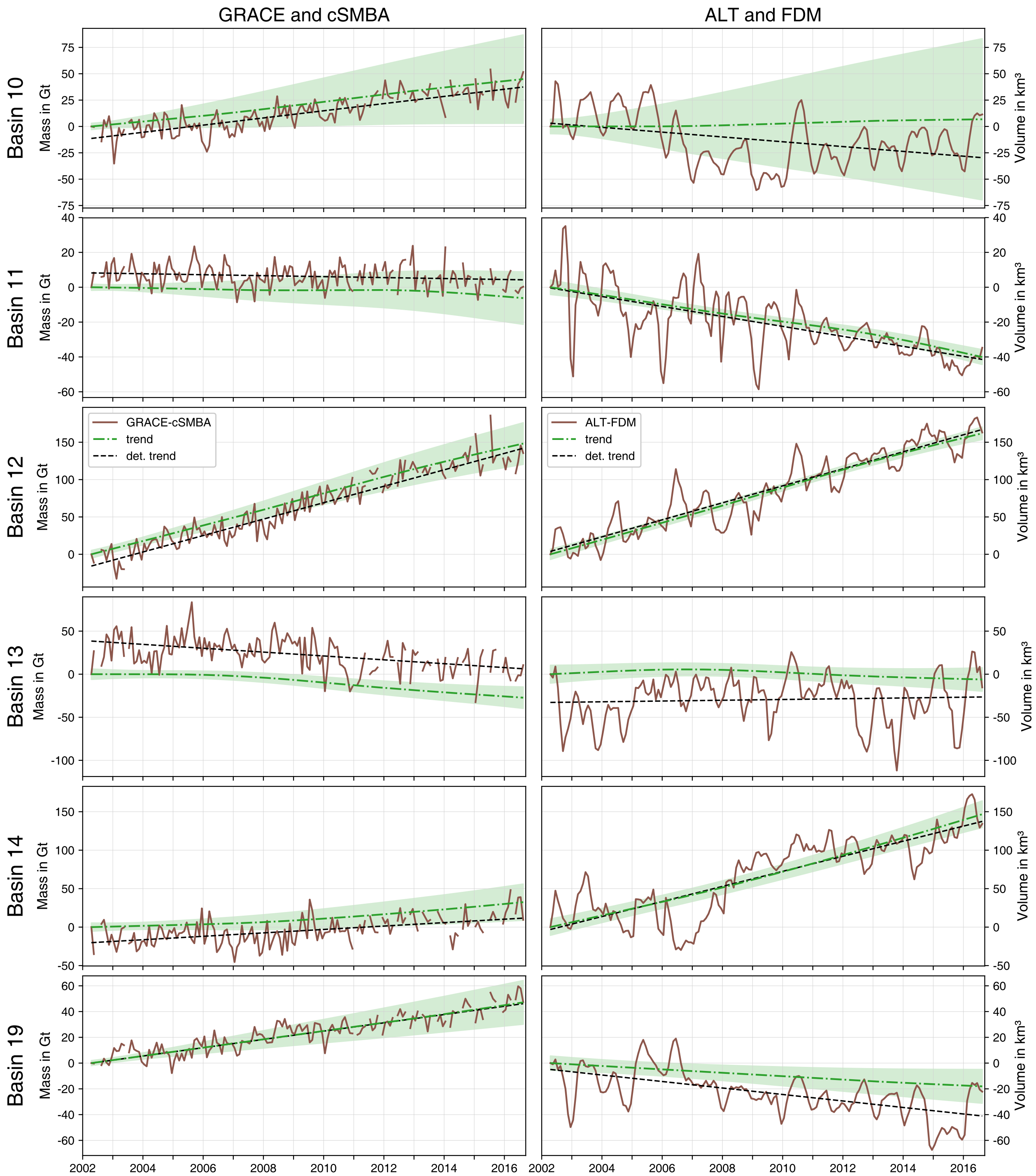

GRACE and cSMBA
ALT and FDM
Basin 10
Basin 11
Basin 12
Basin 13
Basin 14
Basin 19
Mass in Gt
Volume in km³
GRACE-cSMBA
ALT-FDM
trend
det. trend

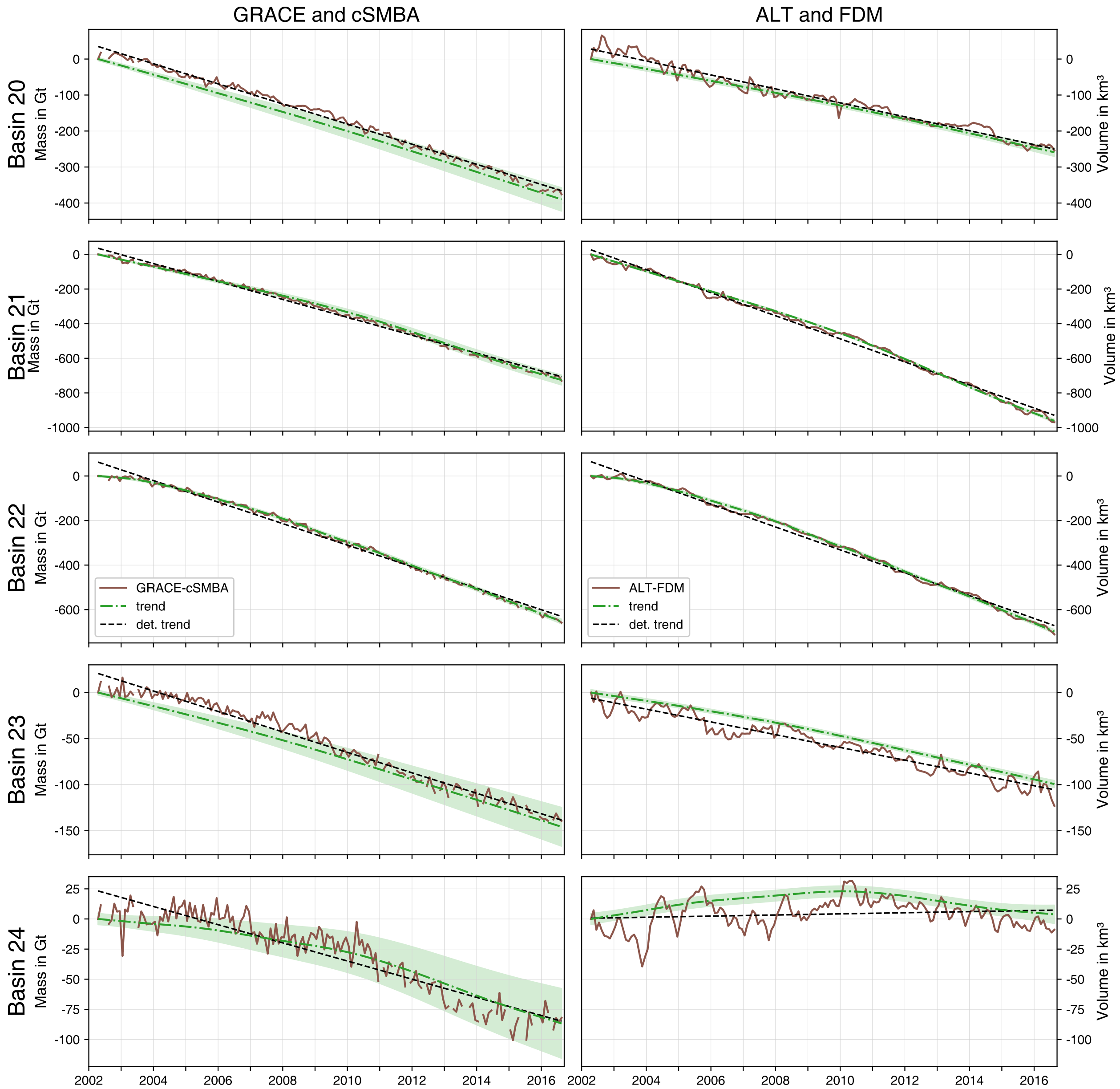

Figure S2: Time series of the difference between satellite observations and model products (brown) with the trend with time-variable rates and its 1-σ-uncertainty (green), an the deterministic trend (black) of all investigated basins for GRACE–cSMBA (left column) and ALT–FDM (right column). GRACE–cSMBA uncertainties include GIA uncertainties.

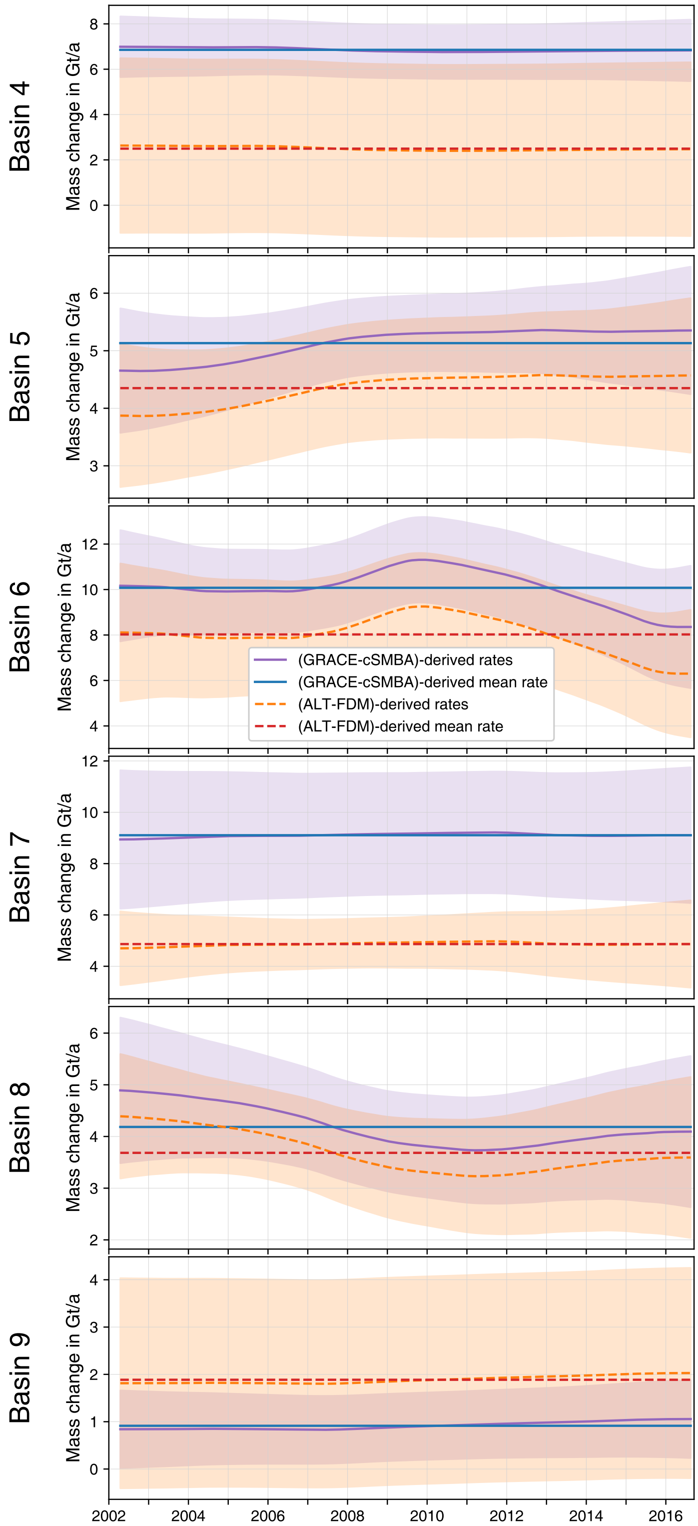

Basin 4
Basin 5
Basin 6
Basin 7
Basin 8
Basin 9
Mass change in Gt/a
(GRACE-cSMBA)-derived rates
(GRACE-cSMBA)-derived mean rate
(ALT-FDM)-derived rates
(ALT-FDM)-derived mean rate
2002
2004
2006
2008
2010
2012
2014
2016

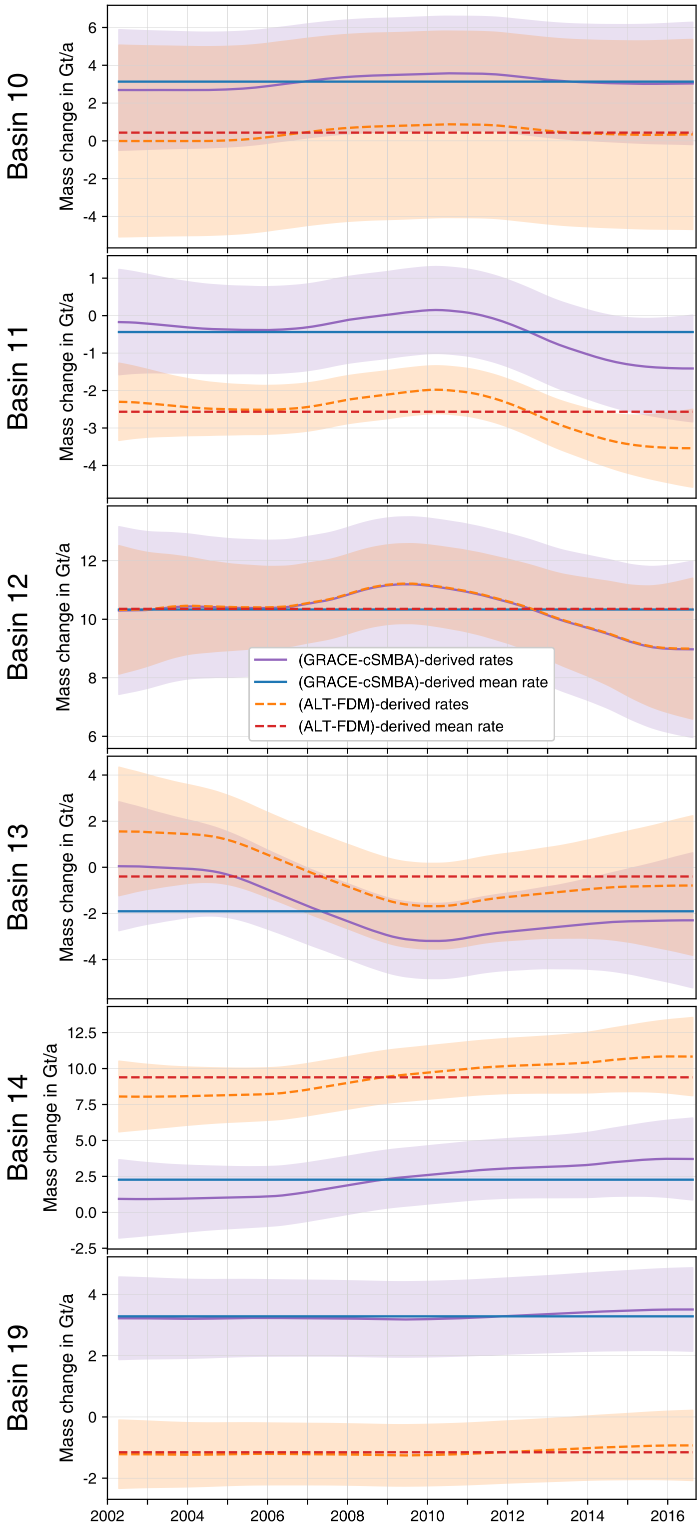
Basin 10
Basin 11
Basin 12
Basin 13
Basin 14
Basin 19
Mass change in Gt/a
(GRACE-cSMBA)-derived rates
(GRACE-cSMBA)-derived mean rate
(ALT-FDM)-derived rates
(ALT-FDM)-derived mean rate
2002
2004
2006
2008
2010
2012
2014
2016

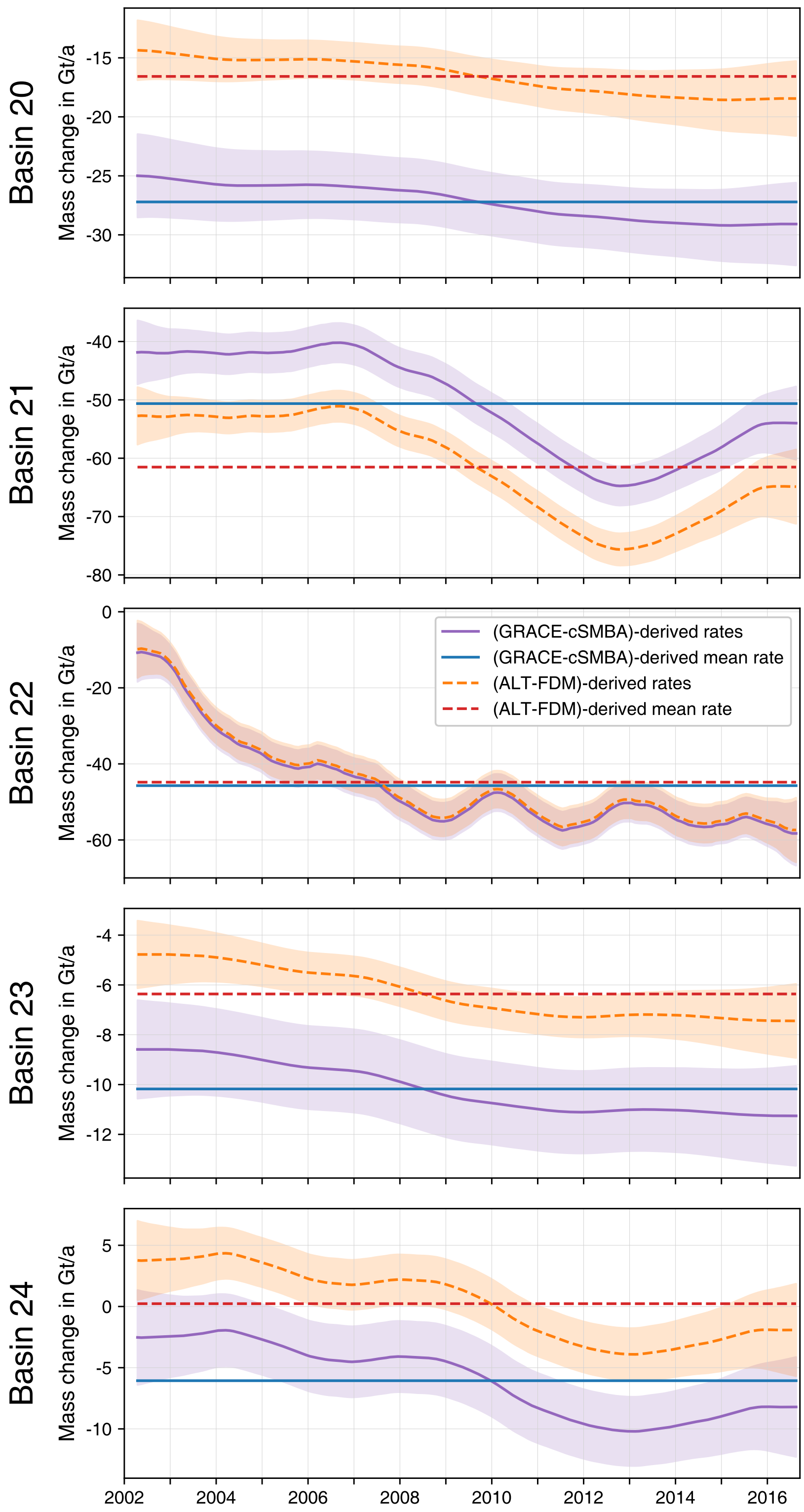

Figure S3: Time series of the rates of the trend and their 1-σ-uncertainties along with the mean rates for GRACE–cSMBA (purple and blue) and ALT–FDM (orange and red) of all investigated basins. GRACE–cSMBA uncertainties include GIA uncertainties.

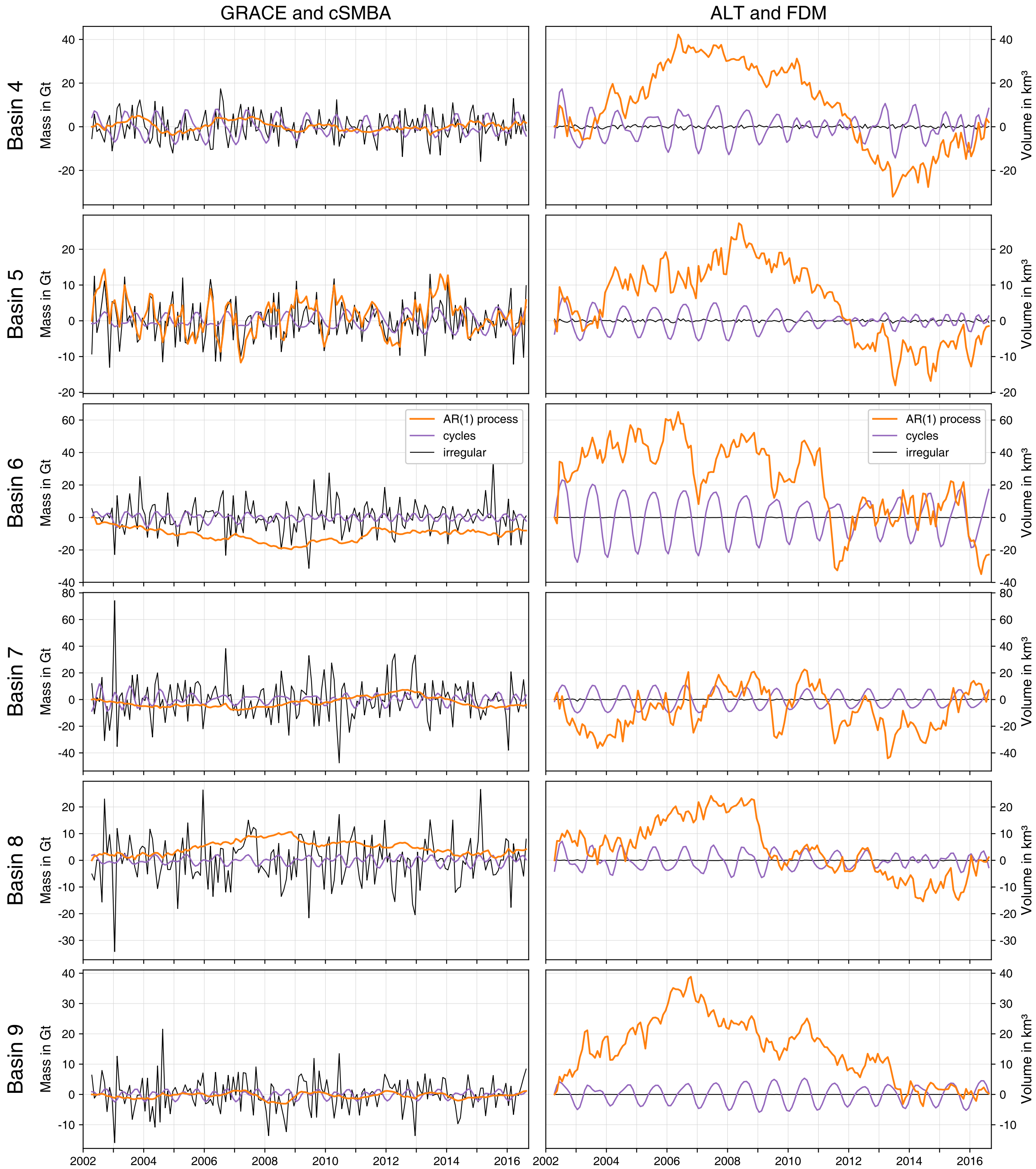
GRACE and cSMBA
ALT and FDM
Basin 4
Basin 5
Basin 6
Basin 7
Basin 8
Basin 9
Mass in Gt
Volume in km³
AR(1) process
cycles
irregular

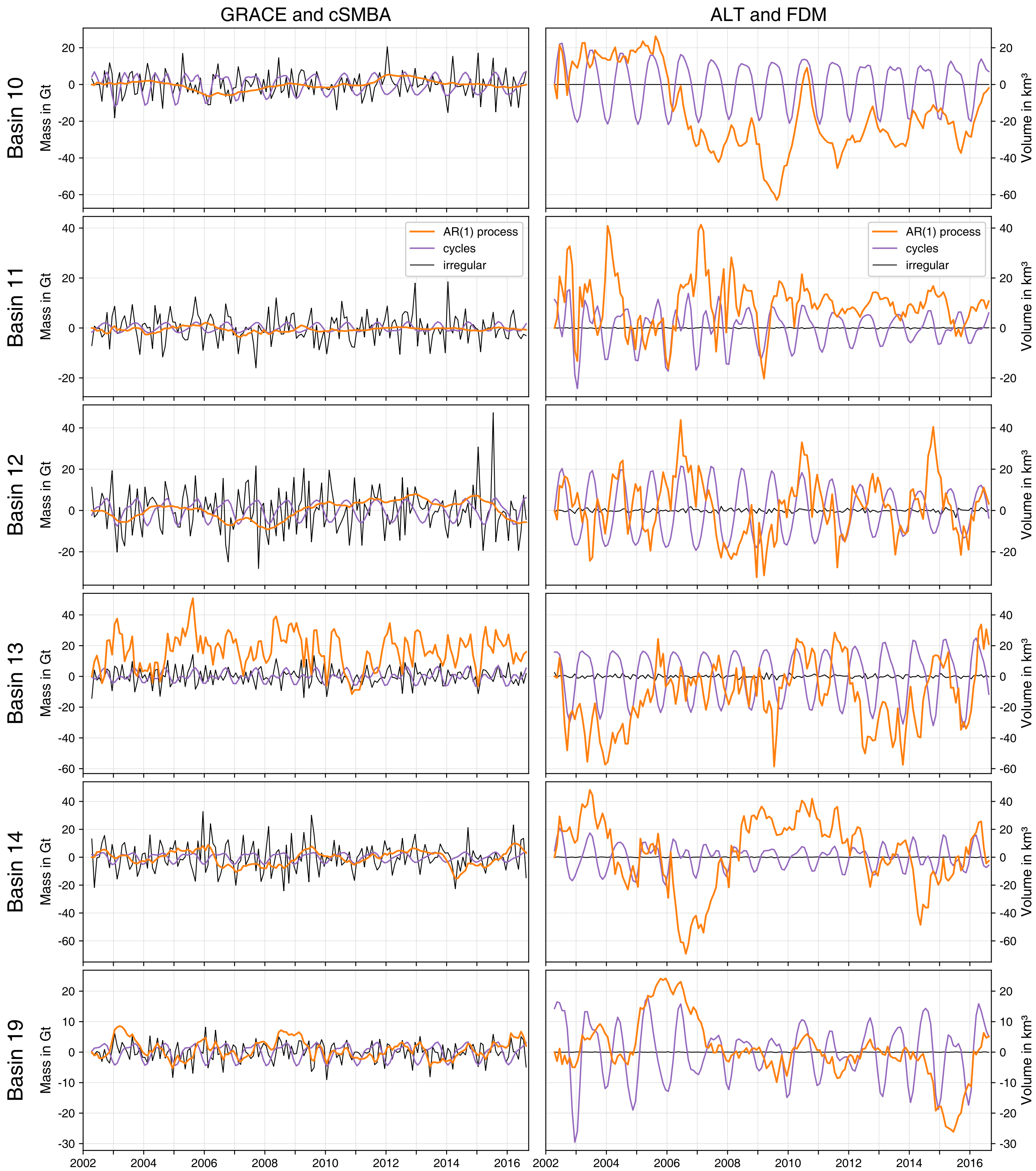

GRACE and cSMBA
ALT and FDM
Basin 10
Basin 11
Basin 12
Basin 13
Basin 14
Basin 19
Mass in Gt
Volume in km³
AR(1) process
cycles
irregular
2002
2004
2006
2008
2010
2012
2014
2016

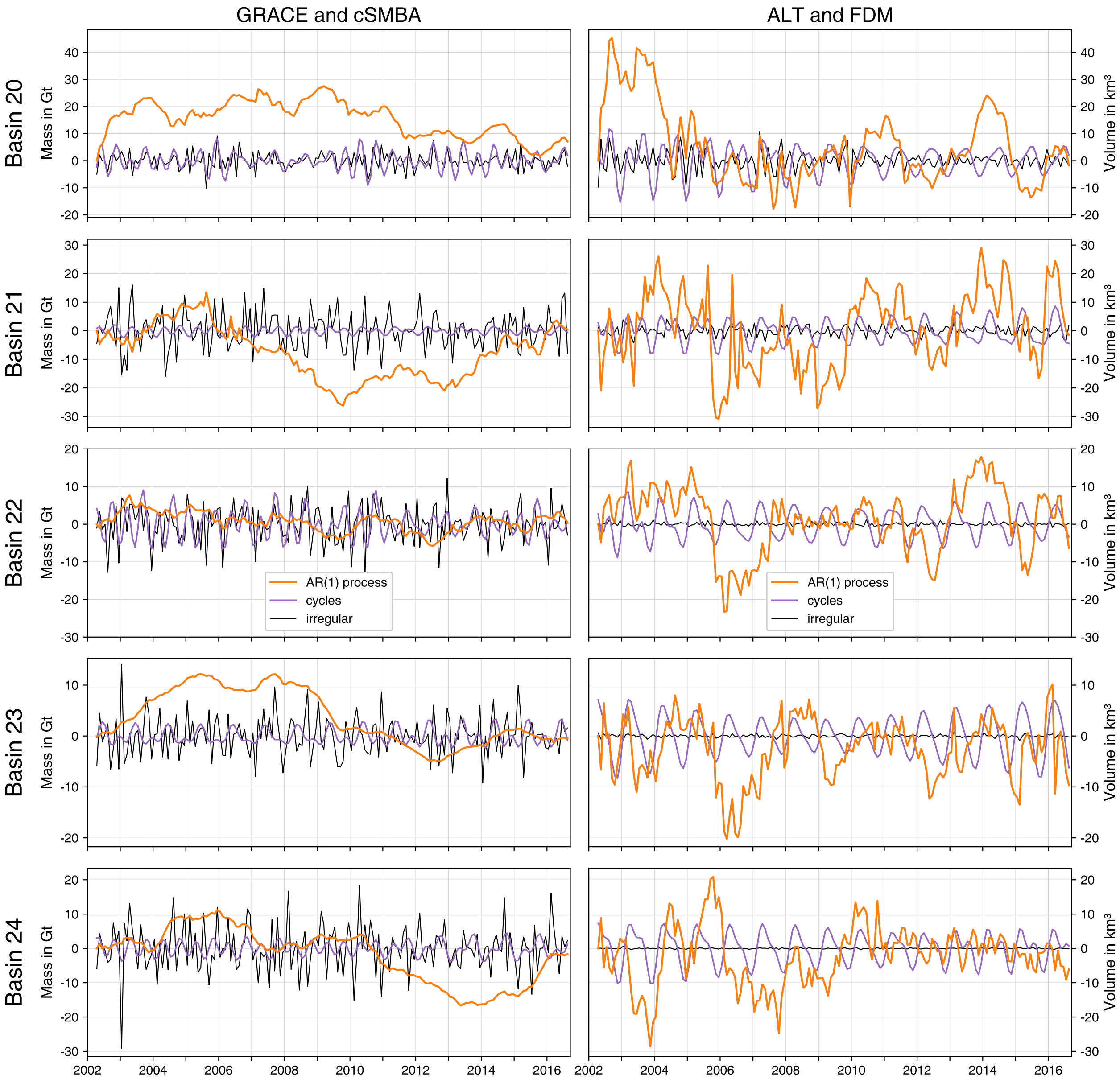

Figure S4: Time series of the remaining short-term signals of the differential time series: AR(1) process (orange), the sum of the cycle components (purple), and the irregular (black) of all investigated basins for GRACE–cSMBA (left column) and ALT–FDM (right column).

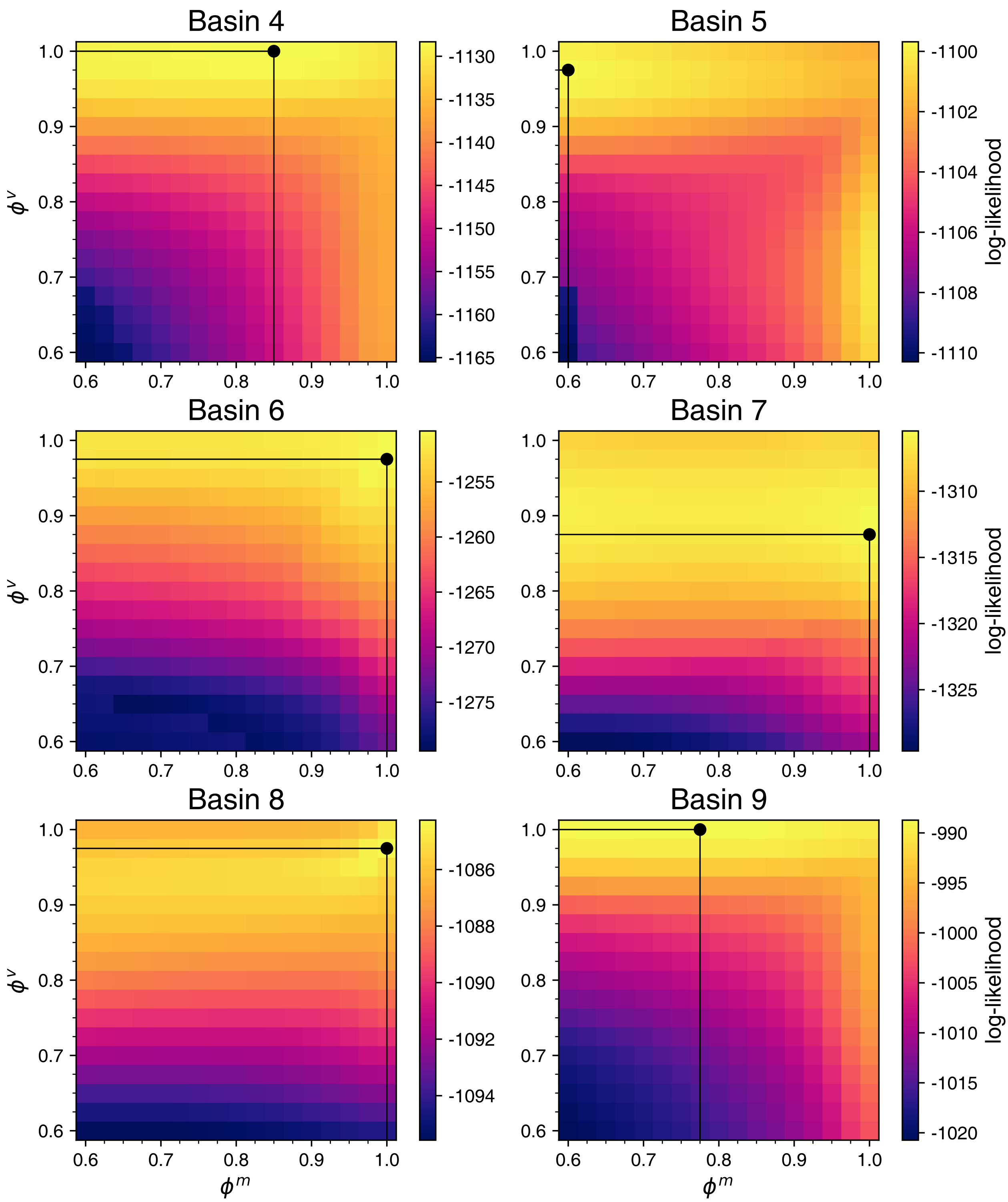
Basin 4
Basin 5
Basin 6
Basin 7
Basin 8
Basin 9
ϕ^v
ϕ^m
log-likelihood

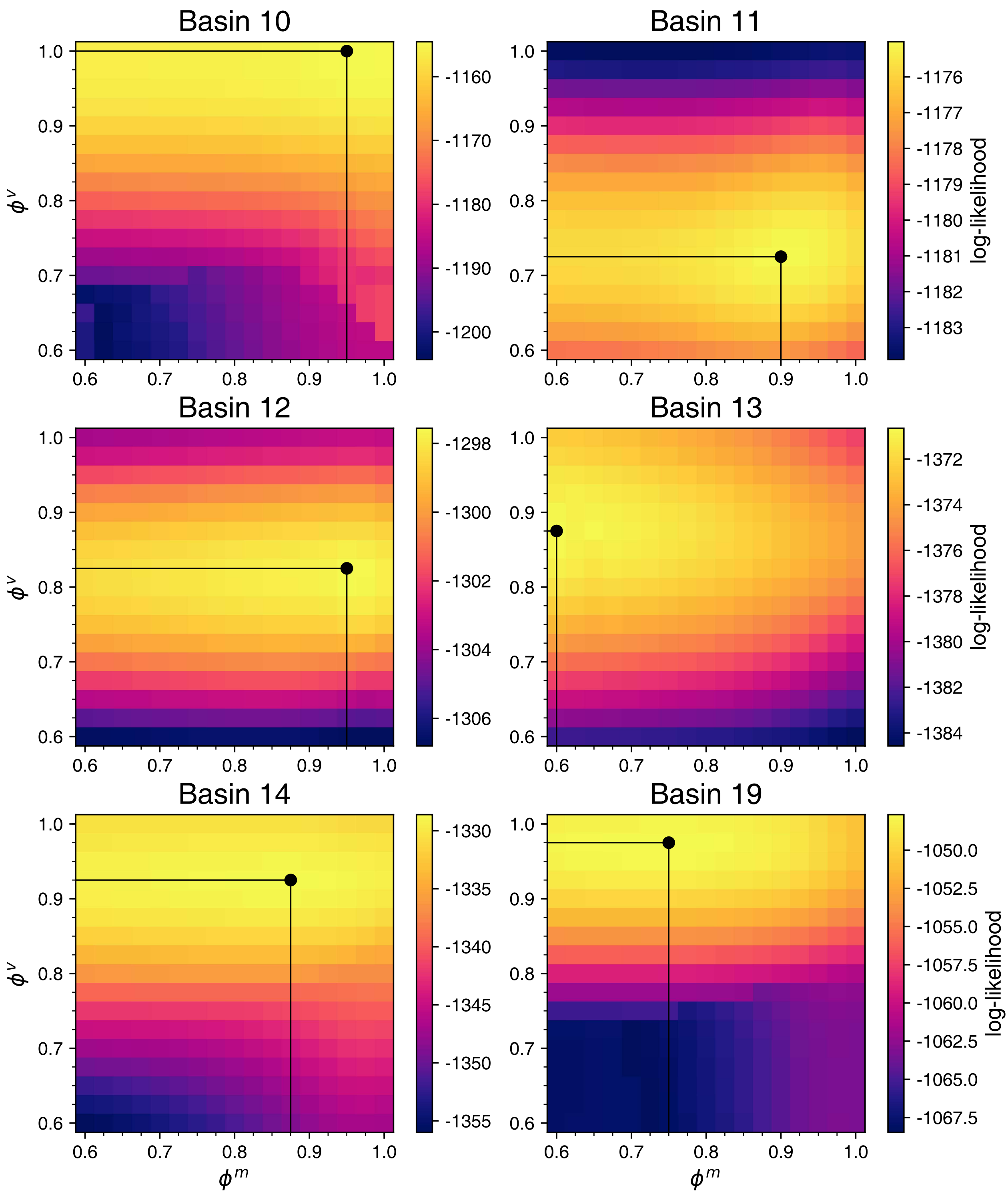
Basin 10
Basin 11
Basin 12
Basin 13
Basin 14
Basin 19
ϕ^v
ϕ^m
log-likelihood
0.6
0.7
0.8
0.9
1.0
-1160
-1170
-1180
-1190
-1200
-1176
-1177
-1178
-1179
-1180
-1181
-1182
-1183
-1298
-1300
-1302
-1304
-1306
-1372
-1374
-1376
-1378
-1380
-1382
-1384
-1330
-1335
-1340
-1345
-1350
-1355
-1050.0
-1052.5
-1055.0
-1057.5
-1060.0
-1062.5
-1065.0
-1067.5

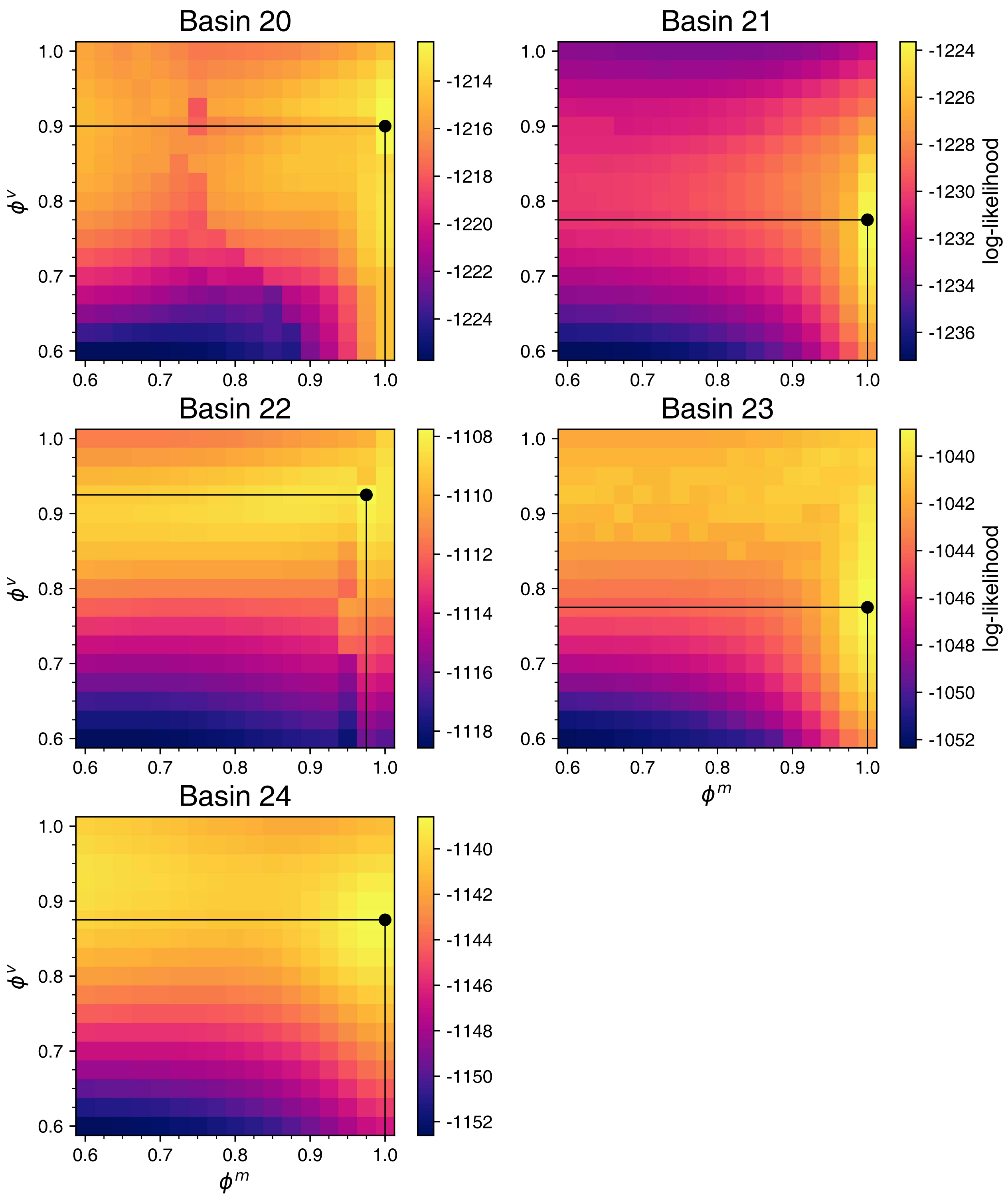

Figure S5: The log-likelihood for ϕ^{v}-ϕ^{m} combinations for all basins, ϕ^{v}: ALT–FDM and ϕ^{m}: GRACE–cSMBA. The picked maximum is highlighted with a black dot.

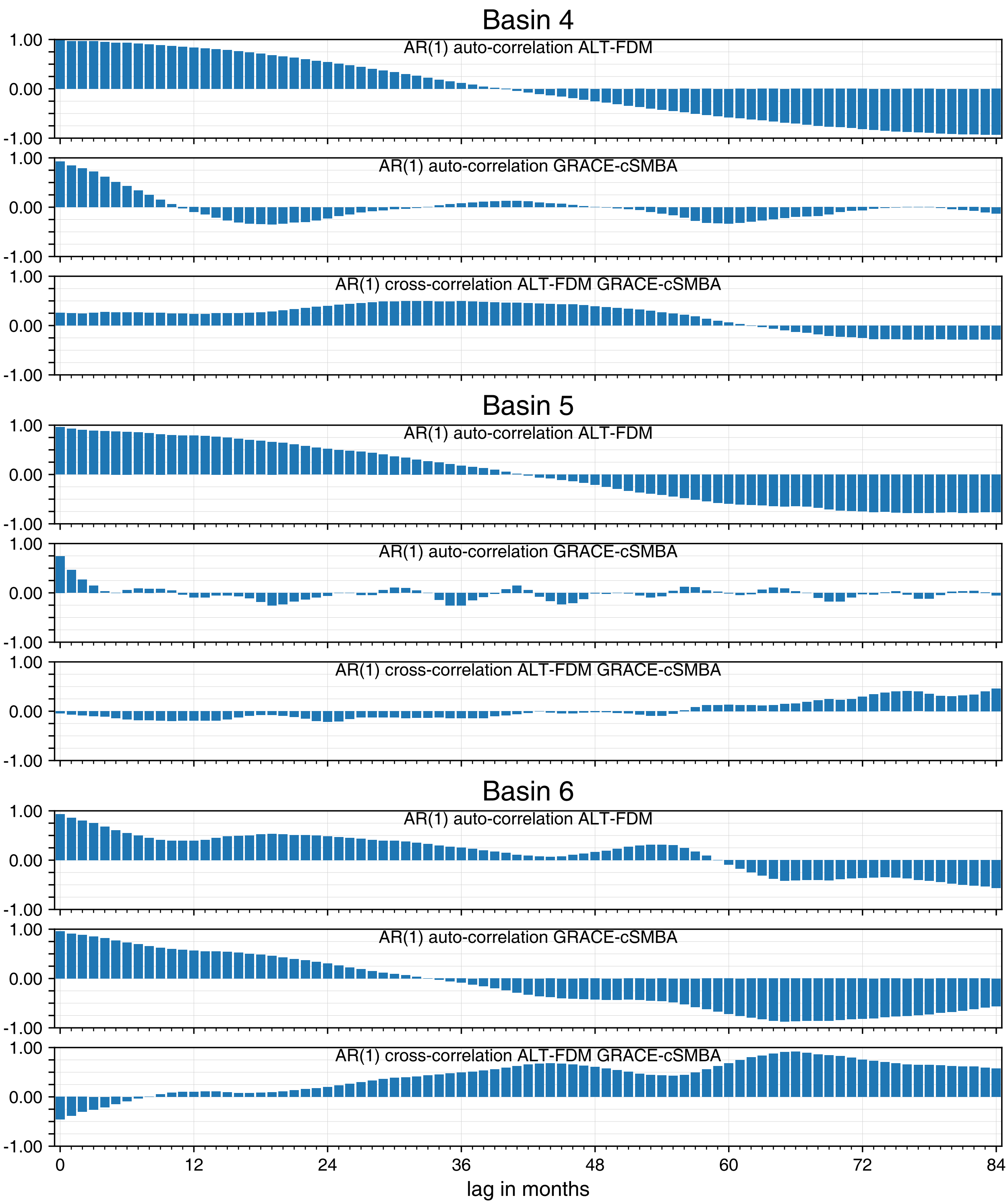
Basin 4
AR(1) auto-correlation ALT-FDM
AR(1) auto-correlation GRACE-cSMBA
AR(1) cross-correlation ALT-FDM GRACE-cSMBA
Basin 5
AR(1) auto-correlation ALT-FDM
AR(1) auto-correlation GRACE-cSMBA
AR(1) cross-correlation ALT-FDM GRACE-cSMBA
Basin 6
AR(1) auto-correlation ALT-FDM
AR(1) auto-correlation GRACE-cSMBA
AR(1) cross-correlation ALT-FDM GRACE-cSMBA
1.00
0.00
-1.00
0
12
24
36
48
60
72
84
lag in months

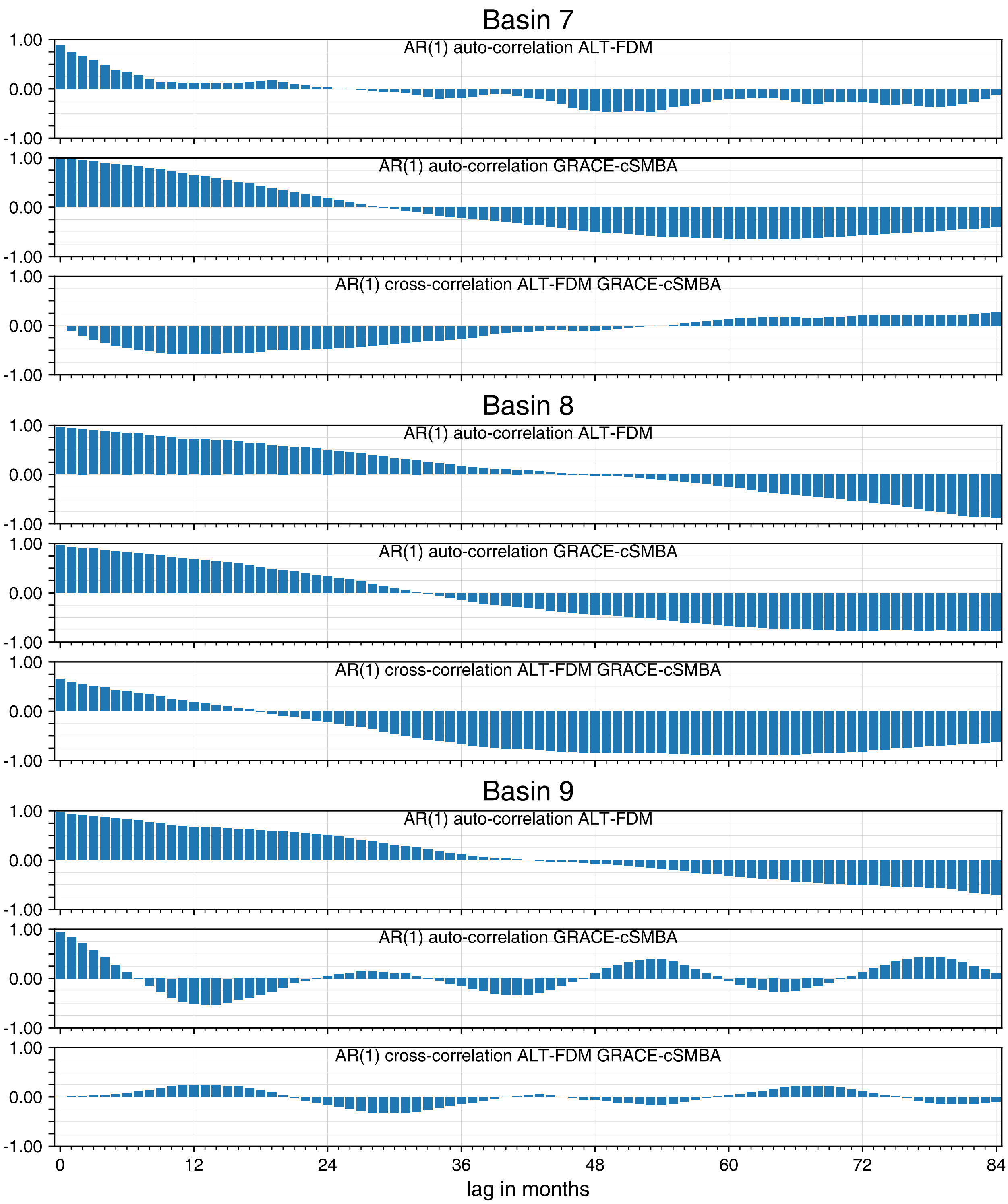
Basin 7
AR(1) auto-correlation ALT-FDM
AR(1) auto-correlation GRACE-cSMBA
AR(1) cross-correlation ALT-FDM GRACE-cSMBA
Basin 8
AR(1) auto-correlation ALT-FDM
AR(1) auto-correlation GRACE-cSMBA
AR(1) cross-correlation ALT-FDM GRACE-cSMBA
Basin 9
AR(1) auto-correlation ALT-FDM
AR(1) auto-correlation GRACE-cSMBA
AR(1) cross-correlation ALT-FDM GRACE-cSMBA
1.00
0.00
-1.00
0
12
24
36
48
60
72
84
lag in months

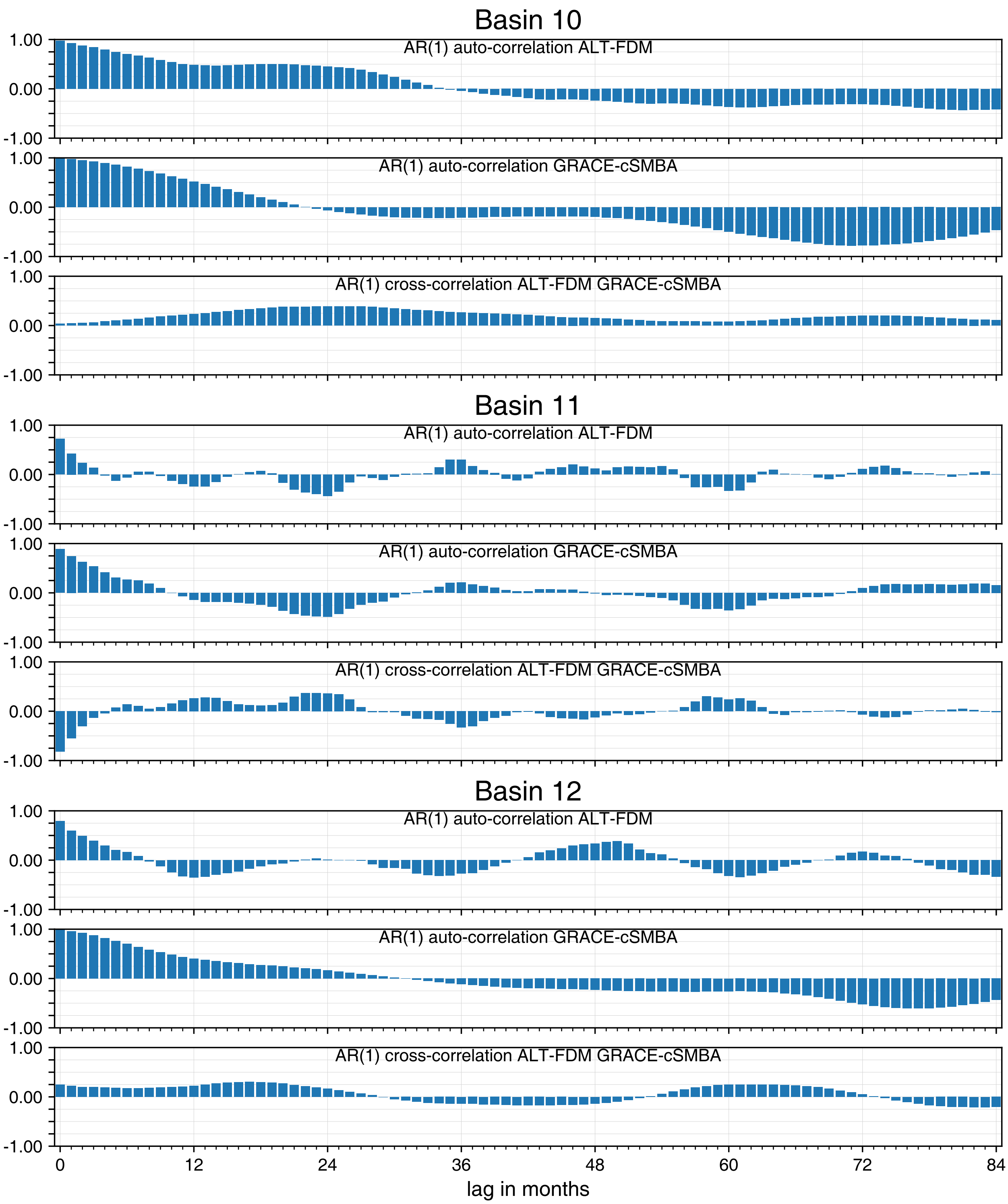
Basin 10
AR(1) auto-correlation ALT-FDM
AR(1) auto-correlation GRACE-cSMBA
AR(1) cross-correlation ALT-FDM GRACE-cSMBA
Basin 11
AR(1) auto-correlation ALT-FDM
AR(1) auto-correlation GRACE-cSMBA
AR(1) cross-correlation ALT-FDM GRACE-cSMBA
Basin 12
AR(1) auto-correlation ALT-FDM
AR(1) auto-correlation GRACE-cSMBA
AR(1) cross-correlation ALT-FDM GRACE-cSMBA
1.00
0.00
-1.00
0
12
24
36
48
60
72
84
lag in months

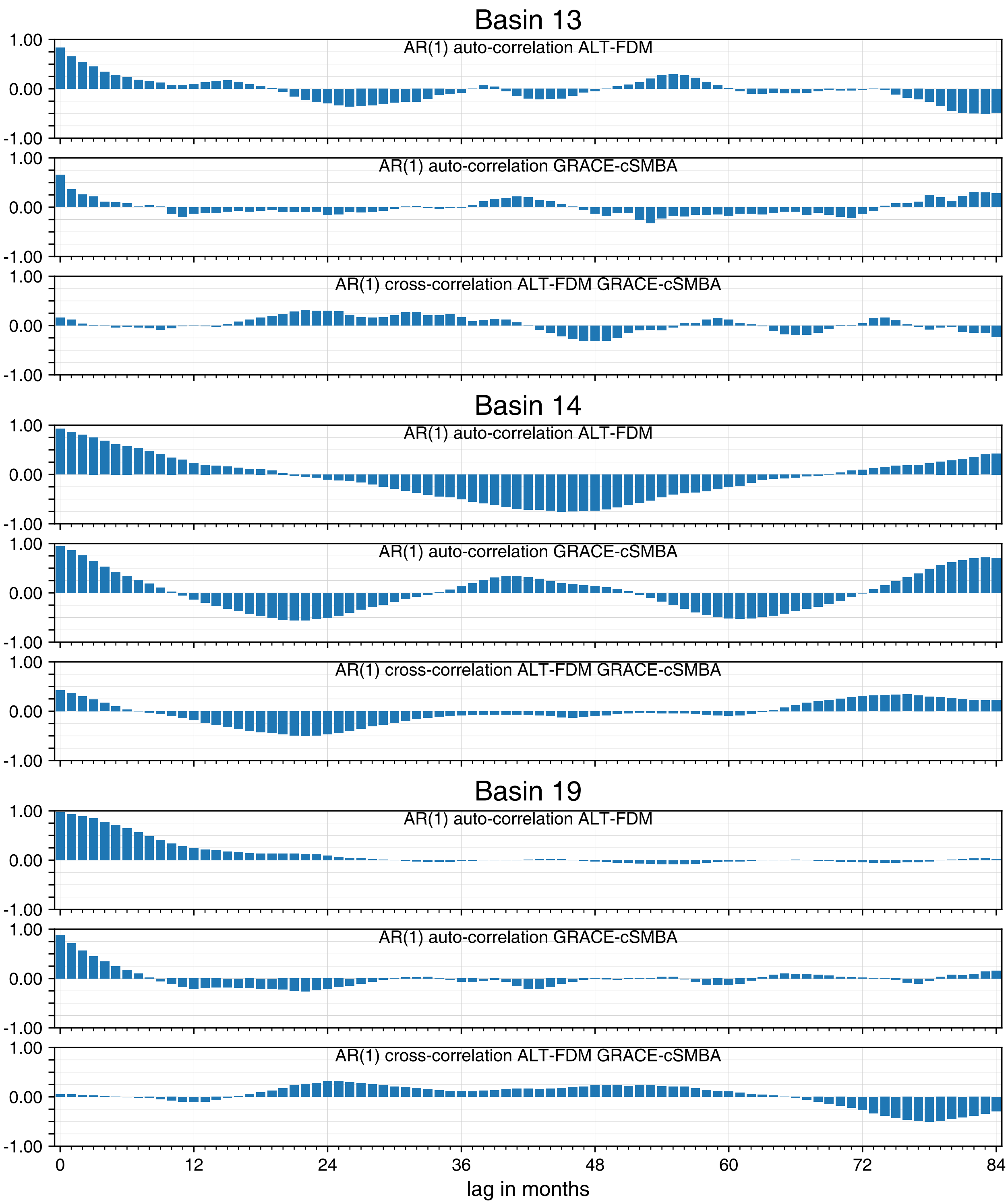
Basin 13
AR(1) auto-correlation ALT-FDM
AR(1) auto-correlation GRACE-cSMBA
AR(1) cross-correlation ALT-FDM GRACE-cSMBA
Basin 14
AR(1) auto-correlation ALT-FDM
AR(1) auto-correlation GRACE-cSMBA
AR(1) cross-correlation ALT-FDM GRACE-cSMBA
Basin 19
AR(1) auto-correlation ALT-FDM
AR(1) auto-correlation GRACE-cSMBA
AR(1) cross-correlation ALT-FDM GRACE-cSMBA
1.00
0.00
-1.00
0
12
24
36
48
60
72
84
lag in months

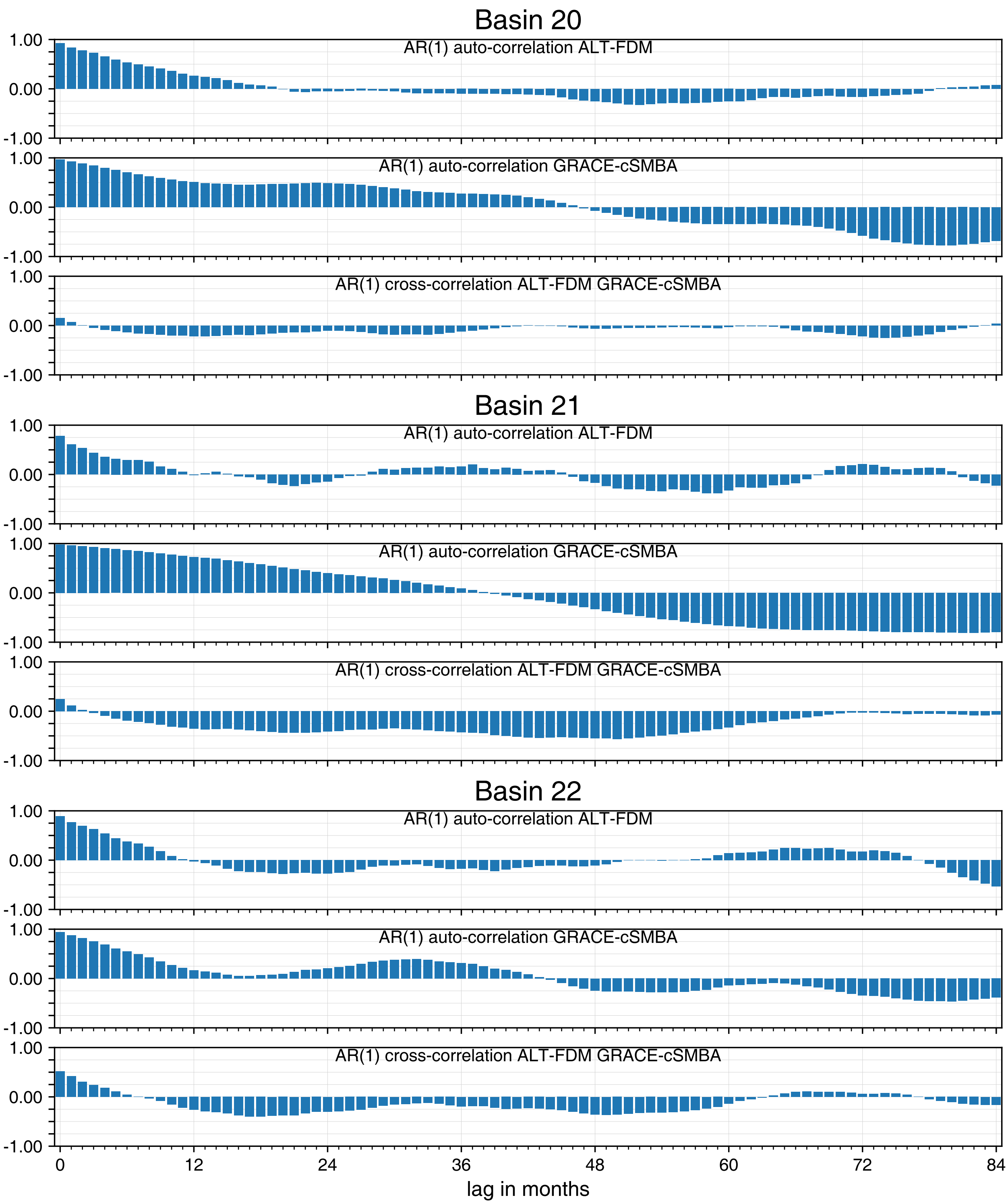

Basin 20
AR(1) auto-correlation ALT-FDM
AR(1) auto-correlation GRACE-cSMBA
AR(1) cross-correlation ALT-FDM GRACE-cSMBA
Basin 21
AR(1) auto-correlation ALT-FDM
AR(1) auto-correlation GRACE-cSMBA
AR(1) cross-correlation ALT-FDM GRACE-cSMBA
Basin 22
AR(1) auto-correlation ALT-FDM
AR(1) auto-correlation GRACE-cSMBA
AR(1) cross-correlation ALT-FDM GRACE-cSMBA
1.00
0.00
-1.00
0
12
24
36
48
60
72
84
lag in months

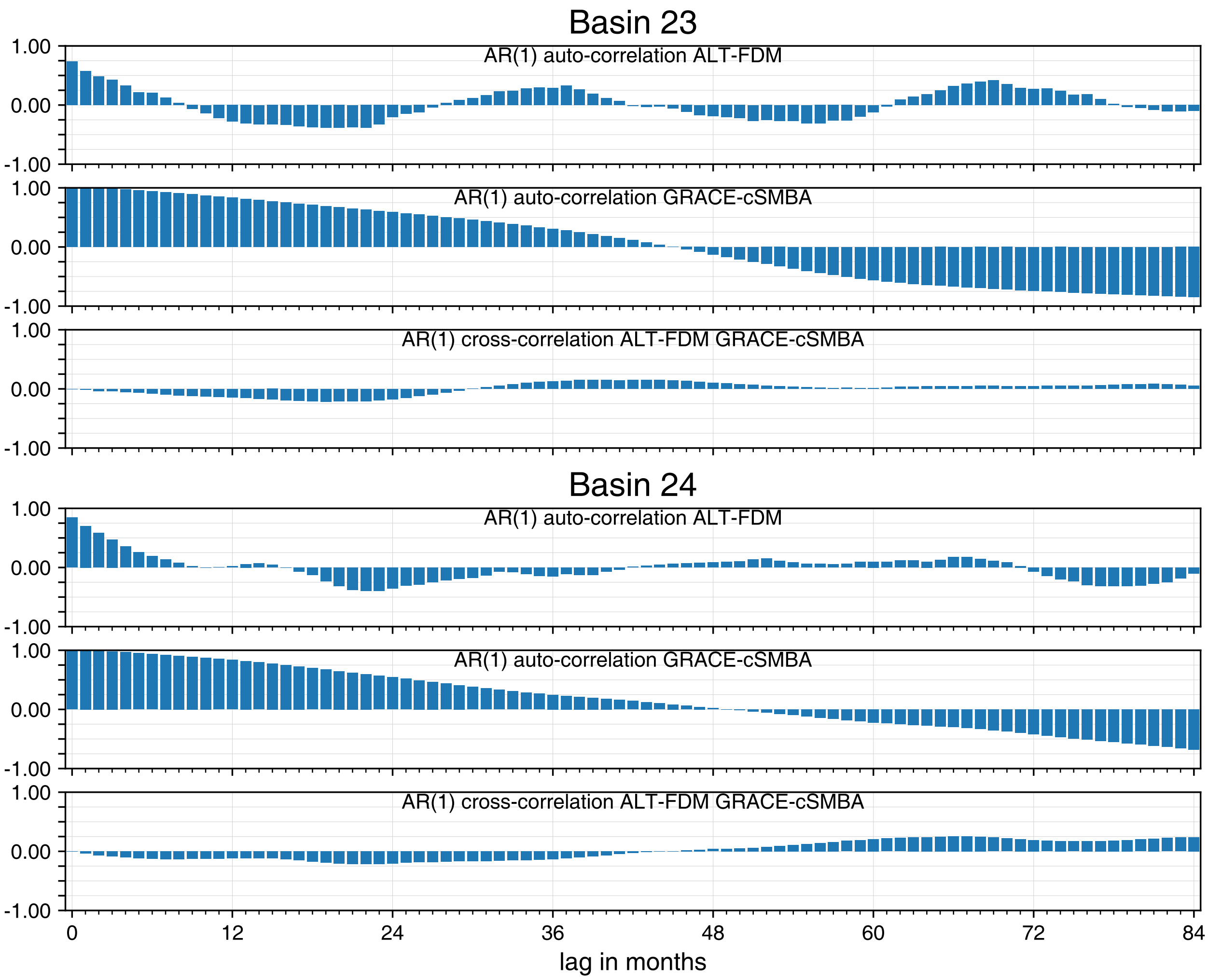

Figure S6: Auto-correlation functions of the AR(1) process from ALT–FDM data, the auto-correlation functions of the AR(1) process from GRACE–cSMBA, and the cross-correlation function of both AR(1) processes for all investigated basins.

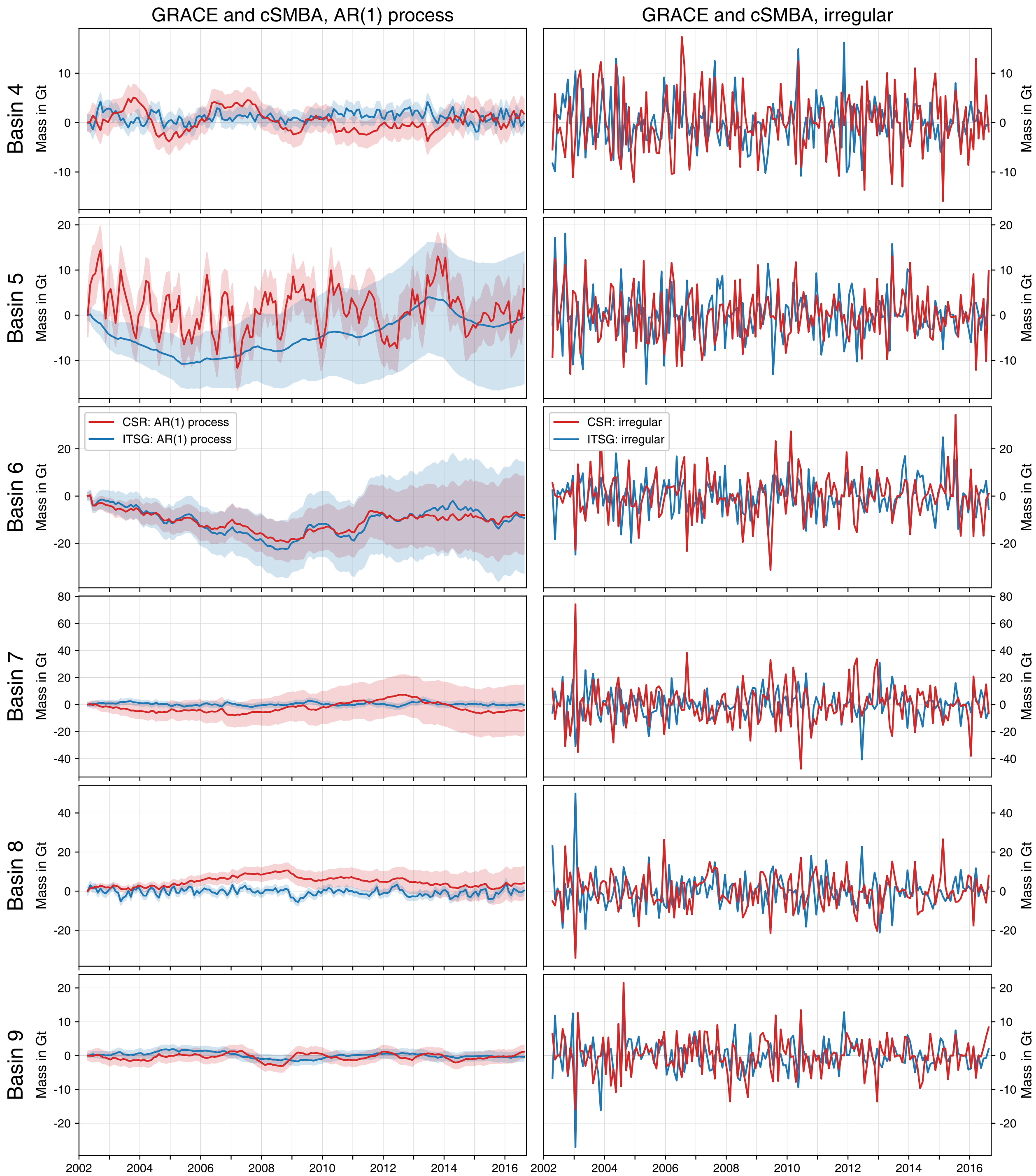
GRACE and cSMBA, AR(1) process
GRACE and cSMBA, irregular
Basin 4
Basin 5
Basin 6
Basin 7
Basin 8
Basin 9
Mass in Gt
CSR: AR(1) process
ITSG: AR(1) process
CSR: irregular
ITSG: irregular
2002
2004
2006
2008
2010
2012
2014
2016

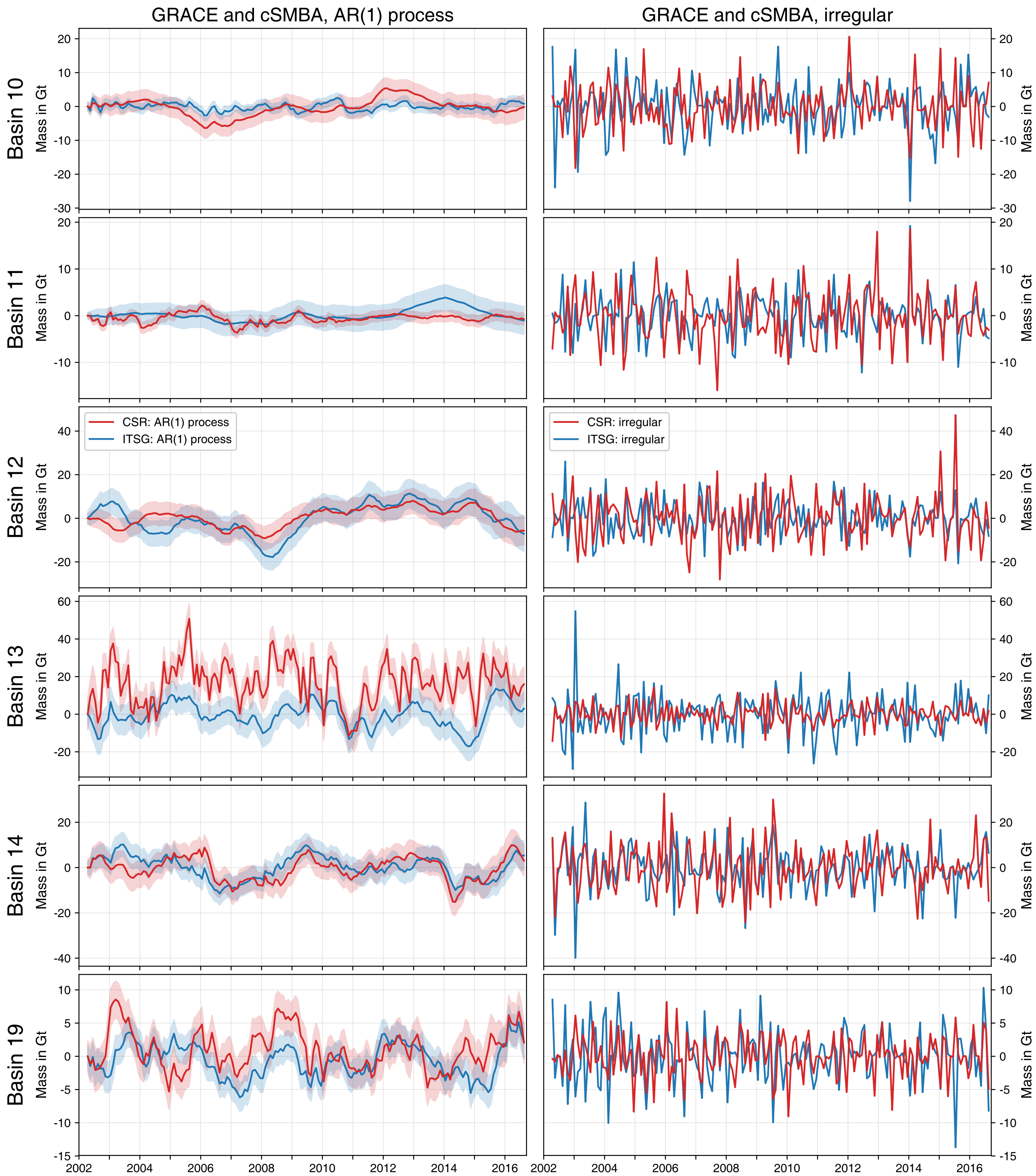
GRACE and cSMBA, AR(1) process
GRACE and cSMBA, irregular
Basin 10
Basin 11
Basin 12
Basin 13
Basin 14
Basin 19
Mass in Gt
CSR: AR(1) process
ITSG: AR(1) process
CSR: irregular
ITSG: irregular
2002
2004
2006
2008
2010
2012
2014
2016

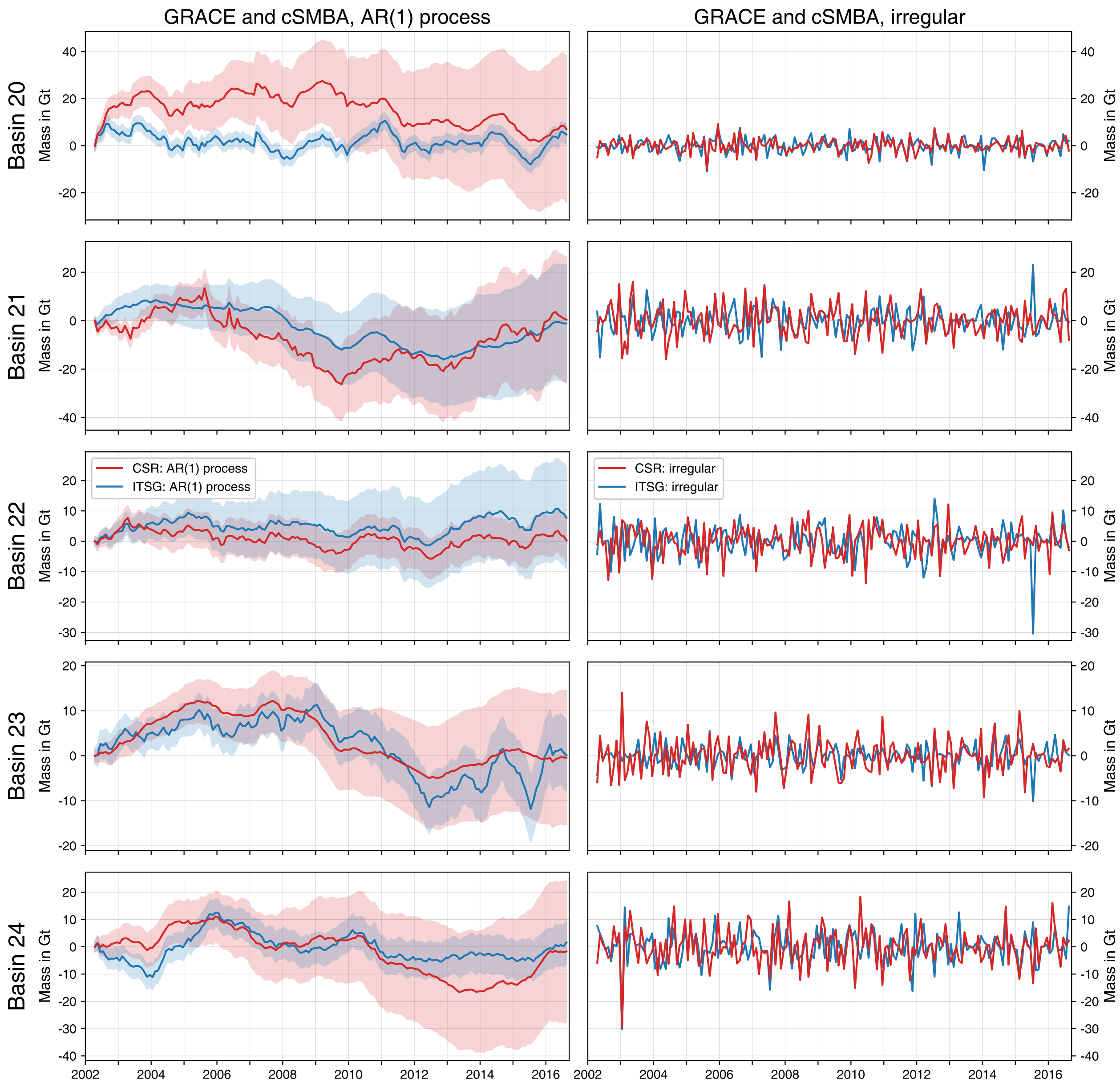

Figure S7: Time series of the AR(1) process along with their 1-σ-uncertainties (left column) and the irregular component (right column) estimated with GRACE solutions from Bettadpur (2018) (red) and with GRACE solutions from Mayer-Gürr et al. (2016) (blue) of all investigated basins for GRACE–cSMBA.

References

Bettadpur, S. (2018). *GRACE field geopotential coefficients CSR release 6.0.* University Of Texas Center For Space Research and NASA Physical Oceanography DAAC. doi: 10.5067/GRGSM-20C06

Durbin, J., & Koopman, S. J. (2012). *Time series analysis by state space methods*. Oxford University Press.

Groh, A., & Horwath, M. (2021). Antarctic Ice Mass Change Products from GRACE/GRACE-FO Using Tailored Sensitivity Kernels. *Remote Sensing*, *13*(9). doi: 10.3390/rs13091736

Koopman, S. J. (1993). Disturbance smoother for state space models. *Biometrika*, *80*(1), 117–126.

Mayer-Gürr, T., Behzadpour, S., Ellmer, M., Kvas, A., Klinger, B., & Zehentner, N. (2016). ITSG-Grace2016 - Monthly and Daily Gravity Field Solutions from GRACE. *GFZ Data Services*. doi: 10.5880/icgem.2016.007

Wouters, B., Martín-Español, A., Helm, V., Flament, T., van Wessem, J., Ligtenberg, S., … Bamber, J. (2015). Dynamic thinning of glaciers on the Southern Antarctic Peninsula. *Science*, *348*(6237), 899–903. doi: 10.1126/science.aaa5727

Supplemental Material for:

Feasibility of a global inversion for spatially resolved glacial isostatic adjustment and ice sheet mass changes proven in simulation experiments

M. O. Willen[1], M. Horwath[1], A. Groh[1], V. Helm[2], B. Uebbing[3], and J. Kusche[3]

[1]Institut für Planetare Geodäsie, Technische Universität Dresden, Germany
[2]Alfred Wegener Institute, Helmholtz Centre for Polar and Marine Research, Bremerhaven, Germany
[3]Institute of Geodesy and Geoinformation, University of Bonn, Germany

Contents

A Test experiments of the GIA parametrization

We test the GIA parametrization by reproducing two global GIA signals in the absence of other signals and of observation errors. We model the first GIA signal with the SELEN software (Spada and Melini, 2019) using the provided ICE-6G glacial history. The second GIA signal is the modelling output from Caron et al. (2018). The model outputs (Fig. S1) are the test observations $\boldsymbol{d}^{\mathrm{GIA}}$ (spherical harmonic coefficients converted to surface densities) which are linked to the parameters $\boldsymbol{\beta}^{\mathrm{GIA}}$ with the design matrix $\boldsymbol{X}_{\mathrm{GIA}}^{\mathrm{GRAV}}$ (Eq. 17):

$$\boldsymbol{d}^{\mathrm{GIA}} = \boldsymbol{X}_{\mathrm{GIA}}^{\mathrm{GRAV}} \boldsymbol{\beta}^{\mathrm{GIA}}. \tag{S1}$$

We estimate $\hat{\boldsymbol{\beta}}^{\mathrm{GIA}}$ by least-squares adjustment following Eq. 12 with $\boldsymbol{P} = \boldsymbol{I}$.
Without the incorporation of patterns that allow for the co-estimation of unconsidered rotational feedback effects, we can only inadequately resolve the GIA model of Caron et al. (2018) (Fig. S4c). Caron et al. (2018) pointed out the differences in the C_{21}-S_{21}-pattern of the model that they created compared to a modelling result based on ICE-6G ice history and VM5a rheology. The incorporation of the C_{21}-S_{21} fingerprints allow us to capture the residual rotational feedback effect (Fig. S3c).
In addition, we conducted a test experiment with the regional GIA modelling output from Barletta et al. (2018). For this purpose, we transferred the GIA patterns in this region to the spatial domain and adjusted them to the modelling output in the spatial domain. In this case the test observations $\boldsymbol{d}^{\mathrm{GIA}}$ are bedrock motion rates from Barletta et al. (2018). This modelling output shows variations on much shorter spatial wavelengths than the localized parametrization can resolve (Fig. S5).

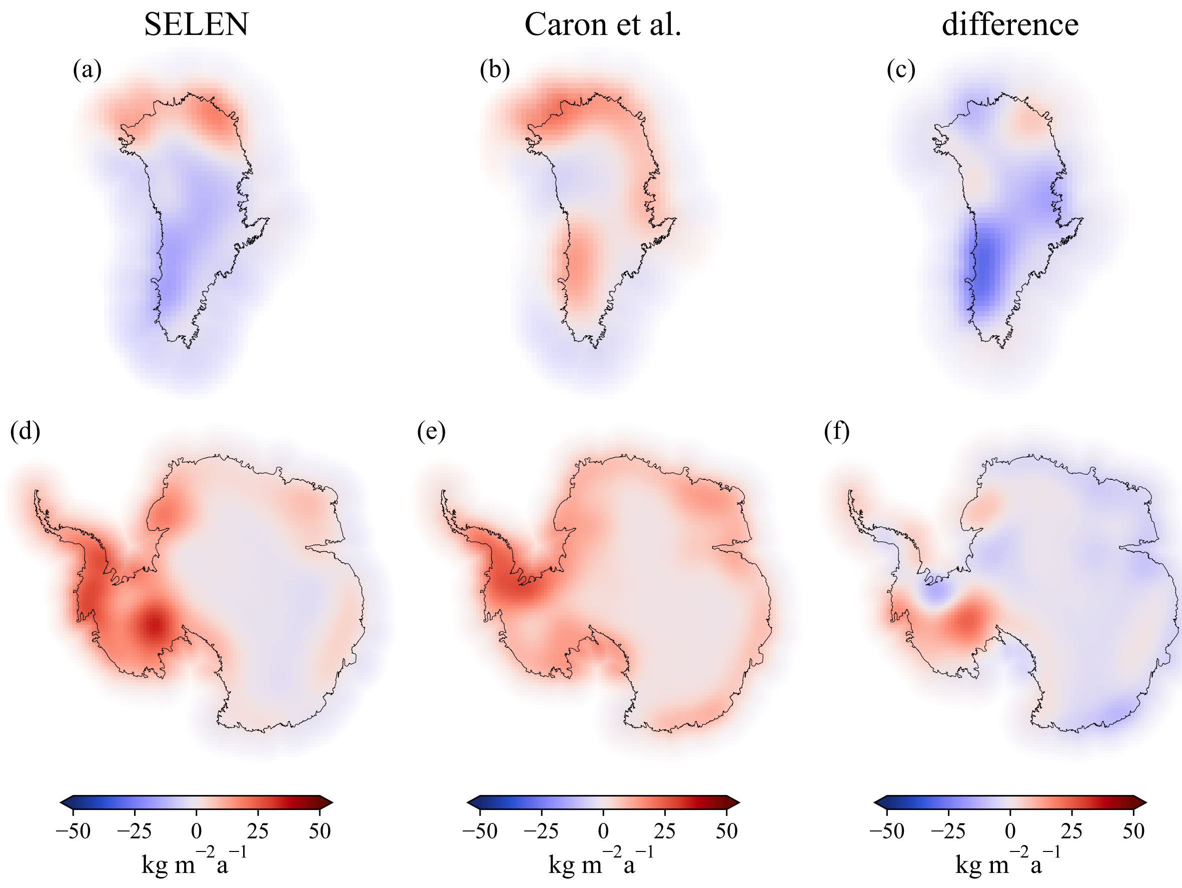

Figure S1: Surface density rates of the GIA modelling output from a SELEN run with ICE-6G ice history and VM5a rheology that we use for the variant A of simulated observations evaluated over GIS (a) and AIS (d). The surface density rates from the modelling output from Caron et al. (2018) that we use for the variant B of simulated observations over both ice sheets (b+e). The difference between both modelling outputs (c+f).

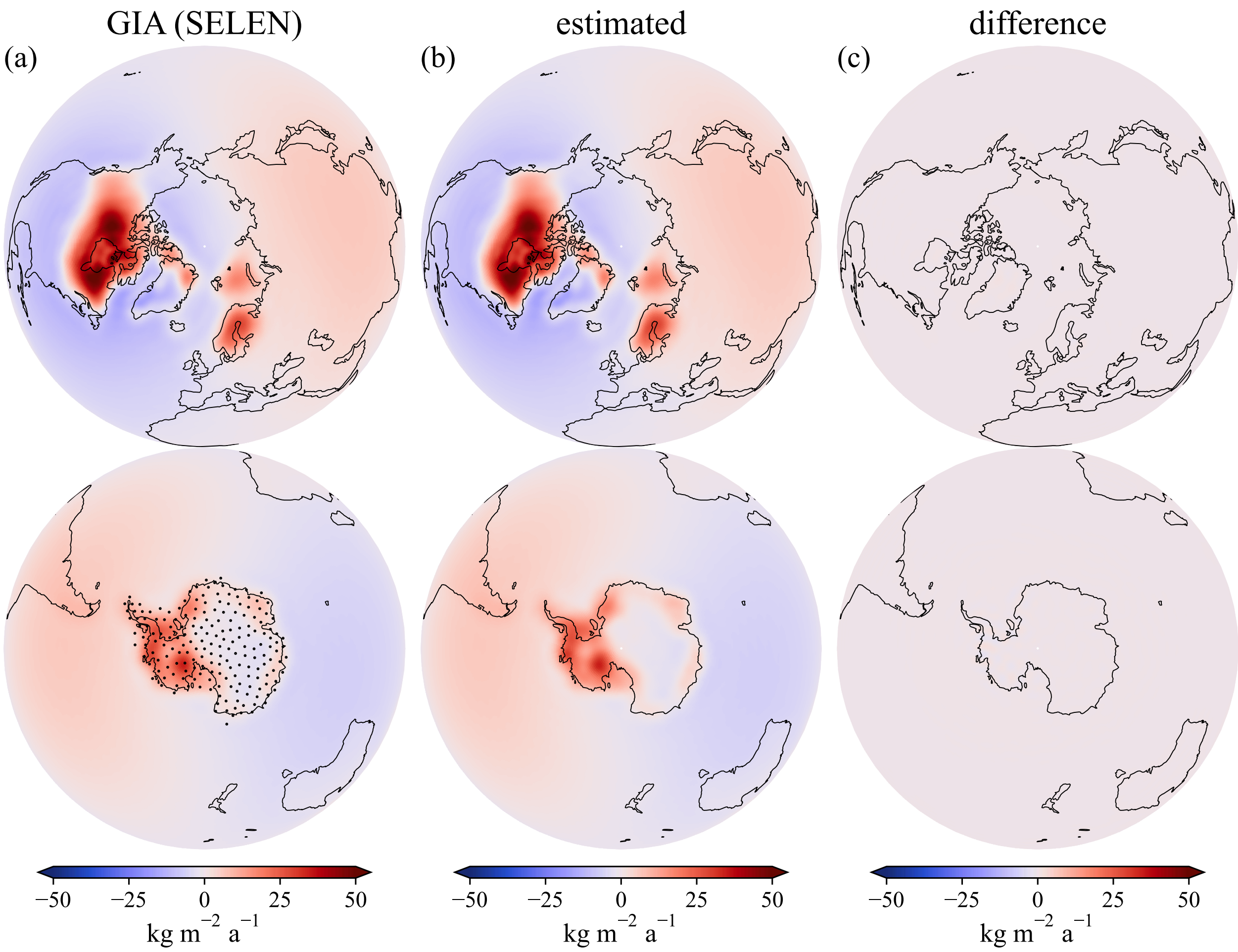

Figure S2: Surface density rates and rate differences associated to a test experiment, where a global GIA signal is estimated in the absence of other signals and of observation errors. Orthographic projections for the two hemispheres. (a): 'true' GIA signal simulated by SELEN based on the ICE-6G glacial history. (b): the estimated GIA signal. (c): differences between the original and the estimated GIA signal

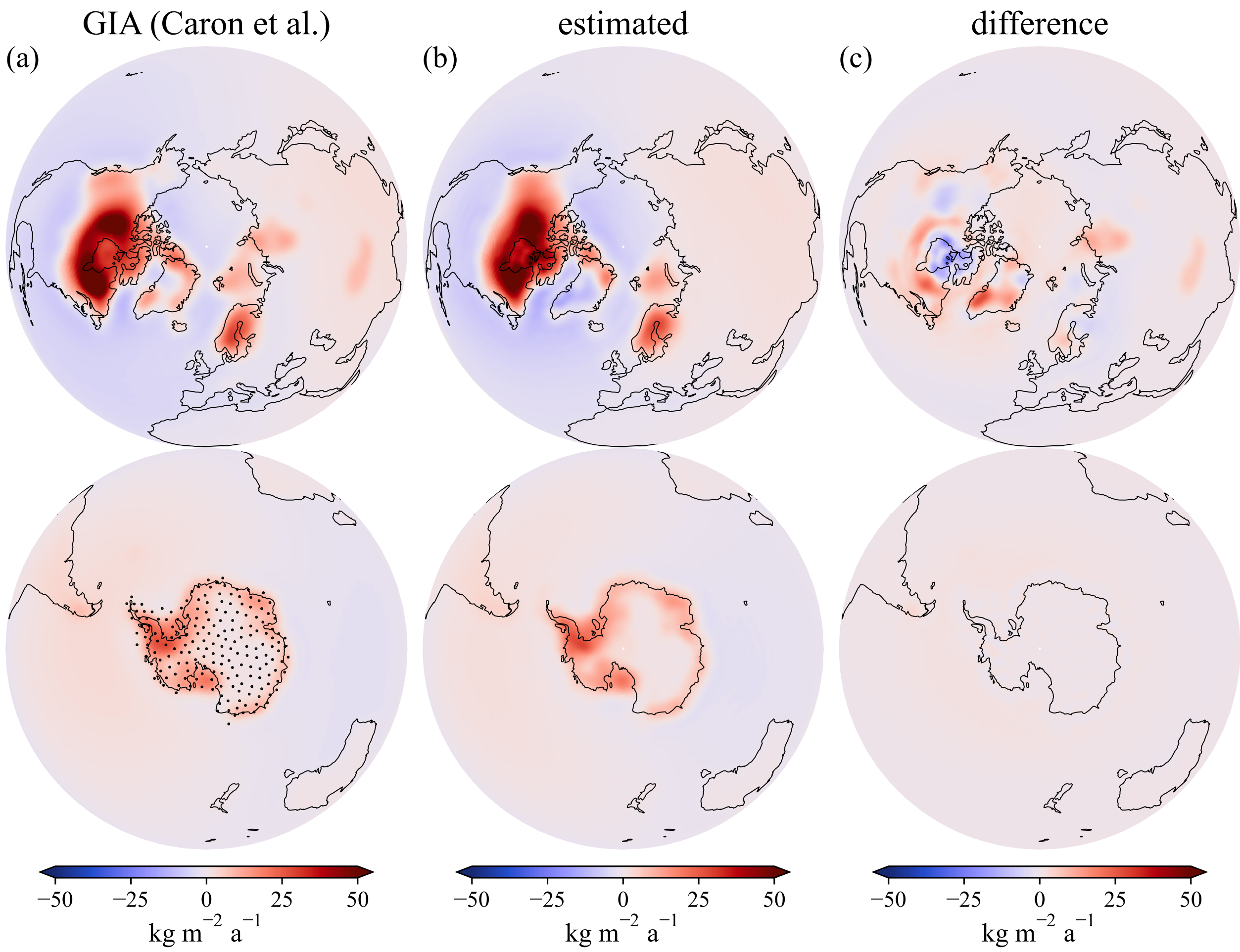

Figure S3: Surface density rates and rate differences associated to a test experiment analogous to Figure S2. Here the 'true' GIA signal (a) is the GIA modelling output from Caron et al. (2018).

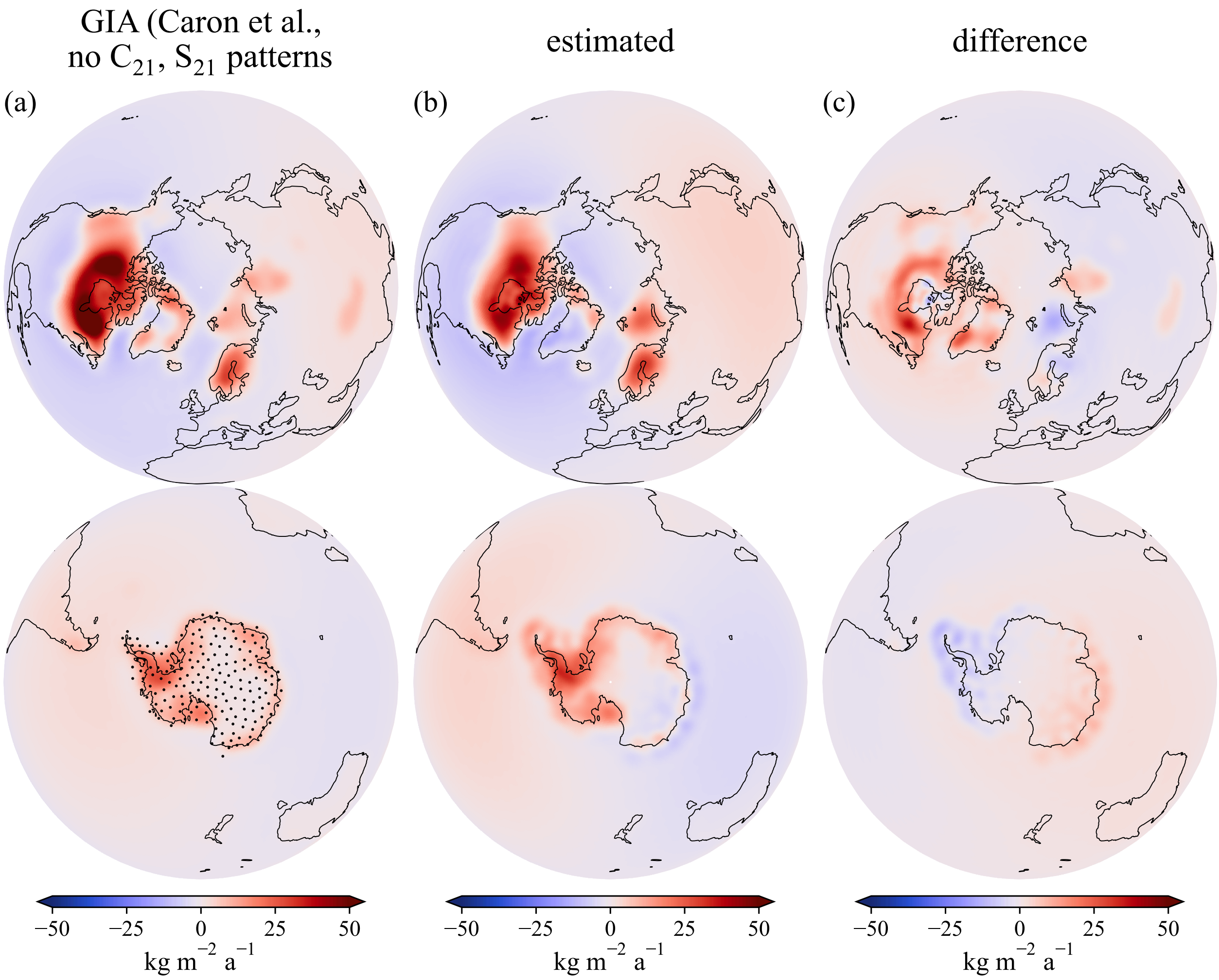

Figure S4: Surface density rates and rate differences associated to a test experiment analogous to Figure S2. Here the 'true' GIA signal (a) is the GIA modelling output from Caron et al. (2018). In this test experiment we do not co-estimate residual rotational feedback effects (we do not include the C_{21} and S_{21} fingerprints).

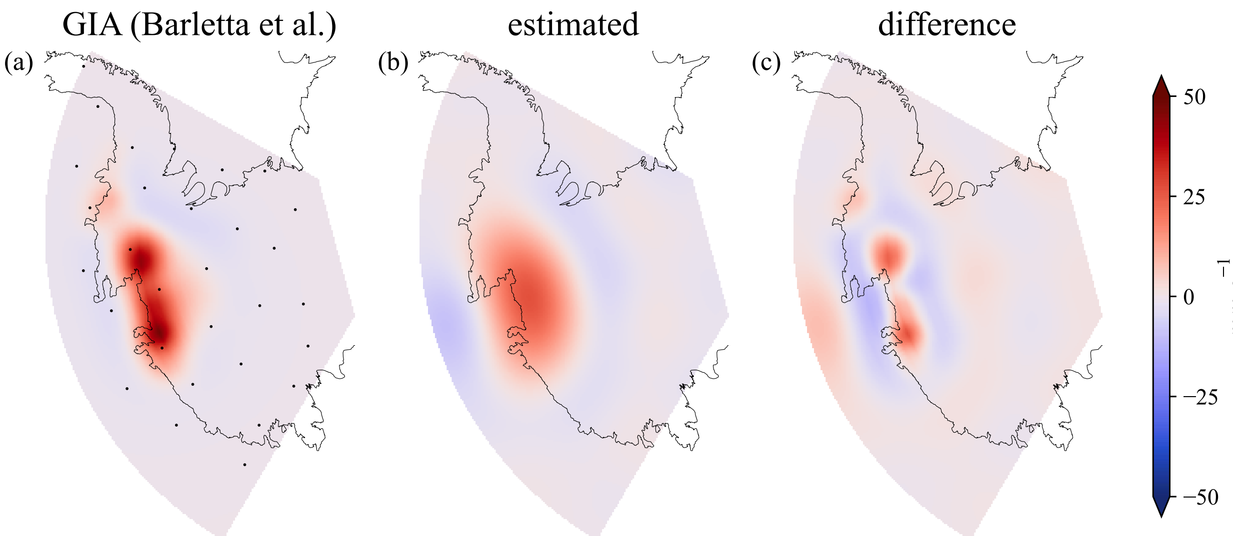

Figure S5: Bedrock motion rates and rate differences associated to a regional test experiment in West Antarctica, where a regional GIA signal is estimated in the absence of other signals and of observation errors. The 'true' GIA signal (a) is the GIA modelling output from Barletta et al. (2018). Black dots indicate the centres of the 30 GIA patterns in this region. (b): the estimated GIA signal. (c): differences between the original and the estimated GIA signal.

B Gravimetric stochastic information

We generate the covariance matrix $C(\boldsymbol{d}^{\mathrm{GRAV}})$ for spherical harmonic coefficients of degree larger than 1 as follows: Along with monthly estimates of Stokes coefficients from GRACE $\hat{\boldsymbol{S}}$, Mayer-Gürr et al. (2018) provide normal equations. The system of normal equations (with the normal equation matrix $\boldsymbol{N}$ and the right side $\boldsymbol{n}$) for every month j is

$$\hat{\boldsymbol{S}}^j = (\boldsymbol{N}^j)^{-1}\boldsymbol{n}^j \tag{S2}$$

From Jan 2003 until Aug 2016, we compute monthly covariance matrices $C^j(\hat{\boldsymbol{S}})$ by

$$C^j(\hat{\boldsymbol{S}}) = (\sigma_0^j)^2(\boldsymbol{N}^j)^{-1}. \tag{S3}$$

We estimate $(\sigma_0^j)^2$ from the weighted square sum of the residuals and the degree of freedoms provided by Mayer-Gürr et al. (2018). The sum of the residuals originate from the difference between observations (K-band range rates and kinematic orbits from GPS data of the GRACE satellites) and computed values. Note that the gravity field recovery approach from Kvas et al. (2019) includes background model uncertainties (Kvas and Mayer-Gürr, 2019). Afterwards, we calculate the mean covariance matrix and propagate it to the covariance matrix of surface densities.

Lastly, we assume a linear-seasonal model over 10-years including 8 parameters (offset, rate, annual cycles, semi-annual cycles, 161-period cycles). $C(\boldsymbol{d}^{\mathrm{GRAV}})$ used in the synthetic experiments is the error covariance matrix of the surface density rates which we retrieve by propagating the mean covariance matrix of the surface densities. Note that the covariance information for degree-1 coefficients is estimated separately (Sect. 3.4).

We compute an ensemble of degree-1 products following Swenson et al. (2008) to estimate the degree-1 covariance information. For this purpose we use the following GRACE Level 2 products: CSR RL06 (Bettadpur, 2018), JPL RL06 (Dah-Ning, 2018), GFZ RL06 (Dahle et al., 2018), and ITSG2018 (Mayer-Gürr et al., 2018). Further we use different GIA models from A et al. (2013), Peltier et al. (2015), and Caron et al. (2018). The ensemble has 12 members, from which we estimate the degree-1 covariance information. The rates are estimated over 10 years from Jan 2003 to Dec 2012.

Figure S6 illustrates the gravimetry error degree amplitudes of the surface density rates we assume in experiments E2A, E2B, E3A, and E3B in comparison to global GIA signal degree amplitudes (Sect. 3.3).

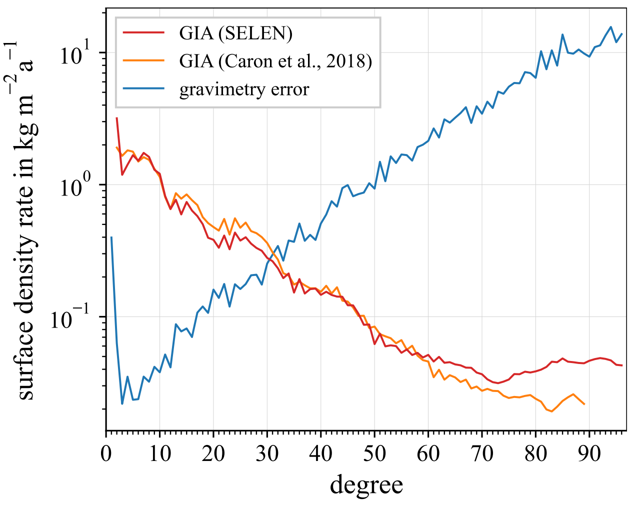

Figure S6: The gravimetry error degree amplitudes of the surface density rates estimated over a 10-year time period we use for the gravimetry observations (blue) in experiments E2A, E2B, E3A, and E3B. The degree amplitudes of the global GIA signal (red) modelled with ICE-6G glacial history with SELEN (Spada and Melini, 2019) and the GIA modelling output from Caron et al. (2018) (orange). Note that degree-1 coefficients of both GIA-signals are zero because the Love numbers are in a reference frame which has its origin in the centre of mass.

C Supplemental results

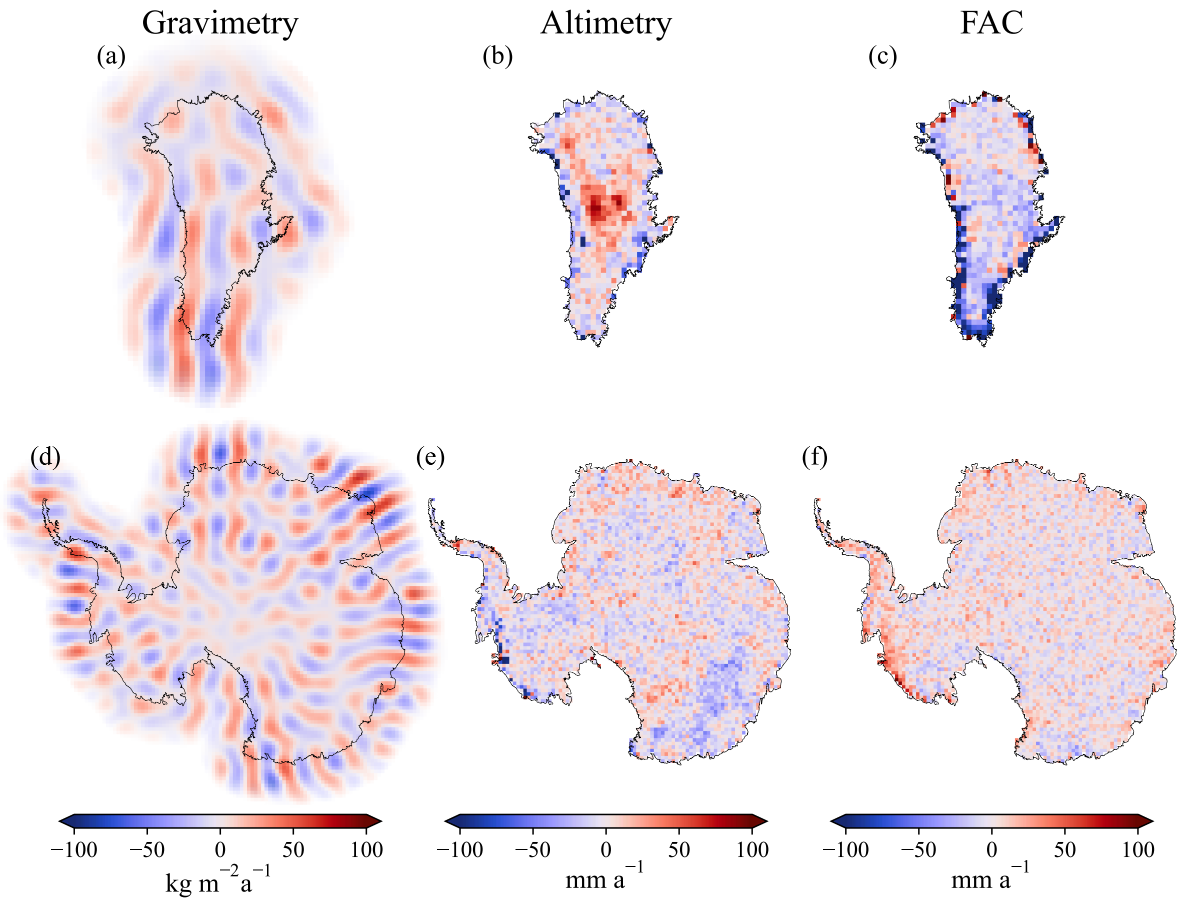

Figure S7: One realization of errors derived from the covariance information (Sect. 3.4) of each data set. Note that the gravimetry data is synthesized to the spatial domain over the GIS (a) and the AIS (d) for illustration purposes only.

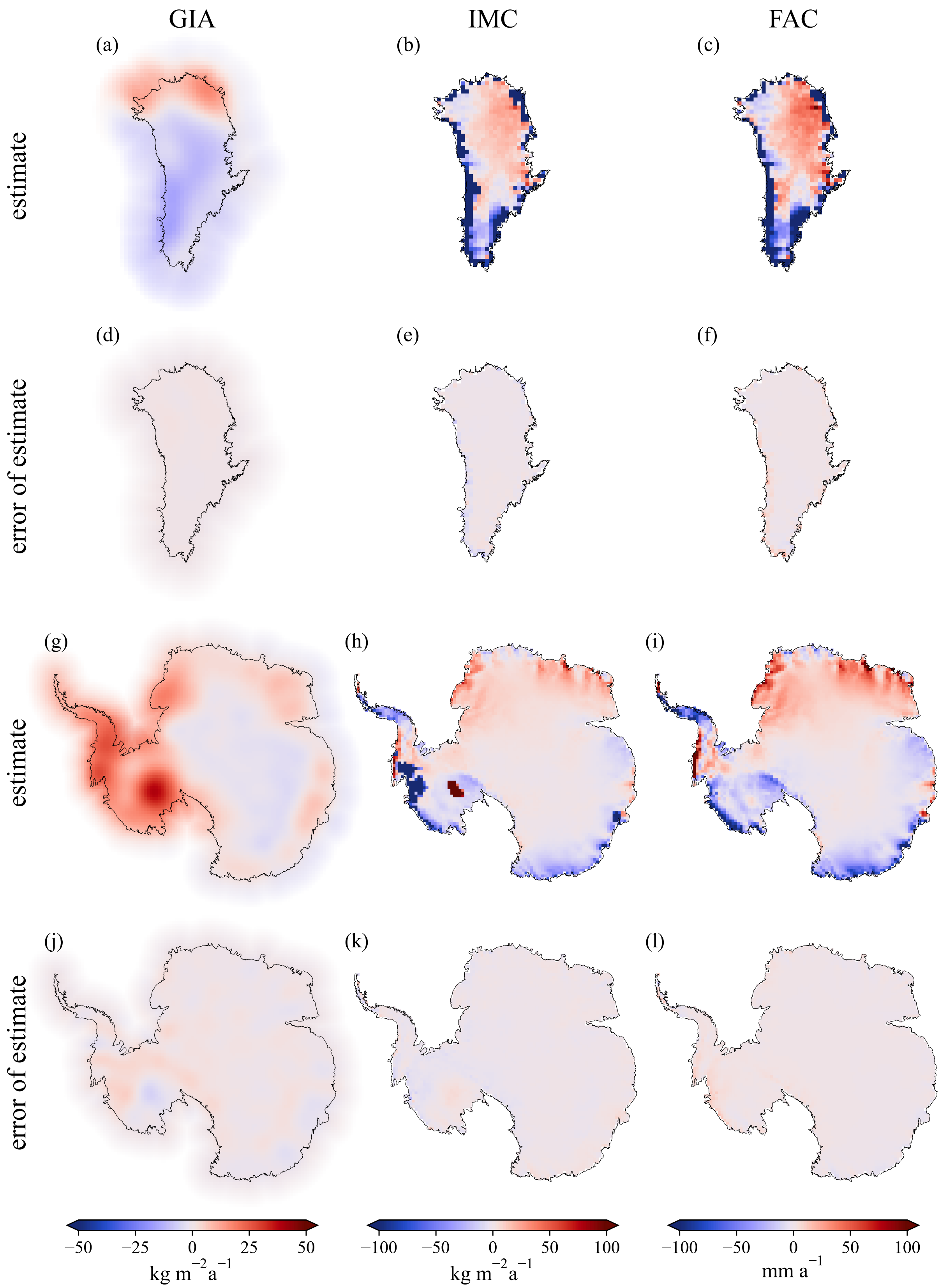

Figure S8: Results from Experiment 1A (E1A): estimated signals (a–c and g–i) and the difference to the original signals (d–f and j–l) for GIA-induced bedrock motion (first column), IMC-induced surface density change (second column), and FAC change (third column). The observations contain no errors, while the weighting is based on the full error covariance information.

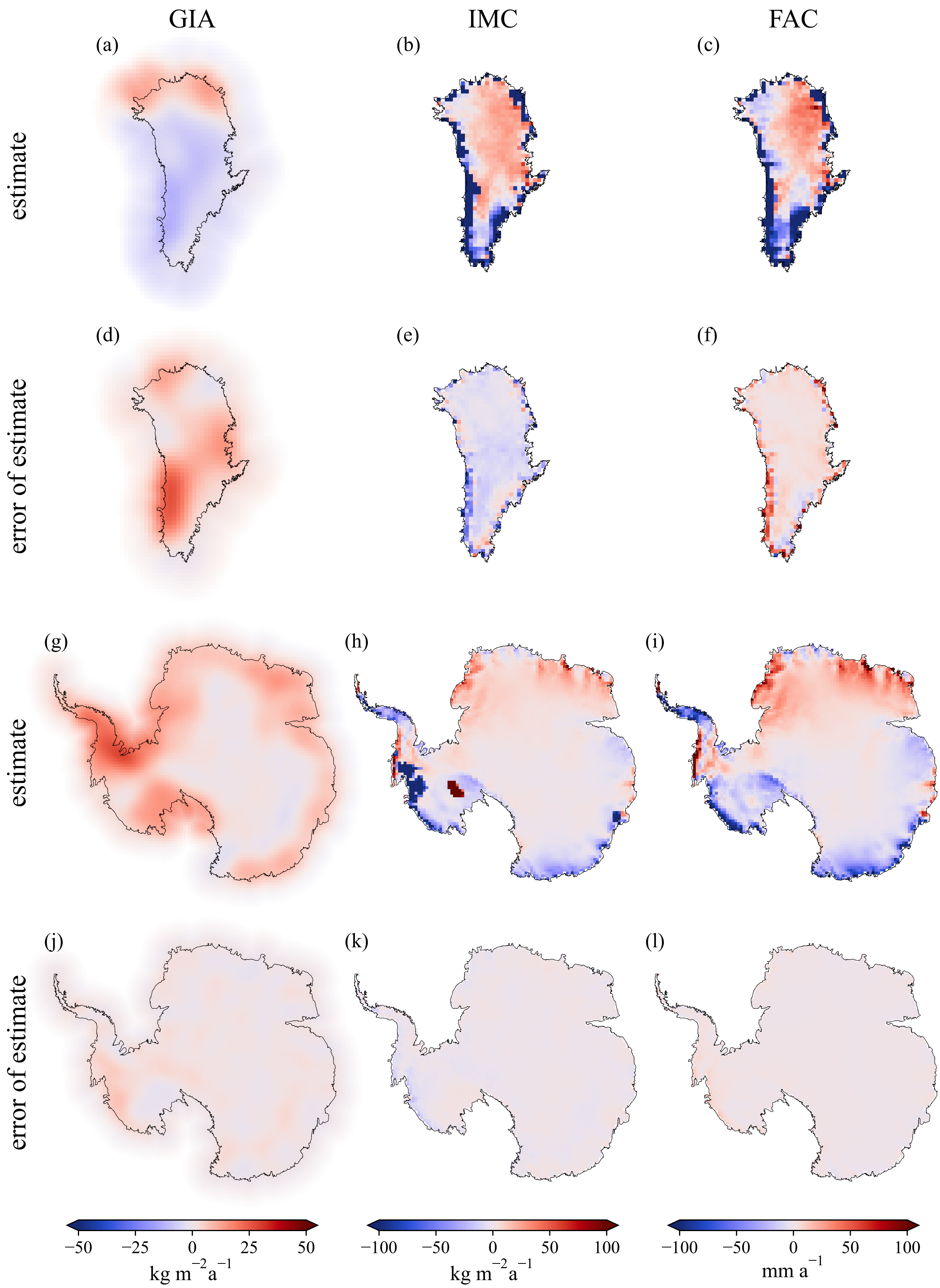

Figure S9: Results from Experiment 1B (E1B): estimated signals (a–c and g–i) and the difference to the original signals (d–f and j–l) for GIA-induced surface density change (first column), IMC-induced surface density change (second column), and FAC change (third column). The observations contain no errors, while the weighting is based on the full error covariance information.

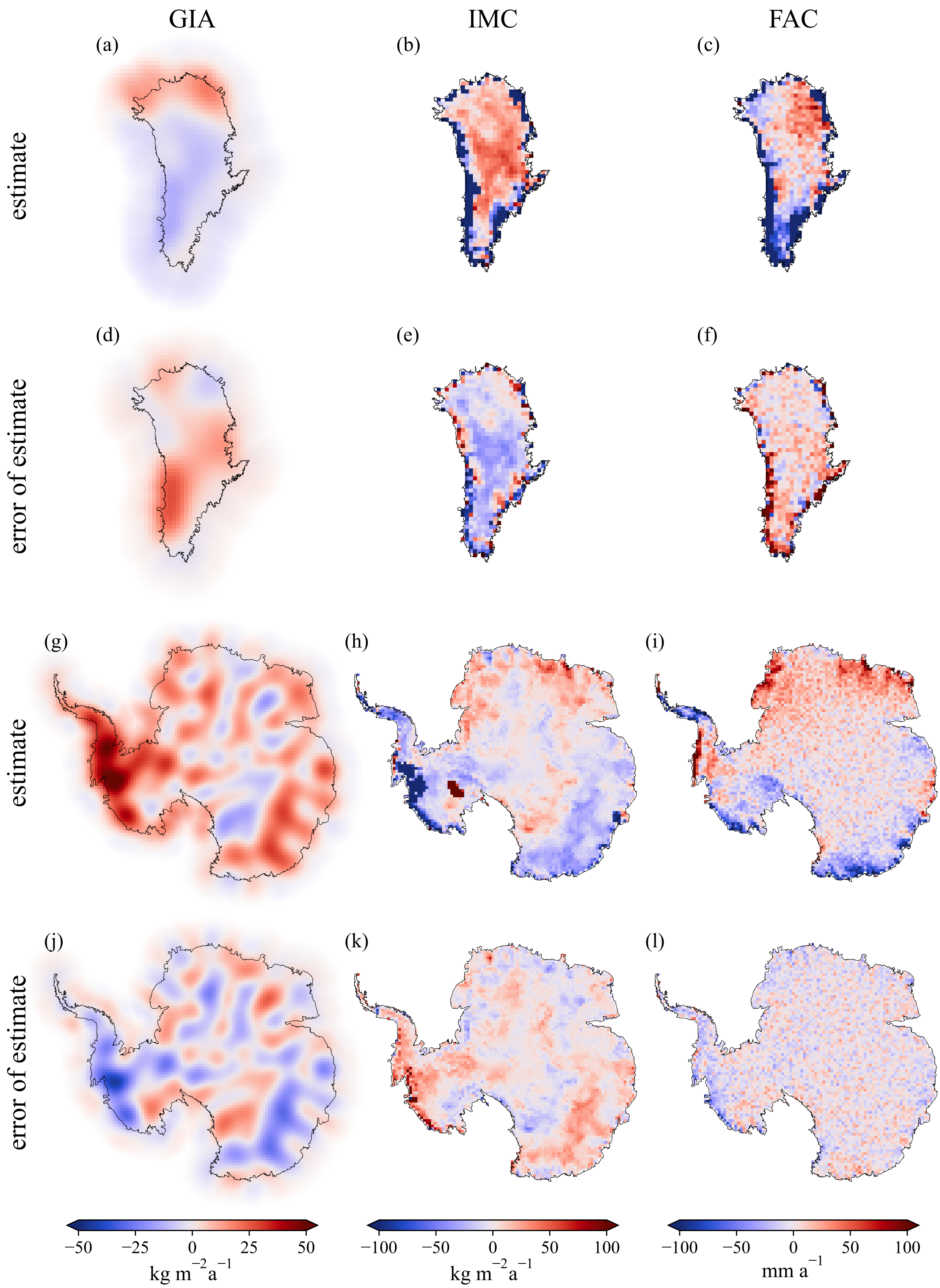

Figure S10: Results from Experiment 2B (E2B): estimated signals (a–c and g–i) and the difference to the original signals (d–f and j–l) for GIA-induced surface density change (first column), IMC-induced surface density change (second column), and FAC change (third column). The observations contain correlated errors and any correlations are neglected during the parameter estimation.

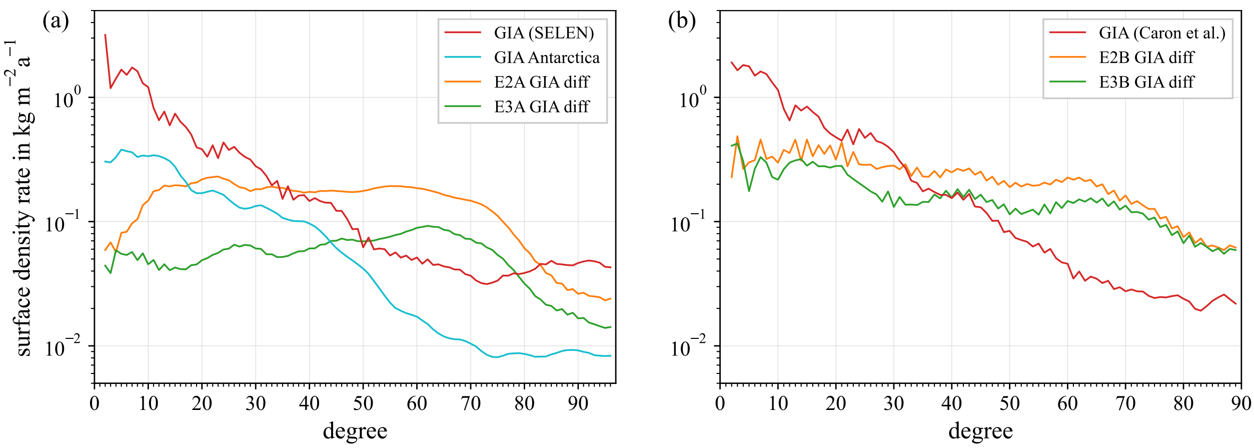

Figure S11: a) Degree amplitudes of the global GIA signal (red) modelled with ICE-6G glacial history with SELEN (Spada and Melini, 2019). The amplitudes of the GIA Signal in Antarctica (cyan line) modelled with SELEN with an ICE-6G ice history tailored to Antarctica. Degree amplitudes of the differences between this global GIA signal and the estimated global GIA signal in Experiment 2A (orange) and Experiment 3B (green). b) Degree amplitudes of the global GIA signal from Caron et al. (2018) (red), the differences between this signal and the results from Experiment 2B (orange), and Experiment 3B (green).

References

A, G., Wahr, J., and Zhong, S.: Computations of the viscoelastic response of a 3-D compressible Earth to surface loading: an application to Glacial Isostatic Adjustment in Antarctica and Canada, Geophys. J. Int., 192, 557–572, https://doi.org/10.1093/gji/ggs030, 2013.

Barletta, V., Bevis, M., Smith, B., Wilson, T., Brown, A., Bordoni, A., Willis, M., Khan, S., Rovira-Navarro, M., Dalziel, I., Smalley Jr., R., Kendrick, E., Konfal, S., Caccamise II, D., Aster, R., Nyblade, A., and Wiens, D.: Observed rapid bedrock uplift in Amundsen Sea Embayment promotes ice-sheet stability, Science, 360, 1335–1339, https://doi.org/10.1126/science.aao1447, 2018.

Bettadpur, S.: GRACE geopotential coefficients CSR release 6.0, University Of Texas Center For Space Research (UTCSR), https://doi.org/10.5067/GRGSM-20C06, 2018.

Caron, L., Ivins, E., Larour, E., Adhikari, S., Nilsson, J., and Blewitt, G.: GIA Model Statistics for GRACE Hydrology, Cryosphere, and Ocean Science, Geophys. Res. Lett., 45, https://doi.org/10.1002/2017GL076644, 2018.

Dah-Ning, Y.: GRACE geopotential coefficients JPL release 6.0, NASA Jet Propulsion Laboratory (JPL), https://doi.org/10.5067/GRGSM-20J06, 2018.

Dahle, C., Flechtner, F., Murböck, M., Michalak, G., Neumayer, H., Abrykosov, O., Reinhold, A., and König, R.: GRACE Geopotential GSM Coefficients GFZ RL06. V. 6.0., GFZ Data Services, https://doi.org/10.5880/GFZ.GRACE_06_GSM, 2018.

Kvas, A. and Mayer-Gürr, T.: GRACE gravity field recovery with background model uncertainties, J. Geod., 93, 2543–2552, https://doi.org/10.1007/s00190-019-01314-1, 2019.

Kvas, A., Behzadpour, S., Ellmer, M., Klinger, B., Strasser, S.and Zehentner, N., and Mayer-Gürr, T.: ITSG-Grace2018: Overview and Evaluation of a New GRACE-Only Gravity Field Time Series, J. Geophys. Res. Solid Earth, 124, 9332–9344, https://doi.org/10.1029/2019JB017415, 2019.

Mayer-Gürr, T., Behzadpur, S., Ellmer, M., Kvas, A., Klinger, B., Strasser, S., and Zehentner, N.: ITSG-Grace2018 – Monthly, Daily and Static Gravity Field Solutions from GRACE, GFZ Data Services, https://doi.org/http://doi.org/10.5880/ICGEM.2018.003, 2018.

Peltier, W., Argus, D., and Drummond, R.: Space geodesy constrains ice age terminal deglaciation: The global ICE-6G_C (VM5a) model: Global Glacial Isostatic Adjustment, J. Geophys. Res. Solid Earth, 120, 450–487, https://doi.org/10.1002/2014JB011176, 2015.

Spada, G. and Melini, D.: SELEN^4 (SELEN version 4.0): a Fortran program for solving the gravitationally and topographically self-consistent sea-level equation in glacial isostatic adjustment modeling, Geoscientific Model Development, 12, 5055–5075, https://doi.org/10.5194/gmd-12-5055-2019, 2019.

Swenson, S., Chambers, D., and Wahr, J.: Estimating geocenter variations from a combination of GRACE and ocean model output, J. Geophys. Res., B113, B08 410, https://doi.org/10.1029/2007JB005338, 2008.